THE HONG KONG POLYTECHNIC UNIVERSITY

DEPARTMENT OF CIVIL AND STRUCTURAL ENGINEERING

FIBER OPTIC MONITORING AND PERFORMANCE EVALUATION OF GEOTECHNICAL STRUCTURES

By

Honghu ZHU

A thesis submitted in partial fulfillment of the requirements

for the Degree of Doctor of Philosophy

Sep 2009

CERTIFICATE OF ORIGINALITY

I hereby declare that this thesis is my own work and that, to the best of my knowledge and belief, it reproduces no material previously published or written, nor material that has been accepted for the award of any other degree of diploma, except where due acknowledgement has been made in the text.

____________________ (Signed)

Honghu ZHU (Name of student)

Abstract of thesis entitled

FIBER OPTIC MONITORING AND PERFORMANCE EVALUATION OF GEOTECHNICAL STRUCTURES

Although health monitoring of civil infrastructures using fiber optic sensors has drawn increasingly attention, the potential of fiber optic monitoring in geotechnical applications is still not well investigated. The advantages of fiber Bragg grating (FBG) sensors in accuracy and reliability make them exceptionally attractive for monitoring strains, temperatures, displacements, etc. of geotechnical structures.

This research has therefore commenced to develop and apply FBG based sensors for geotechnical structures in both laboratory and field conditions, together with conventional transducers. Firstly, a variety of FBG based sensors including surface glued sensors, tube packaged sensors, embeddable sensing bars, in-place inclinometers, and settlement tubes, were developed and fabricated. Calibration test results show that the FBG based sensors are reliable for measuring strains, temperatures, and displacements with high accuracy.

Secondly, the FBG sensors have been installed on steel and glass fiber reinforced polymer (GFRP) soil nails for measuring strain distributions along nail lengths during field pullout tests, respectively. Typical test data indicate that the pullout resistance has an empirical relationship with *N* value in standard penetration tests (SPTs). The pullout-displacement relationships before failure can be fitted by hyperbolic functions. Based on the test results, a simplified pullout model for soil nail is proposed.

Thirdly, newly developed FBG sensing bars have been embedded in two physical models in laboratory for monitoring internal displacements. A two-dimensional (2-D) model of Wudu Dam was overloaded to failure in laboratory. The monitoring results from FBG sensing bars were in good agreement with those from conventional sensors. Based on the experimental and numerical results, the failure mechanism and overloading factor of safety of the gravity dam are studied. A three-dimensional (3-D) physical model has been built to simulate the performance of Shuangjiangkou Cavern Group during excavation. The model was instrumented with FBG sensing bars, multi-point extensometers (MPEs) and a digital photogrammetric system for displacement measurements. The monitoring results indicate that during the whole process of underground excavation, the displacements in the surrounding rock masses were in a considerably small range. After the excavation, the *in-situ* stresses were raised gradually and significant cracking and collapses were observed. The comparison between experimental and numerical results verifies the reliability of these sensors and leads to some conclusions on the deformation and overall stability condition of the cavern group.

Finally, FBG based sensors have been applied for monitoring geotechnical structures in the field. An FBG based monitoring system consisting of various FBG sensors has been installed in a mat foundation site during construction. Implications on the current design assumptions are discussed on the basis of the monitoring results. For a newly stabilized slope, slope movements, strains in a soil nail and two soldier piles were measured by an FBG based monitoring system during and after slope stabilization. The long-term monitoring results show that the slope movements fluctuated with time, indicating that rainfall infiltration was a main factor affecting the slope stability. The strains and stresses in a soil nail had the same tendency as the rainfall magnitude. The soldier piles at the slope toe came to play a role in resisting the potential sliding after the slope movements towards downhill accumulated to certain values.

Summary and findings are presented in Chapters 3 to 8. In Chapter 9, the original works and major conclusions of this research are summarized. The further research work related to this research topic is also suggested in this chapter.

RELATED PUBLICATIONS

Refereed Journal Articles

1. **Zhu, H. -H.**, Yin, J. -H., Yeung, A. T., and Jin, W. (2009). Field pullout testing and performance evaluation of GFRP soil nails. *Journal of Geotechnical and Geoenvironmental Engineering, ASCE*. (in review)
2. **Zhu, H. -H.**, Yin, J. -H., Dong, J. -H., and Zhang, L. (2009). Physical modelling and analysis of sliding failure of concrete gravity dam under overloading condition. *Geomechanism and Engineering*. (in review)
3. **Zhu, H. -H.**, Zhu, W. -S., Yin, J. -H., Zhang, Q. -B., and Jin, W. (2009). Application of fiber optic displacement monitoring technology in underground excavation model test. *Journal of China University of Mining and Technology*. (in Chinese) (in review)
4. **Zhu, H. -H.**, Yin, J. -H., Zhang, L., Jin, W., and Dong, J.-H. (2009). Monitoring internal displacements of a model dam using FBG sensing bars. *Advances in Structural Engineering*. (in press)
5. **Zhu, H. -H.**, Yin, J. -H., Jin, W., and Kuo, K. K. T. (2009). Health monitoring of foundation engineering using fiber Bragg grating sensing technology. *China Civil Engineering Journal*. (in Chinese) (in press)
6. **Zhu, H. -H.**, Yin, J. -H., Hong, C. -Y., Jin, W., and Ho, A. (2009). Fiber optic based monitoring technologies of slope engineering. *Geotechnical Investigation and Surveying*. (in Chinese) (in press)
7. **Zhu, H. -H.**, Yin, J. -H., Dong, J. -H., Zhang, L., Fung, K. W., and Jin, W. (2008). Deformation monitoring of dam model test by optical fiber sensors. *Chinese Journal of Rock Mechanics and Engineering*, 27(6), 1188-1194. (in Chinese)

Conference Presentations and Publications

1. Yin, J. -H., **Zhu, H. -H.**, and Jin, W. (2008). Monitoring of soil nailed slopes and dams using innovative technologies. Landslides and Engineered Slopes-From the Past to the Future, Proceedings of 10th International Symposium on Landslides and Engineered Slopes, Xi'an, China: Taylor & Francis, 1361-1366.
2. Yin, J. -H., **Zhu, H. -H.**, Fung, K. -W., Jin, W., Mak, L. M., and Kuo, K. (2008). Innovative optical fiber sensors for monitoring displacement of geotechnical structures. The HKIE Geotechnical Division 28th Annual Seminar, Hong Kong, 287-294.
3. **Zhu H. -H.**, Yin, J. -H., Jin, W., and Zhou, W. -H. (2007). Soil nail monitoring using fiber Bragg grating sensors during pullout tests. The Joint 60th Canadian Geotechnical and 8th IAH-CNC Conferences, Ottawa, Canada, 821-828.
4. Yin, J. -H., **Zhu, H. -H.**, and Jin, W. (2007). Development and application of two types of optical fiber sensors for monitoring soil nails during pull-out testing. The 4th Cross-strait Conference on Structural and Geotechnical Engineering, Hangzhou, China: Zhejiang University Press, 1003-1009.
5. Yin, J.-H., **Zhu, H.-H.**, Jin, W., Yeung, A. T., and Mak, L. M. (2007). Performance evaluation of electrical strain gauges and optical fiber sensors in field soil nail pullout tests. Geotechnical Advancements in Hong Kong since 1970s, The HKIE Geotechnical Division 27th Annual Seminar, Hong Kong, China, 249-254.

ACKNOWLEDGEMENTS

I would like to express my deepest gratitude to my supervisor, Professor Jian-Hua Yin, for his encouragement, support and guidance during this period of study. The privilege of working with him has appreciably influenced my professional development and perspectives.

Financial supports for this research from the Hong Kong Polytechnic University (PolyU) are gratefully acknowledged. I am also very grateful to Professor Wei Jin and his research group members including Dr Hoi Lut Ho and Dr Jian Ju in Department of Electrical Engineering, PolyU, who are always so kind to provide me with their support in fabricating FBG sensors. The physical model tests of Shuangjiangkou Cavern Group and Wudu Dam were co-investigated with Professor Wei-Shen Zhu of Shandong University and Professor Lin Zhang of Sichuan University, respectively. From the conversation and discussion with them, I have learnt a lot. In the field testing and instrumentation work, Dr Albert Yeung of the University of Hong Kong, Ir L. M. Mak and Ir Kelvin Kuo of LMM Consulting Engineers Ltd, Ir Ronald Li of Jacobs China, Ltd, Dr W. Sun of Geotechnical Engineering Office, Ir Albert Ho and Ir Locus Wong of Ove Arup & Partners Hong Kong Ltd and their colleagues have provided numerous assistance, which made this work possible.

I am also very thankful for the comments and suggestions from the members of my oral examination committee, Professor Kam-Tim Chau, Professor Buddhima Indraratna, and Dr Jun Yang. Thanks are also extended to Dr Wan-Huan Zhou, Dr Wen-Bing Wei, Mr Ka Wai Fung, Mr Cheng-Yu Hong, and Mr Hua-Fu Pei in Department of Civil and Structural Engineering, PolyU for their help and encouragement.

Finally, I would like to express my sincere thanks to my wife, Shu-ping Fu, and my parents, for their understanding and constant support throughout my study.

TABLE OF CONTENTS

LIST OF TABLES

LIST OF FIGURES

CHAPTER 1:

INTRODUCTION

1.1 BACKGROUND

Geotechnical structures include deep and shallow foundations, slopes and dams, landfills and excavations, embankments and tunnels, underground and earth retaining structures, etc. In geotechnical engineering, there are lots of uncertainties arising from the complexity of geological conditions, behaviors of soil and rock masses, loading combinations and so on. For a geotechnical structure, the deformation and stability state varies with time, hydraulic and stress conditions. This makes it much more complicated to predict the behavior and assess the factor of safety of a geotechnical structure than other civil infrastructures.

To minimize the possibility of potential failure, which cannot be fully eliminated in engineering practice, the field performance of a geotechnical structure, especially the failure mechanism, should be evaluated in detail before construction (Dunnicliff 1993). This requires in-depth understanding of strength and stiffness of soil and rock, analyzing methods of structures and hydraulics of groundwater flow. Appropriate assumptions have to be made to simplify geotechnical problems under investigation, based on which correct geotechnical design can be implemented. In geotechnical engineering, there are basically three approaches for studying the performance of a geotechnical structure, namely physical modeling, numerical simulation, and field monitoring.

In physical model tests and field instrumentation practices, various geotechnical instruments are employed. However, the obvious disadvantages of the current measurement techniques, such as low resolution, poor durability, and complex installation methods, make them far from attractive. There is therefore an urgent requirement for a monitoring system allowing automatic, long-distance, and long-term measurement of a number of parameters with high precision and spatial resolution. In these domains, the concept of fiber optic sensor (FOS) based monitoring has proved its effectiveness (Inaudi 1997). With the development of fiber optic sensing technologies, fiber optic based instruments play an increasingly important role in structural health monitoring (SHM) of civil infrastructures. A number of geotechnical applications today require automatic and remote monitoring over a considerably long period of time, for instance, several months or several years. Regarding this, fiber optic sensors provide an exceptionally attractive solution. The advantages of incorporating fiber optic sensors in geotechnical instrumentation are now being realized by geotechnical engineers.

An optical fiber is a glass or plastic fiber designed to guide light along its length by total internal reflection. With the rapid development of fiber optics, optical fiber is widely used in telecommunication nowadays, which permits digital data transmission over longer distances and at higher data rates than electronic communication. Moreover, optical fiber can form different types of sensors, which present unique advantages that have no match in conventional sensing techniques, including (Feng et al. 1995; Inaudi 1997; Moyo et al. 2005):

(a) The fiber optic sensor is a passive component requiring no external (electrical) power. They form an intrinsic part of the same optical fiber that transmits the measurement data to a distant receiver free from any electromagnetic interference (EMI) caused by power lines, trains and cars, and thunderstorms.

(b) The fiber optic sensor has relatively high resistance to corrosion. It especially fits for long-term measurement in harsh environments that are occasionally encountered in geotechnical engineering, such as high temperature or submerged conditions.

(c) The fiber optic sensor has a compact profile and a light weight. The miniature size makes it easy to be installed in geo-structures without affecting their structural integrity.

(d) The fiber optic sensor can be multiplexed in parallel or in series. By the technologies of wavelength division multiplexing (WDM) and time division multiplexing (TDM), a number of sensors can form a quasi-distributed or fully-distributed sensing array along a single optical fiber. An internal sensing network consisting of fiber optic sensors and interrogators can be easily constructed using a simple configuration.

(e) The fiber optic sensor has excellent accuracy and sensitivity. For instance, the strain and temperature measurements of fiber Bragg grating (FBG) sensors have typical resolutions of 1 $\mu\varepsilon$ and 0.1 ^{o}C, respectively. This exceeds the requirements of geotechnical instrumentation in most cases.

(f) The fiber optic sensor can perform absolute measurement and self reference, without the requirement of zero point setting. For long-term monitoring, the data acquisition system can be connected to the sensors periodically when measurements should be taken.

(g) The fiber optic sensor is capable of transmitting signals over a long distance without any additional amplifiers. In most cases, the optical loss in a sensing array does not affect the parameters being measured. Thus this technology is suitable for remote and automatic sensing.

(h) The fiber optic sensor allows the monitoring of different parameters. This includes the direct measurement of strain and temperature, and indirect measurement of displacement, pressure, force, rotation, and so on.

However, by far the fiber optic sensor has its own drawbacks when applied in geotechnical engineering, including (Feng et al. 1995; Inaudi 1997; Moyo et al. 2005):

(a) Although recent advances make the theory of fiber optic sensing more mature, there are still a lot to be developed for manufacturing and demodulation technologies. Until now, there are few interrogators with both high resolution and low cost. The fiber optic sensor is potentially low cost in mass production but currently it is still more expensive than conventional sensor.

(b) When applied to civil infrastructures and exposed to harsh environments, the inherent fragility of the fiber optic sensor makes it susceptible to damage due to accidental impacts (from human, animal, or equipment). Thus special encapsulation and protection systems against physical damage should be provided.

(c) The fiber optic sensor is normally sensitive for both strain and temperature. Thus to separate the effect of strain and temperature is a key problem in the analysis of field data. For instance, the strain measurement should be fully temperature compensated.

(d) For geotechnical engineers, fiber optic monitoring is a relatively new technology. A monitoring network tailor-made for geotechnical application, which permits the monitoring of stress, strain, settlement, and even earth pressure and pore water pressure, is still under investigation.

1.2 OBJECTIVES OF THE RESEARCH

The subject of fiber optic sensor based geotechnical monitoring is relatively new but is gathering momentum. This study concerns the application of FBG sensing technology in physical model tests and field instrumentation of geotechnical structures, and investigates their performance using monitoring results and numerical models. The main objectives of this research project are:

(a) To develop various fiber optic sensors based on FBG technology for the measurement of strain, temperature, and displacement of geotechnical structures;

(b) To apply FBG sensors in strain monitoring of steel and glass fiber reinforced polymer (GFRP) soil nails during pullout tests. Empirical functions are proposed based on the monitoring results for determining pullout resistance and analyzing the pullout performance of soil nails.

(c) To apply FBG sensors in the physical model tests of a cavern group and a concrete gravity dam in laboratory, together with conventional sensors. Based on the monitoring results and numerical analysis, the deformation and failure mechanisms of the small-scale models and the prototype are investigated.

(d) To establish fiber optic monitoring systems for field instrumentation and safety assessment of a mat foundation and a newly stabilized slope. The techniques of field installation and data collection are presented in details. The monitoring results are further discussed.

1.3 ORGANIZATION OF THE THESIS

This thesis consists of nine chapters as follows:

Chapter 1: Introduction. This chapter briefly presents the research background, the objectives, specific issues to be investigated, and the organization of the thesis.

Chapter 2: Literature review. The review finds out the current methods for performance evaluation of geotechnical structures and the techniques of conventional geotechnical instrumentation. Previous research work on the development of FBG sensors for geotechnical applications will be presented as well.

Chapter 3: Development of FBG sensors for geotechnical applications. The design, fabrication and calibration of FBG sensors for monitoring strain, temperature and displacement are presented in detail.

Chapter 4: Fiber optic monitoring and evaluation of soil nail pullout performance. The results of laboratory and field pullout tests of steel soil nails are presented. The empirical relationship between the pullout resistance and SPT *N* value will be discussed. The pullout behaviors of GFRP soil nails are studied through field pullout tests. A simplified model to simulate the pullout behavior of soil nails is proposed. The effects of nail diameter, interface shear resistance, and nail stiffness on the pullout performance of soil nails are further evaluated.

Chapter 5: Fiber optic monitoring and performance evaluation in the model tests of Shuangjiangkou Cavern Group. Laboratory model tests have been carried out to study the deformation and failure mechanism of Shuangjiangkou Cavern Group with high *in-situ* stresses. The model construction, test set-up and procedures are introduced in this chapter. The monitoring results of displacements in the excavation and overloading stages are presented and analyzed. Comparisons between the experimental results and corresponding numerical results are conducted.

Chapter 6: Fiber optic monitoring and performance evaluation in the model test of Wudu Dam. The effectiveness of using physical modeling for analyzing the behavior of Wudu Dam in overloading condition has been evaluated in this chapter. The materials properties, test set-up and procedures of the laboratory model test are briefly introduced. The monitoring results presented in this chapter indicate that sliding within foundation is one of the failure modes of concrete gravity dams, especially when the foundation is highly jointed. A finite element model has been established for simulating the whole test procedures. The numerical results indicate that the failure process of sliding within foundation can be predicted by finite element method (FEM) as well.

Chapter 7: Fiber optic monitoring and performance evaluation of a mat foundation. FBG embedded strain sensors, settlement tubes and in-place inclinometers were installed on site and used to monitor concrete strains, settlements and their distributions in the construction stage. From the monitoring results, some implications for foundation design are further discussed.

Chapter 8: Fiber optic monitoring and performance evaluation of a newly stabilized slope. Strain sensors, temperature sensors, and an in-place inclinometer based on FBG technology were installed on site to measure the strains in a soil nail and two soldier piles and the slope movements. Long-term monitoring results are presented and interpreted in this chapter.

Chapter 9: Summary, conclusions and suggestions. A summary and main conclusions made from this research project are presented. Suggestions are provided for further research in this area.

CHAPTER 2:

LITERATURE REVIEW

2.1 INTRODUCTION

The review of previous investigations relevant to the present research topic is conducted in this chapter, which is divided into three parts. The first part is an introduction to the methods for performance evaluation of geotechnical structures. The second part summarizes the current technologies of geotechnical instrumentation. The last part is devoted to the development of FBG sensors and their application for measuring strains, temperatures, displacements, etc. in geotechnical engineering.

2.2 PERFORMANCE EVALUATION OF GEOTECHNICAL STRUCTURES

The performance of geotechnical structures can be investigated by physical modeling, numerical simulation and field monitoring. The results from these approaches can be compared to each other for calibration, validation and demonstration purposes (Figure 2.1).

2.2.1 Physical modeling

Although full-scale field testing is the most preferred means of performance evaluation of geotechnical structures, the cost, time duration, and experimental difficulties make it unattractive (Wood 2004). Physical model tests include pressure chamber tests in 1-g gravity field, centrifuge model tests, shaking table tests, and geo-environmental tests.

Since 1970s, a wide range of geotechnical problems have been investigated using physical modeling techniques, which provide a comprehensive and visible interpretation of field performance of geotechnical structures under well-controlled laboratory conditions. (e.g. Bray et al. 1993; Zornberg et al. 1997; Chang et al. 1999; Tinawi et al. 2000; Liu et al. 2003a).

Similarity materials are used to construct small-scale models and then appropriate boundary and loading conditions are applied on these models. According to similarity theory of physical modeling, the following laws of similitude should be met (Liu et al. 2003a; Chen et al. 2006):

$$\frac{C_\sigma}{C_\gamma C_L} = 1 \tag{2.1}$$

$$C_\varepsilon = C_\gamma = C_\nu = 1 \tag{2.2}$$

$$\frac{C_o}{C_E} = \frac{C_s}{C_L} = \frac{C_o}{C_f} = 1 \tag{2.3}$$

where the symbols L, γ, s, E, ν, σ, ε, f denote the parameters of geometry, density, displacement, deformation modulus, Poisson's ratio, stress, strain and strength, respectively.

If the dimensions and properites of a physical model satisfy the similitude criteria, the demonstrated behaviors of the scaled model, which are measured by difficult types of sensors, can be used to identify the actual deformation and failure mechanisms of the prototype. The results from physical model testing can also be used to a) demonistrate the applicatbitliy of conceptual model, and b) provide valuable insights regarding the validation of numerical analysis (Wood 2004). By this means, theoretical or empirical hypotheses can be validated and design guidelines can be established. However, these studies have encountered fundamental difficulties pertaining to similitude requirements and specifically modeling of the construction phase, as well as to the proper instrumentation of scaled models.

2.2.2 Numerical modeling

Numerical simulation techniques include finite element method (FEM), finite difference method (FDM), boundary element method (BEM), and discrete element method (DEM) (Carter et al. 2006). In most of these methods, the entire region is discretised into a number of sub-regions or elements. The governing equations of the problem under investigation are applied separately and approximately within every element, translating the governing differential equations into matrix equations for every element. Compatibility, equilibrium and boundary conditions are enforced at the interfaces between elements and at the boundaries of the numerical model. Due to the simplification of constitutive models and boundary conditions, the numerical results should to be checked prior to application. The results are also affected by meshing techniques and model parameters. The validation of numerical models still relies on the development of geotechnical instrumentation, which can provide accurate and reliable data in laboratory or from the field.

2.2.3 Field monitoring

For geotechnical engineers, to ensure that their design to be safe and efficient, field monitoring data is very important. In field monitoring of geotechnical structures, the following contents are measured by various geotechnical instruments (Dunnicliff 1993):

(1) Groundwater level and pore water pressure;

(2) Lateral ground movement and deformation;

(3) Settlement or heave;

(4) Tilt or rotation;

(5) Load or stress on structural members;

(6) Earth pressure;

(7) Vibration (for dynamic and seismic study);

(8) Ground temperature and so on.

Apart from laboratory-scale physical modeling, field monitoring of geotechnical structures and ground soils has been acknowledged as an effective tool to assist with field observations. Various geotechnical instruments have been developed to characterize site conditions, verify design assumptions, monitor construction effects, enforce the quality of workmanship, and provide early warning of impending failures. The full-scale field monitoring may consist of permanent continuous, periodical or periodically continuous recording of representative parameters, over short or long terms. The knowledge concerning the monitored geotechnical structures is increased based on the monitoring results. However, the field monitoring data are highly affected by installation quality of the instruments, EMI, and other factors.

2.3 GEOTECHNICAL INSTRUMENTATION

The birth of geotechnical instrumentation occurred in the 1930s and 1940s. In the past few decades, manufacturers of geotechnical instruments have developed a large assortment of products. Basically, geotechnical instruments can be grouped into two categories (Dunnicliff 1993). Some instruments are used for in-situ determination of geotechnical related parameters, such as shear strength, compressibility and permeability, normally during the design phase of a project. Others are used for field monitoring, normally during the construction or operation phase of a project.

2.3.1 Instrumentation in physical modeling

For geotechnical structures, displacements are considered to be a direct response to loading and thus the most apparent indication of stability conditions (Dunnicliff 1993). In physical model testing, the measurement of displacements is generally a key issue.

Instruments for measuring displacements of small-scale models can be categorized into two groups: a) those for surface displacement measurement, and b) those for internal displacement measurement. Taking model dams as an example, conventional optical, mechanical and electrical instruments have been widely employed to monitor surface displacements. Examples of the instruments include linear variable differential transformers (LVDTs) (Ghobarah and Ghaemian 1998; Barpi et al. 1999), wire transducers (Tinawi et al. 2000; Morin et al. 2002), displacement proximity probes (Plizzari et al. 1995), inductive displacement sensors (Liu et al. 2003a), and digital photogrammetric technique. However, most of these instruments are based on surface point and one-dimensional (1-D) measurements (normally in vertical or horizontal direction). A large number of measurement points are required in order to obtain a satisfactory displacement profile.

The measurement of internal displacements is necessary for studying the internal deformation and failure mechanism of the model under investigation. For field applications, conventional subsurface instruments, such as extensometers, inclinometers and settlement plates, are normally installed within a borehole. However, due to space limit, these instruments can hardly be used for small-scale physical models. Based on the electrical time domain reflectometry (TDR) technique, Lin and Thaduri (2006) have developed a distributed strain sensor to monitoring internal structural deflections of a beam. However, the resolution was low and the data collection was time consuming. Baek et al. (2007) introduced a new magnetic technology for measuring the radial displacement in a model ground. Their tests show that the deterioration of magnet intensity with elapsed time was hard to calibrate and the magnetic pole had to be placed accurately to obtain reliable data. Sometimes strain-gauged cantilevers are utilized to measure internal displacements in an indirect way (Liu et al 2003a). The installation difficulties and adverse influence of lead wires make this approach unattractive.

2.3.2 Field instrumentation in foundation engineering

Foundations of civil infrastructures are either shallow or deep. The current foundation design methods have some apparent limitations. The real behavior of natural soils is non-linear, time-dependent and anisotropic. The theoretical model in foundation design, which is on the basis of soil mechanics principles, may not represent the actual field situations with the required degree of accuracy. Additionally, based on limited site investigation techniques and laboratory testing, the routine approach to foundation design is not satisfactory.

The construction quality of foundations is another concern. In Hong Kong, there has been a series of building scandals arising from substandard piling works (Independent Commission against Corruption). The first Short Pile Incident was found in the Hong Kong Central Station development site in 1997. Among all the short pile cases, the Tin Shui Wai Piling Incident and the Shatin Piling Incident were the two most serious. In 1999 and 2000, several housing blocks under construction in Tin Shui Wai and Yuen Chau Kok were found to have piles shortened up to about 15 m. The incidents were uncovered when excessive uneven settlements occurred.

For ground movement measurement, apart from the conventional survey techniques, various geotechnical instruments are currently available, which can monitor deformation at the ground surface, under a shallow and deep foundation, and within the soil mass.

With shallow foundations, the most common instrumentation program is settlement monitoring of individual footing bases (Hanna 1973). Foundation settlements can be measured by settlement plates and gauge monitoring tubes. Single and multiple point settlement gauges, vertical tube settlement gauges, and full profile gauges are also frequently used in the field. Settlement in a certain depth may be measured by using probe extensometer buried in boreholes, which can obtain the distance between two or more points in the vertical direction. Measuring points are identified either mechanically or electrically by a probe.

For horizontal displacements, telescoping tubes, tensioned wire devices and strain meters are normally used. Inclinometers, both horizontal and vertical, are used extensively to monitor movements of ground soil under foundations. However, most of them need manual operation and the readings are affected by a number of factors.

Pore water pressure is one of the most critical factors that have to be measured to determine the stability of foundations. It is normally measured by various types of piezometers. There are mainly three types of piezometric cell used for pore pressure measurement, (a) pneumatic piezometric cells, in which the pressure on a membrane is measured by the gas pressure; (b) vibrating wire piezometers, in which the pressure measurement is done by vibrating thread extensometers; and (c) strain gauges piezometers, in which vibrating thread extensometers are replaced by electrical extensometers. All of the piezometric cells require strict installation operations.

Measurement of total stress in soil masses and adjacent to soil/foundation boundaries can be achieved by earth pressure cells. However, the cost makes it not so applicable. When concerned with stresses acting on a structure during or after the construction activities, it is usually preferable to isolate a portion of the structure and to determine stresses with the use of embedded load cells and strain gauges.

For deep foundations, geotechnical engineers are interested in loads, settlements and their distributions in the longitude direction of piles or caissons. In special cases, the performance of the pile and the piling equipment may also require evaluation during pile driving operation.

The distribution of loads along piles may be obtained by using the deformation gauge, which normally consists of a steel sounding rod protected inside a steel tube embedded in a concrete pile or welded to the outer face of a steel H-pile. The instrumentation of large clusters of piles is a tougher task than that of a single pile. Measurement of load distribution within a pile group may be achieved by inserting a load cell on the top of each pile. Different types of load cells such as mechanical, vibrating wire or strain gauged cells are normally used. The photoelastic load indicator is another device which is relatively cheap and easy to install. However, observing the photoelastic interference fringe pattern requires a short distance.

Contact pressure between the ground surface and the pile cap can be recorded by earth pressure cells placed in contact with the soil prior to the pouring of the pile cap.

Settlement and distribution of settlement with depth below the pile cap may be measured by one or more sets of multiple position borehole extensometers (rod or wire type). The testing of piles subject to lateral loads is fairly common and the instrumentation may be used to record pile deflection, bending stress and lateral movement of the pile top. Different types of inclinometers are widely used to measure the bending of piles during driving.

Sometimes, special vibration and ground temperature monitoring is required for foundations of high rise buildings.

2.3.3 Field instrumentation in slope engineering

In Hong Kong's hilly terrain, there are thousands and thousands of natural slopes. The development of construction projects has also led to the formation of more than 57000 of man-made slopes. In recent decades, serious landslides have caused deaths of over 470 persons and loss of property in billions of dollars. In 1972, Sau Mau Ping landslide (Figure 2.2) and Po Shan Road landslide (Figure 2.3) caused 71 and 67 fatalities, respectively (Cheung et al. 2006). Although the government of the Hong Kong Special Administrative Region (HKSAR) has devoted a huge amount of resources to slope investigation and stabilization since 1977, landslide still poses a threat to the safety and property of Hong Kong citizens.

In order to reduce the losses and eliminate the possibility of landslide, slope monitoring is one of the most effective approaches, which can compensate for design limitations and construction uncertainties, and perform early warning for impeding failure (Wong et al. 2006; Millis et al. 2008).

The movement of a slope is a direct indication of slope failure. In recent years, site formation works for construction of highways and buildings require a lot of cutting on the existing slopes on one side and filling on the other side. The potential movement and collapse of these cuts and fills may impose great dangers to the construction activities and the future operation of the civil structures.

The conventional survey technique using movement or settlement markers provides useful information on horizontal and vertical surface deformation. The global positioning system (GPS) is more advanced because of its automatic characteristics (Ding et al. 2003). However, the limitations of GPS for practical applications include low resolution, high cost, and requirement of flat ground condition. For underground deformation measurement, tape extensometer is a simple and economical tool. However, manual measurement and special temperature compensation techniques are required.

Different types of inclinometers are by far the most useful instruments available for geotechnical engineers who are concerned with the movements within slopes. Shown in Figure 2.4, a conventional inclinometer comprises an access tube grouted into a borehole, which should be extended to a depth well below any potential failure planes. The subsurface horizontal deformation profile is recorded by lowering a uniaxial or biaxial probe to the bottom of the access tube, and then effectively measuring the slope at regular intervals (normally 1 m) as the probe is pulled back up to the tube top. Of course, the whole operation is done manually. In-place inclinometer is automatic, which can be divided into three main types: electrolevel, servo accelerometer, and vibrating wire. However, they are either too expensive or unstable for long-term monitoring. In some cases, vertical magnetic settlement sensors are combined with inclinometer to provide additional information.

Portable crack / deformation gauges and lateral extensometers are widely used to monitor lateral ground movement of slopes for a couple of years. However, the installation is complex and requires much experience and skills.

Recently, Lin and Tang (2005) established subsurface movement identification systems using the TDR technology. The TDR system utilizes a coaxial cable installed in a borehole. Wherever there is a deformation change of the cable due to ground movements, a portion of the voltage is reflected back to the source and the relative magnitudes of distortion are measured for interpretation. TDR can achieve remote and real-time monitoring with an attractive cost. The disadvantage of TDR is that accurate movement magnitudes, rates and directions cannot be determined.

Tilt or rotation of slopes can be monitored by tiltmeters. They can determine the direction of movements, delimit the areas of deformation and, in many cases, reveal the mechanism of movement (slumping, slope creep, settlement, etc.). However, the installation should be very accurate and the readings are affected by many factors.

Landslides almost always occur in the raining seasons, especially under heavy rain conditions. Since 1978, an automatic rain gauge network has been established in Hong Kong to provide real-time rainfall monitoring (Wong et al. 2006; Millis et al. 2008). In slopes, groundwater level and pore water pressure are the primary monitoring parameters, which are normally measured by different types of piezometers. Standpipe and Casagrande piezometers are the most frequently used type of piezometers in the field (Spalton et al. 1997). However, they have the problems of blocking and are not applicable for low permeability clays. Sometimes twin-tube hydraulic piezometers are used in dams and embankments but installation of these types of piezometers is quite difficult and the monitoring can hardly be automatic. Recently, automatic integral electronic water level sensor and built-in data logger are developed for monitoring transient variation of groundwater levels in piezometer. However, they are seldom used in practice due to their high prices.

When slope masses are anchored, the addition of load cells will provide valuable information of the changing conditions on the slopes. Vibrating wire type load cells are commonly used to measure forces of ground anchors with an accuracy of ± 2 to ± 10%. But they require special manufacturing techniques and the cost is high. A load cell working on a hydraulic principle is sometimes useful. The simplest form is a calibrated hydraulic jack with oil pressure measurement by a pressure gauge. However, friction effect in the ram of the jack and low reading accuracy are the shortcomings of this method.

Soil nails are commonly used to stabilize sub-standard slopes in Hong Kong. Every year, tens of thousands of soil nails are installed in soils for stabilizing existing sub-standard or new cut/filled slopes. Stability is satisfied by the mobilization of shear stresses at the soil-cement interface. In soil nailing design, only tensile force is considered (GEO 2008). Thus the distribution of stress and strain along soil nail is of great importance to estimate tensile force and skin friction correctly. Existing techniques for monitoring performance of soil nails include using strain gauges, instrumented rebar, and sister bar (Byrne et al. 1998). These instruments are in general robust, simple and easy to use. However, the disadvantages of sensitivity to electromagnetic field and the data collection difficulties, make them suspicious for long-term and remote monitoring.

Earth pressure cells are sometimes installed within slopes to measure the magnitude of total stress acting against retaining structures such as gravity retaining wall. There are mainly two types of earth pressure cells, electrical and hydraulic. Due to the instrumentation expense and installation difficulties, earth pressure cells are primarily used in research and special field applications.

It can be found that the instruments used for the monitoring of geotechnical structures, such as slopes and foundations, are mainly based on conventional optical, mechanical, hydraulic, electrical, and pneumatic transducers, all of which have certain shortcomings. Field instrumentation is often of tedious applications and requires the intervention of specialized operators. The resulting complexity and costs limit the frequency of these measurements. The obtained spatial resolution is in general low. Automatic, remote and long-term monitoring cannot be fully achieved. Moreover, most of these conventional instruments are powered by electricity, and hence the output quality is influenced by the existence of electromagnetic fields.

2.4 GEOTECHNICAL MONITORING USING FBG TECHNOLOGY

In recent years, advanced optical fiber sensors have been developed rapidly for structural health monitoring (SHM) of civil infrastructures. As stated in Chapter 1, in comparison with conventional transducers, fiber optic sensors have apparent advantages such as immunity to EMI, insensitivity to corrosion, high precision and tiny size. Fiber Bragg gratings (FBG), low-coherence interferometry (LCI), optical time domain reflectometry (OTDR) and Fabry-Perot interferometry (FPI) and nonlinear techniques such as Raman and Brillouin scattering, are among the various types of fiber optic sensing technology (Inaudi 1999). This study mainly concentrates on the FBG technology due to its particular advantages.

2.4.1 FBG sensing technology

In 1978, Hill et al. (1978) discovered photosensitivity in optical fiber and fabricated the first FBG with a visible laser beam propagating along the fiber core. Since then, FBG sensors are by far the most commonly used in civil engineering, accounting for over 50% of the fiber optic sensors in structural health monitoring, as well as in fiber-optic communication as the optical filter. One reason for this popularity is that FBG can measure multiple parameters, such as temperature and strain, and offer excellent measuring resolution and range, absolute measurement, and modest cost per channel. Furthermore, because FBG are passive sensors, they can be either time- or wavelength-multiplexed, which allows for distributed sensing - a key advantage for geotechnical monitoring.

(1) Functional principle

An FBG is written into a segment of Ge-doped single-mode fiber in which a periodic modulation of the core refractive index is formed by exposure to a spatial pattern of ultraviolet (UV) light. The periodic structure can be created either by interference or by using an appropriate phase mask.

According to Bragg's law, when a broadband source of light has been injected into the fiber, FBG reflects a narrow spectral part of light at certain wavelength, which is dependent on the grating period and the refractive index of fiber (Morey et al. 1989). The structure of an FBG sensor is shown in Figure 2.5. In the reflected spectrum of an FBG sensor, the wavelength at which the reflectivity peaks is called the Bragg wavelength λ_B and can be calculated by

$$\lambda_B = 2n_{eff}\Lambda \tag{2.4}$$

where n_{eff} is the effective core index of refraction; Λ is the periodicity of the index modulation.

The Bragg wavelength is strain-dependent through physical elongation or thermal change of the sensor and through the change in the fiber refractive index due to photo-elastic effect. A change in strain or temperature will alter the Bragg wavelength and can be formulated by (Othonos and Kalli 1999)

$$\Delta\lambda_B = 2n_{eff}\Lambda\left[\left(1-\frac{n_{eff}{}^2}{2}\right)\left[p_{12}-\nu\left(p_{11}-p_{12}\right)\right]\Delta\varepsilon+\left(\alpha+\frac{\frac{dn_{eff}}{d\Delta T}}{n_{eff}}\right)\Delta T\right] \quad (2.5)$$

where $\Delta\lambda_B$ is the change in Bragg wavelength due to applied strain and temperature change; $\Delta\varepsilon$ and ΔT are the changes in strain and temperature; p_{ij} are the Pockel's coefficients of the stress-optic tensor; ν is Poisson's ratio; α is the coefficient of thermal expansion (CTE) of the fiber material.

Considering a standard single mode silica fiber, the relationship between the Bragg wavelength, strain, and temperature of the sensing fiber can be simplified as (Othonos and Kalli 1999)

$$\frac{\Delta\lambda_B}{\lambda_{B0}} = \left(1-p_{eff}\right)\Delta\varepsilon+\left(\alpha+\xi\right)\Delta T \quad (2.6)$$

where λ_{B0} is the original Bragg wavelength under strain free and 0 ^{o}C condition; ξ is the thermo-optic coefficient; p_{eff} is the photo-elastic parameter defined by the below equation

$$p_{eff} = \frac{n_{eff}{}^2}{2}\left[p_{12}-\nu\left(p_{11}-p_{12}\right)\right] \quad (2.7)$$

Temperature and strain directly affect the period of the index modulation as well as the effective index of refraction. Thus, any change in temperature and strain directly affects the Bragg wavelength. To measure wavelength shifts that result from changes in temperature or tension, FBG sensor systems must include an optical source that continuously interrogates the reflection spectrum, and a detection module that records the shifts in the peak reflectivity versus wavelength. The functional principle of FBG sensor system is schematized in Figure 2.6.

(2) Manufacturing methods

Currently there are several grating methods available, including internal grating method, holographic method, phase mask method, and point-by-point method. These manufacturing methods use different set-up but all of them involve interference between two coherent UV laser beams, as shown in Figure 2.7.

a. Internally written (inscribed) Bragg grating method

This method is first demonstrated by Hill et al. (1978) using a simple experimental set-up. The fiber optic photosensitivity was discovered and the fiber Bragg gratings was made with a visible laser beam propagating along the fiber core. Grating reflectivity of about 90% within bandwidths <200 MHz was measured.

b. Transverse holographic method

In 1989, Meltz et al. (1989) reported a more versatile fabricating method of FBG. This involved a holographic interference set-up, and the grating was written from the side of fiber by interferometric superposition of ultraviolet beams. The angle between the ultraviolet beams allows to control the period of the light pattern in the fiber core and thus the Bragg wavelength.

c. Phase mask method

In 1993, Hill et al. (1993) proposed another effective method to fabricate FBG using a phase mask, which is a piece of diffractive grating with depth modulation on fused silica. Phase masks are designed to suppress 0th order diffraction efficiency (<5%) and increase +/-1st order efficiency (>35%). When the UV beam passes through a phase mask, the +/- 1st order beam will credit an interference pattern. This pattern will write the FBG on the photosensitive single mode fiber, as shown in Figure 2.8 (b). Currently, phase mask method is the most popular manufacturing method of FBG.

d. Point-by-point writing

In 1990, Hill et al. (1990) fabricated coarse-period fiber gratings using a point-by-point writing technique. In this method, one index perturbation of the grating is photo-imprinted in the fiber by irradiating the fiber with ultraviolet light through a slit. Subsequent index perturbations are formed by accurately controlled translation of the fiber (or mask) followed by another irradiation step. Thus, the grating is built up point by point. The method is particularly useful for fabricating mode converter gratings that require tilted index perturbations, or rocking filters which used photo-induced birefringence.

Instead of ultraviolet light, one may also use infrared light in the form of intense femtosecond pulses for writing FBG (Mihailov et al. 2003) in various kinds of glasses. In that case, two-photon absorption occurs near the focus of the laser beam, but not in regions outside the focus. It is even possible to write such gratings through the polymer coating of a fiber (Martinez et al. 2006), since the intensity in the coating is much lower when the beam is focused to the fiber core. A totally different method also using infrared light is the fabrication of long-period FBG in photonic crystal fibers by irradiation with a CO_2 laser beam.

The techniques used for fabricating Bragg gratings are still an active area of research.

The goal of this work is to improve the quality of photo-imprinted gratings and reduce the manufacturing costs. Since stripping the fiber and re-applying a coating reduce the fiber resistance, techniques have been developed to write FBG directly in the draw tower before the primary coating is applied. These systems will probably bring the unit price of FBG sensors down to a few US dollars.

(3) Demodulation methods

Different interrogation methods have been used for reading out the shift in the Bragg wavelength experienced by FBG, from which strain and temperature are evaluated. There are basically two techniques for determining the precise wavelength of the peak in the FBG reflected spectrum. The first method, as shown in Figure 2.9, is to send light from a broadband source into the fiber and analyze the reflected spectrum for the wavelength of the FBG peak. The optical circulator is a device that efficiently transmits the outgoing light into the transmission fiber and redirects the back-reflected light to an optical spectrum analyzer (OSA). The best type of OSA for accurate wavelength measurements is based on Michelson interferometry (Othonos and Kalli 1999). This method has been used for many years in wavelength meters to determine the wavelength of laser sources with high accuracy.

The second method, as shown in Figure 2.10, is to sweep a narrowband tunable laser source over the spectral range including the FBG spectral peak. The laser wavelength measurement module records the wavelength of the scanning laser when a peak in the reflected intensity is recorded by the power meter.

Both techniques work well for detecting the FBG reflected wavelength. The main difference lies in the accuracy and reliability of the wavelength determination.

(4) Special issues in instrumentation

a. Sensor packaging method

In most cases, the coating of an optical fiber has to be stripped prior to the fabrication of FBG. Therefore, the FBG sensor has inherent vulnerability and it is difficult to apply bare FBG sensors directly in infrastructures without appropriate protection. The application of FBG sensors depends utterly on the availability of suitable packaging (Baldwin et al. 2001; Zhou et al. 2003; Lin et al. 2005). Existing encapsulation methods include gluing bare FBG to the target and embedding with adhesives, which is the simplest packaging method, putting FBG into metallic plates or tubes (Leng et al. 2006), and embedding FBG into composite materials (Frank et al. 1999; Kalamkarov et al. 1999, 2000a, 2000b, 2005; Lau et al. 2001).

b. Temperature compensation

Because FBG sensors are sensitive to both strain and temperature, the discrimination of strain and temperature is necessary. If temperature variations are expected during strain monitoring, it is important to consider and compensate for their influence on the measurement precision.

There are two basic approaches to reduce the temperature influence for strain measurement, including a) designing an FBG sensor that has intrinsically low dependence of temperature, and b) measuring the temperature independently. Using the first approach, Lo and Sirks (1997) utilized only one FBG sensor to measure strain and temperature simultaneously. For the second approach, the simultaneous measurement of strain and temperature usually consists of a sensor sensitive to both strain and temperature in a linear way, and a second one responding only to temperature variation. The data from the temperature sensor is then used to correct the strain data. In this case, two sensors are installed side by side. The first, usually called the measurement sensor is installed in mechanical contact with the host material, and the other, called the reference sensor, is mechanically uncoupled from but in thermal contact with host material. The temperature sensor can be based on FBG technology or other technologies such as Brillouin scattering or polarization-maintaining fiber. Other set-ups have been advocated by researchers, where the temperature and strain measurements are performed on both sensors but with different linear response coefficients. For simultaneous temperature and strain measurements, Posey and Vohra (1999) proposed an FBG and stimulated Brillouin sensor (SBS) system. Instead, Du et al. (1999) and Kang et al. (2001) combined the technologies of FBG and FPI to measure these two parameters.

c. Multiplexing techniques

One of the most useful attributes of FBG is the ability to be serially multiplexed so that a string of such sensors can be located along any given optical fiber. In the past, there were two well established methods of interrogating such a string of sensors. The first approach is time division multiplexing (TDM), in which the reference Bragg wavelength is the same for each grating and time of flight using short duration light pulses is used to determine which grating is being interrogated. The second approach is called wavelength division multiplexing (WDM), which requires the Bragg wavelength of each grating to be sufficiently different from all of the others so that there is no spectral overlap. Sometimes, WDM and TDM can be combined to form FBG sensing network.

2.4.2 Development of FBG based sensors

Owing to the harsh environments in the construction industry, and the large size of civil engineering structures, the FBG sensors should be robust, rugged, easy to use and economical. A variety of strain sensors based on FBG technology have been developed for monitoring civil infrastructures in recent years. Most of them are embedded or surface mounted on structures with different types of sensor protection system (SPS).

(1) Strain sensor

Schroeck et al. (2000) monitored the strain of steel rock bolts in underground cavities using FBGs. In order to allow measurements of up to 20 % relative strain, special arrangements of the FBG sensors had to be found to extend their measuring range. Leng et al. (2006) developed two types of SPS for extrinsic FPI and FBG sensors and proved their performance in concrete cylinders.

(2) Temperature sensor

Ren, et al. (2004) utilized FBG temperature sensors to monitor underground temperature variations. Dewynter et al. (2005) installed FBG thermal probes in a borehole surrounding a central heating borehole to conduct in-situ thermal measurements of argillaceous rocks. The results from FBG temperature sensors were in good agreement with those from conventional resistive probes.

(3) Displacement sensor

For displacement measurement, Kim and Cho (2004) utilized surface mounted FBG sensors to measure the beam deflection induced by vertical load at the mid-span. Falciai and Trono (2005) developed a displacement FBG sensor with temperature compensation. Two FBGs were installed to the opposite surfaces of a straight elastic beam, which was bent in a horizontal direction. The beam curvature variation can be measured by means of the two FBG wavelength differences, while the mean value is taken in order to compensate for the temperature effects. Metje et al. (2008) developed a smart rod instrumented with FBG sensors for structural displacement measurement and verified this technology under simple loading condition.

For field applications, the FBG sensors are normally fixed on tubes, which are installed in boreholes for internal displacement monitoring. Schmidt-Hattenberger and Borm (1998) developed an FBG-based extensometer to monitor rock deformations in tunnels. The FBG sensors are designed to be embedded in glassfiber reinforced polymer (GRP) rock bolts. Yoshida et al. (2002) developed a slope monitoring system with FBG borehole inclinometers. This inclinometer shown in Figure 2.11 is installed within the casing-tube and has several 1 m elements connected to each other with a hinge plate and two sensing tubes. One of the tubes contains FBG and the other is only used for fiber transmission. It has been applied to monitor the deformation of an artificial slope under construction for 4 months. Zhao et al. (2005) developed a fiber-optic cantilever-type inclinometer for tilt measurement. In their design, there is only a pair of FBGs for both tilt sensing and signal demodulation. To allow automated data logging, Ho et al. (2006) developed an FBG segmented deflectometer (FBG-SD), which can be inserted into the conventional inclinometer casing and measure the relative deflection between the segments of the inclinometer casing. To verify the effectiveness of the new ground movement monitoring system, they performed indoor and field experiments and verified the reliability of this instrument. Kashiwai et al. (2008) developed a borehole multiple deformation sensor system with inner FBG sensor units. When displacement occurs, the plate element installed with two FBG sensors will bend accordingly. The reading of these two FBG sensors can be self-compensated. This sensor system has been applied successfully for the monitoring of ground deformation of a tunnel.

(4) Pressure sensor

Tjin et al. (1998) developed a fiber optic pressure sensor utilizing FBG as a sensing element. The FBG sensor was embedded in carbon fiber material. In tests, nonlinear axial strain versus perpendicular force was captured. The time stability was shown to be better than that of the direct sensing technique. Chang et al. (2000) developed an FBG based soil pressure transducer for measuring pavement response. The FBG transducers can be used for performance evaluation of pavements and weigh-in-motion measurement. Three methods for bonding the FBG to the diaphragm were considered in their study. Owing to the disc shape of the bulkhead, the FBG sensor is designed to be installed circumferentially so that the optical spectrum of the sensor will show a clear peak. An FBG load cell was developed by Rossi and Rondini (2003) for stress measurement. The experimental and numerical results verified the reliability of this instrument. A system for temperature compensation has been realized and tested inside a climatic room. Legge et al. (2006) developed an FBG stress cell for geotechnical engineering applications. In the stress cell, a 5 mm long FBG sensor is encapsulated in a softer material of high Poisson’s ratio. The reliability of this sensor has been verified by laboratory experiments and numerical study. Ho et al. (2008) developed a self temperature-compensated chirped/differential FBG pressure sensor and demonstrates its capabilities through laboratory calibrations over a wide range of temperatures. This sensor can be used for measuring pore water pressure with high accuracy.

(5) Accelerometer

Teng et al. (2006) developed an FBG Based Accelerometer. The resonance frequency is increased via the sensing element design, which combines the big beam and the two tiny beams. The differential double FBGs design increases the accelerometer sensitivity and resolves the temperature compensation. Au et al. (2008) developed a novel design of

FBG based accelerometer using chirp-free mechanism. The shake-test experiments were conducted to validate its reliability. A low frequency fiber optic accelerometer was developed by Talebinejad et al. (2009). Acceleration is measured by the FBG in response to the vibration of the fiber optic mass system. The accelerometer was first evaluated in laboratory and then employed in a demonstration project for condition assessment of a bridge.

2.4.3 FBG based geotechnical monitoring and evaluation

The use of fiber optic sensing technology for geotechnical monitoring has been advocated by many researchers (Li et al. 2004; Majumder et al. 2008). Recently, FBG sensors have been successfully applied in a number of geotechnical applications in Europe, North America and Asia.

(1) Tunnels

Nellen et al. (2000) successfully monitored distributed strain field and temperature of tunnels with embedded FBG sensor arrays, which were attached to glass fiber reinforced polymers (GFRP) rock bolts.

(2) Foundations

An FBG sensor network was installed in a large diameter concrete pile on a real construction site and used to monitor its deformation during several quasi-static loading cycles (Liu et al. 2002; Schmidt-Hattenberger et al. 2003b). Comparison between the results of the FBG sensors and conventional concrete strain gauges has shown excellent agreement.

Sponsored by Federal Highway Administration (FHA), Baldwin et al. (2001) utilized

FBG sensors in the filament-wound composite tube of a load carrying pile to monitor its long-term performance, as shown in Figure 2.12. All the FBG sensors survived the pile driving process but the breakage of an optical fiber lead during pile transit resulted in the loss of monitoring data.

Lee et al. (2004) conducted laboratory and field tests to evaluate the applicability of FBG based multiplexed sensor system in the instrumentation of piles. From the strains measured by FBG sensors, the distributions of axial load in three model piles and a field test pile are found to be comparable, in terms of both magnitude and trend, to those obtained from vibration wire strain gauges (Figure 2.13).

Kister et al. (2007) reported the application of an FBG based strain and temperature monitoring system on reinforced concrete foundation piling. FBG sensors were fixed on two reinforcing cages and protected using carbon–fiber composites. The monitoring of the reinforcing cages during concrete pouring highlighted the presence of thermal tensile strains applied to the steel rebars. A change in the strain distribution along the whole depth of the foundation piles was observed half way through the concrete curing. A variation in the strain distribution was captured, which resulted from the simultaneous effect of the construction of the building floors and the ground heave.

(3) Laboratory geotechnical tests

Sato et al. (2000) proposed a ground strain measurement system using FBG sensors. Employment of fiber optic sensor makes the device simple in mechanism and highly durable. In the dynamic shaking table experiments, displacement values measured by ground strain measuring devices and displacement meter were found to be in good agreement.

Ren et al. (2006) monitored a roller compacted artificial concrete dam model using stainless steel tube packaged FBG. The dam model is subjected to dynamic loads of noise, sine wave and random wave. The results show that possible fatigue and breakage damages can be monitored conveniently by embedded FBG sensors.

In laboratory uniaxial compression (UC) tests, FBG strain transducers were used to measure the deformation of rock samples (Schmidt-Hattenberger et al. 1999; Schmidt-Hattenberger et al. 2002; Schmidt-Hattenberger et al. 2003a). The monitoring results were compared well with those from mechanical and laser extensometers. Yang et al. (2007) applied surface bonded FBG strain and temperature sensors on granite rock specimens, together with piezo-impedance transducers. The experimental results demonstrate the effectiveness of new smart sensor for monitoring rock-structures.

For a three-dimensional fork tunnel model, Chang et al. (2007) utilized FBG based strain sensor modules for measuring the in-site strain during the process of excavation. From the comparison of experimental and numerical results, the FBG sensors have proved their reliability and effectiveness for monitoring small-scale models.

(4) Others

Possibility of application of fiber optic sensors to differential settlement measurement has been presented by Sklodowski (2003). Beam theory is used to model deformations of tight bolts under displacement driven conditions at their end points and to find the relation between bending strains and rotations of bolts and their relative vertical settlement. This theoretical result is used to show that existing smart fiber optics sensors can measure these settlements with resolution of tens of millimeters.

The ground-source heat pump system is used to heat or cool a building by utilizing the thermal energy of the underground soil. Ren et al. (2004) successfully installed FBG sensors in an underground pipe to monitor the temperature distribution of the soil and the thermal difference of the circulating water system.

For Qinghai-Tibet Railway in China, an FBG sensor network has been established for roadbed temperature monitoring (Zhang et al. 2007). This sensor network is composed of FBG sensor chains embedded in the roadbed, slave optical cables, work stations comprising FBG sensor interrogator and the optical router, master optical cables, and central workstation. The monitoring results show that the temperature field within two meters under the ground varied a lot but under the depth of 8 m, the soil temperature was stable in general.

2.5 SUMMARY

This chapter covers the literature review of the evaluation methods for the performance of geotechnical structures and related geotechnical instrumentation techniques. The recent research work associated with the applications of FBG monitoring technology in geotechnical engineering is reviewed.

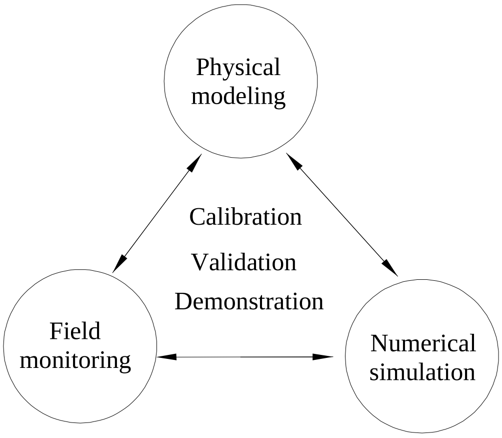

Figure 2.1 Schematic illustration of the relationship between physical modeling, field monitoring and numerical simulation

Figure 2.2 Sau Mau Ping Landslide (1972)

Figure 2.3 Po Shan Road landslide (1972)

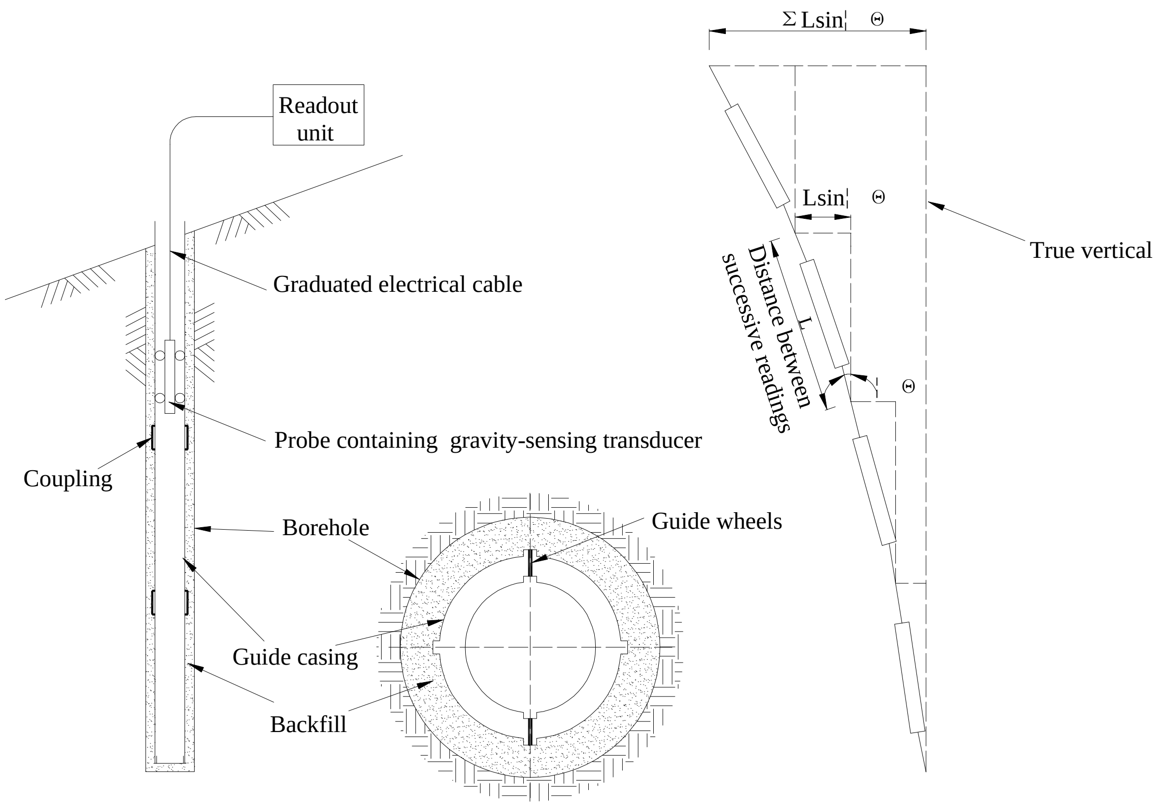

Figure 2.4 Operation principle of the inclinometer

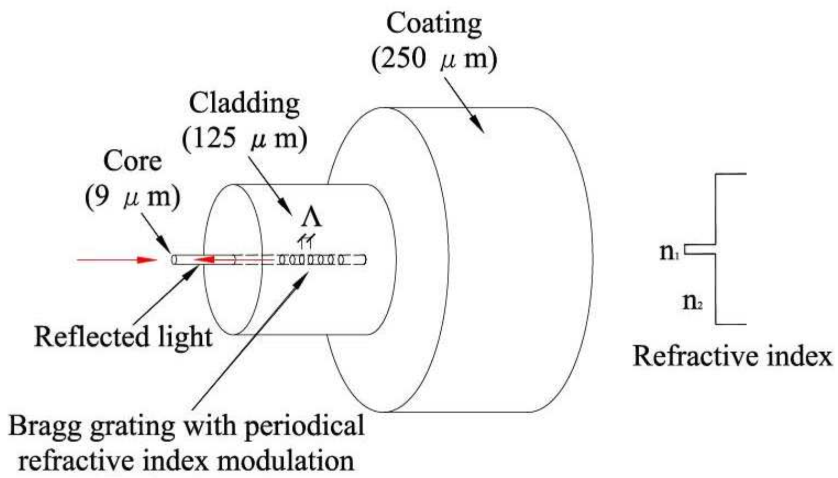

Figure 2.5 Details of an FBG sensor

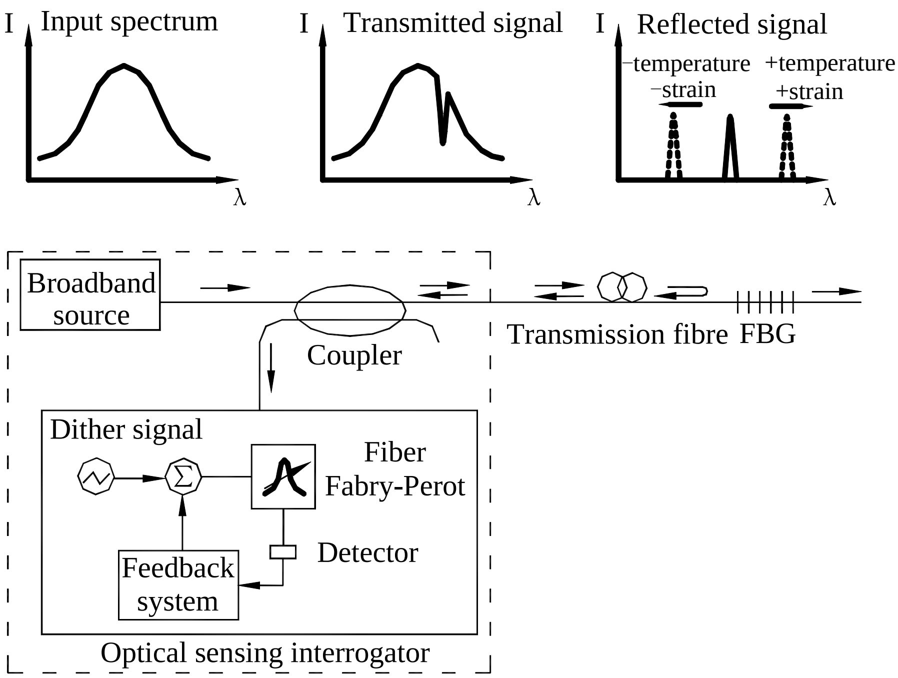

Figure 2.6 Functioning principle of the FBG sensor for measuring strain and temperature

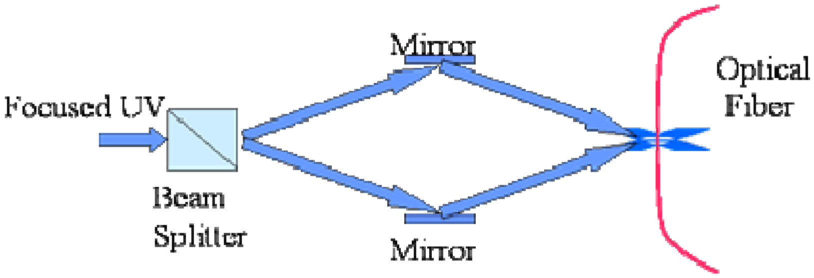

(a) Holographic method

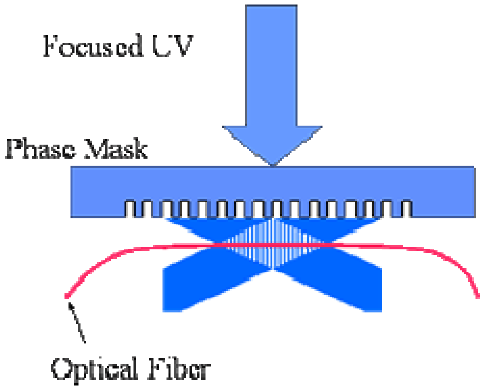

(b) Phase mask method

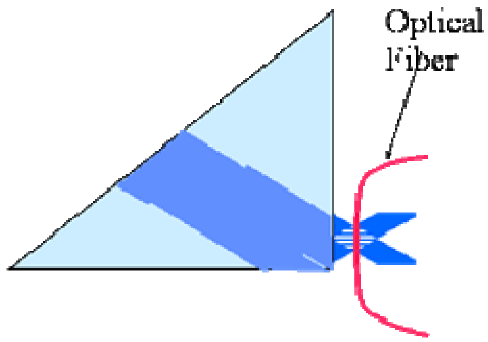

(c) Lloyd mirror method

Figure 2.7 Various set-up for fabricating FBG sensors

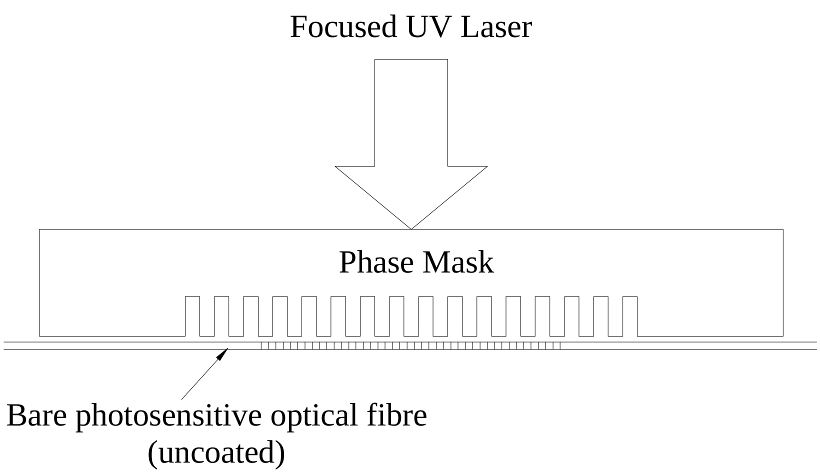

(a) Principle of phase mask method

(b) Photograph of writing reflection grating using UV laser

Figure 2.8 Phase mask method for fabricating FBG sensors

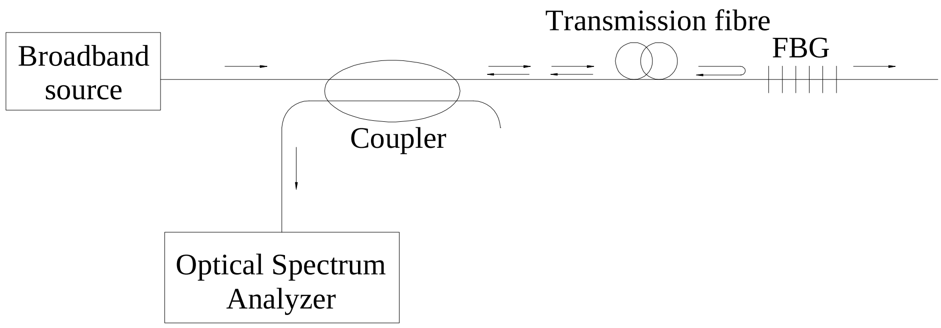

Figure 2.9 FBG measurement with a broadband source and an OSA

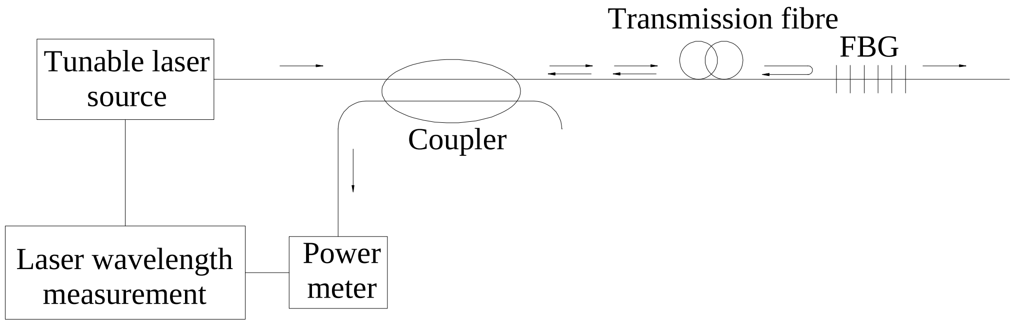

Figure 2.10 FBG measurement with tunable laser and reflected power detection

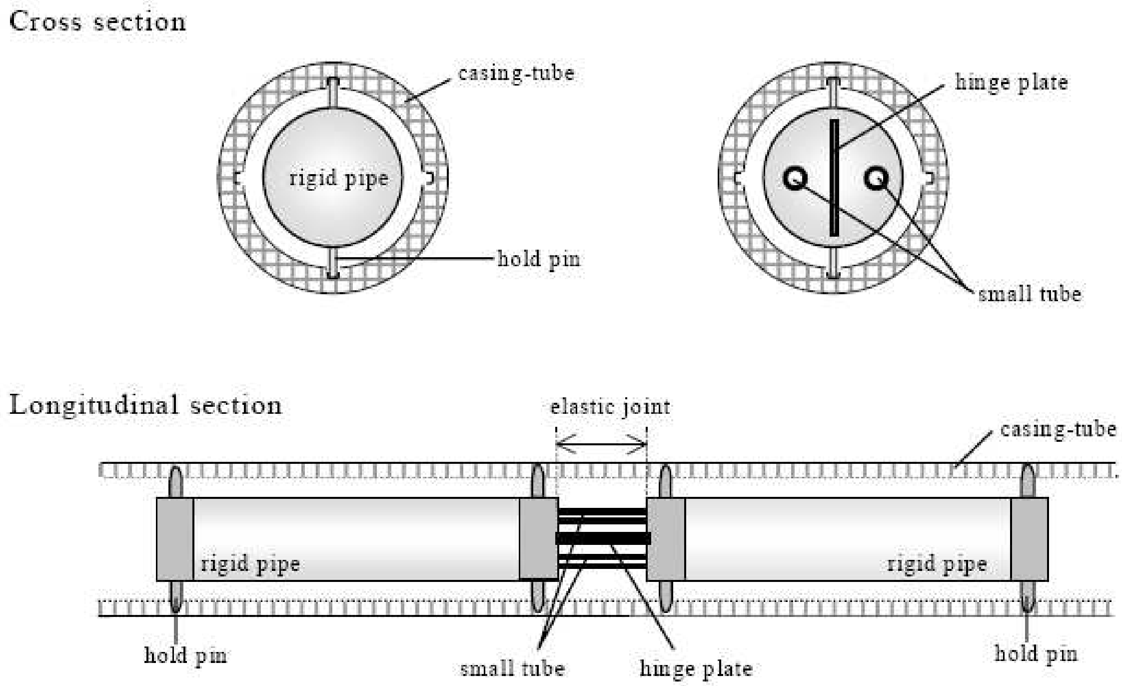

Figure 2.11 Structure of an FBG borehole inclinometer (after Yoshida et al. 2001)

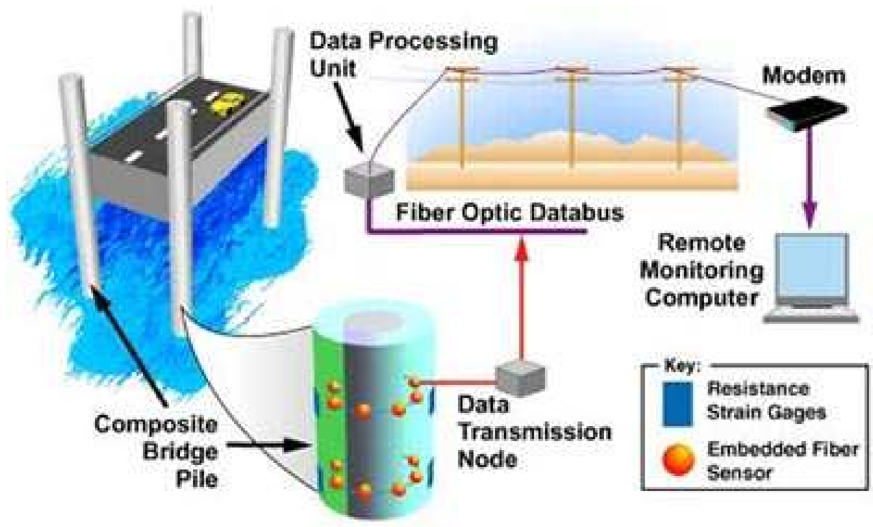

Figure 2.12 Composite bridge pile monitoring using FBG sensors (after Baldwin et al. 2001)

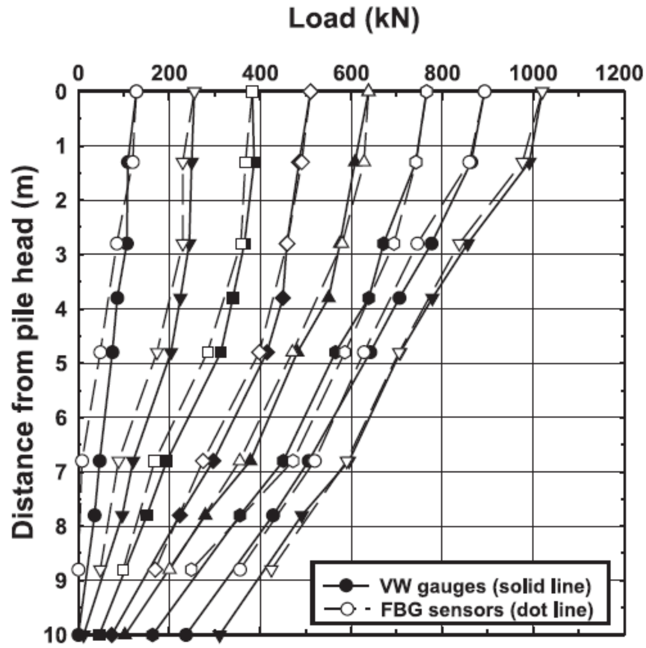

Figure 2.13 Distribution of axial pile load measured by FBG sensors and vibration wire strain gauges (after Lee et al. 2004)

CHAPTER 3:

DEVELOPMENT OF FBG SENSORS FOR GEOTECHNICAL APPLICATIONS

3.1 INTRODUCTION

Existing techniques for geotechnical monitoring have obvious limitations. During the past decade or so, a significant progress has been made on the commercialization of fiber optic sensing technologies. Owing to their advantages such as immunity to electromagnetic field, high resolution and multiplexable capacity, the future of FBG sensors looks promising. Nevertheless, there are several technical obstacles when FBG sensors are used in geotechnical instrumentation. At present, the cost of FBG monitoring system is still expensive for applications where a large amount of sensors are required. The cable and connector sensitivity may still be an issue for those measurements that require high precision, repeatability, and interchange ability. In order to ensure the survival of FBG sensors in harsh construction environments, the robustness of the sensors should be enhanced.

As reviewed in Chapter 2, the Bragg wavelength of an FBG sensor changes according to the applied temperature and strain, which can be described by

$$\frac{\Delta\lambda_B}{\lambda_{B0}} = c_\varepsilon \varepsilon + c_T \Delta T \qquad (3.1)$$

where λ_{B0} is the original Bragg wavelength under strain free and 0 ^{o}C condition; $\Delta\lambda_B$ is the change in the Bragg wavelength due to strain and temperature variations; c_ε and

c_T are the calibration coefficients of strain and temperature. For FBG sensors made from germanium-doped silica fiber, the typical values of c_ε and c_T are 0.78×10^{-6} $\mu\varepsilon^{-1}$ and 6.67×10^{-6} $^{o}C^{-1}$, respectively.

If $\Delta T = 0$,

$$\frac{\Delta\lambda_B}{\lambda_{B0}} = c_\varepsilon \varepsilon \tag{3.2}$$

If $\varepsilon = 0$,

$$\frac{\Delta\lambda_B}{\lambda_{B0}} = c_T \Delta T \tag{3.3}$$

In this chapter, the development of FBG sensors for the purpose of geotechnical instrumentation is presented. These sensors can form a fiber optic monitoring system, which is suitable for static and dynamic monitoring of geotechnical structures and have the potential to measure a number of different parameters, including strain, temperature, and displacement. To performance laboratory calibration of these sensors, about one thousand pieces of FBG with a gauge length of 15 mm were manufactured using phase mask method in Laboratory of Laser, Department of Applied Physics, the Hong Kong Polytechnic University (Hill et al. 1993).

3.2 FBG SENSORS FOR STRAIN MEASUREMENT

3.2.1 Surface glued FBG strain sensor

In some cases, FBG sensors can be glued directly on the surface of host materials, such as steel and GFRP, for strain measurements. To study the performance of surface glued FBG strain sensor, a series of calibration tests were conducted.

(1) Calibration of bare FBG strain sensors

a. Calibration of one bare FBG strain sensor

To study the relationship between the Bragg wavelength and applied strain, a number of calibration tests were conducted on bare FBG sensors. First of all, 30 loading and unloading cycles were applied to single-mode optical fibers containing one bare FBG strain sensor. Figure 3.1 shows the arrangement of testing equipments. The two ends of each fiber were embedded in protection sleeves and fixed on the translation stages by plastic clamps. The total length of the tested optical fiber was recorded beforehand. Elongation applied to the fiber in stages was measured by digital displacement gauges and the corresponding Bragg wavelength was measured by an optical sensing interrogator si425 (Micron Optics 2004).

To interpret the test results, the average strain of the optical fiber was calculated (displacement divided by total length). From the above data, calibration curves of average strain and the Bragg wavelength can be plotted and the values of calibration coefficients can be determined by least square method.

The calibration results shown in Figure 3.2 and Figure 3.3 indicate a linear relationship between the Bragg wavelength and strain for bare FBG strain sensors. For a measuring range of 0 to 3000 $\mu\varepsilon$, the average calibration coefficient of strain is 0.783×10^{-6} $\mu\varepsilon^{-1}$. The variation in calibration coefficient of strain may result from the inherent difference of grating and errors in the testing system.

b. Calibration of three bare FBG strain sensors in series

In order to minimize the system errors arising from the test set-up, a number of calibration tests were conducted on optical fibers containing three FBG strain sensors in series. For each test, 30 loading and unloading cycles were applied on the fiber. Figure 3.4 shows the arrangement of testing equipments. The calibration results shown in Figure 3.5 indicate that, the linear relationship between strain and the Bragg wavelength is excellent. The calibration coefficients c_ε of the FBG sensors in the same sensing array are very close.

c. Calibration of one bare FBG strain sensor on an intentionally uncoated optical fiber

In the manufacturing procedure of FBG, a certain length of optical fiber will be uncoated (see Appendix A3). In most cases, FBG sensors will be recoated before applied for strain measurement. To evaluate the effect of uncoating, a number of calibration tests were conducted on bare FBG sensors on optical fibers with certain portions of coating intentionally removed. The lengths of removed coating range from 150 mm to 300 mm. Figure 3.6 and Figure 3.7 show the arrangement of testing equipments and typical calibration results. It is indicated that the variation in uncoated length of the fiber does not influence the calibration coefficient of strain c_ε significantly. Therefore, despite the consideration of protection, the recoating of FBG strain sensor is not a necessity.

(2) Calibration of FBG Strain sensors glued on stainless steel wires

a. Calibration of one FBG strain sensor glued on a stainless steel wire

In order to evaluate the gluing technique of FBG strain sensors, a number of calibration tests were conducted on FBG strain sensors glued to 1 mm diameter stainless steel wires by cyanoacrylate adhesive. For each test, 30 loading and unloading cycles were applied on the steel wire. The test set-up is shown in Figure 3.8. The calibration results shown in Figure 3.9 indicate a linear relationship between the Bragg wavelength and strain.

However, the average calibration coefficient of strain is now $0.721\times10^{-6}\ \mu\varepsilon^{-1}$. Compared with the calibration coefficients of bare FBG strain sensors, the decrease of this value reveals that, when the tensile strain transferred from the steel wire to the sensor, losses of strain occurred. It can be concluded that quick-set adhesives such as cyanoacrylate cannot ensure the gluing quality of FBG sensors. In order to maintain the accuracy of strain measurement, epoxy resin is a better option.

b. Calibration of three FBG strain sensors glued on a stainless steel wire

To further investigate the performance of quasi-distributed FBG strain sensors glued on steel wires by cyanoacrylate adhesive, a number of calibration tests were conducted. The arrangement of the test equipment and the typical calibration results are shown in Figure 3.10 and Figure 3.11, respectively. It is indicates that the linear relationship between the Bragg wavelength and strain for every sensor is still excellent. The average calibration coefficient of strain is $0.729\times10^{-6}\ \mu\varepsilon^{-1}$, which is similar to that obtained from the calibration of one FBG strain sensor glued on a steel wire.

c. Calibration of one FBG strain sensor with a certain length of optical fiber glued on a stainless steel wire

To study the effect of gluing method on the calibration coefficient of strain, a number of calibration tests were conducted on one FBG sensors with different fiber lengths glued on a stainless steel wire by cyanoacrylate adhesive. For each test, 30 loading and unloading cycles were applied on the steel wire. The gluing lengths of the optical fibers range from 400 mm to 800 mm. The arrangement of testing equipments is shown in Figure 3.12. The calibration results shown in Figure 3.13 indicate that the linear relationship between the Bragg wavelength and strain is excellent. The average calibration coefficient of strain is calculated to be 0.714×10^{-6} $\mu\varepsilon^{-1}$. The glue length does not have significant effect on c_ε.

(3) Calibration of FBG strain sensors glued on a steel bar and grouted in a cement column

To simulate the performance of surface glued FBG in field applications, a number of calibration tests were conducted on FBG strain sensors glued on a steel bar with a diameter of 25 mm or 32 mm, together with electrical strain gauges (SGs), as shown in Figure 3.14. A two component epoxy resin was used to glue the FBG sensors. For each calibration test, about 10 loading and unloading cycles were applied in stages. After the elongation tests, every steel bar was grouted in a cement column and tested again. The arrangement of testing equipments is shown in Figures 3.15. Nearly all the FBG sensors and strain gauges survived the whole testing procedure. If c_ε is assumed to be 0.78×10^{-6} $\mu\varepsilon^{-1}$ for a measuring range of 0 to 3000 $\mu\varepsilon$, there is a good agreement between the readings of FBG sensors and strain gauges on the same locations (Figure 3.16). This demonstrates the reliability of epoxy resin for gluing FBG strain sensors.

3.2.2 Tube packaged FBG strain sensor

(1) Sensor design

Due to fragility of bare FBG sensors, they can hardly be directly used as embedded or surface mounted strain sensors on geotechnical structures without any protection, especially for the concrete aggregate environments. The FBG sensor for field application should be robust, easy for installation and economical. The tube packaged FBG strain sensor shown in Figure 3.17 is developed to fulfill this requirement. According to this design, the FBG sensor is packaged in a 6 mm diameter aluminum tube and used as a long gauge strain sensor, by which the average strain of a certain length can be measured. Since the measured strain is averaged, its magnitude is not influenced by local material discontinuities or inclusions. This allows the collection of data on a global structural level instead of a local material level.

(2) Calibration tests

To conduct calibration of the tube packaged FBG sensor, a universal servo-controlled electromechanical testing machine with computerized control system shown in Figure 3.18 was utilized. Electrical strain gauges, combined with a data logger for data recording, were used to measure the actual tensile strains applied on the aluminum tube. The strain gauge has a gauge factor of 2.08 ± 1%, an electrical resistance of 120 ± 0.1 Ω, and a strain limit up to about 5 %. Combined with a full bridge configuration, it is self temperature compensated. The displacements between the two clamps of the testing machine were recorded during testing. Typical calibration results in Figure 3.19 show a linear relationship between strain and the Bragg wavelength, indicating an average strain calibration coefficient of 0.80×10^{-6} $\mu\varepsilon^{-1}$.

To construct a strain sensing array, four quasi-distributed FBG sensors are designed to be encapsulated in a 1950 mm long aluminum tube and fixed at five points by epoxy resin (Figure 3.20). In the calibration tests, a testing equipment shown in Figure 3.21 was used to apply elongation to the tube. The tensile loadings were applied by weight sets in stages. Strain gauges were installed on the tube surface. Typical calibration results are shown in Figure 3.22. For the results, a linear relationship between applied strain and the Bragg wavelength is found, as well as an average strain calibration coefficient of about 0.80×10^{-6} $\mu\varepsilon^{-1}$.

3.3 FBG SENSORS FOR TEMPERATURE MEASUREMENT

3.3.1 Sensor design

For temperature measurement and temperature compensation of strain, a tube packaged FBG temperature sensor shown in Figure 3.23 is developed. The temperature sensor consists of a loose FBG sensor encapsulated in a copper tube with 2 mm in outer diameter. When applied in the field, this sensor is mechanically uncoupled from but in thermal contact with the host material.

3.3.2 Calibration tests

For calibration purpose, the FBG temperature sensors were merged into a temperature controllable water bath, together with a type-K thermocouple. A digital thermometer was used to measure the temperature variation during testing. Typical calibration results are shown in Figure 3.24. It shows that the relationship between the Bragg wavelength and the applied temperature is fairly linear with R^2 of over 0.999. The average calibration coefficient is calculated to be 6.20×10^{-6} $^{o}C^{-1}$. The resolution of the interrogator system is 1 pm, which is equivalent to temperature resolutions of 0.1 ^{o}C.

3.4 FBG SENSORS FOR DISPLACEMENT MEASUREMENT

3.4.1 FBG sensing bar

For small-scale physical model test, internal displacements are hard to be measured. The miniature FBG sensing bar, which takes advantage of high accuracy and compact size of FBG sensor, is developed to fulfill this requirement.

(1) Concept of an Euler-Bernouli beam subjected to arbitrary transverse and/or axial loading

Figure 3.25 shows an axiasymmetric beam made of an elastic and homogeneous material, with a length of *L* and a radius *R*. This beam is fixed at one end and subjected to arbitrary transverse and/or axial loading. To simplify this problem, the following assumptions are adopted:

(i) The deflection of the beam axis is small compared with the span of the beam.

(ii) The plane section remains normal to the axis after loading.

(iii) The shear strain and the deformation due to shear stress are neglected. Thus, the deflections of the beam are associated principally with the axial or bending strains.

(iv) The additional moments caused by axial loadings are negligible compared to the bending moments due to transverse loads.

Imagine a plane *A* passing through the beam perpendicular to *z* axis. After deformation, the beam axis on this cross section has deflections *u* and *v* in the *x* and *y* directions and a tension or compression *w* in the *z* direction. According to Euler-Bernoulli beam theory, the strain distributions depend on the distribution of normal axial force $N(z)$ and the bending moment $M(z)$ along the neutral line of the beam. The strain at any point can be described by

$$\varepsilon(z)=\frac{N(z)}{EA}\pm\frac{M_x(z)}{EI_x}R\pm\frac{M_y(z)}{EI_y}R=\varepsilon^A(z)\pm\varepsilon^{Tx}(z)\pm\varepsilon^{Ty}(z) \qquad (3.4)$$

where $\varepsilon^A(z)$ is the strains induced by axial loading $N(z)$; $\varepsilon^{Tx}(z)$ and $\varepsilon^{Ty}(z)$ are the strains due to transverse loading in the *x* and *y* directions, which are related to the bending moments $M_x(z)$ and $M_y(z)$, respectively; E, A, I_x and I_y are the

Young's modulus, the cross-sectional area, moments of inertia with respect to the x and y axes of the beam, respectively.

The relationships between displacements and strains induced by tension/compression and bending are

$$\begin{cases} \varepsilon^{A}(z)=\dfrac{dw(z)}{dz} \\ \varepsilon^{Tx}(z)=\dfrac{d^2u(z)}{dz^2}R \\ \varepsilon^{Ty}(z)=\dfrac{d^2v(z)}{dz^2}R \end{cases} \tag{3.5}$$

Therefore, the lateral deflections in the x and y directions and the total tensile (or compressive) displacement can be calculated by double integration of Eq. (3.5), i.e.

$$\begin{cases} u(z)=\dfrac{1}{R}\iint \varepsilon^{Tx}(z)\,dzdz \\ v(z)=\dfrac{1}{R}\iint \varepsilon^{Ty}(z)\,dzdz \\ w(z)=\int \varepsilon^{A}(z)\,dz \end{cases} \tag{3.6}$$

Eq. (3.6) shows that the relative deflections and tensile (or compressive) displacements can be computed on the basis of the strain distribution, together with specified boundary conditions. For a cantilever beam, at the fixed end, the boundary is assumed to have the relationships of $\begin{cases} u_{z=0}=v_{z=0}=w_{z=0}=0 \\ \left(\dfrac{du}{dz}\right)_{z=0}=\left(\dfrac{dv}{dz}\right)_{z=0}=0 \end{cases}$. For a simply supported beam, at both ends, $\begin{cases} u_{z=0}=v_{z=0}=w_{z=0}=0 \\ \left(\dfrac{d^2u}{dz^2}\right)_{z=0}=\left(\dfrac{d^2v}{dz^2}\right)_{z=0}=0 \end{cases}$ and $\begin{cases} u_{z=L}=v_{z=L}=w_{z=L}=0 \\ \left(\dfrac{d^2u}{dz^2}\right)_{z=L}=\left(\dfrac{d^2v}{dz^2}\right)_{z=L}=0 \end{cases}$.

(2) Working principle of the FBG sensing bar

Figure 3.26 shows the design of an FBG sensing bar. The FBG sensing bar is manufactured by grooved plastic or rubber bar with a diameter of 10 mm. Four optical fibers are glued in the grooves with 1 mm depth and covered with epoxy resin. Each optical fiber contains a series of even-distributed FBG sensors, which are connected to each other using fusion splices. The length of the bar and the spacing of FBG sensors are changeable according to the testing situation. All the FBG sensors in series pose sufficient spacing of the Bragg wavelengths so that no signal overlapping will occur. Using the technique of WDM, they can form a quasi-distributed sensing array without affecting the monitoring data of each other.

The FBG sensing bar is designed to be pre-buried or inserted into boreholes in a physical model, working like an elastic beam under arbitrary transverse and/or axial loading. When ground deformation or structural movement occurs, the sensing bar is subjected to bending and tension (or compression) sliding. The quasi-distributed FBG strain sensors measure strain distributions along the bar perpendicularly. Considering the plane *A* shown in Figure 3.25(b), the strains induced by axial loading and transverse loading are described by

$$\begin{cases} \varepsilon_i^A = \dfrac{1}{4}\left(\varepsilon_{ia} + \varepsilon_{ib} + \varepsilon_{ic} + \varepsilon_{id}\right) \\ \varepsilon_i^{Tx} = \dfrac{1}{2}\left(\varepsilon_{ia} - \varepsilon_{ic}\right) \\ \varepsilon_i^{Ty} = \dfrac{1}{2}\left(\varepsilon_{ib} - \varepsilon_{id}\right) \end{cases} \tag{3.7}$$

where ε_{ia}, ε_{ib}, ε_{ic} and ε_{id} are the strains measured by the four FBGs on the plane *A*.

Combining Eq. (3.6) with Eq. (3.7) and conducting linear interpolation of strain distributions, the distribution of displacements in three dimensions can be calculated.

For a 2-D problem, ε_{ia} and ε_{ic} are zero. Thus Eq. (3.7) is reduced to

$$\begin{cases} \varepsilon_i^A = \frac{1}{4}\left(\varepsilon_{ib} + \varepsilon_{id}\right) \\ \varepsilon_i^{Ty} = \frac{1}{2}\left(\varepsilon_{ib} - \varepsilon_{id}\right) \end{cases} \tag{3.8}$$

In this case, only two quasi-distributed FBG sensing arrays are required to be glued to the FBG sensing bar for 2-D measurement, as shown in Figure 3.26(b).

(3) Calibration of the FBG sensing bar

For calibration purpose, several 1 m long FBG sensing bars for 2-D measurement were prepared. Totally twelve FBG sensors were glued on each of the FBG sensing bars.

To verify the effectiveness of the FBG sensing bars, two types of calibration tests have been performed in laboratory, *i.e.* tension tests and deflection tests. For the demodulation of FBG sensors, a four channel interrogator sm125 is employed. It reads the reflected wavelengths of FBG sensors in an ascending order and interrogates up to 512 sensors simultaneously, with 0.1 pm resolution, 2 pm repeatability and 1 Hz acquisition speed (Micron Optics 2007). Ethernet or wireless connections can be employed for automatic data communication between the interrogator and the computer.

The tensile tests shown in Figure 3.27(a) were used to study the performance of FBG sensing bar for displacement measurement in the axial direction. Uniform axial displacements were applied to the FBG sensing bar in stages, which were calculated by the measurements of surface glued strain gauges. In the deflection tests shown in Figure

3.27(b)-(d), the FBG sensing bar with one end fixed or both ends simply supported was subjected to arbitrary lateral movements at discrete points by translation stages and the deflections were measured by digital displacement gauges.

Typical calibration results are illustrated in Figure 3.28. In the tensile tests, the relationship between the Bragg wavelength and the applied tensile or compressive displacement was shown to be fairly linear with R^2 of over 0.999 and no hysteretic or fatigue effects were observed. As the strain resolution of FBG sensors is as high as 1 $\mu\varepsilon$, the resolution of axial displacement of this FBG sensing bar is $1\times10^{-6}\,\text{m}=1\ \mu\text{m}$. Assuming the strain measuring range of the FBG sensor is ±-3000 $\mu\varepsilon$, if the FBG sensing bar is in pure tensile/compression, the maximum/minimum axial displacement that the FBG sensing bar can measure is $1\times3000\times10^{-6}\,\text{m}=3\ \text{mm}$.

Figure 3.28(b) shows a comparison of deflection profiles computed from FBG readings and measured by digital displacement gauges at discrete locations and an excellent agreement was achieved. Consider the special case that the FBG sensing bar is subjected to a lateral displacement at the free end, the relationship between the maximum strain and the applied displacement is $\frac{\text{S}}{\varepsilon_{\max}}=\frac{L^2}{3R}$. In this condition, the resolution of FBG sensing bar for measuring transverse displacement is $\frac{1^2}{3\times5\times10^{-3}}\times10^{-6}=6.7\times10^{-5}\,\text{m}=67\ \mu\text{m}$ and the maximum transverse displacement that the FBG sensing bar can measure is $\frac{1^2}{3\times5\times10^{-3}}\times3000\times10^{-6}$=0.2 m=200 mm. Based on the demonstrated performance and analysis, the FBG sensing bar is considered well suited for laboratory physical model tests.

3.4.2 FBG in-place inclinometer

(1) Sensor design

Shown in Figure 3.29, an FBG in-place inclinometer is a special PVC casing used for the measurement of displacements in geotechnical structures, such as foundations, dams or slopes. FBG strain sensors are glued to each section of the casing (outer diameter R=30 mm or 70 mm, length L=4 m) and used to measure the tensile strains along the casing. The strains can be converted into the deflections of the casing according to Euler-Bernoulli beam theory.

(2) Calibration tests

The manufacturing and calibration set-up are shown in Figure 3.30 and Figure 3.31. The calibration results in Figure 3.32 show that the displacements measured by the FBG in-place inclinometer fit well with those measured by displacement gauges.

(3) Field trial

Recently, a tunnel excavation is being carried out in Lujiazui, Shanghai, which passes above a section of Shanghai Metro No. 2. In order to measure the potential displacements of the tunnel induced by the excavation, a series of FBG in-place inclinometers with a total length of 82 m have been installed along the metro tunnel for a field trial, as shown in Figure 3.33. The PVC casings were fixed on the metro shields by steel clamps, so that the tunnel displacements would be transferred to the casings. In field data analysis, the FBG in-place inclinometers are assumed to be a continuous beam, with simple supports at 4 m intervals.

The monitoring results are presented in Figure 3.34 and Figure 3.35. It is indicated that, until now the excavation activities has induced a maximum tunnel heave of about 0.448

mm. The continuous monitoring results in Figure 3.35 show that, when the moving train arrives, the vibration will cause a sudden change of the Bragg wavelengths of all the FBG sensors. The changes in wavelengths are in the range of ±5 pm, as shown in Figure 3.35. The monitoring results also indicate that, after 3 to 5 min, the influence arising from vibration vanished.

3.4.3 FBG settlement tube

(1) Sensor design

A special FBG settlement tube with a length of 1 m is developed to monitor the settlement inside soil ground at certain depth. In the settlement tube, there is a polyethylene (PE) tube packaged pre-tensioned FBG strain sensor connected to a stainless steel spring. The strain ε measured by the FBG sensor is thus proportional to the compression of the tube S, i. e.

$$S = \left(\frac{\pi dtE}{k} + l\right)\varepsilon = \left(\frac{\pi dtE}{k} + l\right)\frac{\left(\Delta\lambda_B - \Delta\lambda_B^{\Delta T}\right)}{c_\varepsilon \lambda_{B0}} \qquad (3.9)$$

where E, d, l and t are the Young's modulus, outer diameter, length and thickness of the PE tube, respectively; k is the spring coefficient; $\Delta\lambda_B$ and $\Delta\lambda_B^{\Delta T}$ are the shifts in wavelengths of the FBG strain sensor and an FBG temperature sensor for temperature compensation.

The FBG settlement tubes can be connected with each other, as depicted in Figures 3.36. In the field, the FBG settlement tubes can be installed in a drillhole and grouted by cement-bentonite slurry like conventional extensometers. The profile of vertical settlements with respect to depth can be captured in this way.

(2) Calibration tests

Figures 3.37 and Figures 3.38 show the test set-up and typical calibration results. The FBG settlement tube is proved to be reliability and have high accuracy. For trial purpose, two settlement tubes were grouted in predefined holes in laboratory to verify its ability to measure settlement in field application, as shown in Figure 3.36. The mix proportion of cement, bentonite and water is 2:3:20 by weight.

During testing, weight sets were loaded on the ground surface and the Bragg wavelengths of the FBG settlement tubes were observed to decrease with the compression of ground soil, as shown in Figure 3.40. This phenomenon indicates the effectiveness of the FBG settlement tube for field monitoring.

3.5 SUMMARY

Various FBG sensors have been developed for measuring strain, temperature, or displacement of geotechnical structures. In laboratory calibration tests, the reliability and accuracy of these FBG based sensors are verified. The packaging methods of FBG sensor adopted in this chapter are tested to be good to ensure both fiber protection and efficient strain transfer.

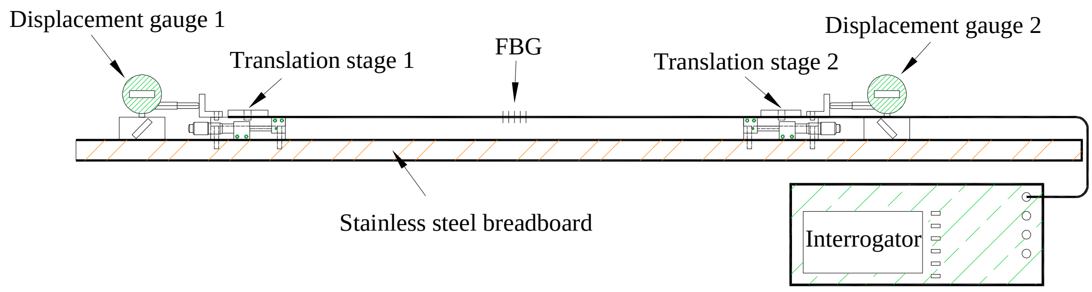

Figure 3.1 Test set-up of the calibration of one bare FBG strain sensor

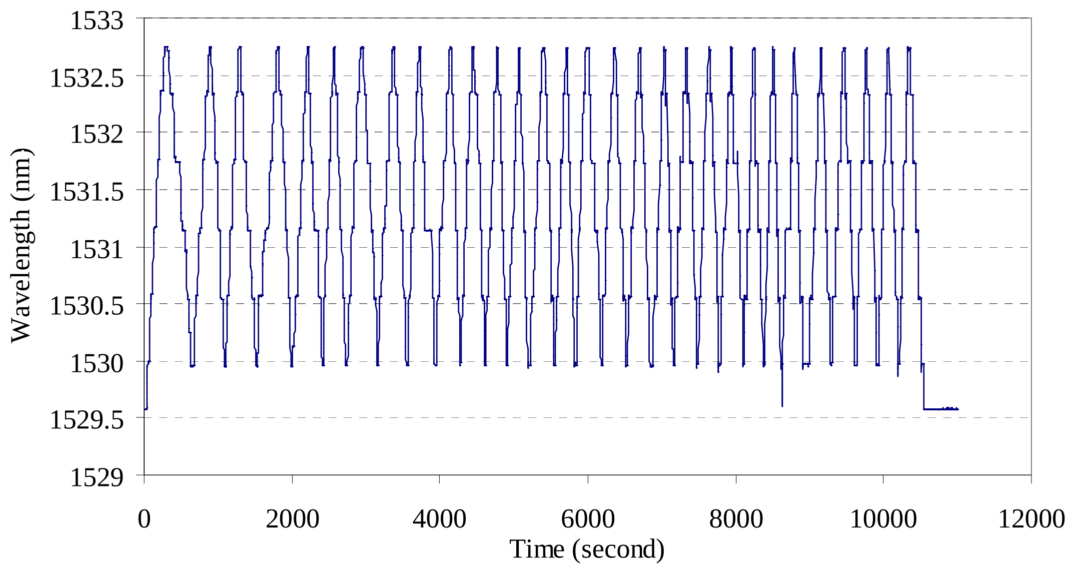

Figure 3.2 Typical wavelength-time curve in the calibration of one bare FBG strain sensor

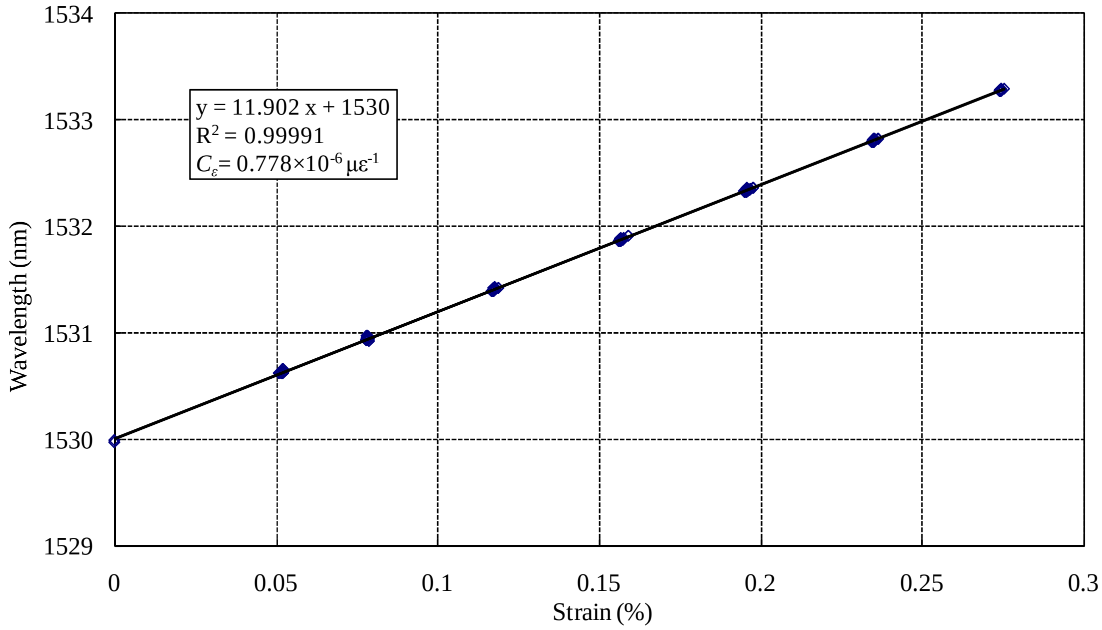

(a) FBG A

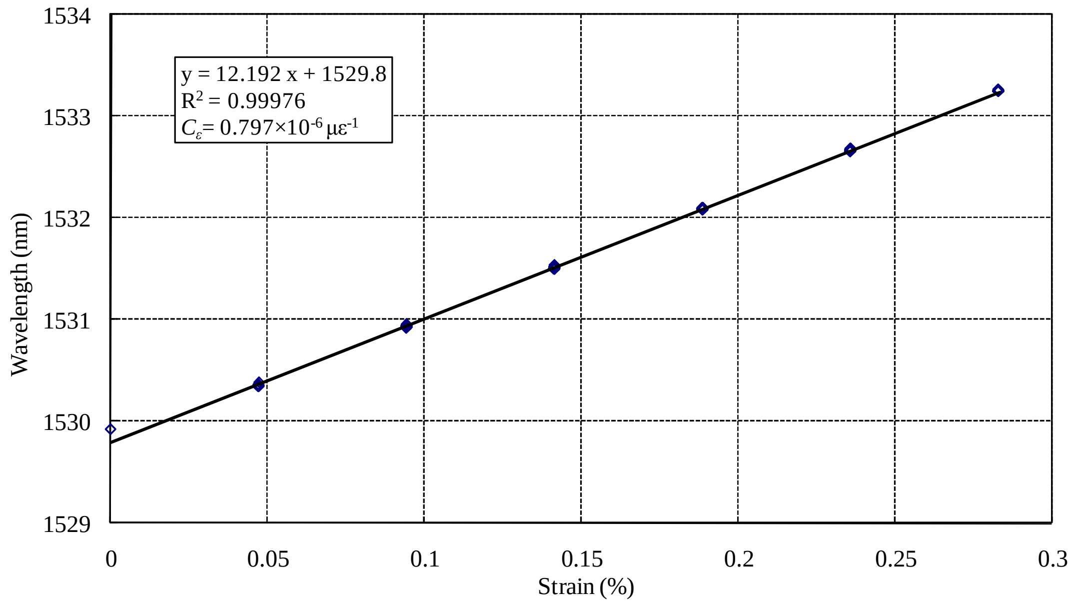

(b) FBG B

Figure 3.3 Typical calibration results of one bare FBG strain sensor

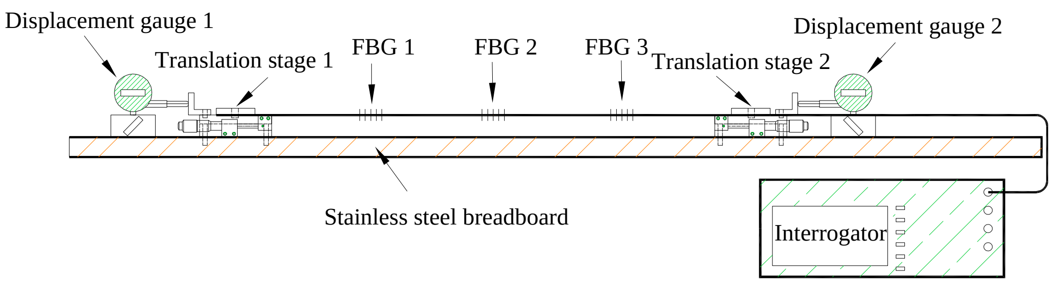

Figure 3.4 Test set-up of the calibration of three bare FBG strain sensors in series

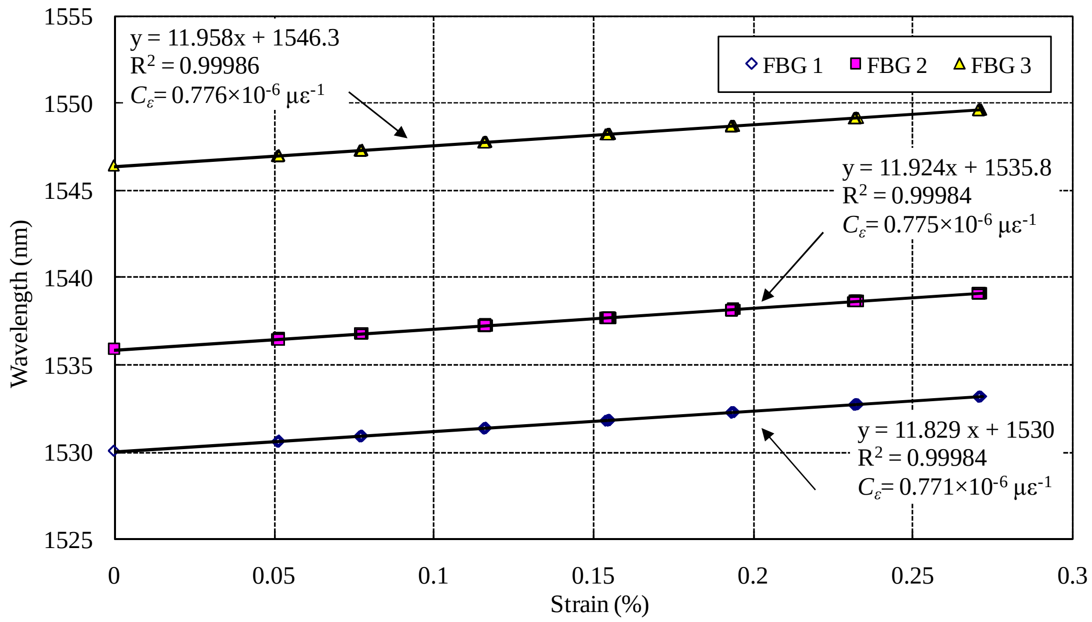

(a) FBG group 1

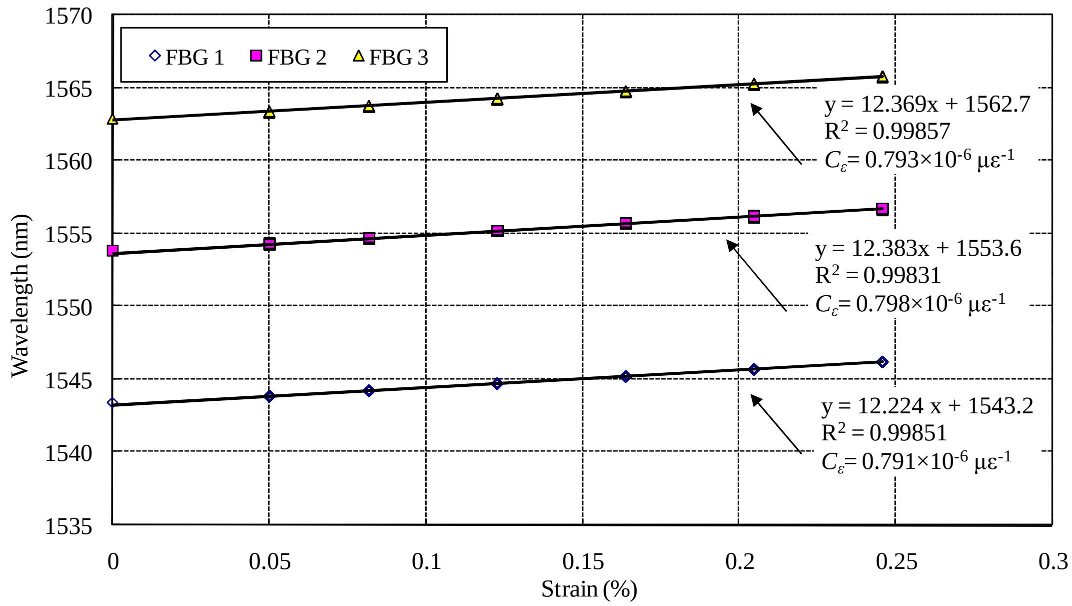

(b) FBG group 2

Figure 3.5 Typical calibration results of three bare FBG strain sensors in series

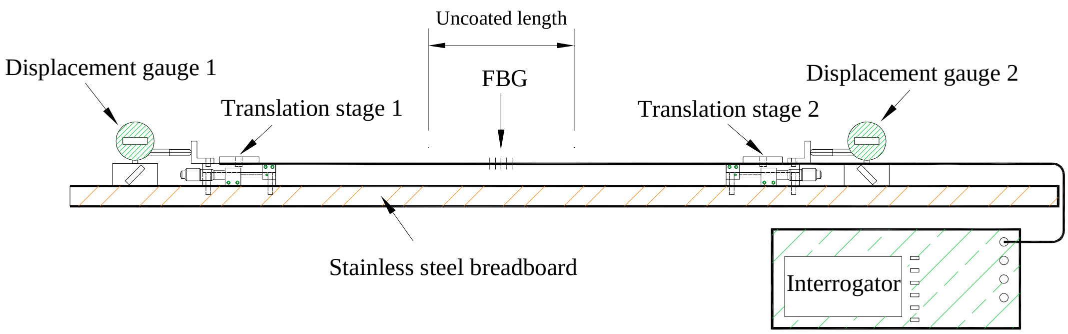

Figure 3.6 Test set-up of the calibration of one bare FBG strain sensor on an intentionally uncoated optical fiber

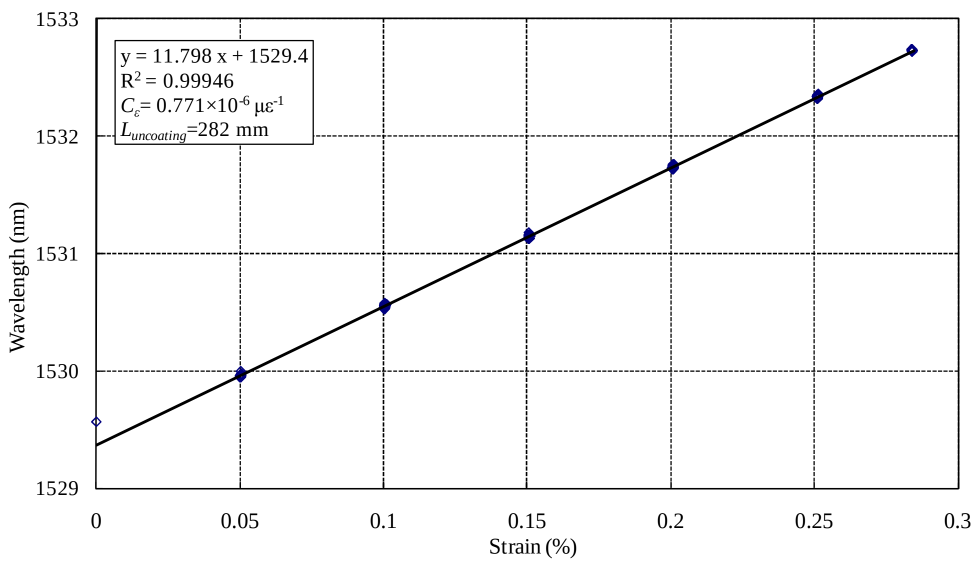

(a) FBG A

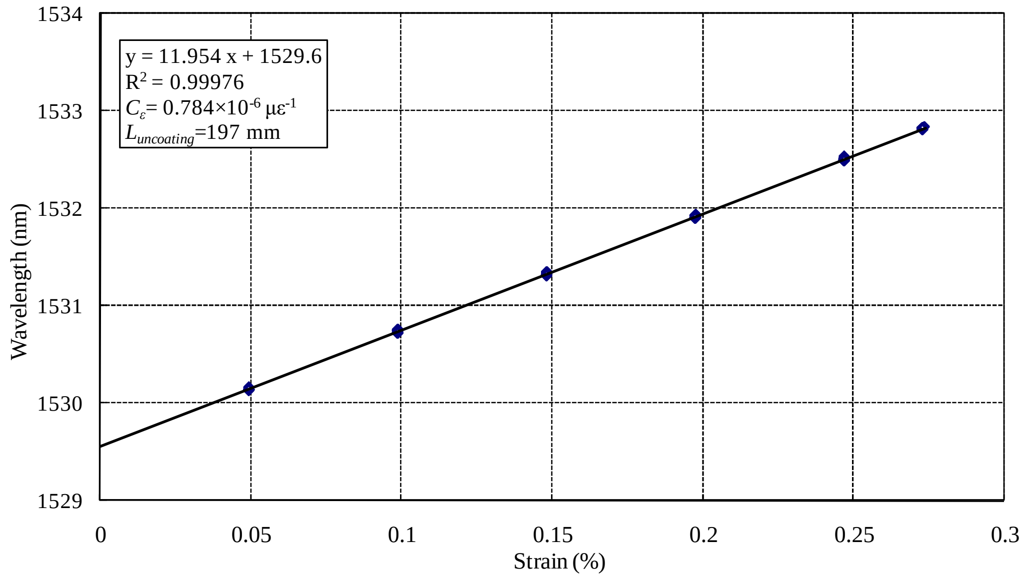

(b) FBG B

Figure 3.7 Typical calibration results of one bare FBG strain sensor on an intentionally uncoated optical fiber

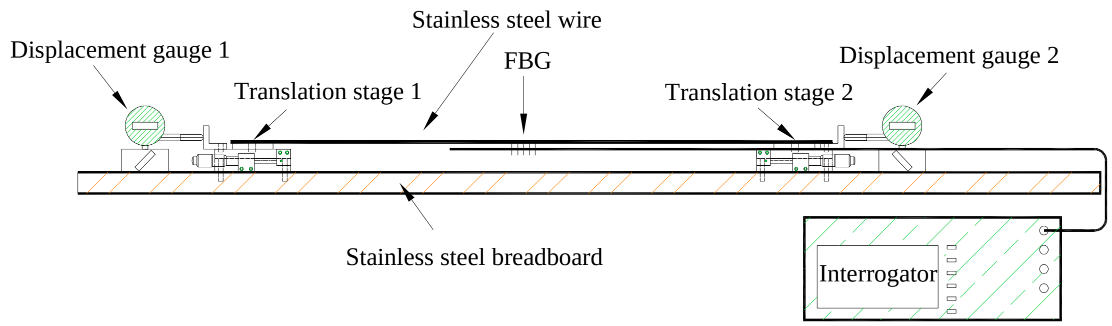

Figure 3.8 Test set-up of the calibration of one FBG strain sensor glued on a stainless steel wire

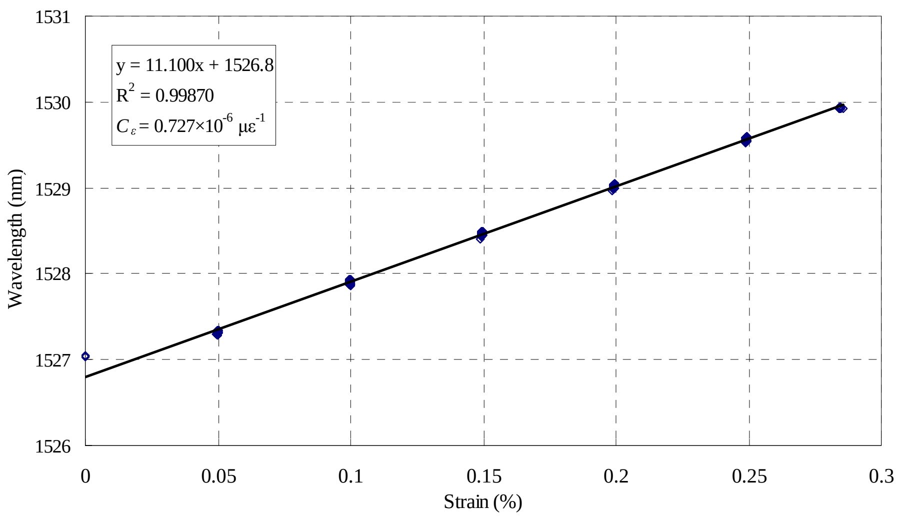

(a) FBG A

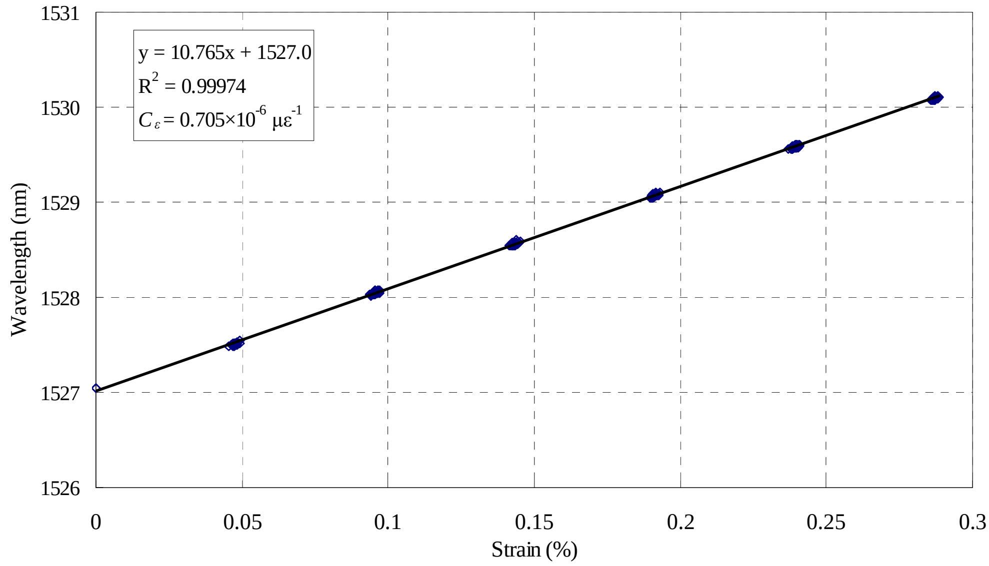

(b) FBG B

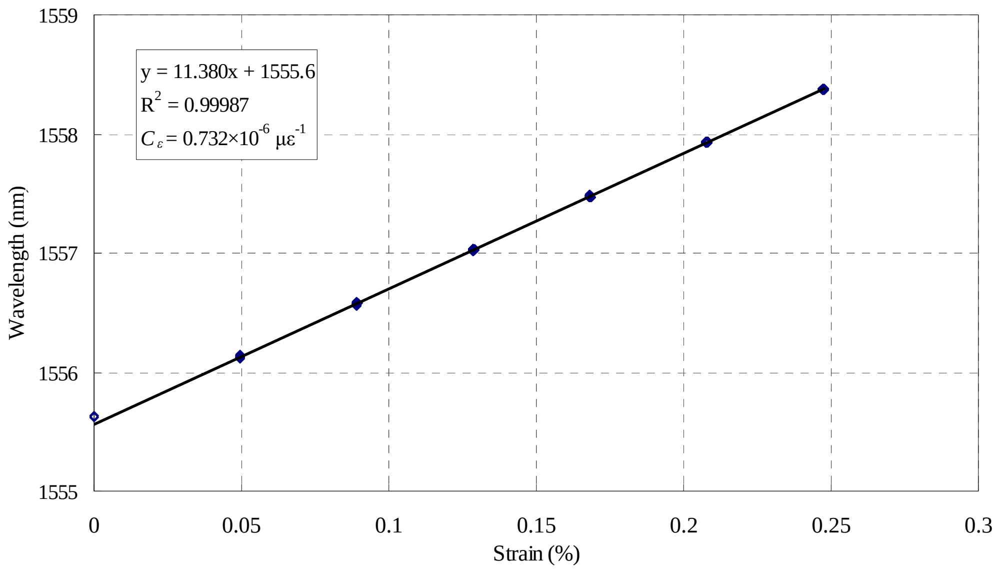

(c) FBG C

Figure 3.9 Typical calibration results of one FBG strain sensor glued on a stainless steel wire

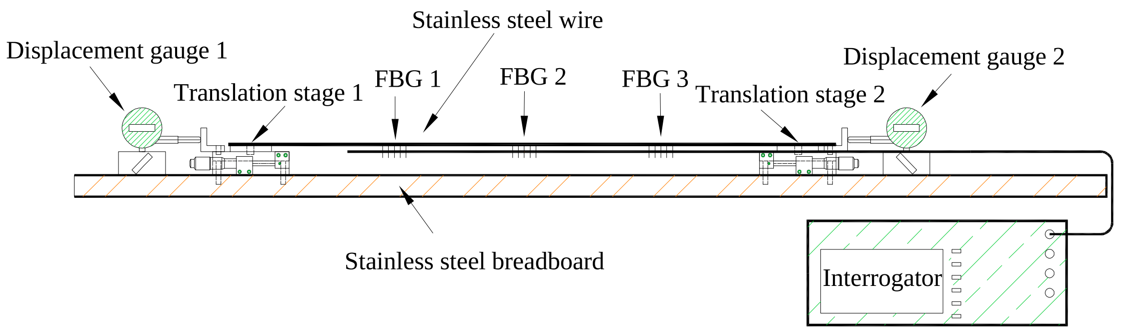

Figure 3.10 Test set-up of the calibration of three FBG strain sensors glued on a stainless steel wire

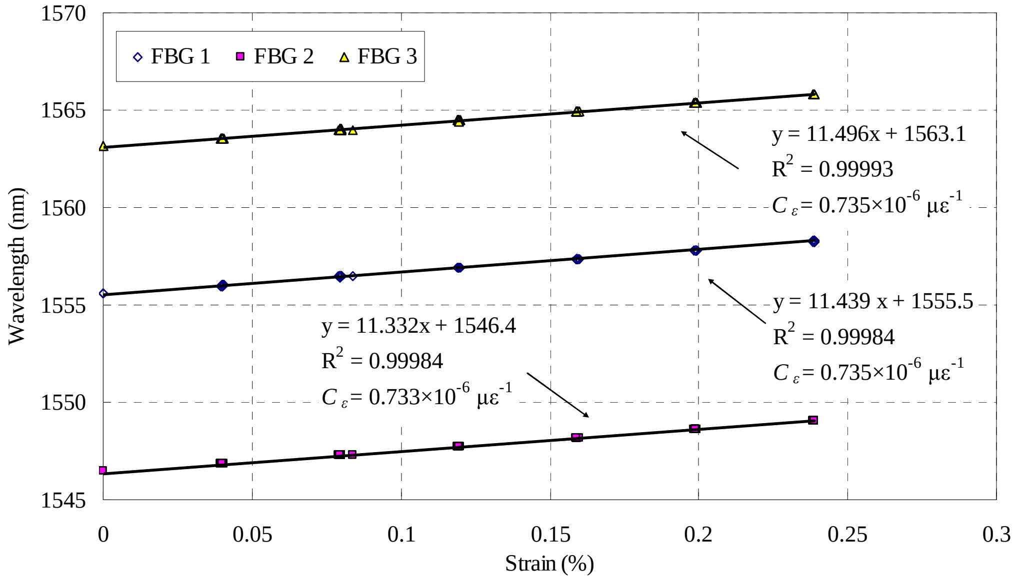

(a) FBG group A

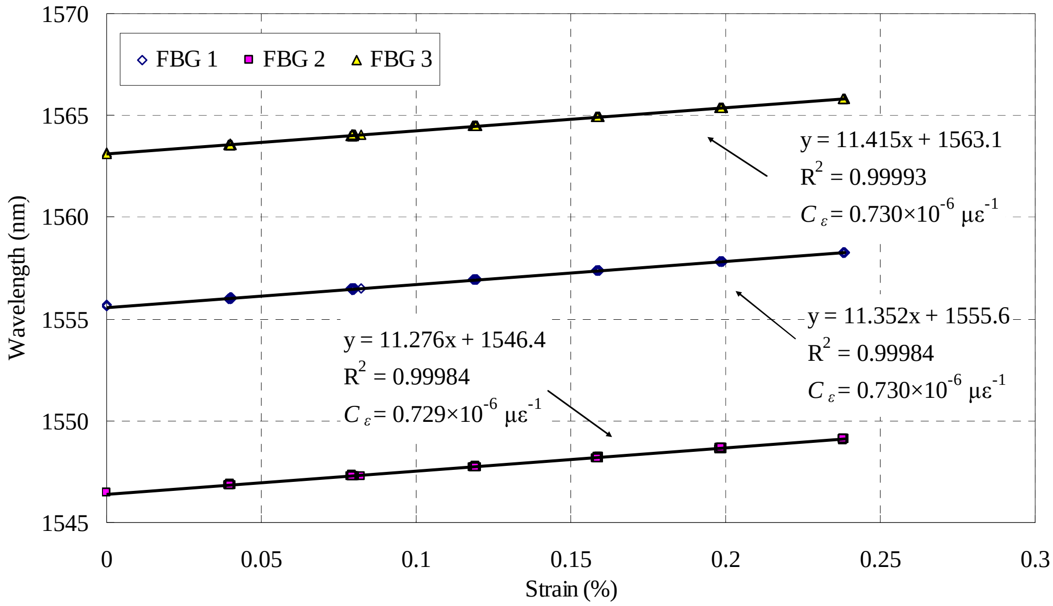

(b) FBG group B

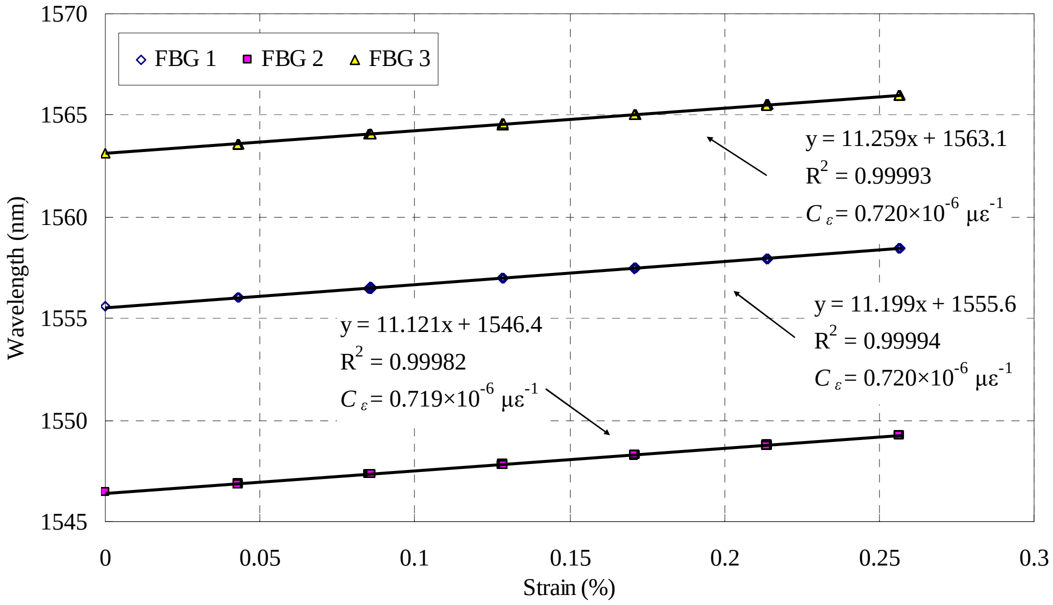

(c) FBG group C

Figure 3.11 Typical calibration results of three FBG strain sensors glued on a stainless steel wire

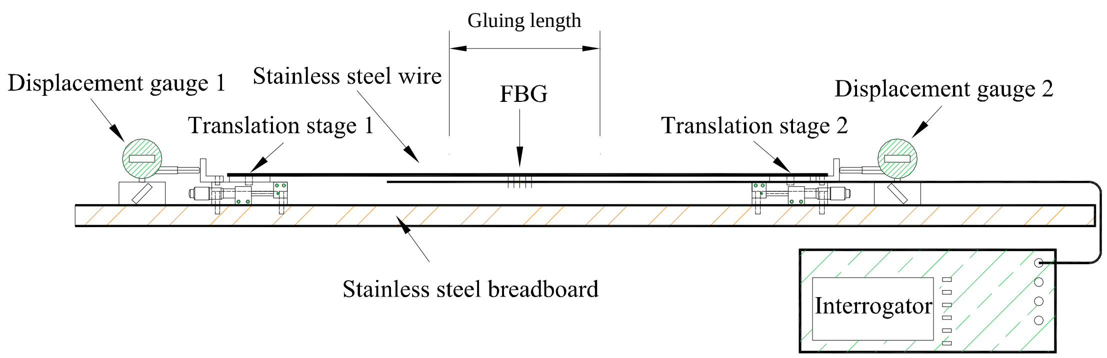

Figure 3.12 Test set-up of the calibration of one FBG strain sensor with a certain length of optical fiber glued on a stainless steel wire

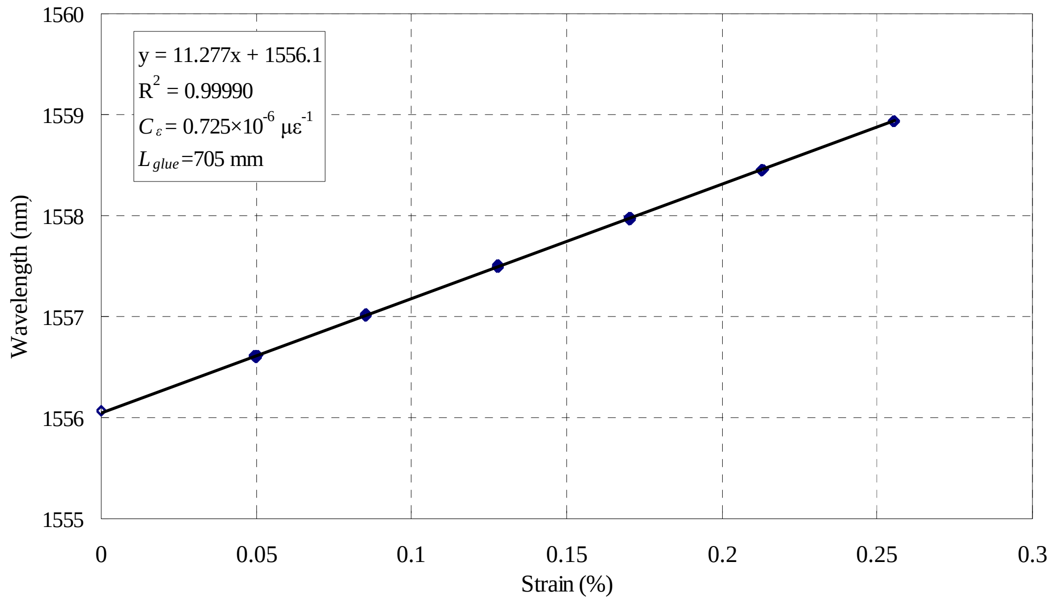
y = 11.277x + 1556.1
R^2 = 0.99990
C_ε= 0.725×10^{-6} $\mu\varepsilon^{-1}$
L_{glue}=705 mm
Wavelength (nm)
1560
1559
1558
1557
1556
1555
0
0.05
0.1
0.15
0.2
0.25
0.3
Strain (%)

(a) FBG A

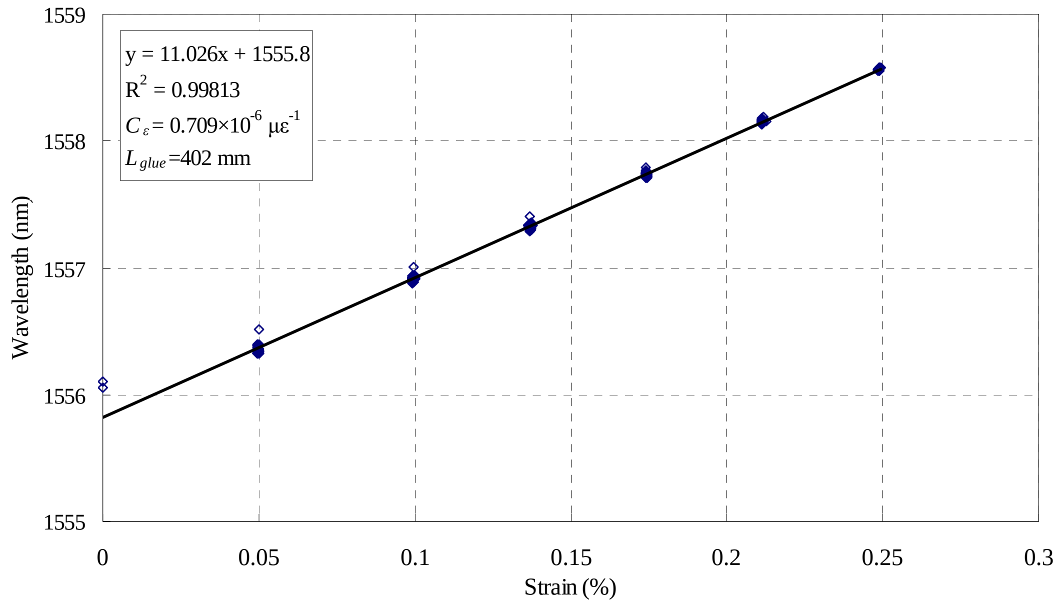
y = 11.026x + 1555.8
R^2 = 0.99813
C_ε= 0.709×10^{-6} $\mu\varepsilon^{-1}$
L_{glue}=402 mm
Wavelength (nm)
1559
1558
1557
1556
1555
0
0.05
0.1
0.15
0.2
0.25
0.3
Strain (%)

(b) FBG B

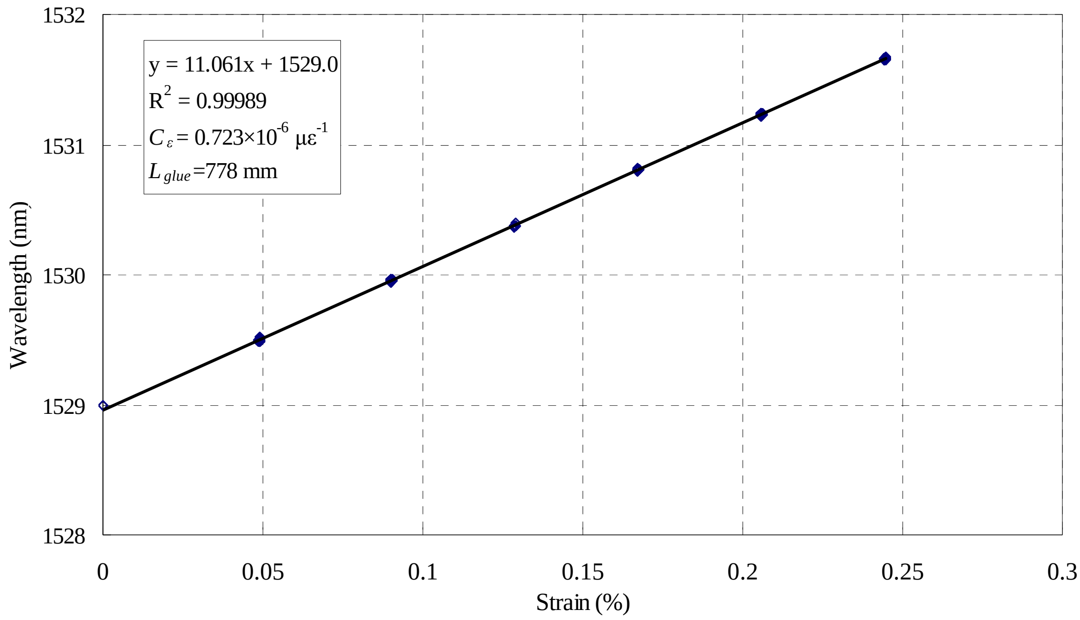

(c) FBG C

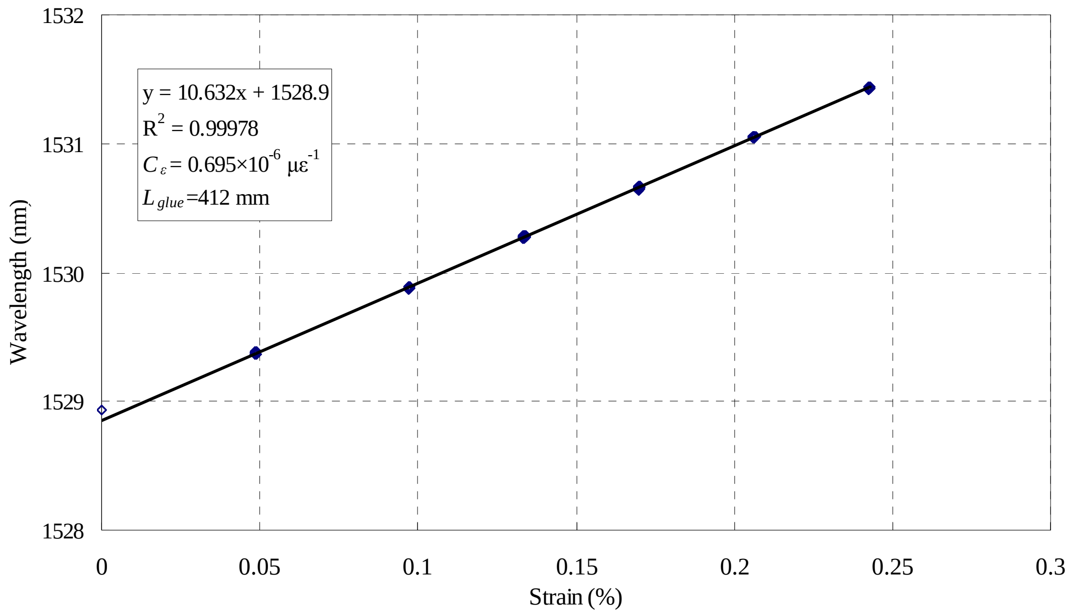

(d) FBG D

Figure 3.13 Typical calibration results of one FBG strain sensor with a certain length of optical fiber glued on a stainless steel wire

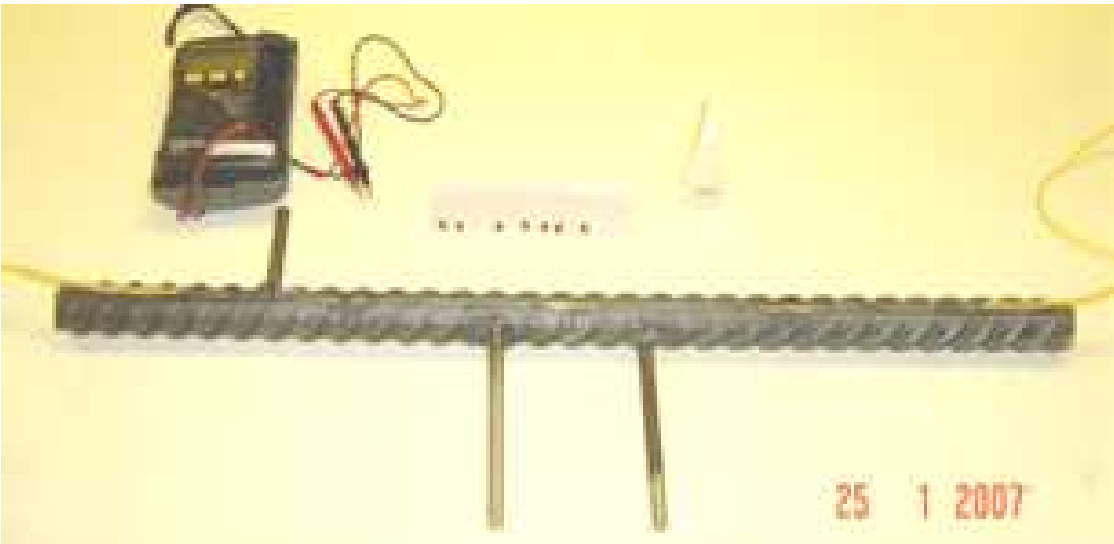

Figure 3.14 Photograph of a steel bar instrumented with three pairs of FBG strain sensors and three pairs of electrical strain gauges

(a) Test set-up of the calibration of a steel bar with surface glued FBG sensors and strain gauges

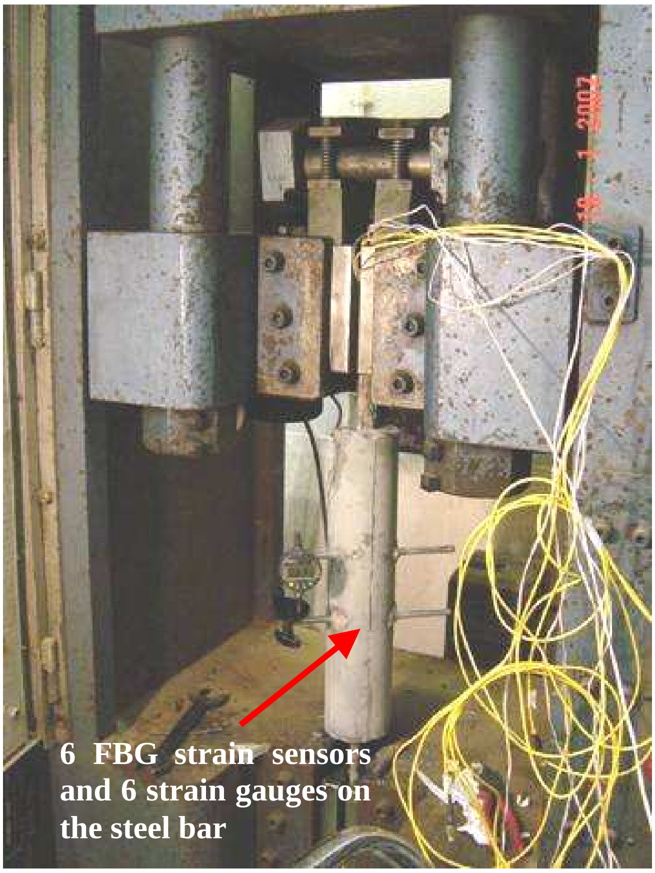

(b) Details of the cement column sample with embedded FBG sensors and strain gauges

Figure 3.15 Photographs of test set-up of the calibration of FBG strain sensors glued on a steel bar

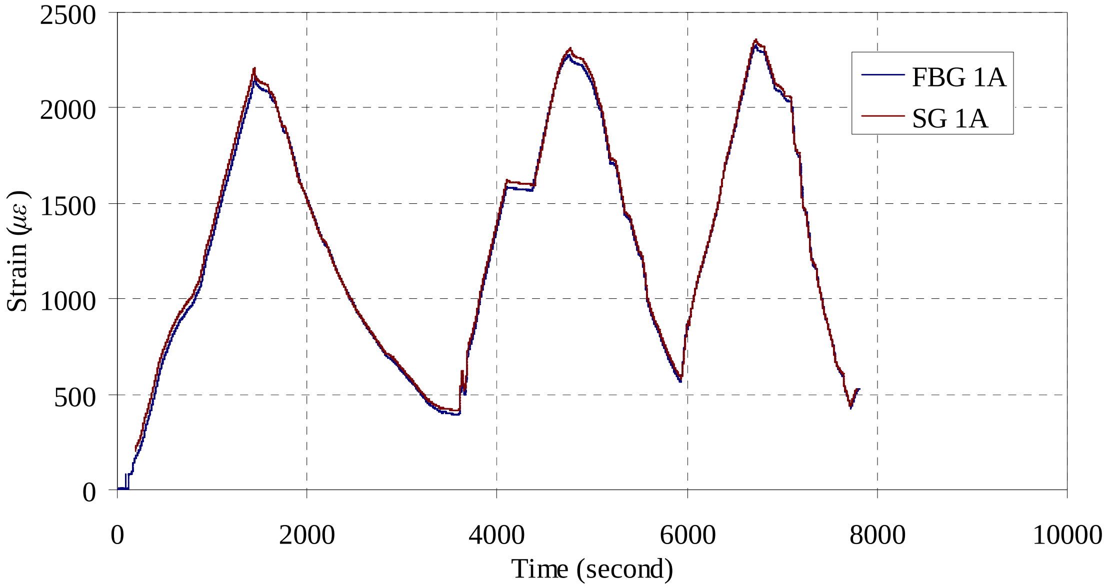

Figure 3.16 Comparison between the reading of FBG No. 1A and strain gauge No. 1A on the steel bar under loading and unloading

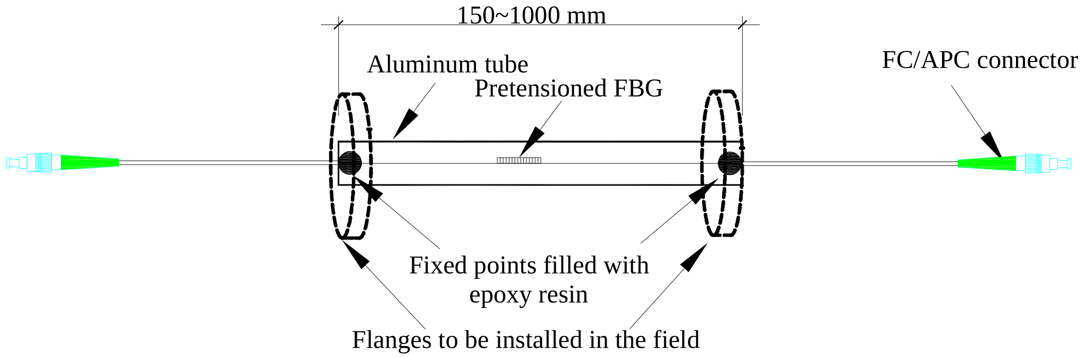

Figure 3.17 Schematic diagram of the tube packaged FBG strain sensor

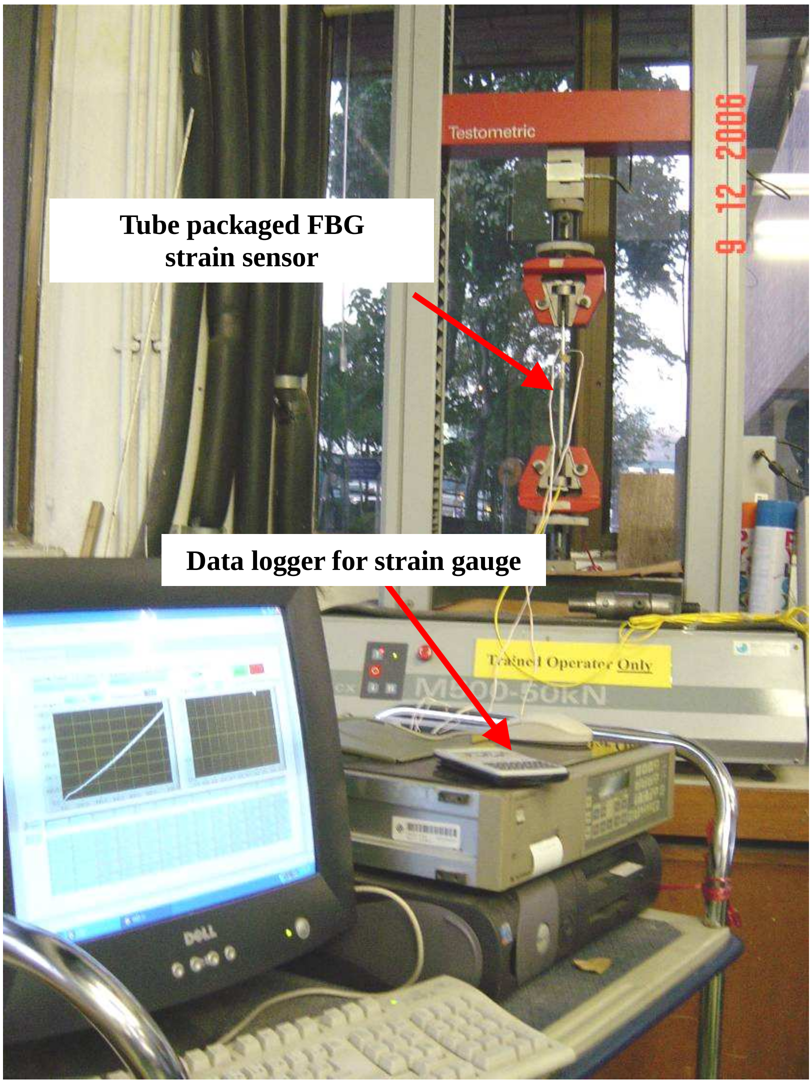

Figure 3.18 Photograph of test set-up of the calibration of the tube packaged FBG strain sensor

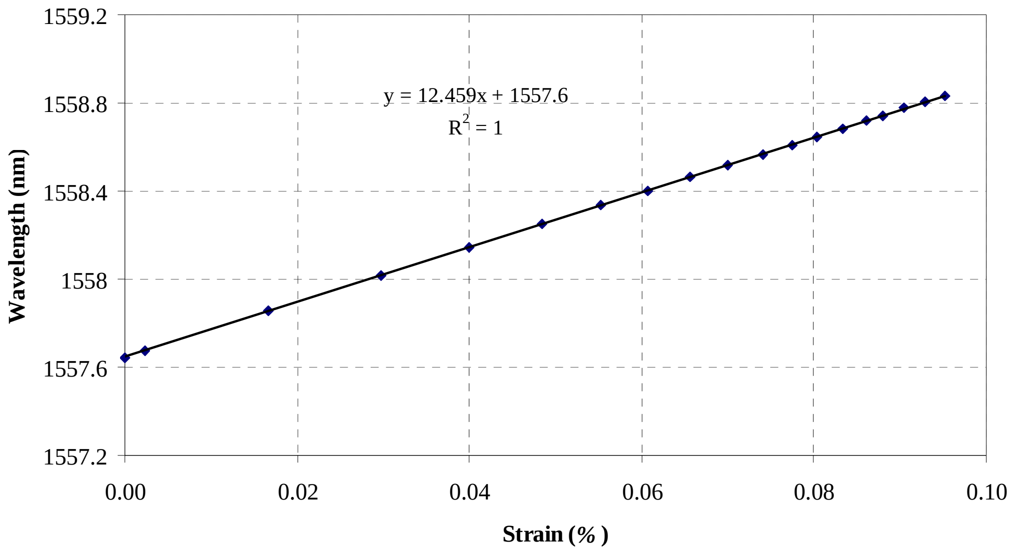

(a) Calibration of the FBG sensor by the strain readings from a strain gauge

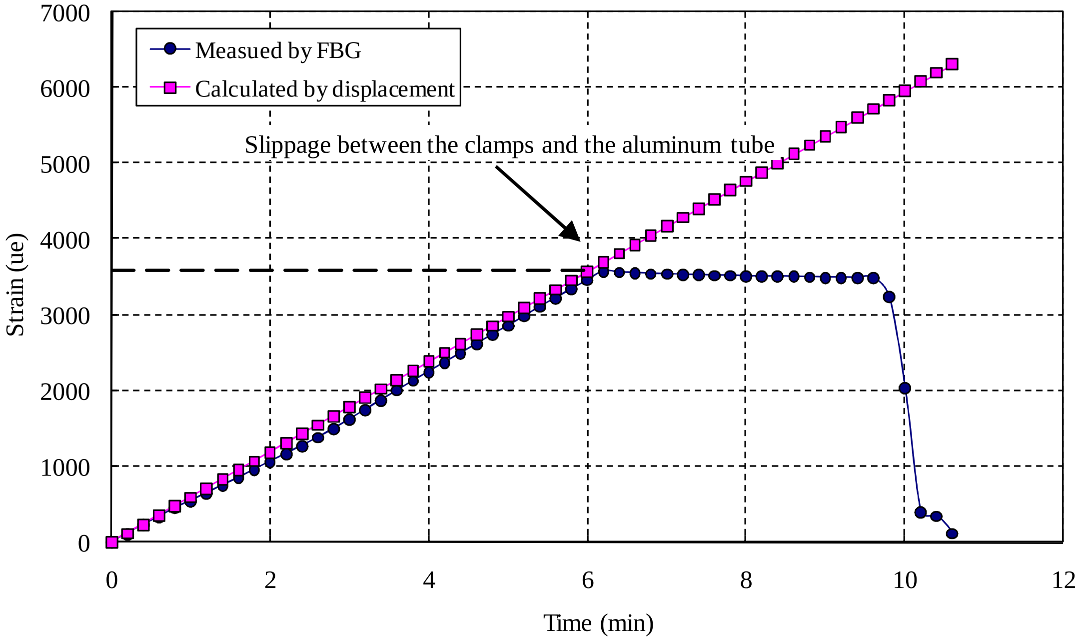

(b) Calibration of the FBG sensor by the displacement readings from the test machine

Figure 3.19 Typical calibration results of the tube packaged FBG strain sensor

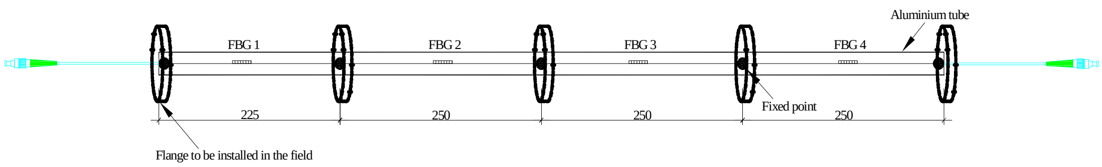

Figure 3.20 Schematic diagram of the tube packaged FBG strain sensing array

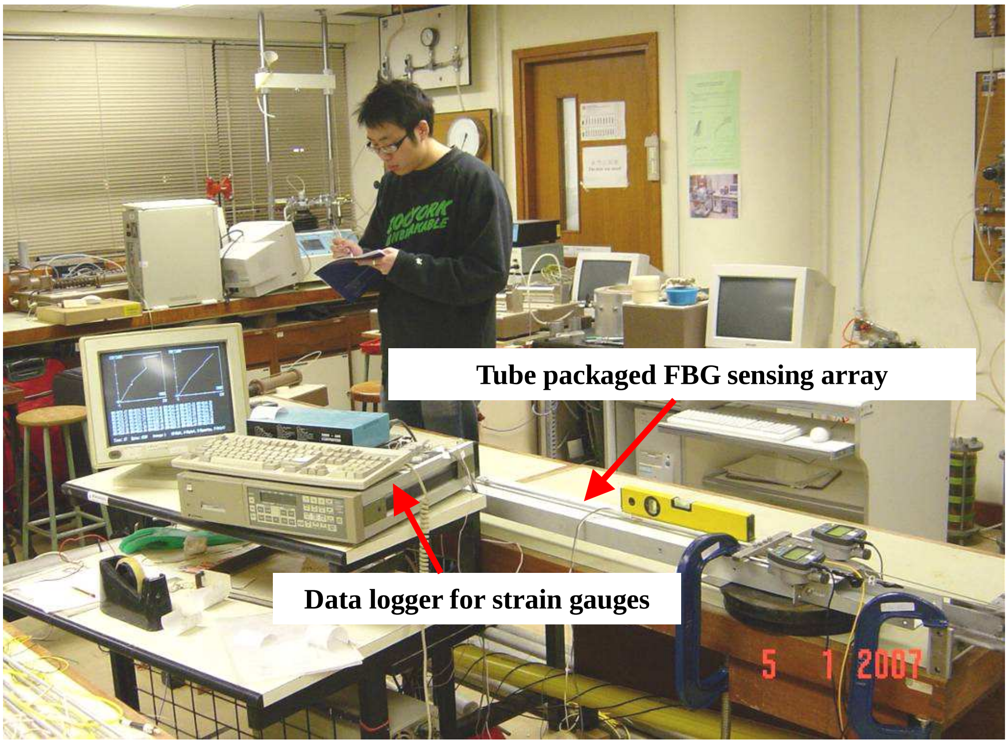

(a) Tensile equipments for calibration tests

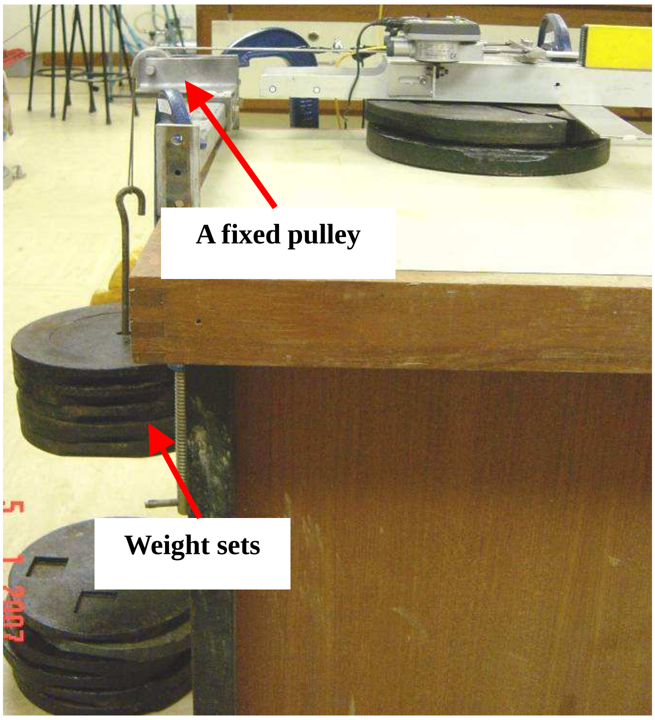

(b) Loading system

Figure 3.21 Photographs of test set-up of the calibration of the tube packaged FBG strain sensing array

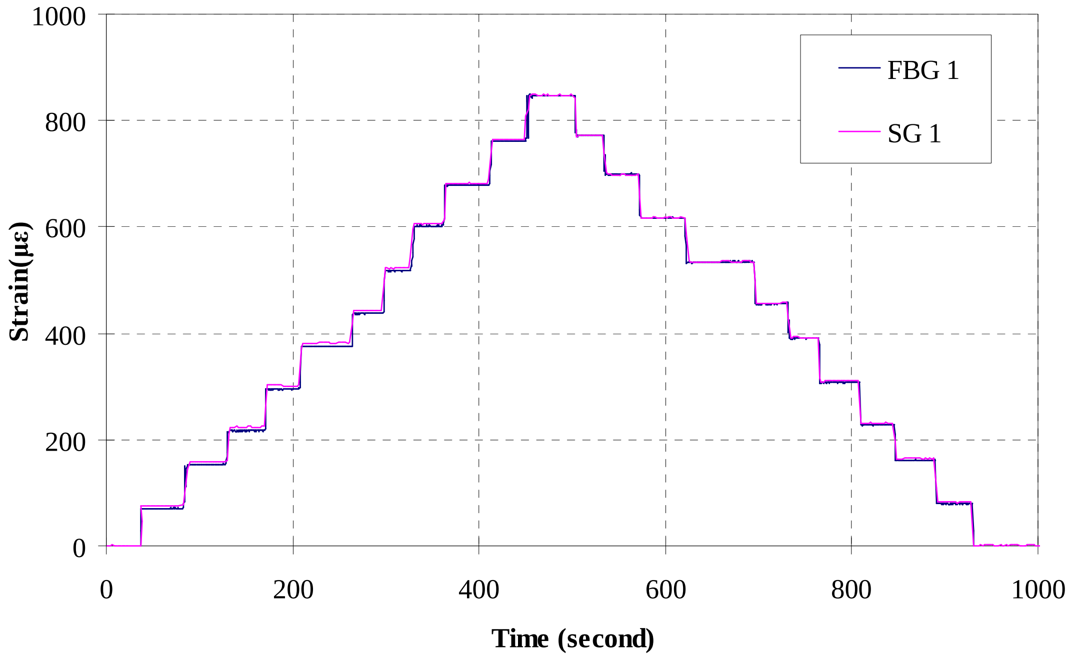
1000
800
600
400
200
0
Strain(με)
0
200
400
600
800
1000
Time (second)
FBG 1
SG 1

(a) FBG 1

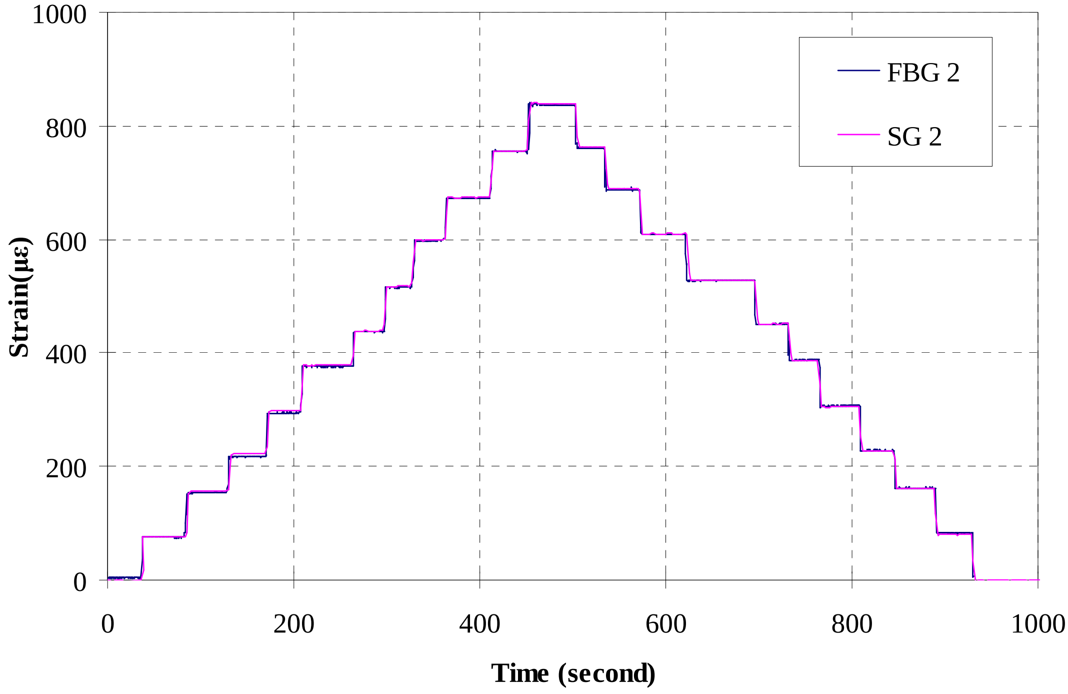
1000
800
600
400
200
0
Strain(με)
0
200
400
600
800
1000
Time (second)
FBG 2
SG 2

(b) FBG 2

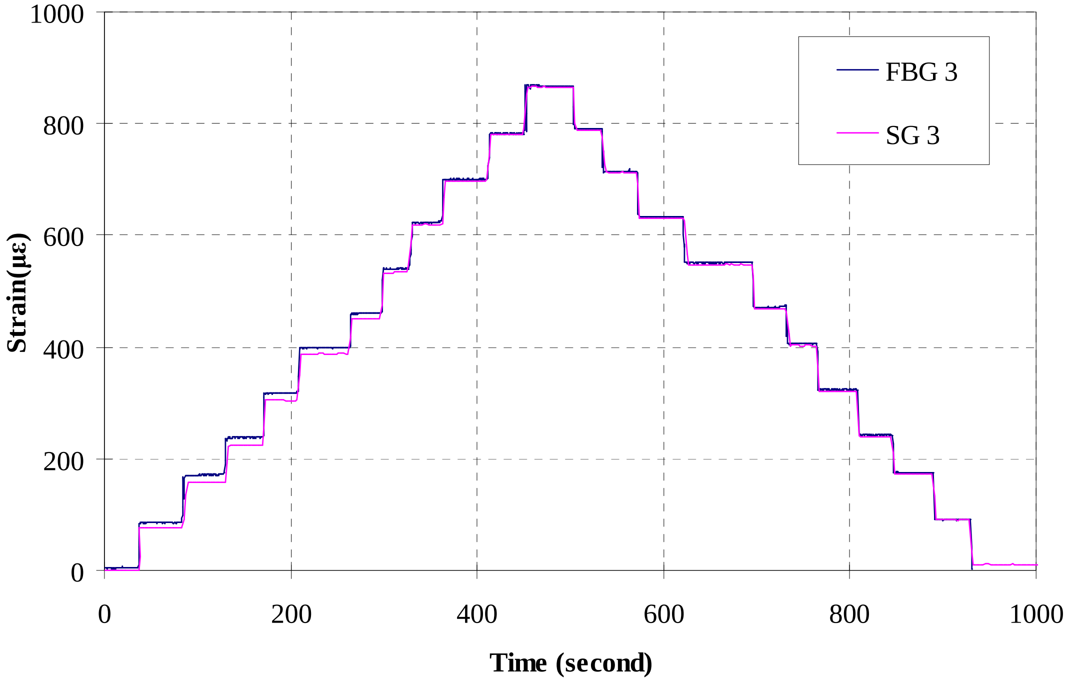

(c) FBG 3

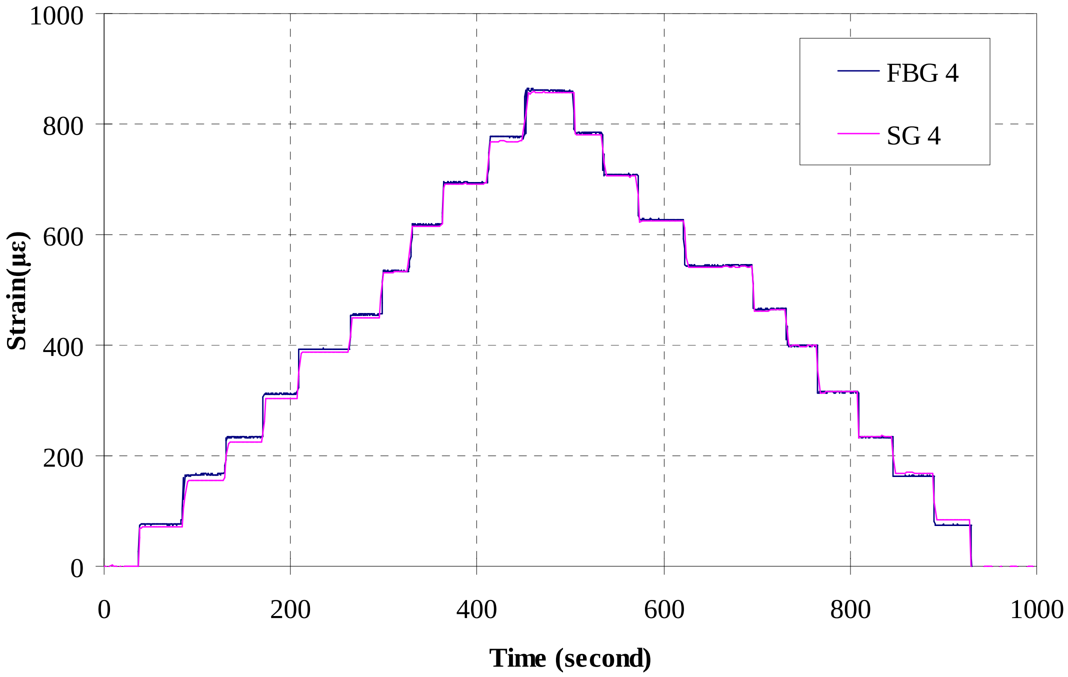

(d) FBG 4

Figure 3.22 Typical calibration results of the tube packaged FBG strain sensing array

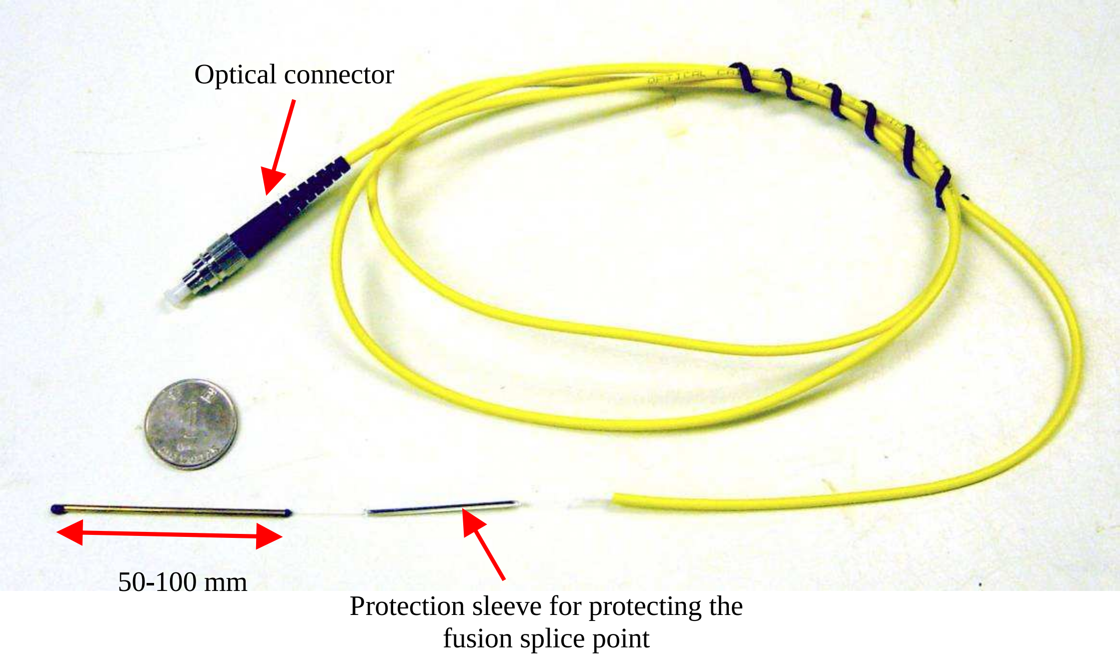

Figure 3.23 Photograph of the tube packaged FBG temperature sensor

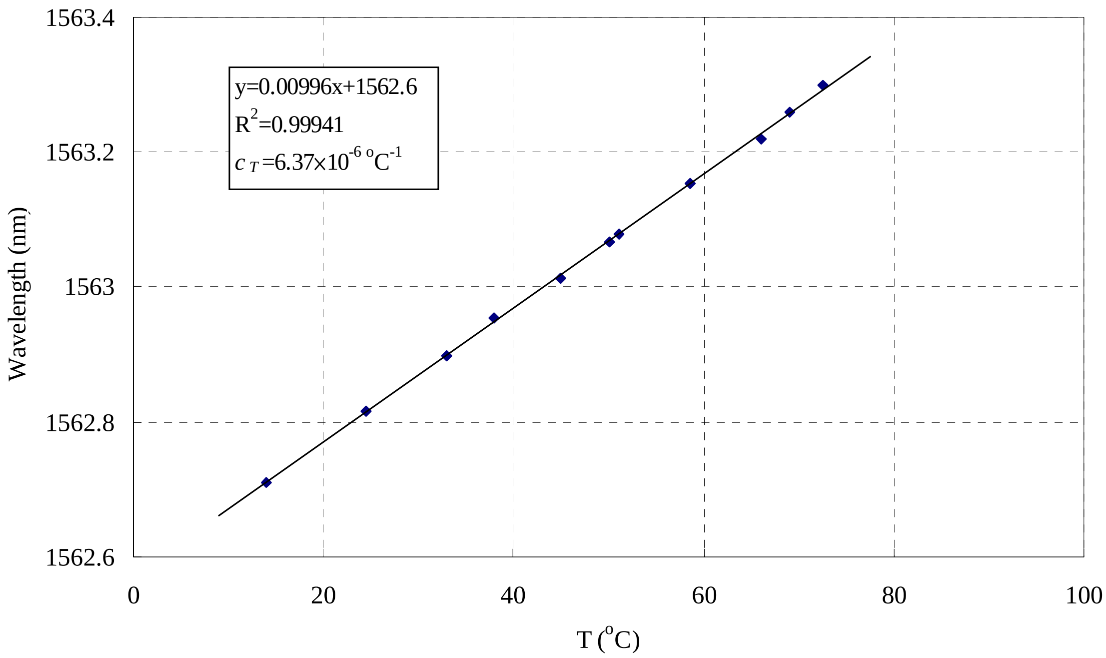

(a) FBG A

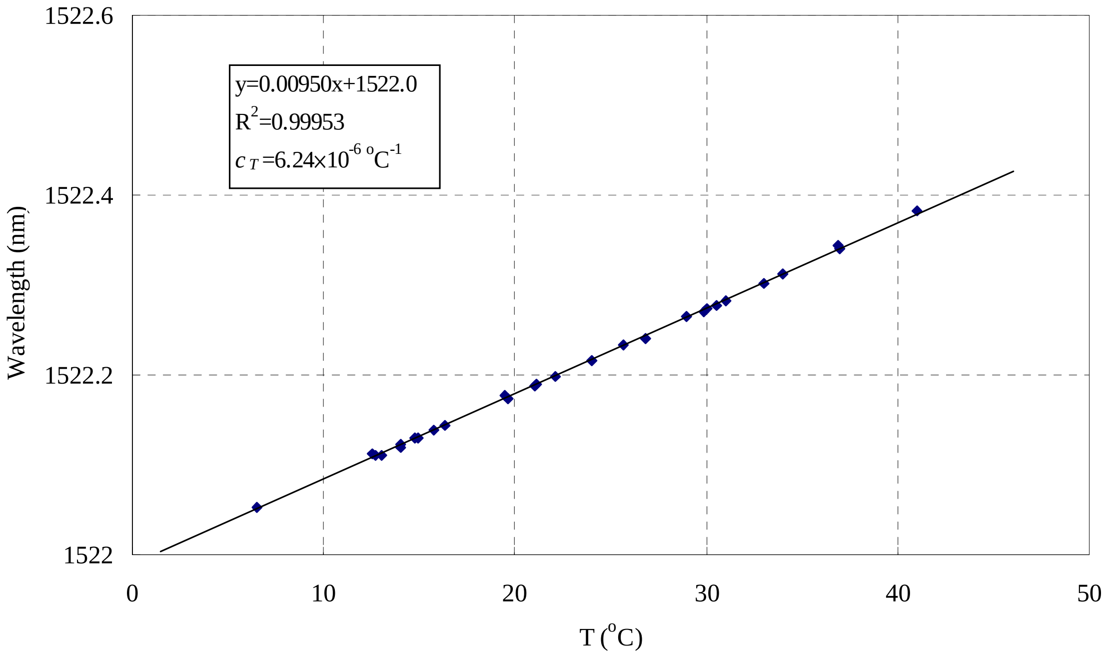

(b) FBG B

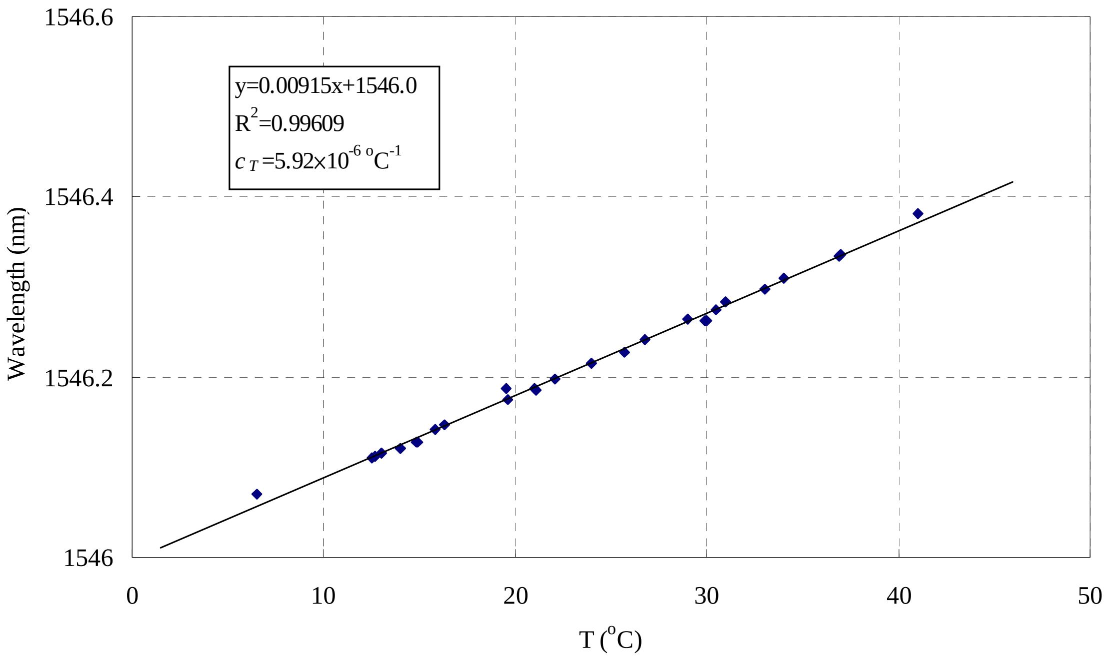

(c) FBG C

Figure 3.24 Typical calibration results of the tube packaged FBG temperature sensor

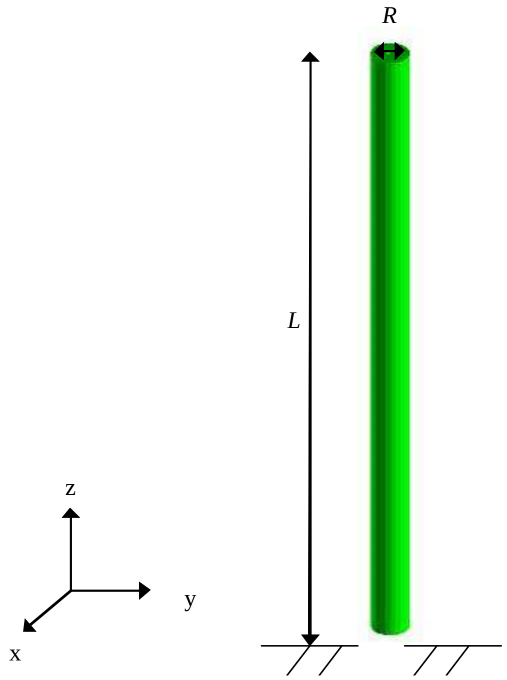

(a) A cantilever elastic beam before loading

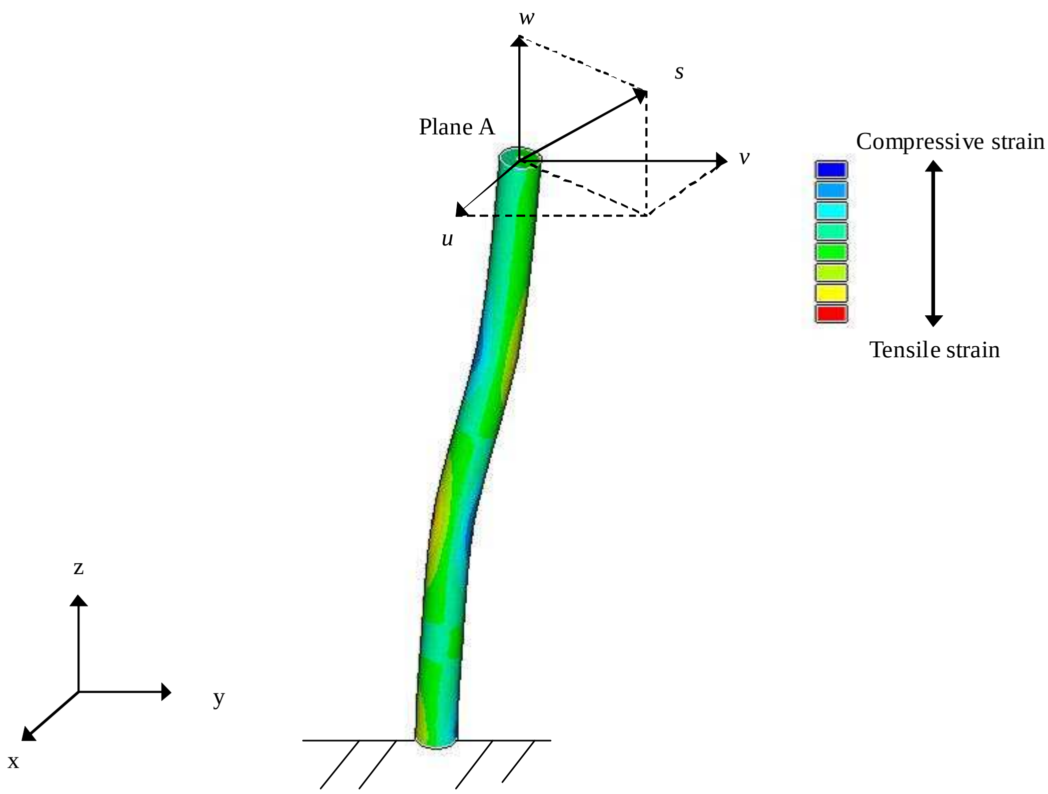

(b) Deformed shape and strain contours of the beam after loading

Figure 3.25 Schematic illustration of a cantilever beam under arbitrary transverse and axial loading

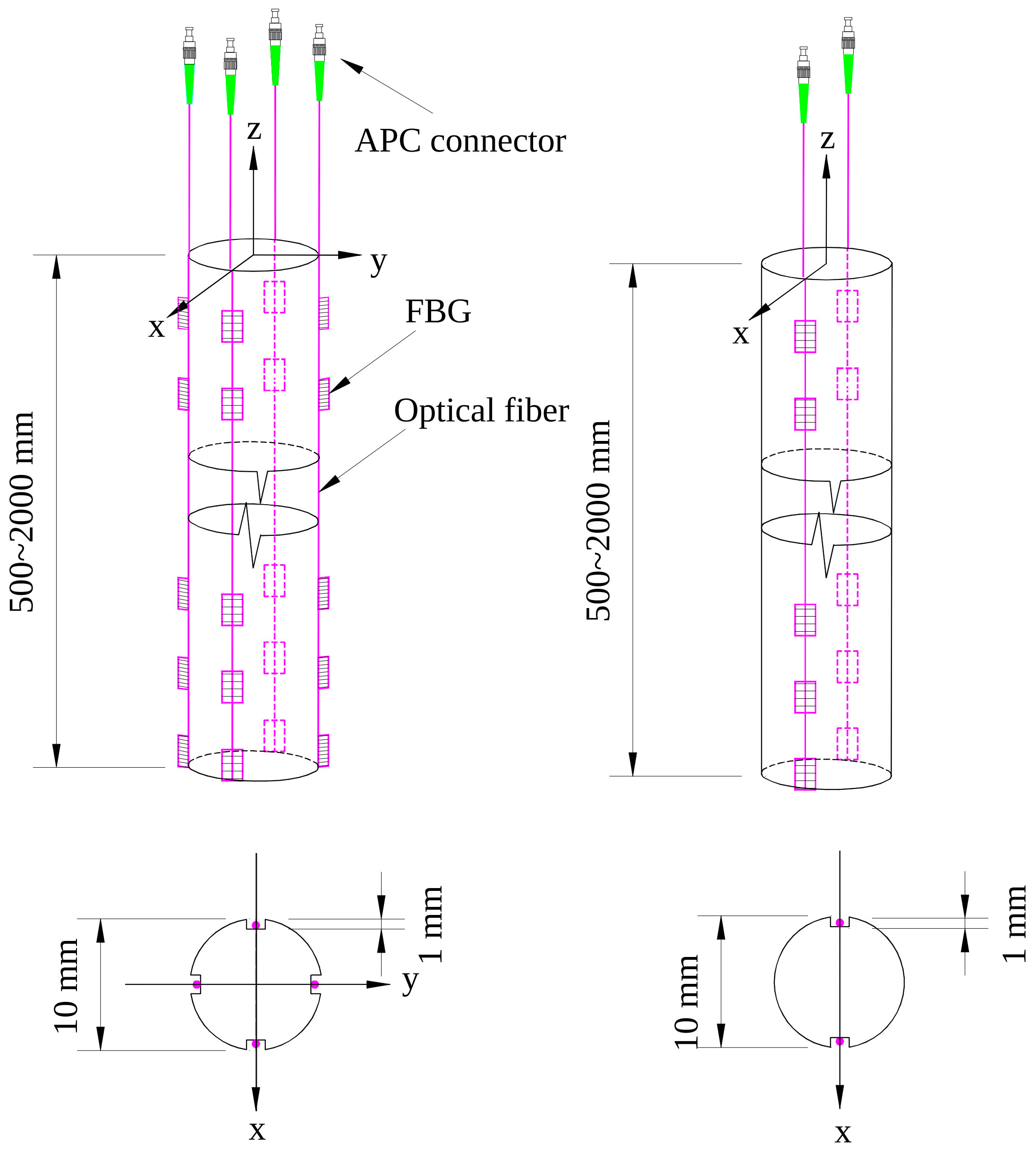

(a) 3-D measurement type (b) 2-D measurement type

Figure 3.26 Design of the FBG sensing bar for 3-D and 2-D displacement measurement

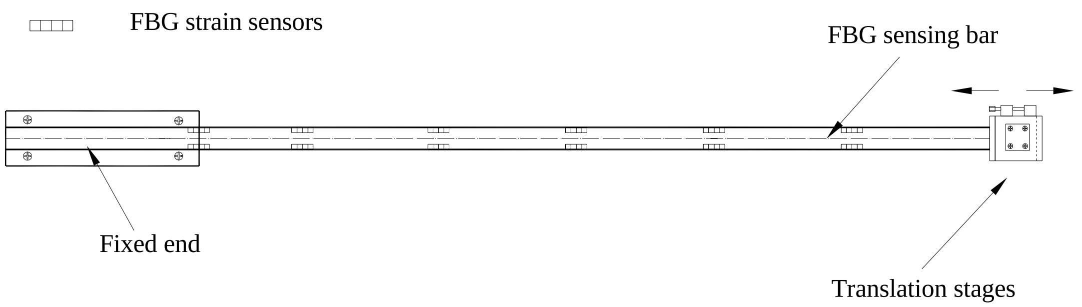

(a) Tensile test

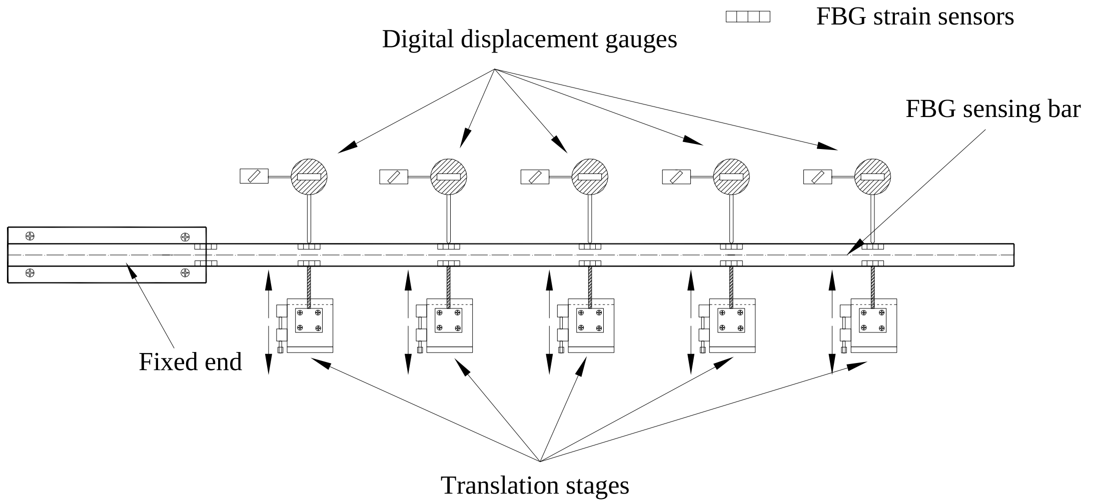

(b) Deflection test for cantilever condition

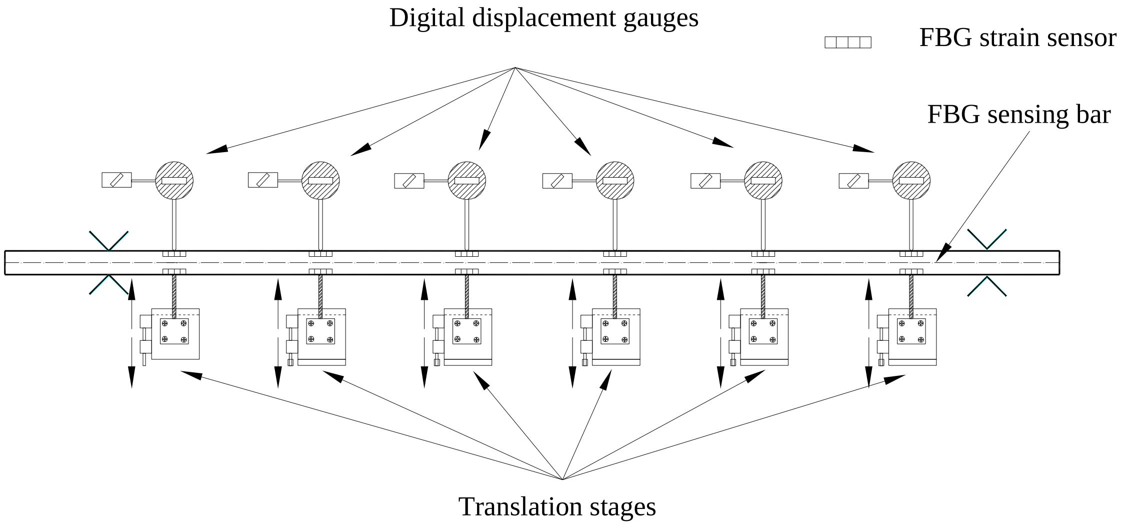

(c) Deflection test for simple-support condition 1

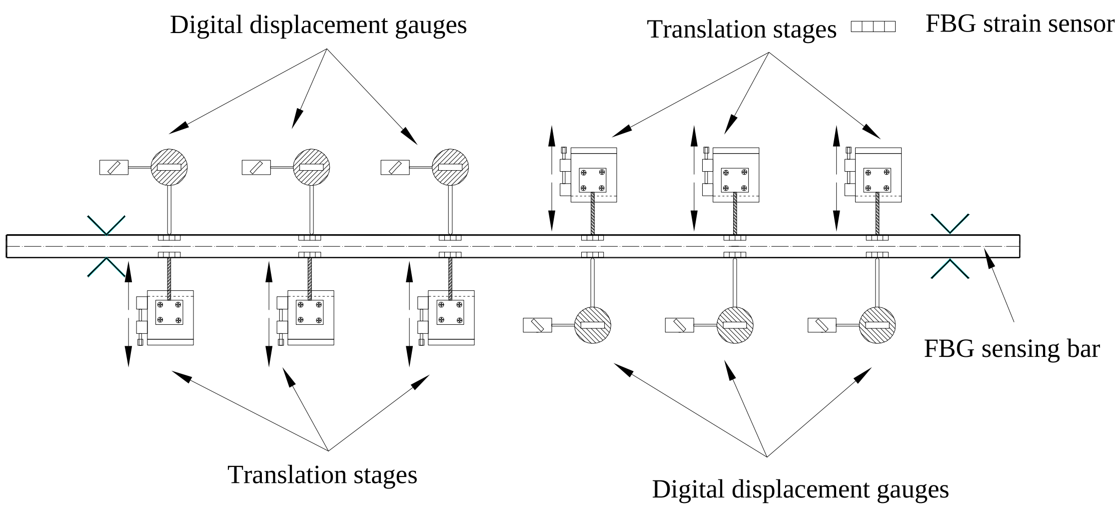

(d) Deflection test for simple-support condition 2

Figure 3.27 Test set-up of the calibration of the FBG sensing bar

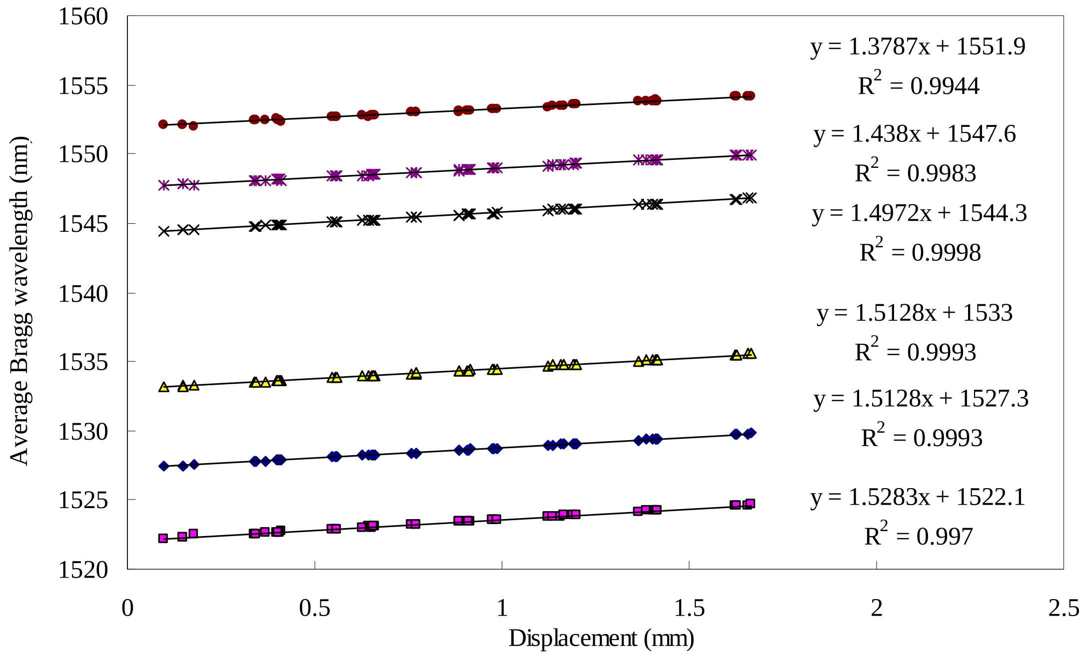

(a) Tensile test results

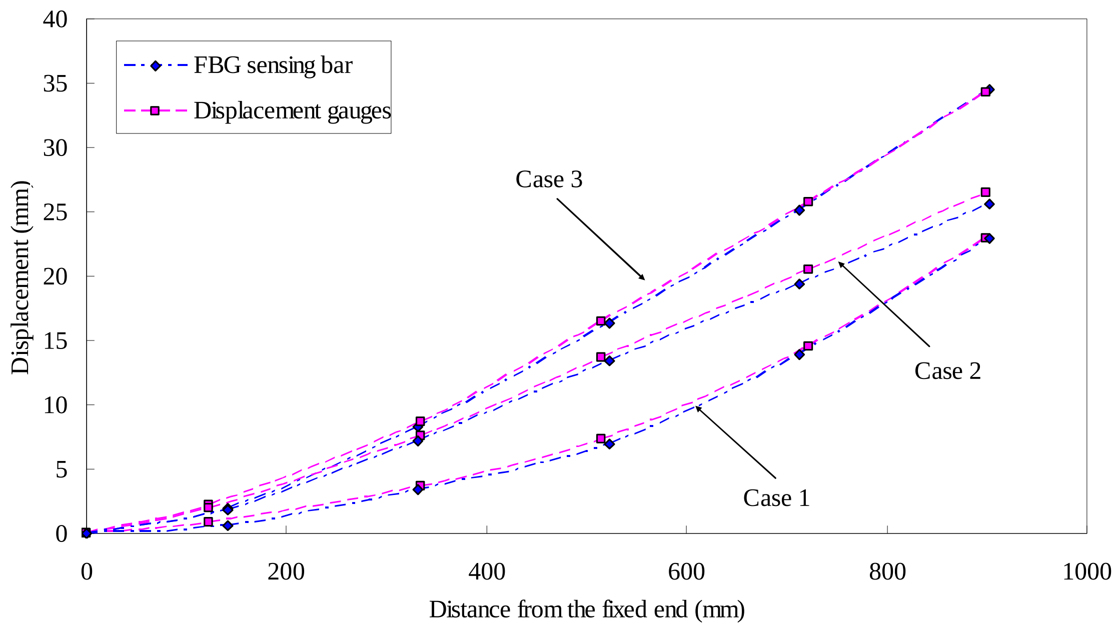

(b) Deflection test results for cantilever condition

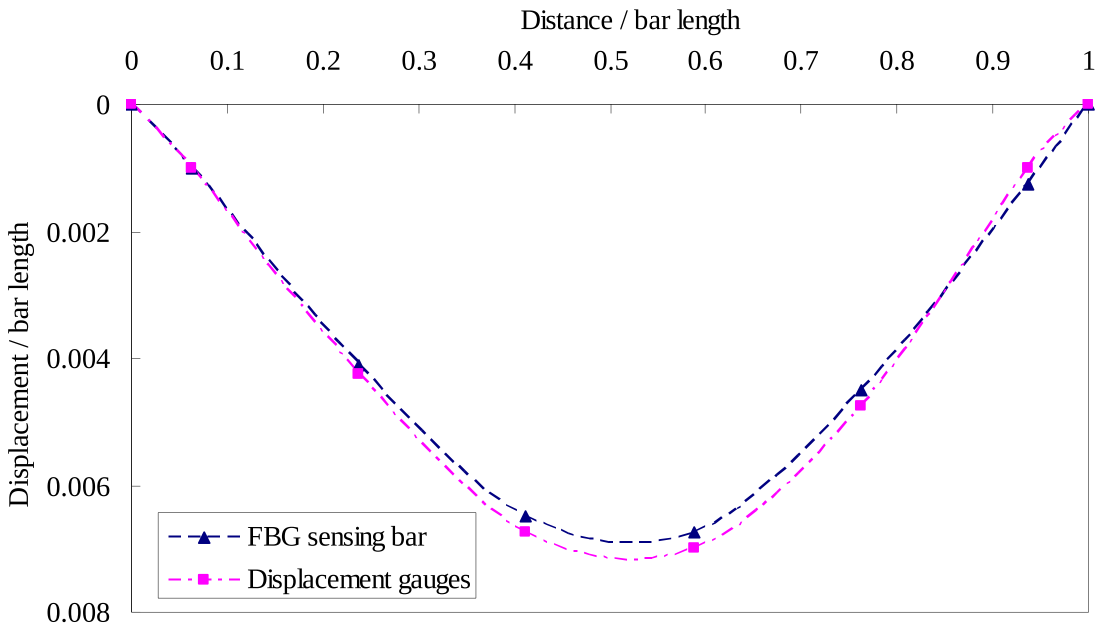

(c) Deflection test results for simple-support condition 1

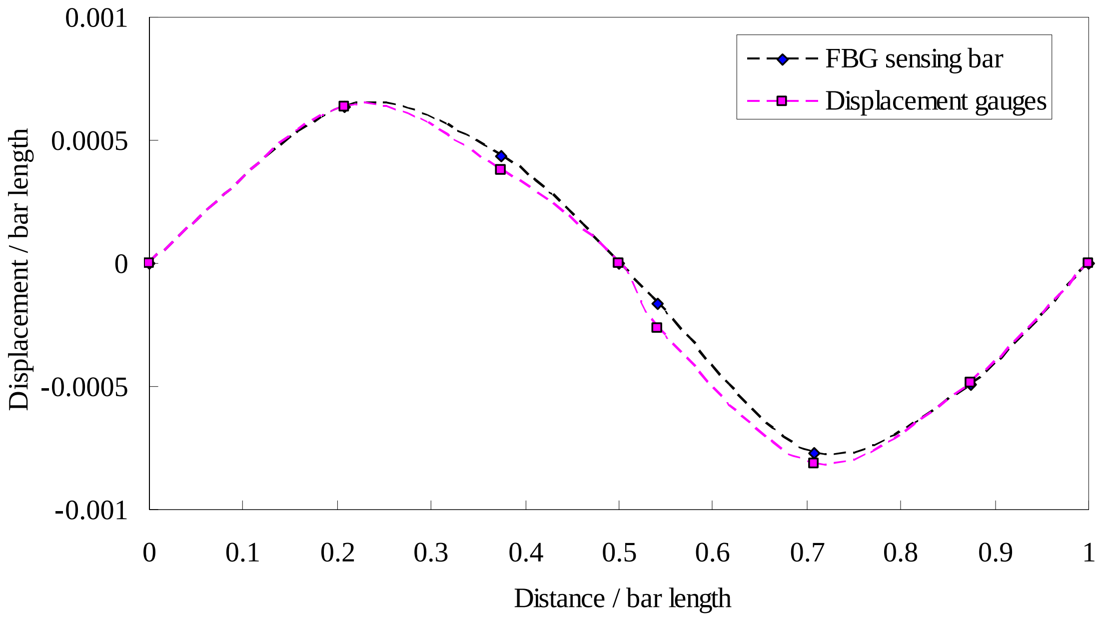

(d) Deflection test for simple-support condition 2

Figure 3.28 Typical calibration results of the FBG sensing bar

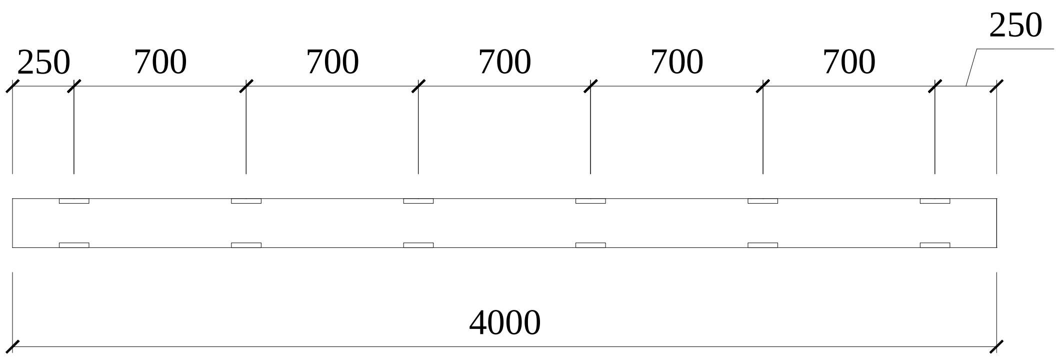

Figure 3.29 Schematic diagram of an FBG in-place inclinometer (unit: mm)

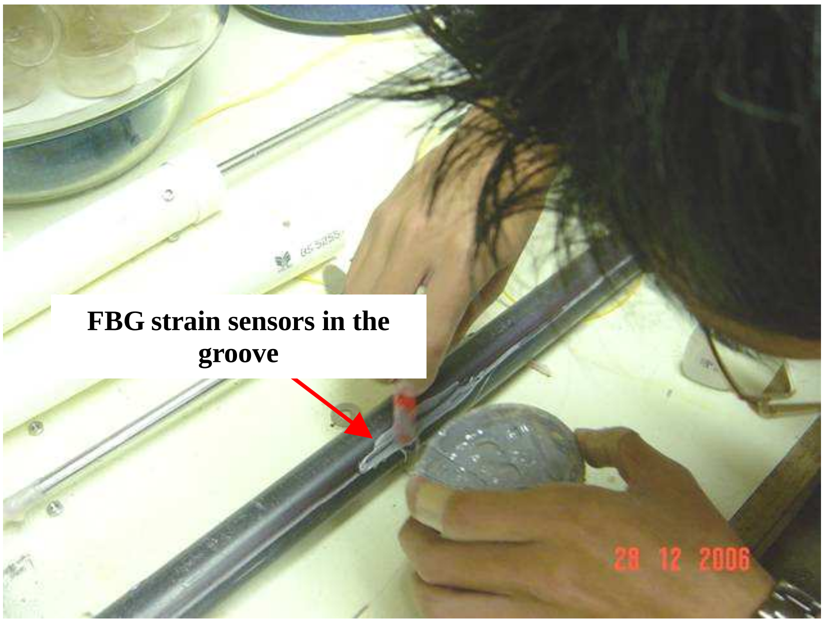

Figure 3.30 Fabrication of the FBG in-place inclinometer

(a) PVC casing of 30 mm outer diameter

(b) PVC casing of 70 mm outer diameter

Figure 3.31 Test set-up of the calibration of the FBG in-place inclinometer

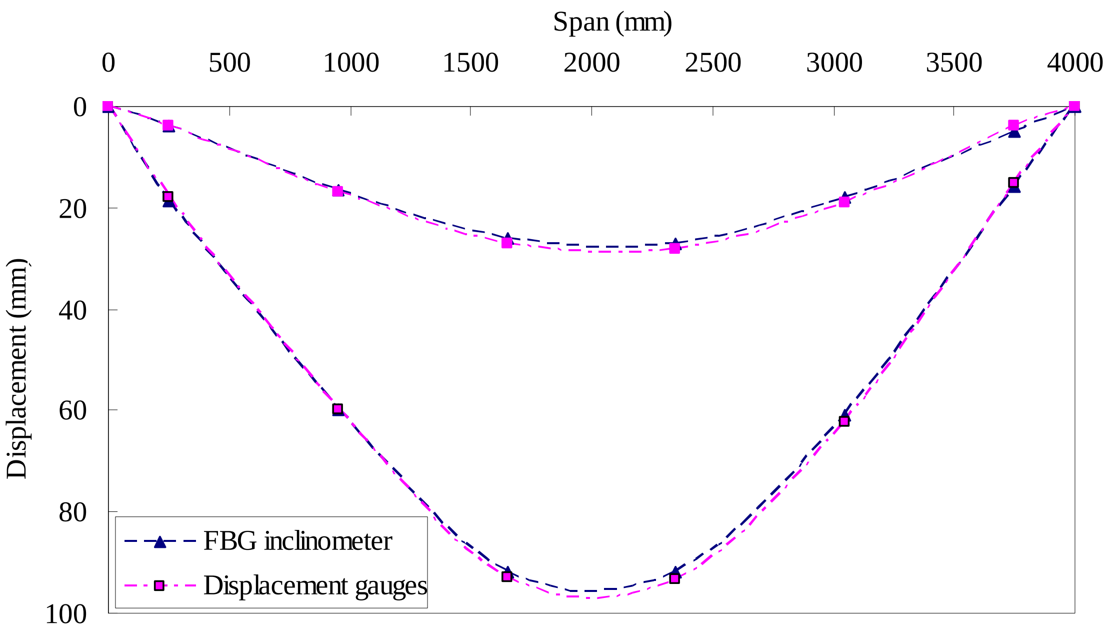

(a) PVC casing of 30 mm outer diameter

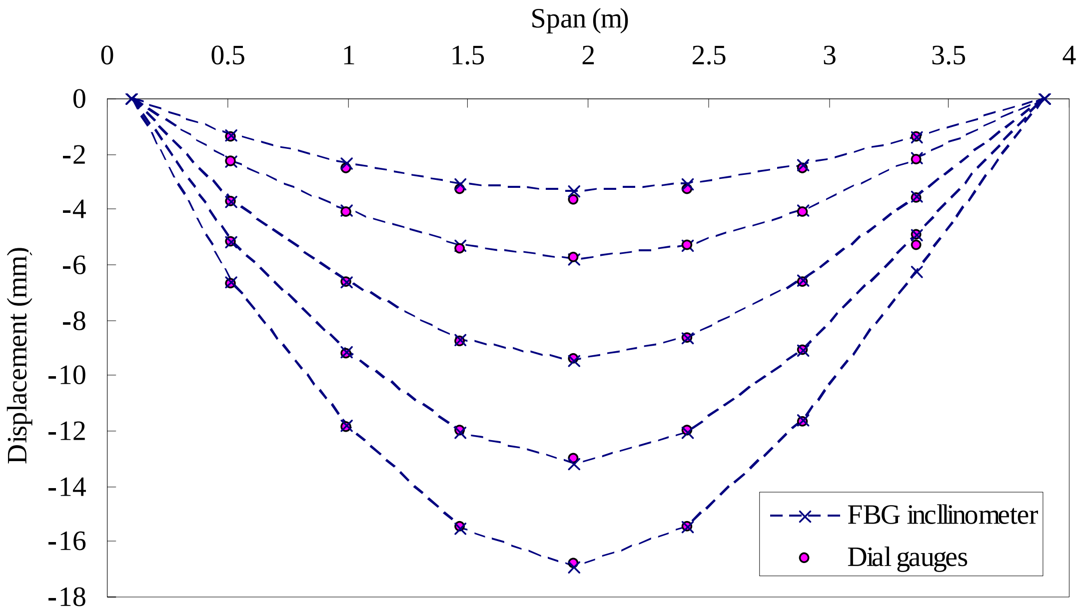

(b) PVC casing of 70 mm outer diameter

Figure 3.32 Typical calibration results of the FBG in-place inclinometer

Figure 3.33 Installation of the FBG in-place inclinometers in Shanghai Metro No. 2 for displacement measurements

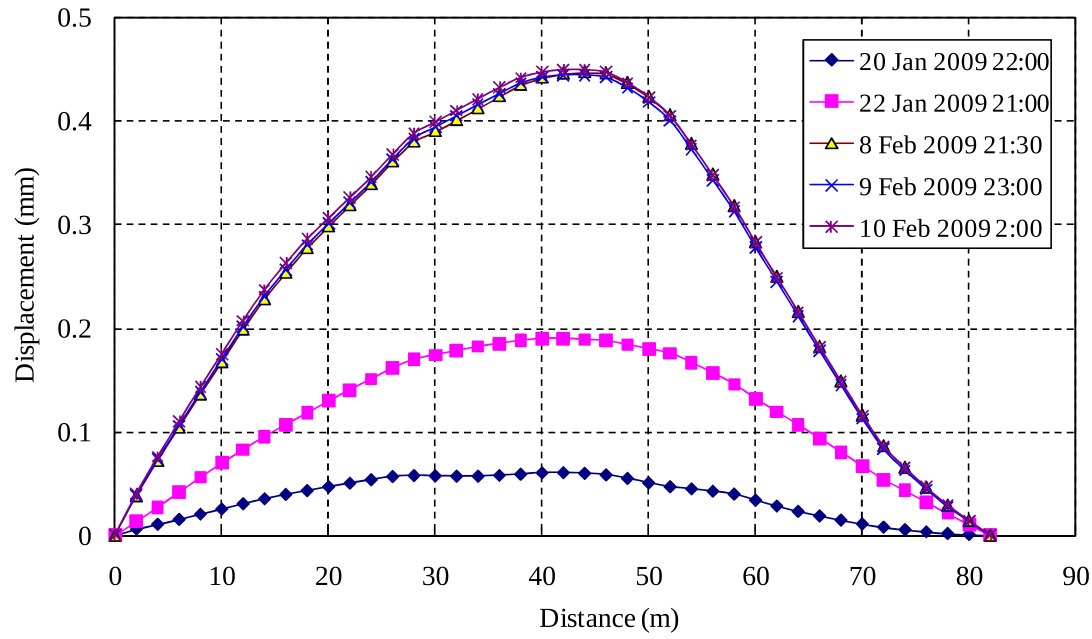

Figure 3.34 Monitoring results of the distribution of displacements by the FBG in-place inclinometers

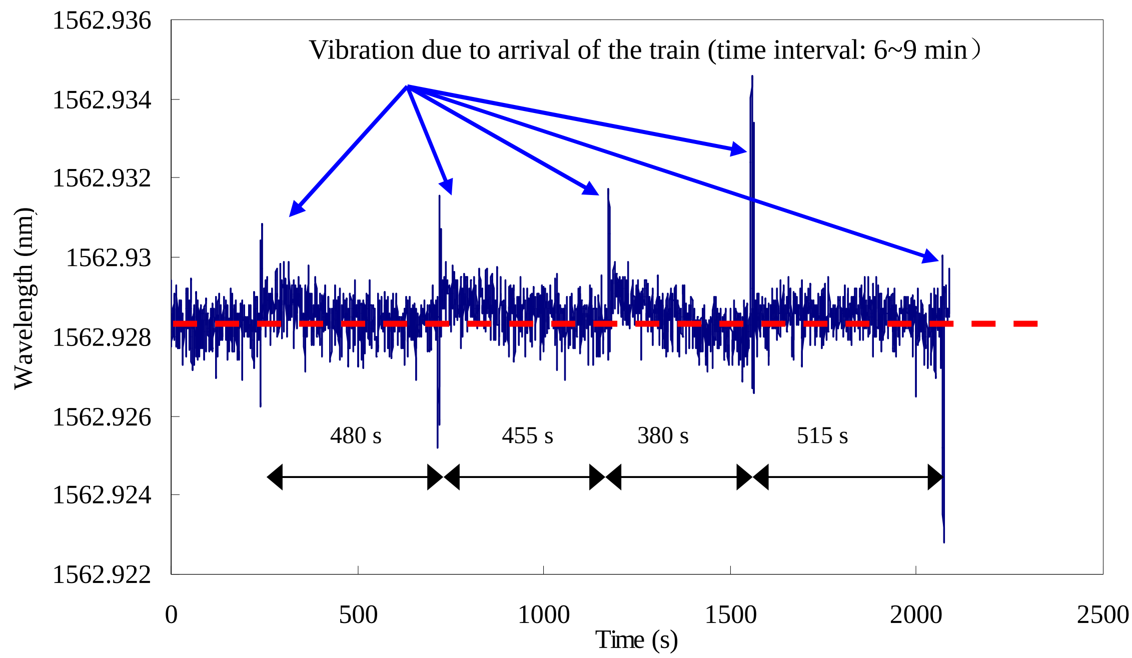

Figure 3.35 Variation in the Bragg wavelength of FBG sensor No. 22A during the operation period of the metro (9 Feb 2009 22:23)

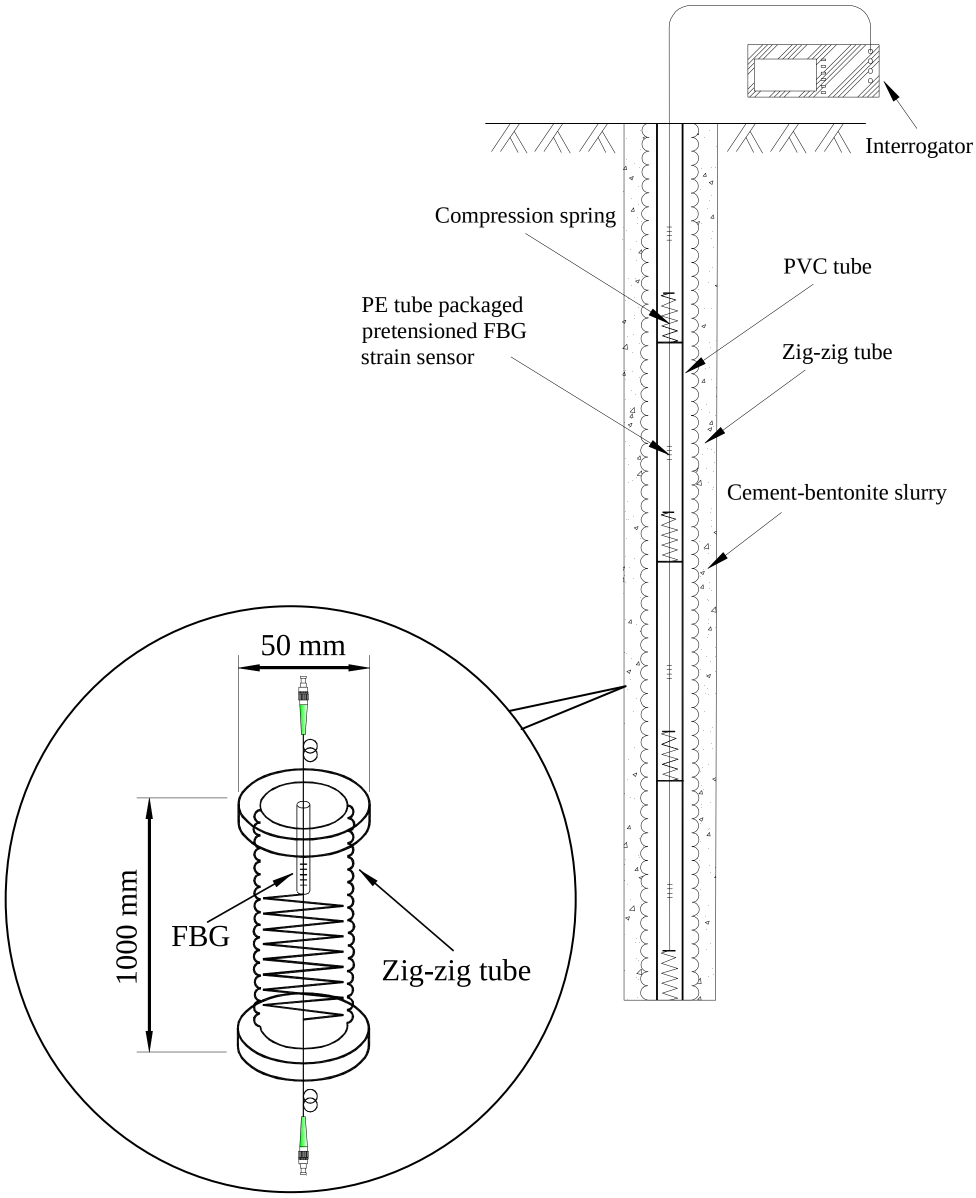

Figure 3.36 Schematic diagram of the FBG settlement tube

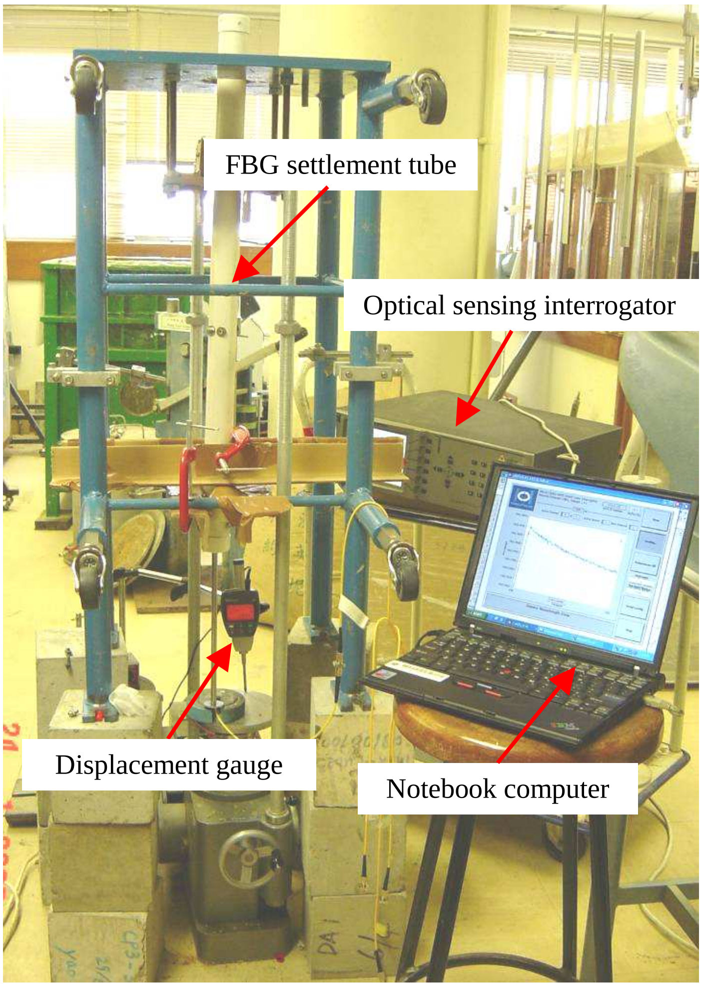

Figure 3.37 Photographs of test set-up of the calibration of the FBG settlement tube

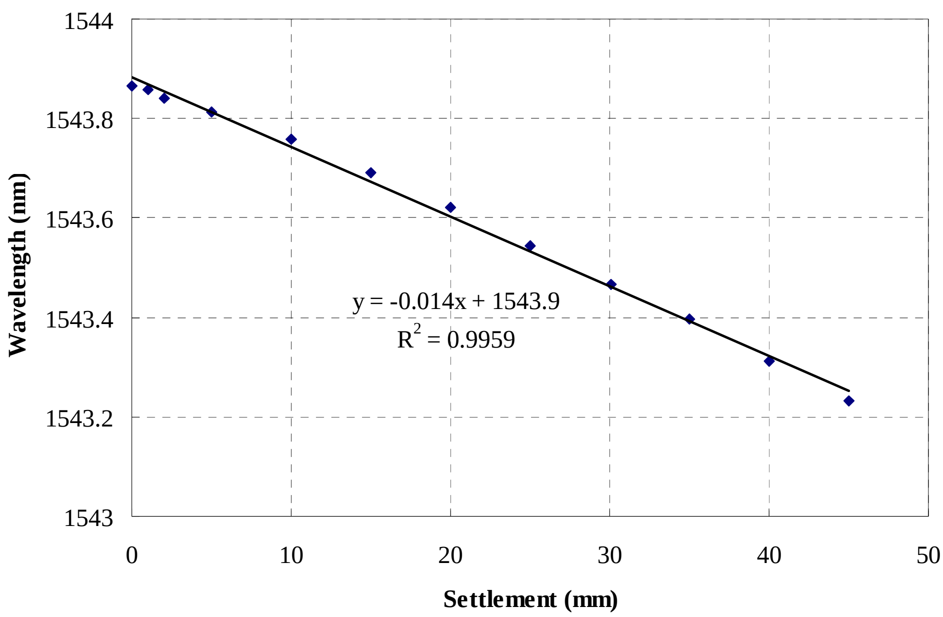

(a) Settlement tube No. 1

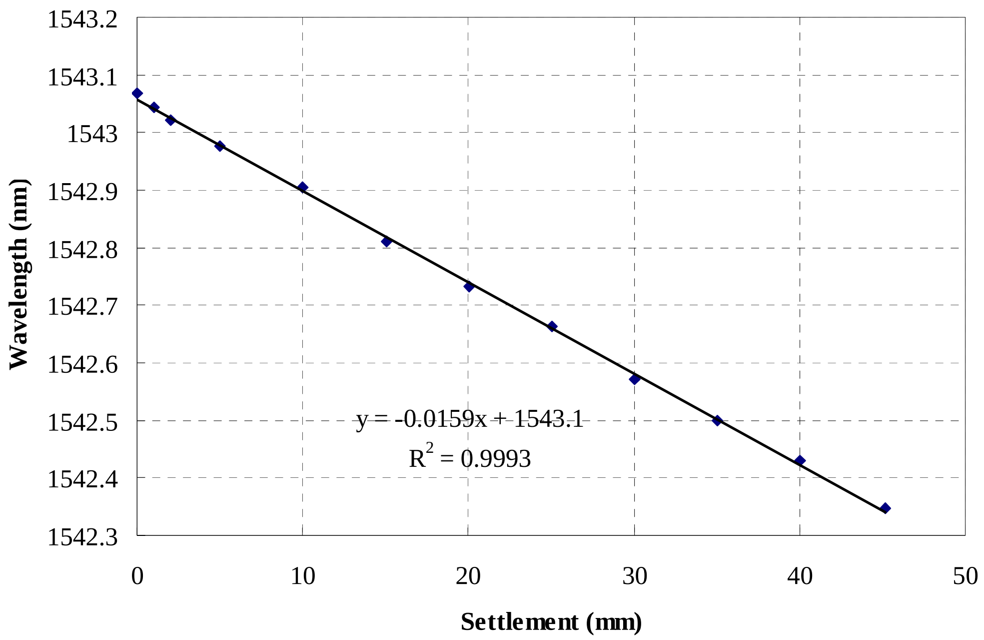

(b) Settlement tube No. 2

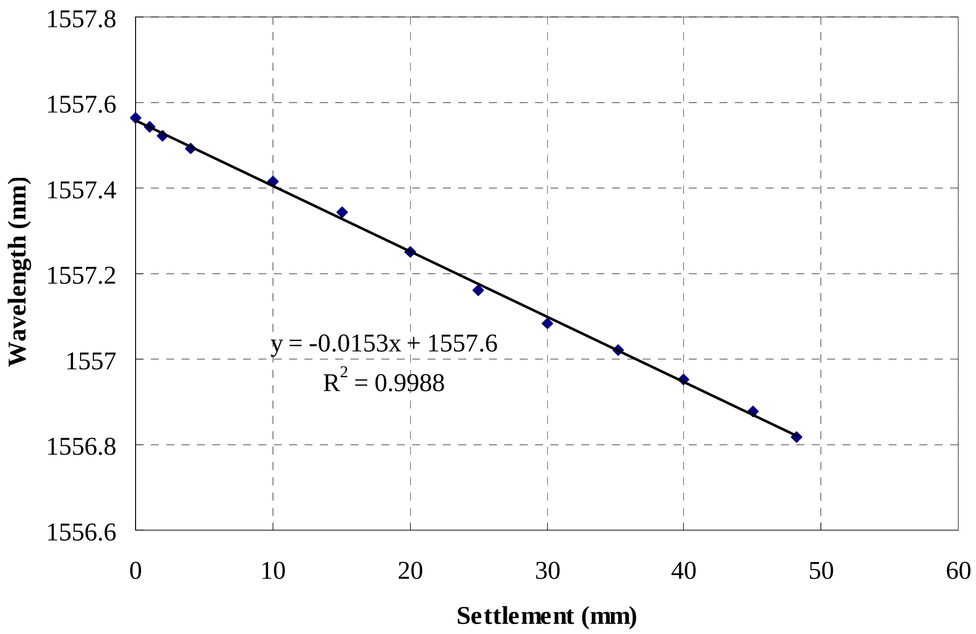

(c) Settlement tube No.3

Figure 3.38 Typical calibration results of the FBG settlement tube

(a) Preparation of a hole for installing the settlement tube

(b) Grouting of the hole by cement-bentonite slurry

Figure 3.39 Laboratory trial test of the FBG settlement tube

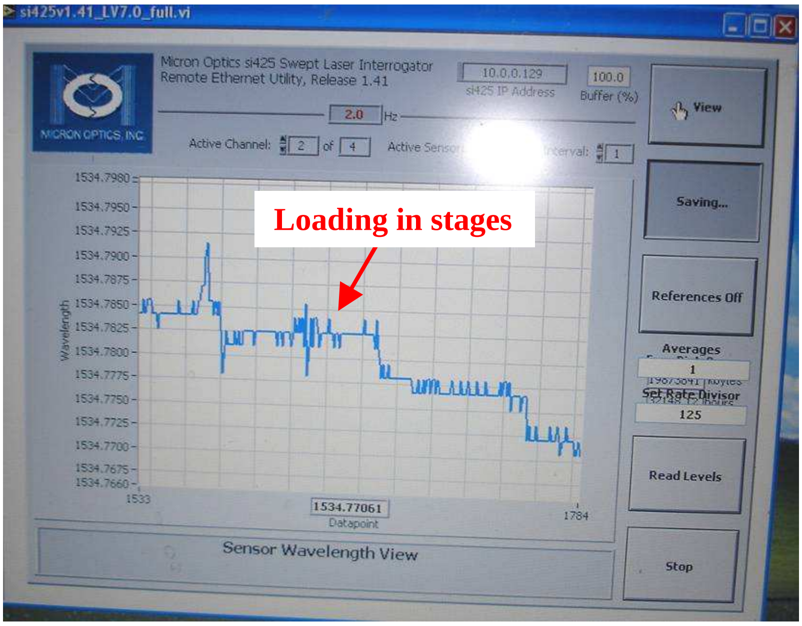

Figure 3.40 Monitoring results of the FBG settlement tube during compression of soil masses

CHAPTER 4:

FIBER OPTIC MONITORING AND EVALUATION OF SOIL NAIL PULLOUT PERFORMANCE

4.1 INTRODUCTION

Since early 1970s, soil nails have been widely used to stabilize slopes and excavations worldwide. Soil nails can be installed by driving, grouting, or jet-grouting. In Hong Kong, a lot of field stabilization works and researches have been carried out on man-made slope features under the Landslip Preventive Measures (LPM) program of the government of HKSAR (GEO 2005). Most unstable slopes were and will be stabilized by grouted soil nails consisting of a steel bar, surrounding cement grout, and a reinforced concrete soil nail head (GEO 2008). The commonly used steel bars are 20 mm to 40 mm in diameter and 3 m to 20 m in length. The drillhole for nail installation has a diameter of 75 mm to 150 mm with a downward inclination of 10 to 20° to the horizontal. Slope stability is improved by the mobilization of shear stresses at the soil-grout interface in the resisting zone below the critical slip surface.

The pullout resistance is a critical parameter in the design of soil nails and is affected by a number of factors, including construction methods and process, properties of soil and cement grout, roughness of soil-grout interface, geometry of slope and drillhole, etc. (e.g. Schlosser 1982; Milligan and Tei 1998; Luo et al. 2000; Hong et al. 2003; Junaideen et al. 2004; Chu and Yin 2005; Pradhan et al. 2006; Su et al. 2008). In Hong Kong, field pullout tests are routinely conducted on sacrificial soil nails to verify (or check) the bond strength between *in-situ* soil and cement grout inside the drillhole (GEO 2005, 2008). The number of pullout tests is at least two or 2 % of the total number of working nails. In a standard pullout test, three loading-unloading cycles are applied, and the pullout force and displacements at the nail head are measured. The test nail is considered to be able to sustain the test load if the difference of soil nail movements at 6 minutes and 60 minutes does not exceed 2 mm or 0.1 % of the bond length of the test soil nail.

In a soil nail system, the cement grout can protect the steel bar from direct exposure to moist soil masses. However, in aggressive environments, steel bars still react with chemicals existing in soil through micro-cracks in the cement grout, which seriously weakens their strengths. This phenomenon is an uncalculated risk to soil nails, especially for those with a design life of two or more years. Several case studies on corrosion of soil nails have been carried out (Shui and Cheung 2003). In Hong Kong, the corrosion protection measures for soil nails carrying transient loads are divided into three classes based on the soil aggressivity assessment (GEO 2008). The steel soil nail should have a layer of galvanized zinc coating, normally accompanied with a sacrificial steel thickness of 2 mm. A corrugated sheathing made of high density thermoplastic material is sometimes used in the “aggressive” and “highly aggressive” ground conditions (GEO 2005, 2008). However, in polluted, water-rich, sulfate or chloride soil environments, these passive measures cannot guarantee the long-term effectiveness of soil nails. In order to enhance the durability of the soil nails, attention has been drawn to the development of new corrosion resistant materials such as glass fiber reinforced polymer (GFRP) to replace steel in soil nail construction.

In recent years, GFRP materials provide practical solutions to corrosion and site maneuvering problems for civil infrastructures using conventional steel bars as reinforcements. In pullout condition, GFRP soil nails were found to behave differently from that of steel soil nails, as reported by Yeung et al. (2007), Beekman et al. (2007), and Cheng et al. (2009).

In this chapter, field investigation of the pullout performance of steel soil nails, especially the pullout resistance, is conducted. A series of pullout test were performed at three slope sites. The feasibility of using GFRP soil nails for slope stabilization is also evaluated through field testing. The pullout behavior of GFRP soil nails is compared to that of steel soil nails. Finally, a simplified pullout model is proposed based on hyperbolic functions and a parameter study is further conducted.

4.2 PULLOUT PERFORMANCE OF STEEL SOIL NAILS

4.2.1 Field pullout tests on steel soil nails

Under Contract No. GE/2006/32 between Civil Engineering and Development Department (CEDD) of HKSAR Government and Jacobs China, Limited, five soil nail pullout tests were conducted in Sha Tau Kok, New Territories, Hong Kong (Slope Registration No. 3NW-D/C 214). The slope is a government owned cut slope consisting mainly of complete decomposed tuff (CDT). The man-made slope has a height of 20 m, a length of 140 m and a slope angle of 44^{o}.

The test nail consists of a 40 mm diameter high yield steel bar and the cement grout of a length of 2 m. The holes for installing test nails were drilled by a pneumatic drilling rig, having 150 mm diameter at an angle 20^{o} to the horizontal. All the soil nails were instrumented with strain gauges and surface adhered FBG sensors for monitoring axial strains during pullout tests. The location of the strain gauges and FBG sensors are shown in Figures 4.1. For each soil nail, two channels were polished and two series of FBG sensors were installed and embedded by epoxy resin (Figures 4.2). To isolate the 2 m bond length for grouting effectively, specially designed inflatable double-packer were utilized (Swann et al. 2007).

The field pullout test follows the procedures specified by GEO (2008). The test nail is subjected to an initial load (T_a), two intermediate test loads (T_{DL1} and T_{DL2}), and then the maximum test load. T_{DL1} is the allowable pullout resistance provided by the bond length of the cement grout of the test soil nail. T_{DL2} is T_{DL1} times a factor of safety of 2.0. The maximum test load should be T_p (90 % of the yield load of the test soil-nail reinforcement) or T_{ult} (ultimate ground-grout bond load), whichever is smaller.

Figures 4.3 show the testing apparatus, set-up and instrumentation details. In each pullout test, the pullout force was applied by a hydraulic jack and calculated by the reading of a pressure gauge. The pullout displacement was calculated by the readings of dial gauge minus the steel bar extension in the free length (outside). The FBG sensors and strain gauges were connected to an automatic data acquisition system comprising a data logger, an optical sensing interrogator and a notebook computer. Real-time monitoring was performed throughout the pullout tests.

The pullout test results are shown in Figure 4.4. It is seen that the pullout force-displacement curves can be fitted using hyperbolic functions. Figure 4.5 presents the strain distributions along the soil nail No. 3 during testing. From the data measured by strain gauges and FBG sensors, the strains in the free length were approximately constant; while in the grouted length, strains were not exactly linear distributed with respect to length, as indicated by the red dash lines.

4.2.2 Prediction of pullout resistance from SPT *N* value

(1) Conditions of the slope sites

As part of the same project that previously stated, additional twenty-nine soil nail pullout tests instrumented with strain gauges were carried out at two cut slopes in the northern New Territories (Slope Registration Nos. 3SW-C/C 359 and 3SW-D/C 79). From the ground investigation results, the geology at these slopes generally comprises a thin layer of residual soil over CDT. The heights of the slopes vary from 21 m to 30 m and the slope angle varies from 35^o to 55^o to the horizontal. The lengths of the test nails range from 5 m to 20 m. Strain gauges were installed in pairs along the total length of the test nails. The intervals in the grouted and free lengths are 0.5 m and 1-1.5 m, respectively.

(2) Standard penetration test results

It has been stated by many researches that for grouted soil nails, pullout resistance seems independent of overburden pressure due to their construction characteristics (Su et al. 2008). In order to investigate how to estimate the pullout resistance of soil nails, standard penetration tests (SPTs) were carried out at 2 m intervals in boreholes in the three slope sites under investigation in this project prior to the pullout tests. SPT was first developed circa 1927 and now is widely used in geotechnical investigation. The SPT is performed by driving a standard split spoon sampler into the ground by blows from a drop hammer of mass 63.5 kg falling 76 cm. The number of blows required for the sampler to penetrate the final 30.4 cm of a total of 45.6 cm is called the standard penetration number (*N* value). The SPT *N* value is extensively used for: a) measuring relative density, strength and elastic modulus of soils (Hettiarachchi and Brown 2009); b) calculating bearing capacity and settlement (Burland and Burbridge 1985); c) for estimating pile load capacity (Meyerhof 1976; Quiros and Reese 1977); d) evaluation of liquefaction triggering (Lai et al. 2005) and so on.

The relationship between depth H and SPT N value at the three slope site is shown in Figure 4.6. From the figure, a lower bound is found, which can be expressed by

$$\frac{N}{H} \geq 0.3 \qquad (4.1)$$

(3) Pullout test results and analysis

Table 4.1 summarizes the pullout test results. It is seen that 32 out of 34, i.e. 94% of the test nails could sustain the T_{DL1} load. For test nail Nos. C/C 359-P10 and D/C 79-P5, which failed prior to reaching T_{DL1}, there may be considerable grouting loss or air bubbles in the grouted length, adversely reducing the pullout resistance of the test nail.

According to the guidance of GEO (2005), the theoretical pullout resistance of a soil nail is calculated by

$$T = \pi Dc' + 2D\sigma_v' \tan\varphi' \qquad (4.2)$$

where c' and φ' are the effective cohesion and friction angle of the soil, D is the test nail diameter, σ_v' is the effective overburden pressure. Laboratory triaxial tests were conducted on CDT samples taken from these three slopes. The test results show that c' and φ' can be estimated to be 2 kPa and 36.0^o (Swann et al. 2007).

A plot of pullout capacity against theoretical pullout capacity is shown in Figure 4.7. It is found that the design pullout resistance will underestimate the field pullout resistance significantly.

The distributions of SPT N value and measured pullout capacity T_{ult} with respect to depth is shown in Figure 4.8. Although there is no apparent relationship between SPT *N* value and pullout capacity in Figure 4.9, the upper and lower bound trend lines can be obtained to correlate them. If discounting the two doubtful test results mentioned previously, the empirical relationship can be expressed by

$$1.4 \le \frac{T_{ult}}{N} \le 9.0 \qquad (4.3)$$

Figures 4.10 and 4.11 indicate that T_{ult} / N appears to follow a normal distribution, with a mean of 3.830 and a standard deviation of 2.016. Thus about 68% of the pullout resistance measurements will fall within the interval of $2.1N \le T_{ult} \le 5.9N$. Determination of the pullout resistance by this relationship is more accurate than conventional method using Eq. 4.2.

4.3 PULLOUT PERFORMANCE OF GFRP SOIL NAILS

GFRP is a new and cost-effective material of promising application potential in geotechnical engineering. GFRP has many advantages over steel, such as better corrosion resistance, high strength to weight ratio, easy maneuvering, etc. GFRP tendons have been used successfully for the construction of piles (Sen et al. 1991; Iskander and Hassan 1998; Ashford and Jakrapiyanun 2001), geogrids (Miyata 1996), and ground anchors (Benmokrane et al. 1996; ACI Committee 440 1996, 2004). Benmokrane et al. (1996) performed pullout tests of anchor bolts installed in concrete blocks and rock mass. The slip displacements of GFRP bars in cement grout at failure were proven to be larger than that of steel bars, mainly owing to their low modulus of elasticity. The experimental results of Frost and Han (1999) have also shown that sands sliding on FRP exhibit different shear stress–horizontal displacement behavior than those on steel. However, limited experience is available on the potential of using GFRP materials as cement grouted soil nails (Haper et al. 1995). Since the mechanical properties of GFRP are different from those of steel, the bonding strength and failure mechanism of GFRP soil nail is to be investigated.

4.3.1 Features of GFRP material used as a soil nail

(1) Advantages

The typical properties of steel, GFRP, and cement grout are listed in Table 4.2. The GFRP soil nail is made from glass fibers embedded in a resin matrix to improve its corrosion resistance and durability. Tedious corrosion protection procedure can be eliminated, resulting in considerable savings in fabrication and field installation.

GFRP materials, with only 15–20% of the density of steel, have high axial tensile strengths comparable or superior to that of steel. GFRP bars of similar diameters may replace steel bars for a required tensile force, without any modification of the drillhole diameter and grouting apparatus. The transportation, handling, and installation of GFRP soil nails are more convenient and efficient, which is especially important for slope engineering where site accessibility is always limited. The improved constructability of GFRP soil nails can thus reduce construction and maintenance costs.

Roger et al. (2002) stated that, considering the fact that the coefficients of thermal expansion of GFRP and steel are similar, the thermal stress is significantly decreased by the reduction of the Young’s modulus of GFRP (normally in the range of 25-30% of that of steel) when temperature suddenly changes. This means that the formation of micro-cracks at the GFRP-grout interface caused by thermal tensile forces during cyclic temperature variation is minimal. While for the steel soil nail, relaxation shrinkage and cracking of cement grout under the combined effects of tensile stress and thermal stress are unavoidable. Simultaneously, the potential corrosion problem will be much more serious and the structural safety may decrease gradually with time.

In the past decade, GFRP materials were proven to be highly adaptable with fiber optic sensors (Frank et al. 1999; Nellen et al. 2000; Bakis et al. 2001; Lau et al. 2001; Zhao and Ansari 2002; Singhvi and Mirmiran 2002; Jiang et al. 2008). These sensors have been more and more widely used for the measurement of strain, temperature, displacement, stress, etc. in civil infrastructures. Fiber optic sensors, such as FBG and Fabry-Perot sensors, can be easily integrated into GFRP reinforcements during the fabrication process (Kalamkarov et al. 1999, 2000a, 2000b, 2005), resulting in the possibility of utilization of "smart" GFRP soil nails for stabilization and health monitoring of slopes and excavations.

(2) Shortcomings

The reduced Young's modulus of GFRP indicates that the elastic elongation of GFRP is four times that of steel under the same tensile stress. For GFRP soil nail, excessive deformation of the reinforcement may adversely affect the safety of the stabilized slopes or excavations, even if the structural stability is achieved. GFRP also has much lower shear modulus than steel (Bank 1989) and may exhibit significantly reduced ultimate strains at breakage. Moreover, the yielding phenomenon does not exist in GFRP material, which may be another crucial drawback of GFRP soil nails.

The results of previous studies report that GFRP reinforcements exhibit significant time-dependent phenomenon when subjected to a high axial tensile stress. In order to avoid failure due to creep-rupture, the GFRP reinforcements are constrained to be used below a safe stress level. The safe stress level of a GFRP bar for reinforcing concrete, adopted by ACI Committee 440 (2001), is only 20% of the initial ultimate strength. Budelmann and Rostàsy (1993) conducted experimental studies and statistical analyses, and proposed forecast models of the long-term behavior of specific FRP elements. Dutta and Hui (2000) studied the creep rupture of a GFRP composite at elevated temperatures experimentally. An empirical model was developed to predict the time-to-failure based on their experimental results. Following the researches of Nkurunziza et al. (2005), Al-Salloum and Almusallam (2007) studied the creep effect of GFRP reinforced concrete due to sustained loads in different environments. The strain in GFRP bars and strain in concrete due to creep were highest in beams placed in seawater at 40±2°C with wet/dry cycles.

Fatigue is another undesirable feature of GFRP materials, especially when tested at elevated stress levels. The poor performance is attributed to the loss of stiffness due to the creeping of resin (Walton and Yeung 1986; Ellyin and Kujawski 1992; Adimi and Benmokrane 1997). For GFRP soil nails, the infiltration of rainfall, earthquake, and fluctuated groundwater level may result in cyclic loading, inducing adverse fatigue effect.

4.3.2 Field pullout test results

(1)An innovative GFRP pipe for soil nails construction

The GFRP soil nail system utilized in this study consists of a GFRP pipe of an outer diameter of 55 mm and an inner diameter of 37 mm, which is developed by Dae Won Soil Company, Limited of South Korea. The GFRP pipe is fabricated by a pultrusion process. Built-in centralizers were installed on the pipe at 1 m interval in factory. More details on the manufacturing methods and its field applications as soil nails were reported by Yeung et al. (2007), and Cheng et al. (2009). The effectiveness of the pipe to reinforce rock slope and excavation has been demonstrated through various laboratory and field studies (Kim et al. 2001; Choi et al. 2003).

(2) Sensor installation and construction of GFRP soil nails

Two GFRP pipes of length 3.6 m were instrumented with electrical strain gauges (SGs), surface adhered FBG (FBG-A), and tube packaged FBG (FBG-B) sensors as shown in Figures 4.12 and 4.13. During the installation of strain gauges, painstaking precautions were taken to waterproof the gauges to ensure survivability. Only three strain gauges were installed on each pipe to avoid the negative effect of 3-core shielded lead wires of the strain gauges on the structural integrity of GFRP soil nail. To install the surface adhered FBG sensors for point strain measurement, groves of 2 mm wide and 2 mm deep were cut on the pipe surface to accommodate the optical fiber with eight FBG sensors. The sensors were glued on the surfaces of the groves and covered by quick-set epoxy resin. Tube packaged FBG sensors of a gauge lengths of 0.5 m were used to measure the average tensile strains. For each pipe, a total of four tube packaged FBG sensors were fixed along the pipe length. As the temperature variation in the soil during testing was negligible, no temperature compensation of the FBG sensors was conducted.

The GFRP soil nails were installed in a man-made slope (Slope Registration No. 10SW-C/C237) in Lantau Island, Hong Kong for the field trial. The geological profile of the test slope is depicted in Figure 4.14.

To install the GFRP soil nails on site, two holes of 120 mm in diameter and 3.4 m in length inclining at 20° to the horizontal were drilled using the pneumatic rotary-percussion drilling technique, and the GFRP pipes were installed centrally in each drillhole. A two-stage grouting was then applied for each nail. In the first stage, the annular space between the pipes and the drillholes along the length was sealed with cement using gravity grouting. After initial setting of the cement grout, an inflation packer was inserted into the bore of the pipe and a predefined length of the nails (2 m and 1.2 m for GFRP soil nail No. 1 and No. 2, respectively) was grouted using a grout pressure of approximately 1.5 MPa pressure. Through the predrilled small holes on the GFRP pipe, the annular cement grout was fractured by the 2nd stage grouting and the surrounding soil would be permeated by cement grout.

(3) Set-up and instrumentation of the pullout tests

The pullout test procedure consisted of three loading / unloading cycles. The field pullout set-up and instrumentation are shown in Figure 4.15. Prior to the pullout test, a 32 mm-diameter steel bar was inserted into the GFRP pipe and glued by epoxy resin, as a reinforcement and extension to be connected to the hydraulic jack. The FBG-A sensor nearest to the nail head of GFRP soil nail No. 1 was damaged when the workers tried to insert the steel bar. A load cell and two LVDTs were used to measure the pullout force and displacements at nail head, respectively. A data logger and an optical sensing interrogator were used for automatic data acquisition.

(4) Pullout test results

The pullout test results are presented in Figures 4.16 to 4.18. The maximum pullout forces for GFRP soil nail No. 1 and No. 2 reached approximately 213 and 236 kN, respectively. Although GFRP soil nail No. 1 had a pressurized grouted length longer than that of GFRP soil nail No. 2, their maximum pullout forces were showed to be independent of this length. Assuming the shear stresses were uniformly distributed along the nails, the maximum shear stresses mobilized at the soil–grout interface can be estimated to be $213/(\pi\times0.12\times3.4) = 166$ kPa for GFRP soil nail No. 1 and

236/(π×0.12×3.4) = 184 kPa for GFRP soil nail No.2. From the pullout force versus displacement curves presented in Figure 4.16, it can be observed that this relationship can be best-fitted by a hyperbolic function. The unloading and reloading curves are quite linear, with a slope similar to that of the initial loading stage. The GFRP soil nails exhibited elastic behavior when they were unloaded.

A comparison of axial strains in the 2 m pressurized grouted zone measured by two types of FBG sensors and strain gauges of GFRP soil nail No.1 when the pullout force was 100 kN is presented in Figure 4.17. The strains measured by all types of sensors are in good agreement and shown to be approximately linear with respect to the nail length.

The distributions of axial strain along the length of GFRP pipes measured by FBG-A sensors during the tests are depicted in Figure 4.18. When the pullout forces were at a low range, axial strain distributions in the pressurized grouted zone were approximately linear, indicating uniformly distributions of shear stresses along the nail lengths. However, when shear stresses were gradually mobilized by the increasing pullout forces, the strain distributions became nonlinear. In the zone without pressurized grouting, as shown in Figure 18(b), the strain became considerably larger than the corresponding strains in the pressurized grouted zone. Comparing the strain measurements of GFRP soil nail No. 1 and No. 2, it can be observed that pressurized grouting can significantly enhance the bonding efficiency of the soil-grout interface and the stiffness of the GFPR soil nail. The maximum tensile strains on the GFRP pipe can be decreased by the double grouting technique.

The maximum axial strain of GFRP soil nail No. 2 occurred in the non-pressurized grouted zone was 7734 με under the maximum pullout force. Although this value was smaller than the strain limit of GFRP and thus no pipe breakage can occur, such a large axial strain is seldom observed in steel soil nails. For other locations, the tensile strains measured on the pipe surface were also much larger than the strain that cement grout can sustain (having a tensile strain limit of about 70 $\mu\varepsilon$). Considering there are no ribs on the GFRP pipe surface, it is reasonable to assume there have been significant debonding and slippage between the GFRP pipe and the cement grout, though the built-in centralizers on the GFRP pipes may have restrained the development of slippage to some extent.

4.3.3 Comparison of pullout performance between GFRP and steel soil nails

The pullout mechanism for GFRP soil nail and steel soil nail is depicted in Figure 4.19. Comparing these two types of reinforcements, the difference of pullout performance lie in:

(1) For steel soil nails, considerable small strains and elongation of the steel bar are induced when pullout failure occurs, especially if the steel bar has a large diameter such as 32 and 40mm. Cracking of cement grout is restricted in the vicinity of the steel-grout interface. Slippage at this interface is effectively avoided by the rough surface of ribbed steel bar. Thus the soil nail can be treated as a composite material with averaged Young’s modulus. As the soil nail is stiffer than soil, in most cases the ultimate failure is due to the sliding at the soil-grout interface, when the shear strength cannot resist the shear stresses mobilized at this interface.

(2) For GFRP soil nails, the significantly reduced nail stiffness makes the nail more extensible and thus results in quite large strains at failure. The pullout performance is not only dependent on the cement grout-soil interface, but also the sliping/debonding of

the pipe-cement grout interface. Nail breakage or the pullout of GFRP pipe from cement grout may happen, if the thickness and roughness of the GFRP pipe is not well controlled. For simplicity, the GFRP soil nail can still be assumed to be an integrated component with the averaged Young's modulus of GFRP pipe and cement grout. In this case, considering the discontinuity of the nail (cement cracking and debonding effect), the axial strain is no longer uniformly distributed along the radius direction at any cross section of the GFRP soil nail.

Considering the above mechanisms, the GFRP pipe can be identified as an isolated reinforcement to transfer the pullout force to the cement grout, and then to the surrounding soil. The strains $\varepsilon(x)$ may be used to back-calculate the tensile force $F(x)$ in the soil nail.

$$F(x) = E_{GFRP} A_{GFRP} \varepsilon(x) \tag{4.4}$$

where E_{GFRP} and A_{GFRP} are the Young's modulus and cross-sectional area of the GFRP pipe, respectively.

The tensile forces results from strains presented in Figure 4.18 are shown in Figure 4.20. The dash lines represent the assumption of a linear distribution of tensile forces along the GFRP soil nail. It is found that for the nail with longer pressurised grouted zone (GFRP soil nail No.1), the distribution of tensile forces is more uniform than that of a shorter pressurised grouted zone (GFRP soil nail No.2). When the pullout force was increased to above 140 kN to GFRP soil nail No.2, the pullout force is completely transferred into the zone without pressurised grouting. Due to the reinforcement of the steel rebar, the measured strains were much smaller in the vicinity of the nail head.

4.4 A SIMPLIFIED MODEL FOR SOIL NAIL PULLOUT BEHAVIOR

4.4.1 Hyperbolic shear stress-strain relationship

The hyperbolic function is commonly used to describe the stress-strain relationship of soil and soil-reinforcement interface (Kondner 1963; Hirayama 1990; Milligan and Tei 1998; Gomez et al. 2003). The relationship between the shear stress and shear strain can be expressed by

$$\tau = \frac{\gamma}{a + b\gamma} \tag{4.5}$$

where a and b are experimentally determined coefficients. It can be observed in Eq. (4.4) that the shear stress has an ultimate value,

$$\tau_{ult} = \lim_{\gamma \to \infty} \frac{\gamma}{a + b\gamma} = \frac{1}{b} \tag{4.6}$$

The initial shear modulus G_0 can be defined as

$$G_0 = \left(\frac{d\tau}{d\gamma} \right)_{\gamma=0} = \frac{1}{a} \tag{4.7}$$

Thus, Eq. (4.5) becomes

$$\tau = \frac{\gamma}{\frac{1}{G_0} + \frac{1}{\tau_{ult}}\gamma} \tag{4.8}$$

The secant shear modulus G is now

$$G = \frac{\tau}{\gamma} = \frac{1}{\frac{1}{G_0} + \frac{1}{\tau_{ult}}\gamma} \tag{4.9}$$

For unloading conditions, the shear stress-strain relationship can be simplified as a straight line having a slope of G_0, i.e.

$$\tau = \tau_0 - G_0\left(\gamma_0 - \gamma\right) \tag{4.10}$$

where γ_0 is the maximum shear strain that the soil has experienced before unloading; and τ_0 is the maximum shear stress that the soil has experienced before unloading. The simplified model is shown in Figure 4.21.

4.4.2 Formulation for the pullout behavior of soil nail

In the mechanical model of the pullout of a soil nail shown in Figure 4.19, the resistance of the soil nail against the pullout force is provided by the shear stress acting on the soil-grout interface. The following well-known differential equation can be derived from the equilibrium of a uni-axial soil nail element (Sawicki 2000),

$$\frac{dF\left(x\right)}{dx} = \pi D \tau\left(x\right) \tag{4.11}$$

where $F\left(x\right)$ is the tensile force in the soil nail, D is the diameter of the soil nail.

Assuming the soil nail is made of a composite material, the uni-axial strain in the soil nail is given by

$$\varepsilon\left(x\right) = \frac{du\left(x\right)}{dx} \tag{4.12}$$

where u is the pullout displacement (positive in the x direction) of the soil nail at the cross section.

Taking $\bar{E}$ the average Young's modulus of the soil nail,

$$\bar{E} = \frac{E_c A_c + E_s A_s}{A_c + A_s} \tag{4.13}$$

where E_c, E_s are the Young's modulus of cement grout and steel (or GFRP). A_c, A_s are the cross-sectional areas of the cement grout and the internal reinforcement, such as a steel bar or a GFRP pipe.

Thus

$$F(x)=\frac{\pi}{4}D^2\bar{E}\frac{du(x)}{dx} \tag{4.14}$$

Assuming a thin layer of soil at the soil-grout interface is subjected to shearing, the axial displacements of the soil in contact with the nail surface can be regarded as equal to that of the nail, i.e. $u(x)=u_s(x,r)_{r=\frac{D}{2}}=\int_{\frac{D}{2}}^{\frac{D}{2}+h(x)}du_s=\int_{\frac{D}{2}}^{\frac{D}{2}+h(x)}\frac{\tau(x,r)}{G}dr$ where G is the shear modulus of soil, $h(x)$ is the thickness of the soil layer along the soil nail which is influenced by the pullout force (the deforming zone). For simplicity, the shear stress is assumed to be constant (simple shear) in the radius direction and the soil layer thickness is a constant along the nail. Thus $\gamma(x,r)=\gamma(x)$, $\tau(x,r)=\tau(x)$, and $h(x)=h_0$, thus $u(x)=\frac{\tau(x)}{G}h_0$.

Take $G_0^*=\frac{G_0}{h_0}$ as the shear coefficient at the soil-grout interface. Assuming $\tau(x)=\frac{\gamma(x)}{\frac{1}{G_0}+\frac{1}{\tau_{ult}}\gamma(x)}$ at the loading condition, thus

$$\tau(x)=\frac{u(x)}{\frac{1}{G_0^*}+\frac{1}{\tau_{ult}}u(x)} \tag{4.15}$$

From Eqs. (4.12), (4.13) and (4.14), we get

$$\frac{d^2F}{dx^2}=\frac{4G_0^*F}{\pi^2\bar{E}D^3\tau_{ult}^2}\left(\frac{dF}{dx}-\pi D\tau_{ult}\right)^2 \quad (4.16)$$

This two-order differential equation shall be solved numerically, with appropriate boundary conditions. In a pullout test, the pullout force F_0 can be measured by a load cell or a pressure gauge, thus

$$F\left(x=0\right)=F_0 \quad (4.17)$$

$$F\left(x=L\right)=0 \quad (4.18)$$

Thus in the loading condition, for a given F_0, $F\left(x\right)$ can be calculated by Eqs. (4.16), (4.17) and (4.18). The corresponding $\tau\left(x\right)=\frac{1}{\pi D}\frac{dF\left(x\right)}{dx}$ and $u\left(x\right)$ $=\frac{\tau_{ult}\tau\left(x\right)}{G_0^*\left[\tau_{ult}-\tau\left(x\right)\right]}$ can also be captured.

In the unloading and reloading condition, the maximum pullout force F_0 is used to calculate $\tau_0\left(x\right)$ and $u_0\left(x\right)$. Then $F\left(x\right)$, $\tau\left(x\right)$ and $u\left(x\right)$ is calculated by introducing Eq. (4.10).

4.4.3 Parameter determination from pullout test results

Eq. (4.16) indicates that the distribution of force and other parameters are dependent on three parameters, nail diameter D, interface shear resistance τ_{ult} and the ratio of $G_0^*/\bar{E}$. The first parameter is predefined by design requirements. To determinate the other two parameters used in the governing equations (4.16) and (4.10), the following procedure can be used.

(1) As stated before, $\bar{E}$ is taken as the average Young's modulus of steel (or GFRP) and cement grout. G_0^* can be determined by conducting direct shear tests of soil-grout interface. It can also be fitted by measuring the pullout displacements u_0 and corresponding force F_0 in stages.

(2) τ_{ult} can be calculated by the ultimate pullout force at which the soil nail is eventually pulled out. In this situation, τ_{ult} is achieved at the soil-grout interface along the nail and $F(x)$ becomes linear distributed with respect to nail length, i.e.

$$\tau(x) = \tau_{ult} = \frac{F_{ult}}{\pi DL} \tag{4.19}$$

and

$$F(x) = \frac{L-x}{L} F_{ult} \tag{4.20}$$

However, this critical condition where $u(x) = \infty$ is hard to achieve in common practice due to the limits of experimental techniques. Regard this, it is reasonable to assume

$$F_{ult} = \xi F_{\max} \tag{4.21}$$

where $F_{\max}$ is the maximum pullout force in the pullout test, ξ is a coefficient ($\xi \geq 1$).

Figure 4.22 presents the results that simulate the GFRP soil nail pullout test results shown in Figure 4.16. The parameters used here are determined by curve fitting, which are listed in Table 4.3. It is seen that, at the initial stage, the axial force is approximately linearly distributed along the nail, indicating a constant shear stress distribution. With the increase of pullout force, shear stresses along the total length are gradually mobilized and the distribution of shear stress and displacement become highly nonlinear with respect to nail length.

4.4.4 Influential factors of soil nail pullout performance

In order to study the factors affecting the pullout performance of GFRP soil nail, the diameter of GFRP soil nail D, shear resistance of soil-grout interface τ_{ult} and the ratio of $G_0^* / \bar{E}$ were varied individually while other two parameters were kept constant. The effect of these parameters on the pullout force-displacement relationships are depicted in Figures. 4.23 to 4.25. From the parametric study, the curves for higher values of D and $G_0^* / \bar{E}$, and lower values of τ_{ult} exhibit relatively smaller pullout displacement at a given pullout force.

As $G_0^* / \bar{E}$ represents the relative stiffness of the GFRP soil nail and the surrounding soil, the pullout performance is proved to be highly sensitive with the properties of the nail material. In pullout tests, the pullout resistance is normally defined as the maximum pullout force or the pullout force at which a certain value of displacement is achieved. Remarkable decrease of $G_0^* / \bar{E}$ for steel soil nails will result in higher pullout resistance given the same maximum allowable pullout displacement.

4.5 SUMMARY

Based on this study, the following conclusions can be drawn:

(1) The theoretical pullout resistance deduced by the current design methodology is very conservative compared with the results of field pullout tests. An empirical correlation between the field pullout resistance of steel soil nails and SPT *N* value in completely decomposed tuff slopes is proposed.

(2) GFRP is applicable for using as soil nails. GFRP material has the advantages of high corrosion resistance, high strength to weight ratio, low thermal stress and high adaptability with fiber optic sensors. However, the reduced stiffness, creep effect and fatigue possibility of GFRP soil nails should be noted.

(3) The GFRP soil nails under investigation were proved to have satisfactory workability. The double grouting method could reduce the tensile strains of the GFRP pipe at a certain pullout force, with little contribution to the pullout resistance. During pullout, GFRP soil nails shows different pullout performance compared with steel soil nails. This results from the debonding and slip at the GFRP-grout interface.

(4) A simplified method based on hyperbolic shear stress-strain relationship is proposed to model the pullout behavior of soil nail. The nail diameter, shear resistance of soil-grout interface, and the ratio of interface shear coefficient and the average nail Young's modulus has significant effect on the pullout force-displacement relationship. Compared to steel soil nail, GFRP soil nail is more extensible and may have lower pullout resistance.

Table 4.1 Summary of pullout test results of the steel soil nails at three slope sites

Site No.	Test Nail No.	Length (m)	T_a (kN)	T_{DL1} (kN)	T_{DL2} (kN)	T_p (kN)	T_{ult} of T_p (kN)
CC359	P1	16	10	56	112	520	191
	P2	14	10	48	96	520	121
	P3	12	10	40	80	520	135
	P4	10	10	31	62	520	232
	P5	7	10	21	42	520	213
	P6	5	10	14	28	520	77
	P7	19	10	57	114	520	175
	P8	16	10	48	96	520	194
	P9	14	10	40	80	520	155
	P10	11	10	32	64	520	28
	P11	8	10	23	46	520	97
	P12	6	10	15	30	520	41
	P12A	6	10	15	30	520	65
	P13	7	10	23	46	520	317
	P14	5	10	16	32	520	471
	P15	10	10	35	70	520	520
DC79	P1	6	10	23	46	520	65
	P2	4	10	30	60	520	80
	P3	20	10	76	152	520	187
	P4	6	10	23	46	520	191
	P5	17	10	67	134	520	51
	P6	4	10	30	60	520	275
	P7	12	10	50	100	520	177
	P8	10	10	41	82	520	229
	P9	8	10	32	64	520	107
	P10	6	10	23	46	520	98
	P11	17	10	63	126	520	266
	P12	9	10	32	64	520	289
	P13	7	10	23	46	520	80
DC214	P1	6.5	10	24	48	520	164
	P2	6.5	10	24	48	520	145
	P3	8	10	33	66	520	106
	P4	8	10	33	66	520	92
	P5	8	10	33	66	520	182

Table 4.2 Typical physical and mechanical properties of steel, GFRP and cement grout

Material	Density (Mg/m^3)	Young's modulus (GPa)	Coefficient of expansion ($\times 10^{-6}$ $^oC^{-1}$)	Tensile strength (kPa)	Ultimate tensile strain (%)
Steel	7.85	210	12	400	10
GFRP	1.6-2.0	20-50	12	400	2
Cement grout	2.0-2.5	20	10	2-4	0.007

Table 4.3 Parameters used for simulating the GFRP soil nail pullout tests

GFRP soil nail			Soil-grout interface	
Diameter D (m)	Length L (m)	Average Young's modulus $\bar{E}$ (GPa)	Shear resistance τ_{ult} (kPa)	Shear coefficient G_0^* (GPa/m)
0.12	3.4	22.3	260	4

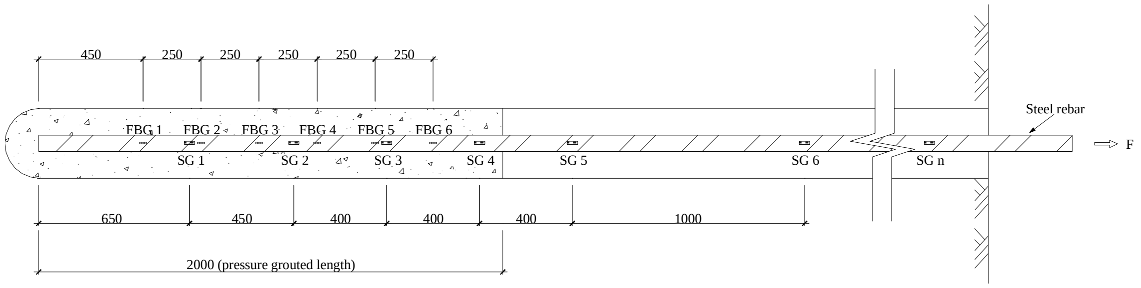

Figure 4.1 Diagram of soil nail instrumented with FBG sensors and strain gauges (unit: mm)

(a) Polishing of soil nails

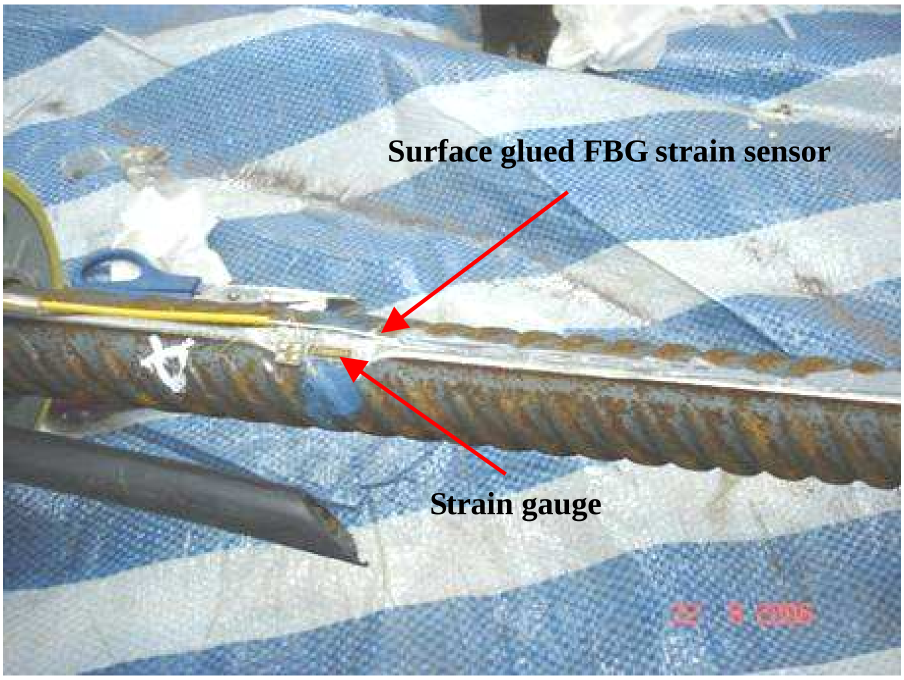

(b) Details of soil nail with FBG sensor and strain gauge

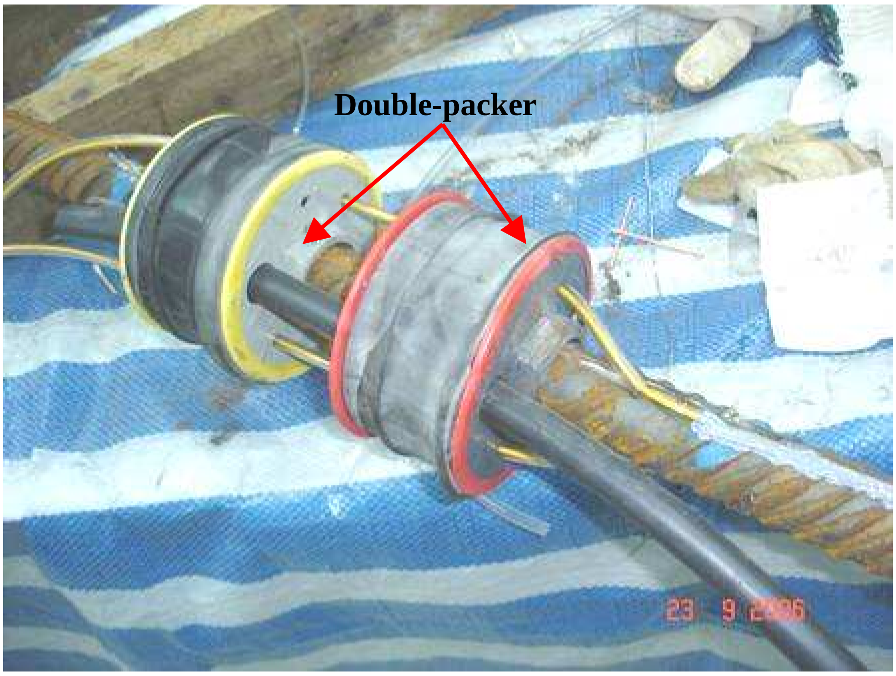

(c) Details of the double-packer on the soil nail

Figure 4.2 Installation of stain gauges, FBG sensors and a double-packer on the soil nail

(a) Pullout test set-up

(b) An optical sensing interrogator si425 for measuring FBG readings

Figure 4.3 Testing apparatus, set-up and instrumentation in the pullout tests of steel soil nails

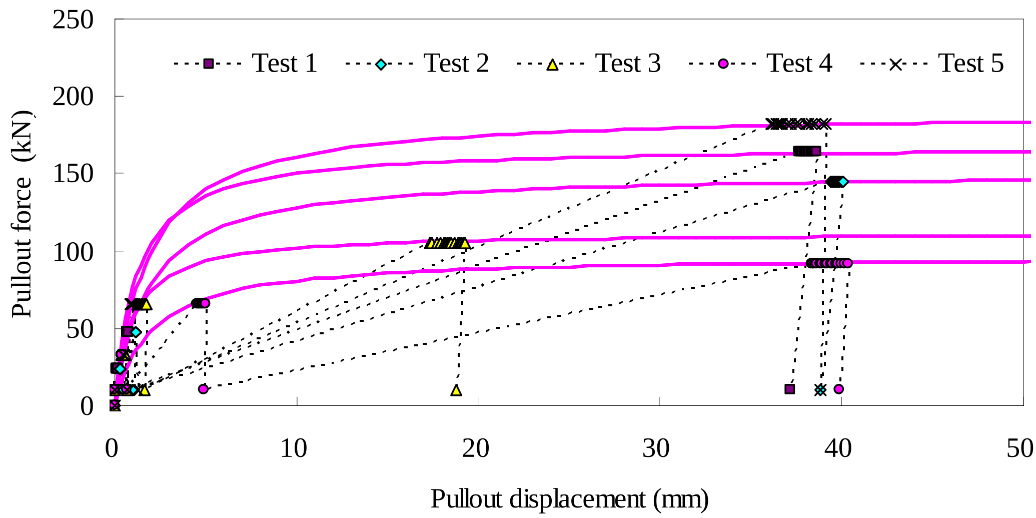

Figure 4.4 Pullout force *vs* displacement curves in the pullout tests of steel soil nails

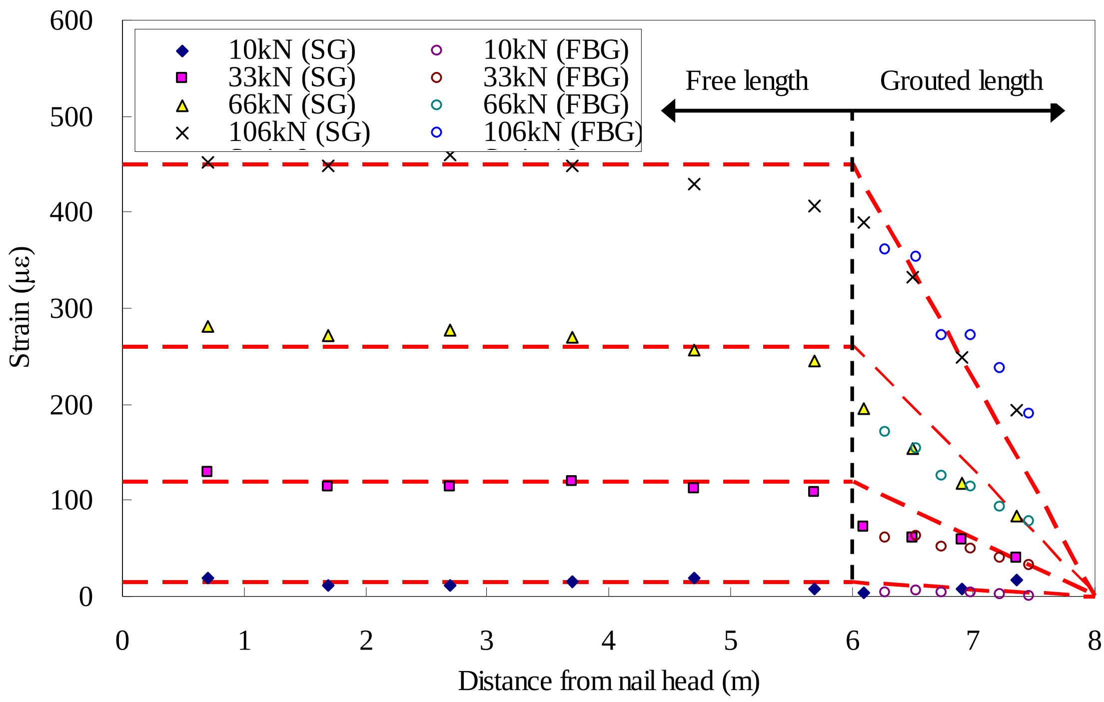

Figure 4.5 Strain distributions along the steel bar in Test 3

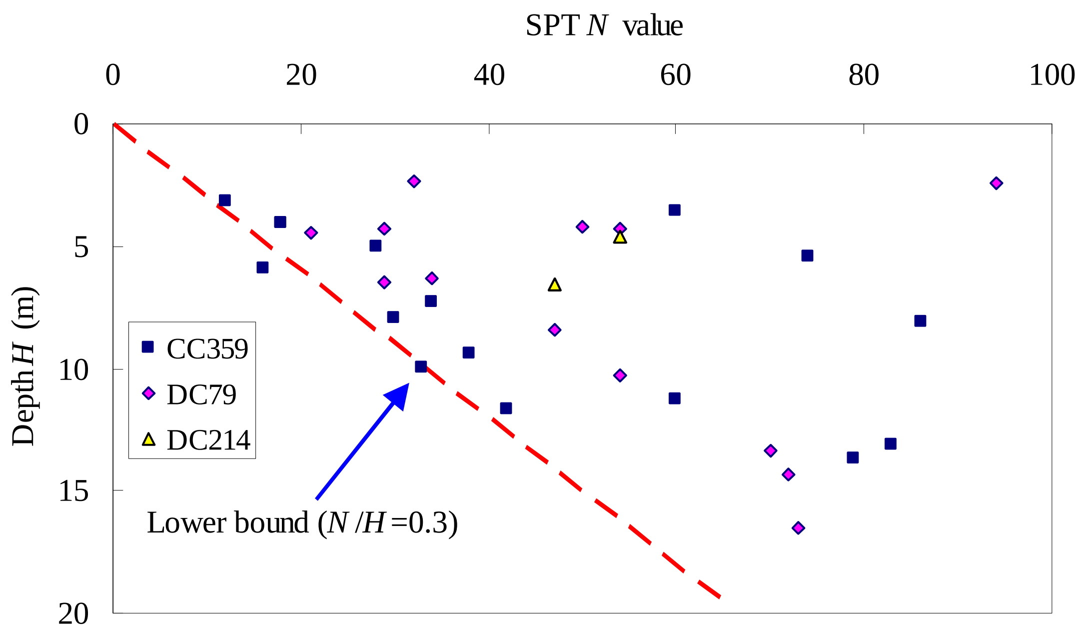

Figure 4.6 Relationship between depth and SPT N value at the slope sites

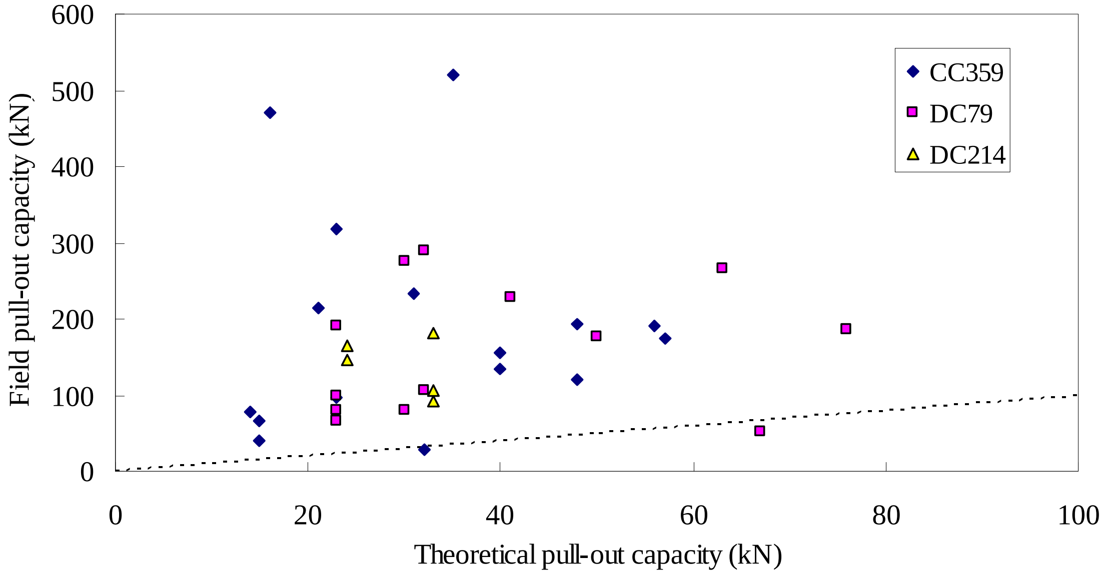

Figure 4.7 Relationship between the experimental and theoretical pullout resistance

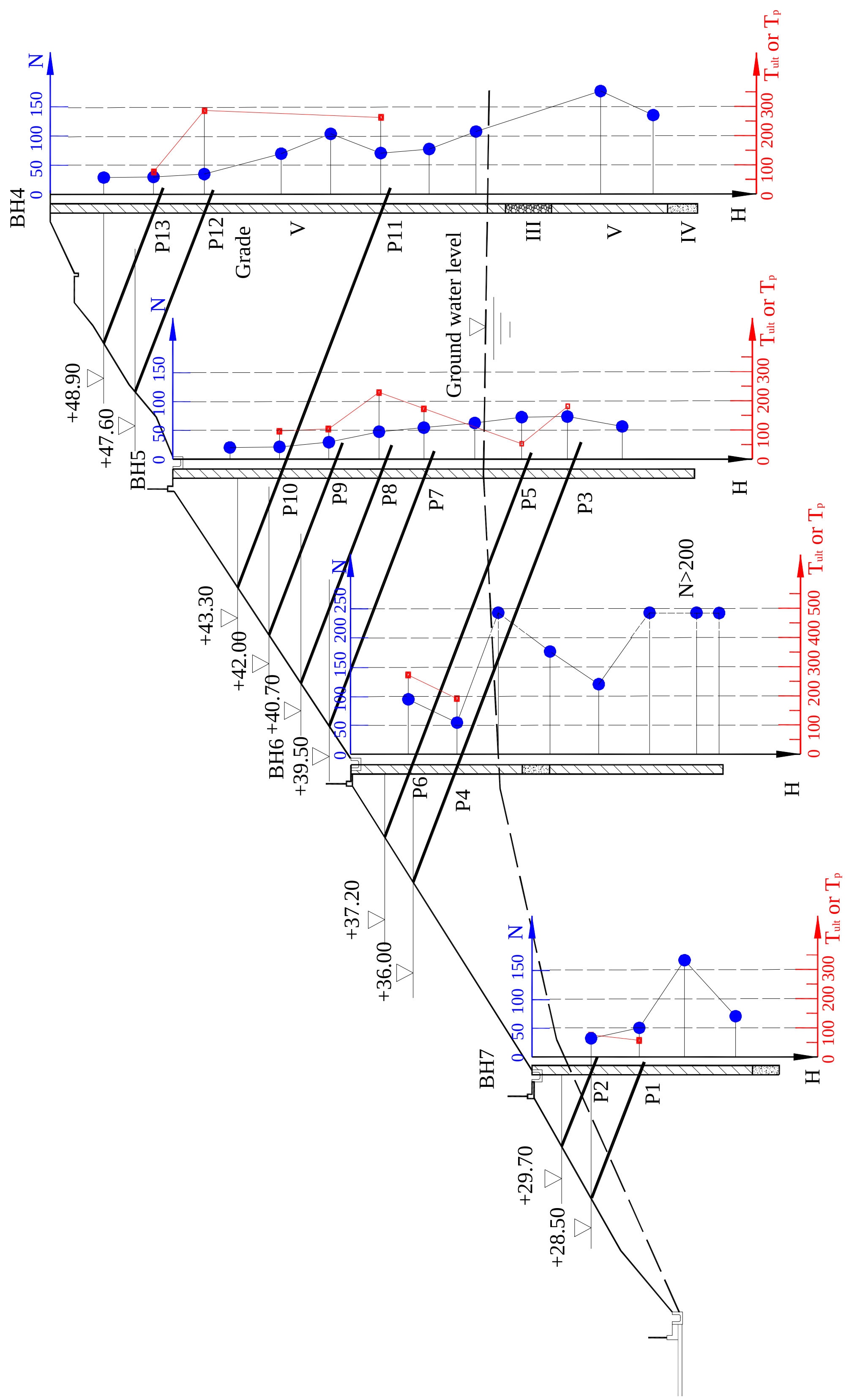

(a) Slope Registration No. 3SW-D/C 79

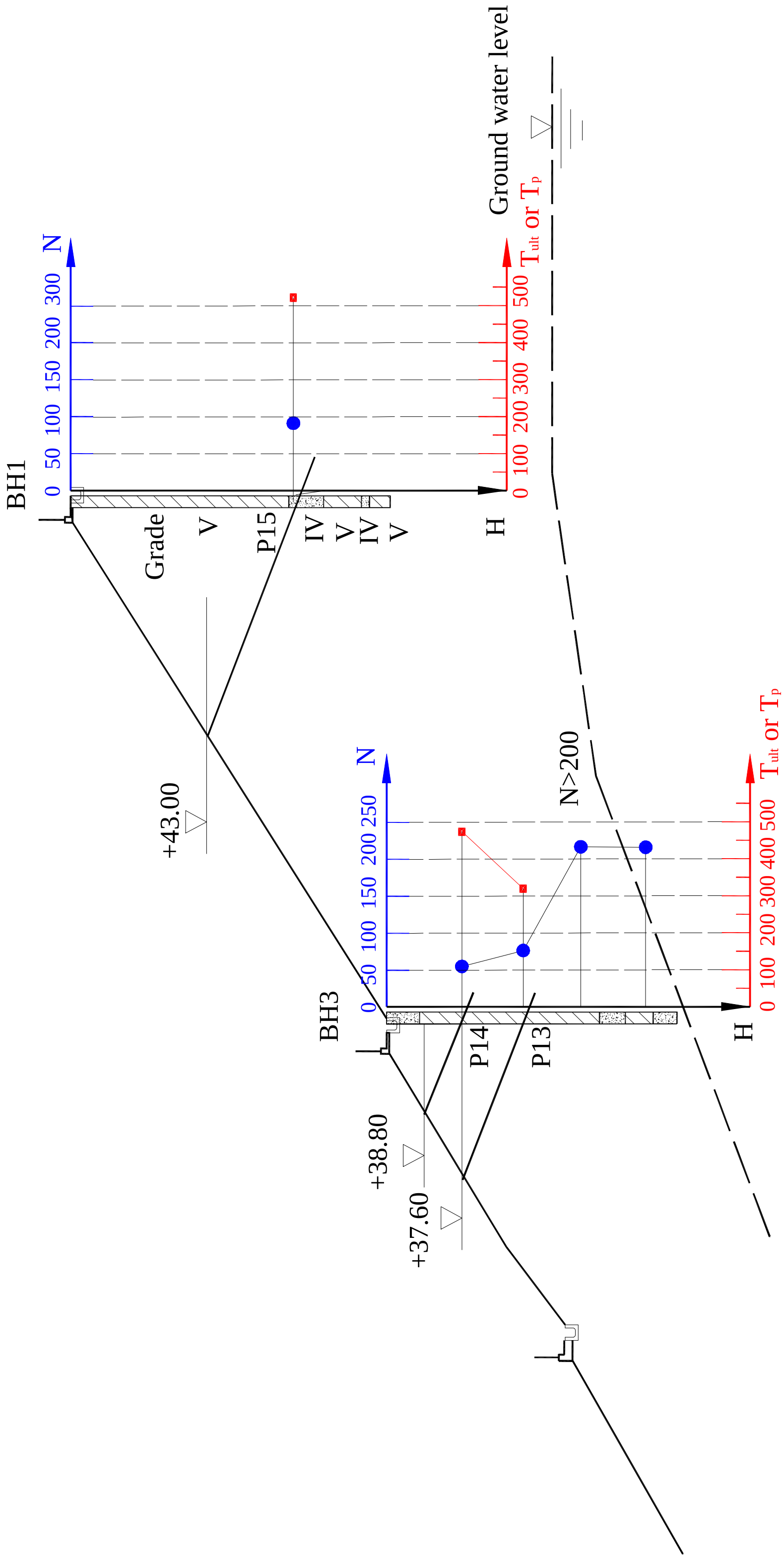

(b) Slope Registration No. 3SW-C/C 359 (Section I-I)

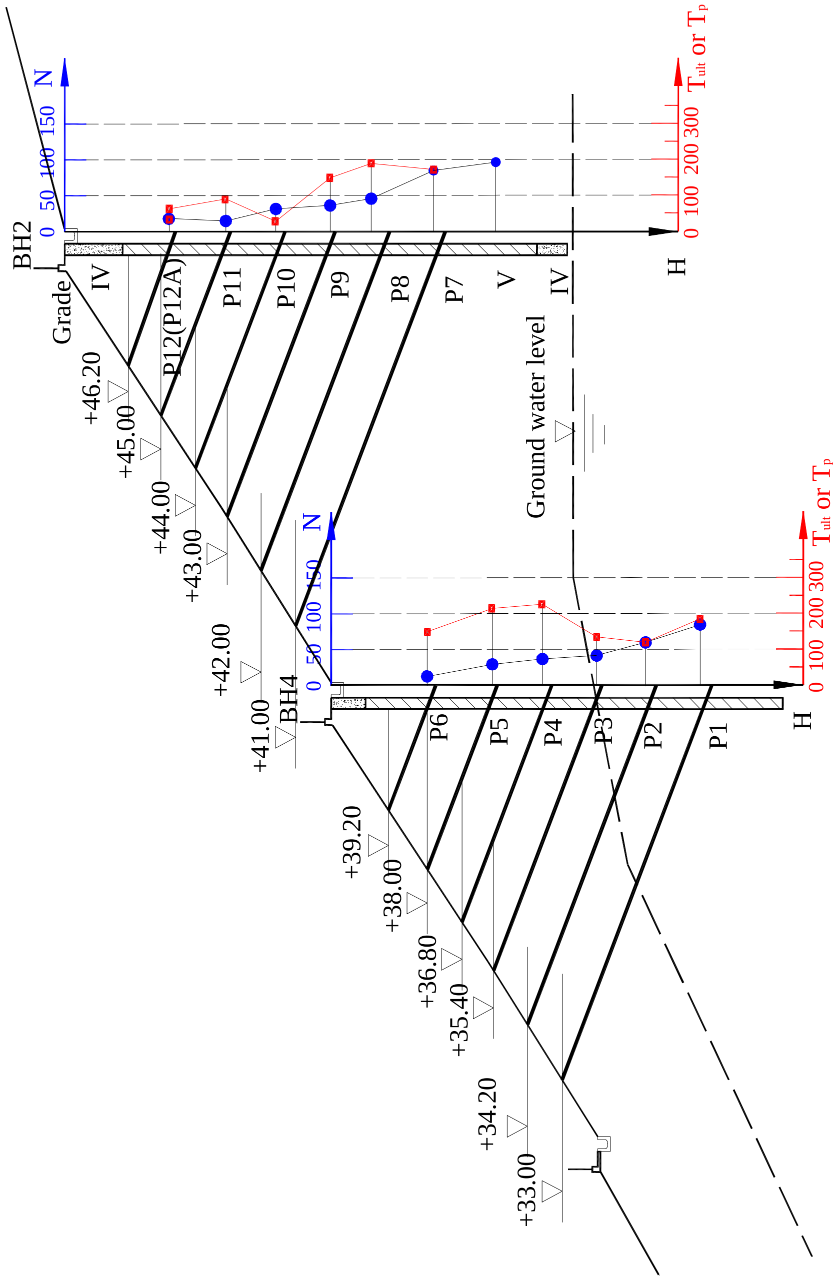

(c) Slope Registration No. 3SW-C/C 359 (Section II-II)

Figure 4.8 Distributions of SPT *N* value and pullout resistance with respect to depths

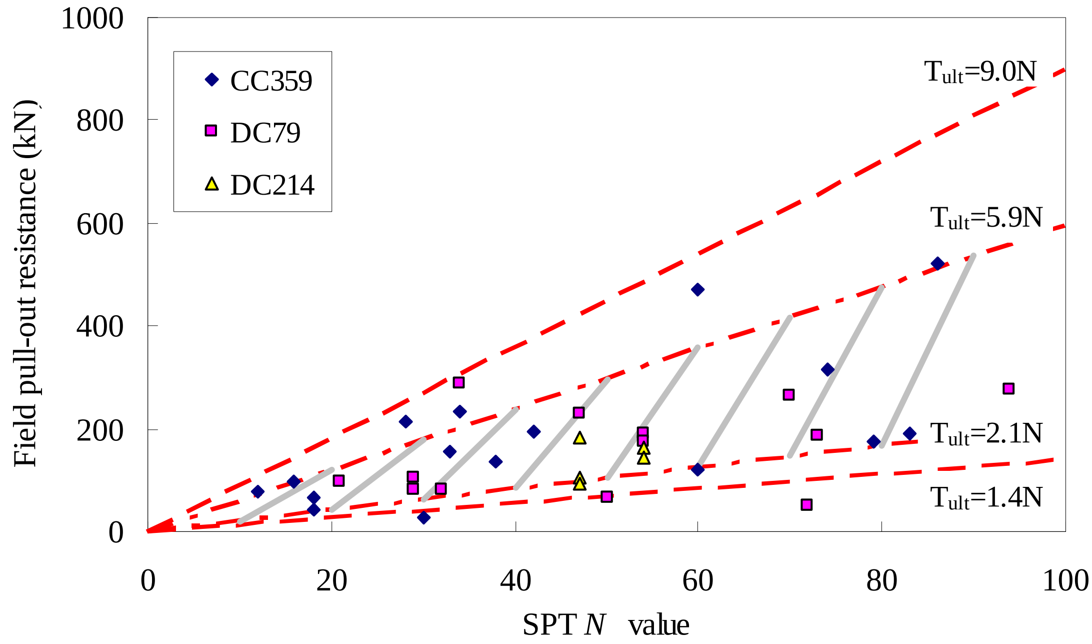

Figure 4.9 Plot of measured pullout resistance of test nails and the SPT *N* value

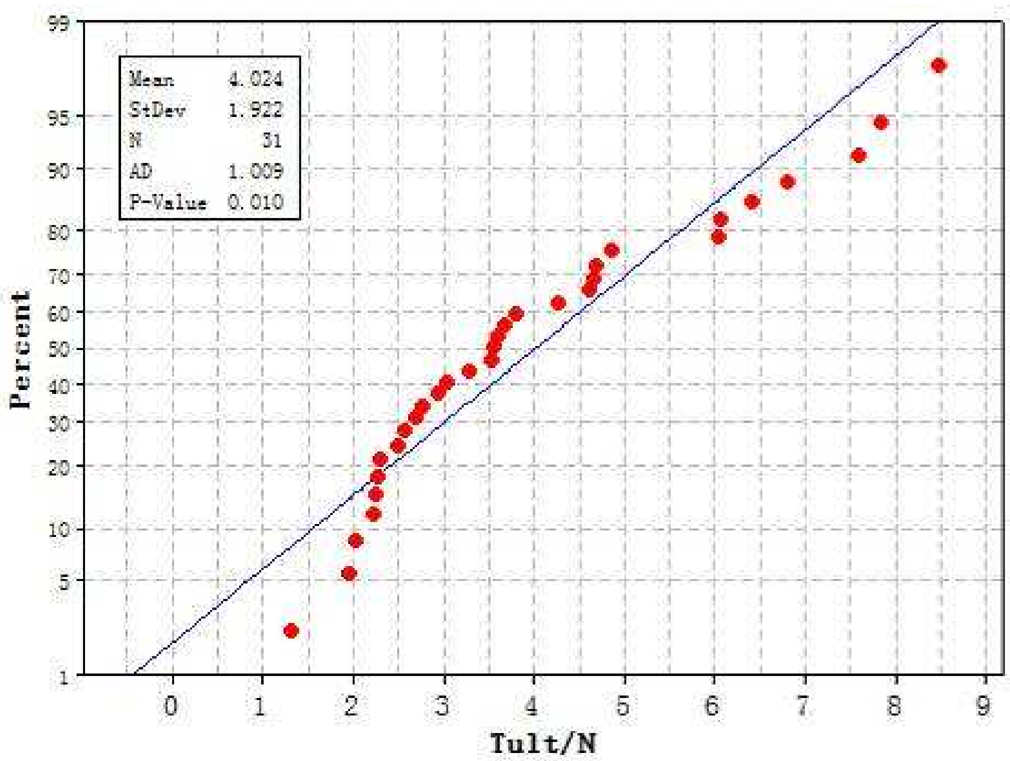

Figure 4.10 Normal probability plot of T_{ult}/N

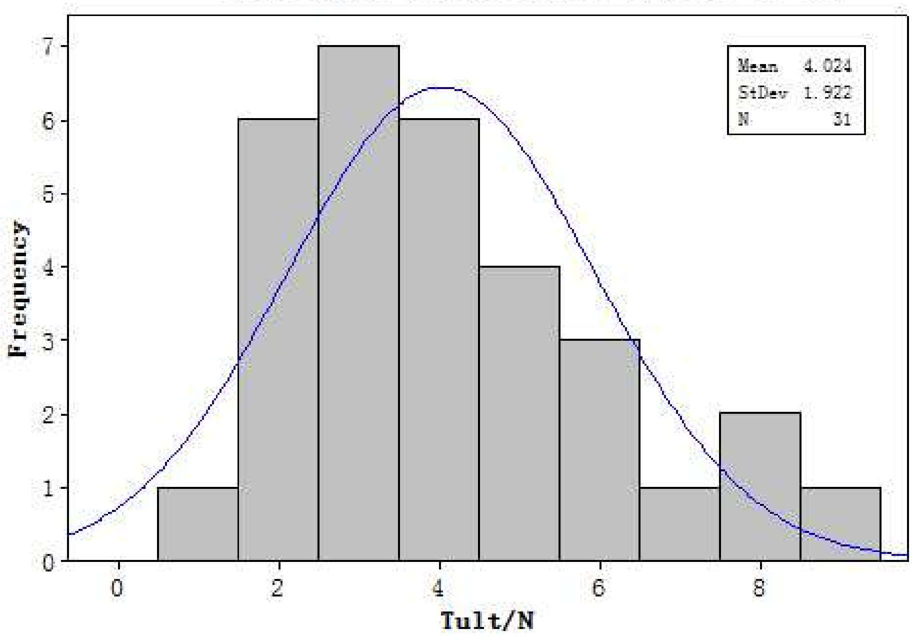

Figure 4.11 Histogram plot of T_{ult}/N with the normal curve

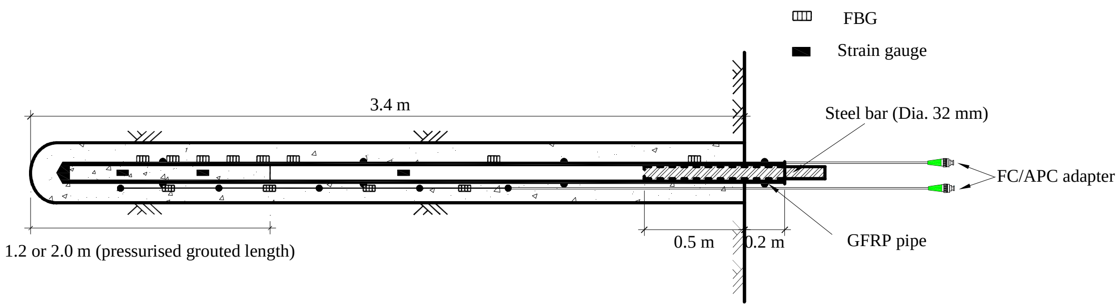

Figure 4.12 Details of the GFRP soil nail instrumented with strain gauges and FBG strain sensors

(a) FBG-A sensors on the surface of soil nail for point strains

(b) FBG-B sensors in an aluminum pipe for continuous average strains

Figure 4.13 Installation of FBG strain sensors on the GFRP soil nail

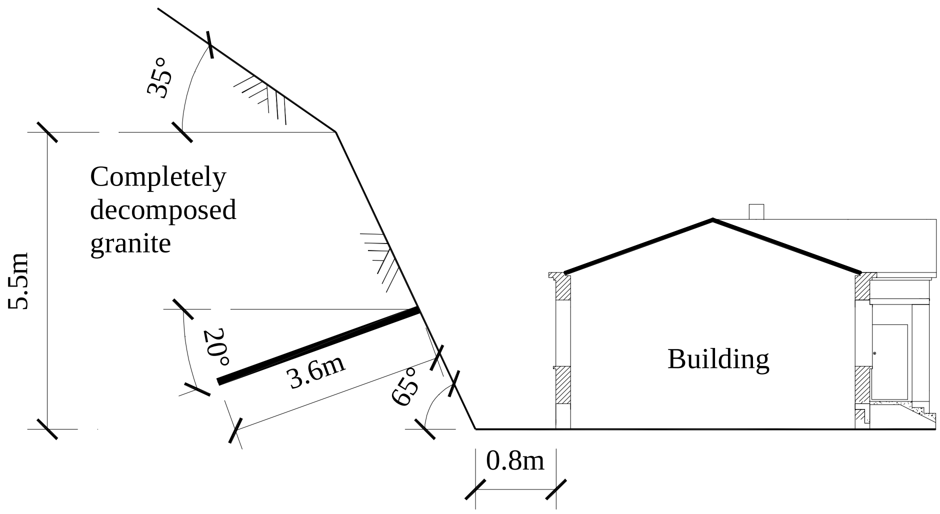

Figure 4.14 Cross section of the slope site

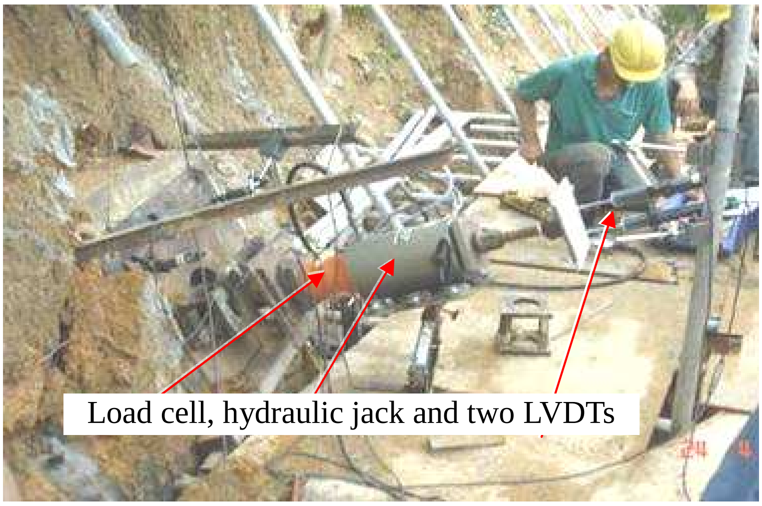

(a) Set-up of pullout devices

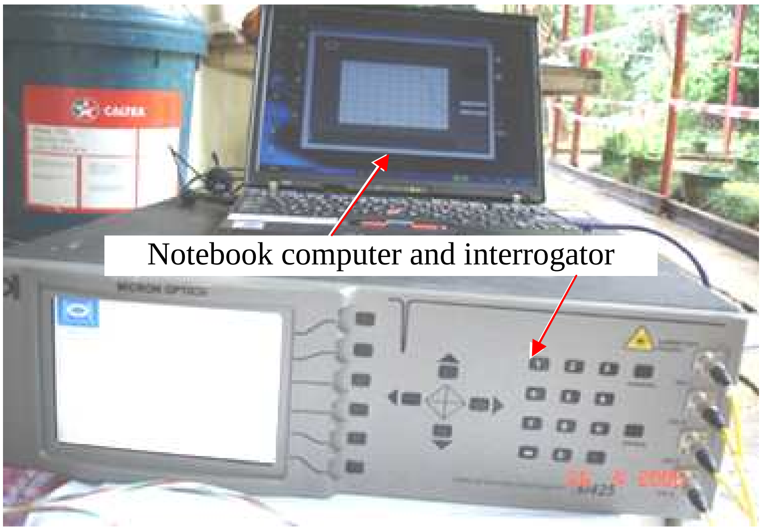

(b) An optical sensing interrogator si 425 for measuring FBG readings

(c) A data logger for taking data of strain gauges, LVDTs and a load cell

Figure 4.15 Testing apparatus, set-up and instrumentation in the pullout tests of GFRP soil nails

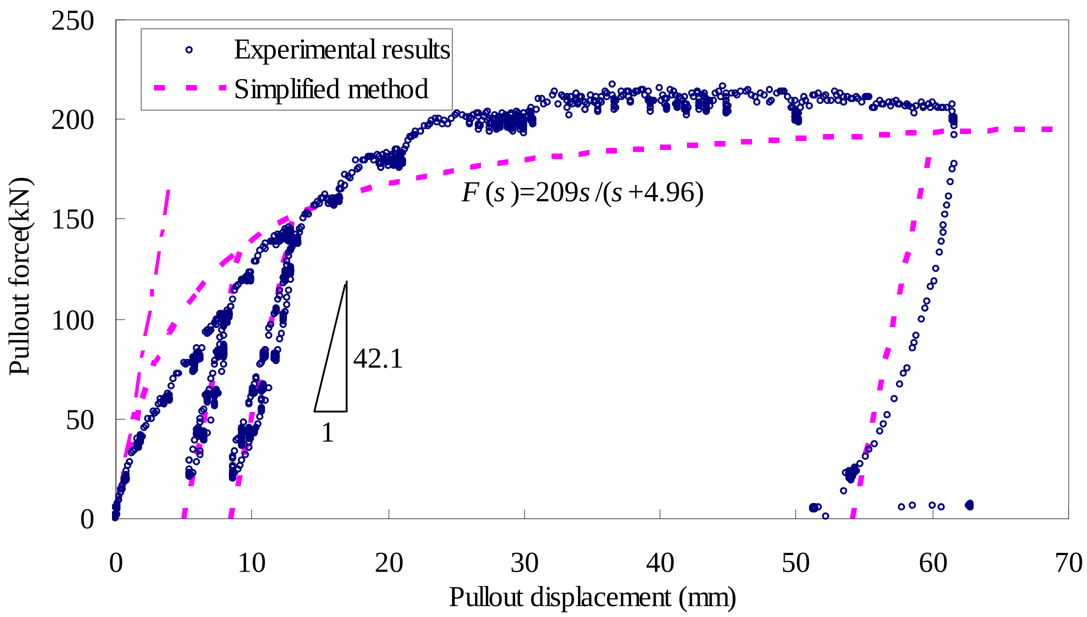

(a) GFRP soil nail No.1

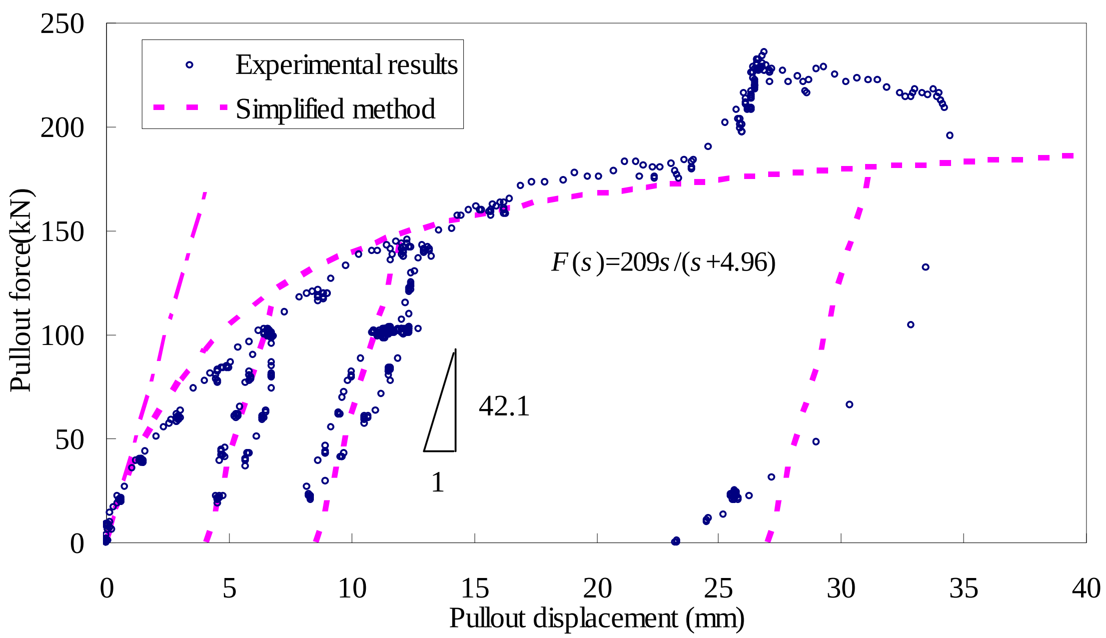

(b) GFRP soil nail No.2

Figure 4.16 Pullout force *vs* displacement curves in pullout tests of GFRP soil nails

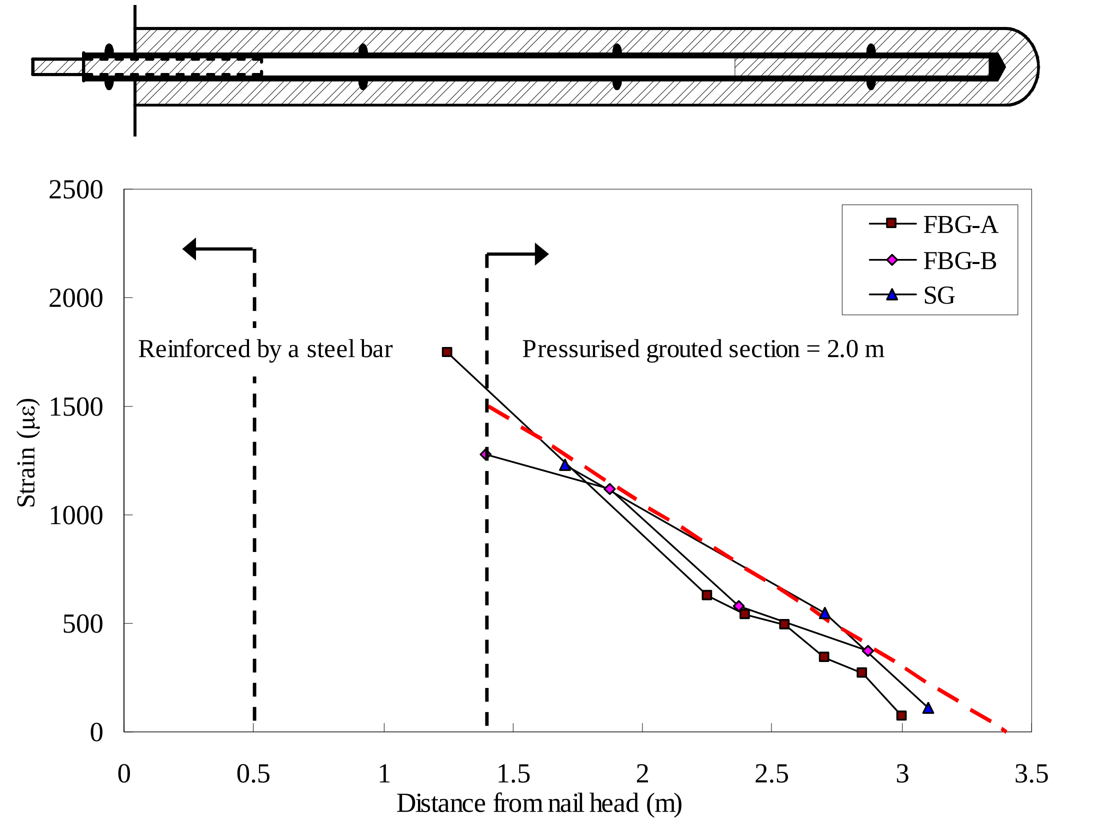

Figure 4.17 Comparison of strains measured by two types of FBG sensors and strain gauges on GFRP soil nail No. 1

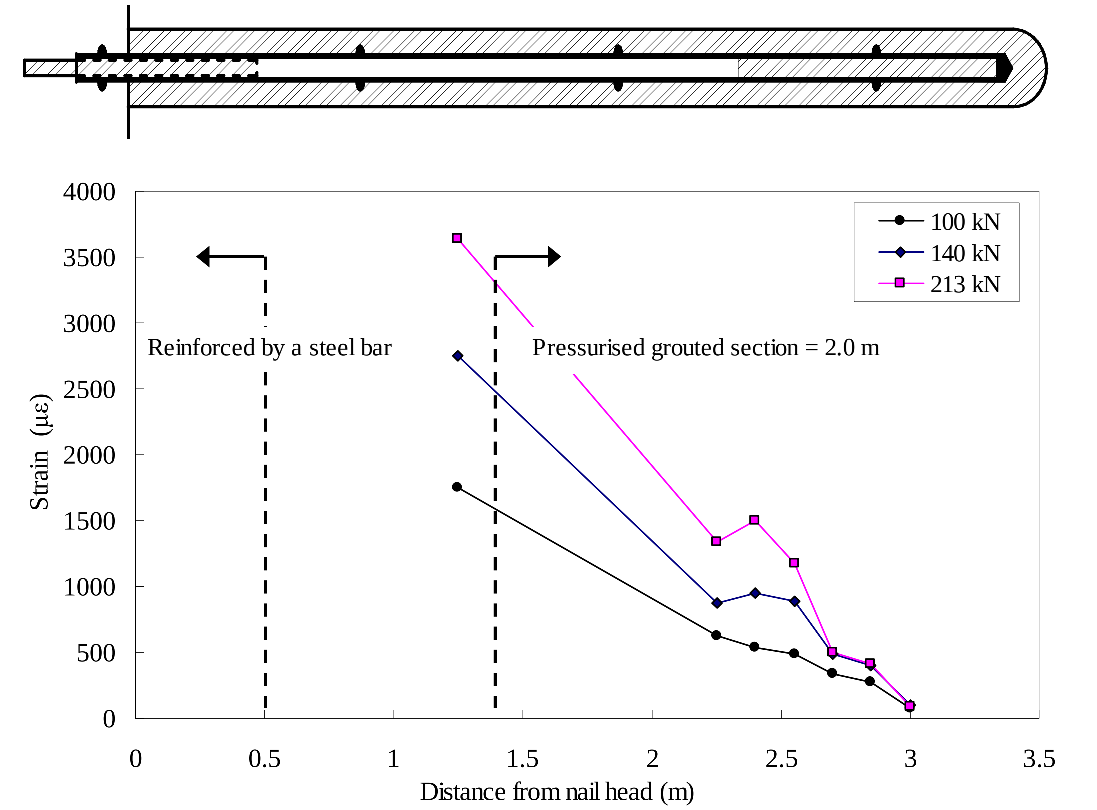

(a) GFRP soil nail No. 1

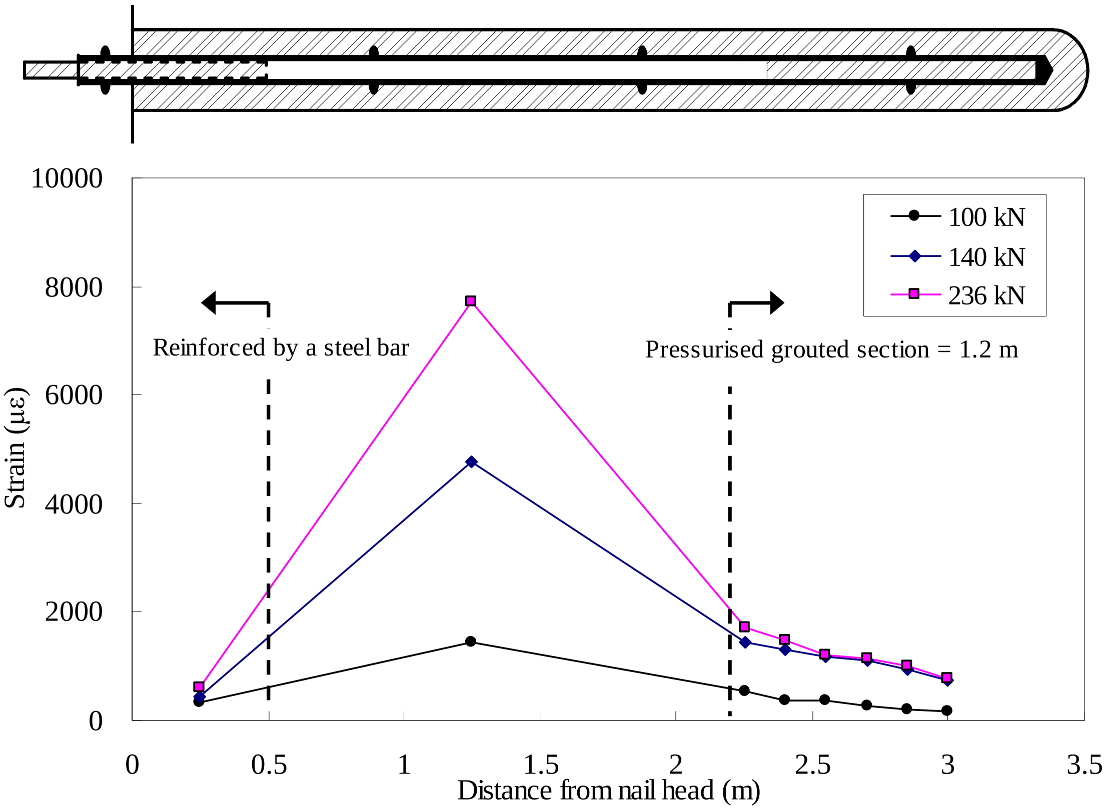

(b) GFRP soil nail No. 2

Figure 4.18 Distribution of axial strains measured by FBG-A sensors along GFRP pipes in pullout tests

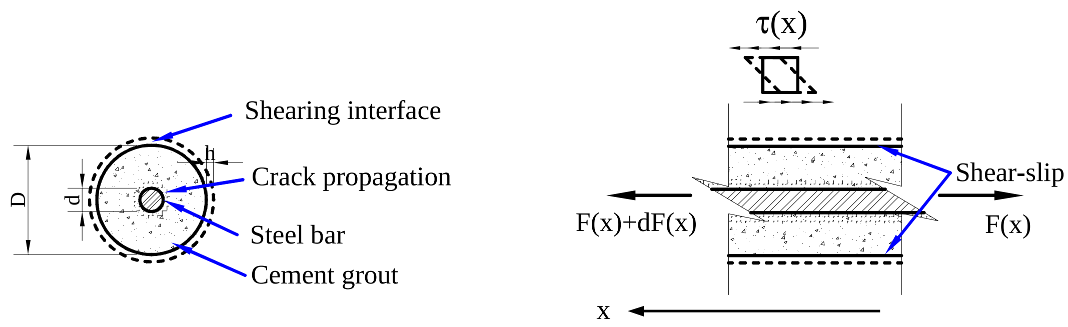

(a) Steel soil nail

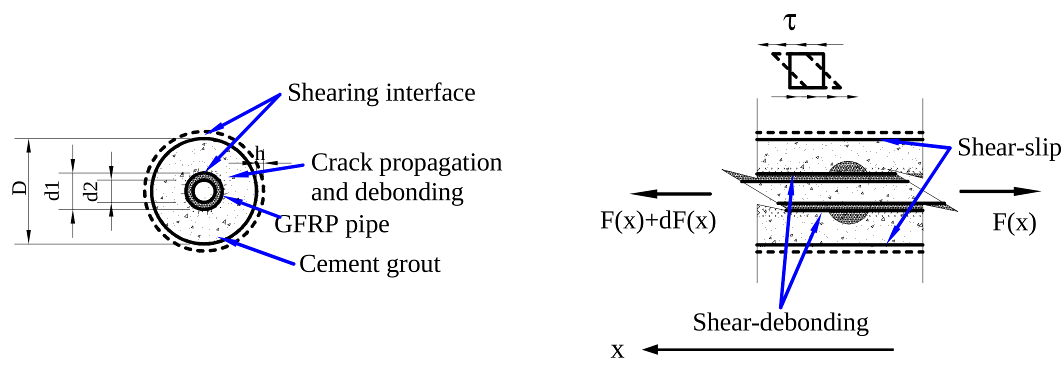

(b) GFRP soil nail

Figure 4.19 Schematic illustration of pullout mechanism of steel and GFRP soil nails

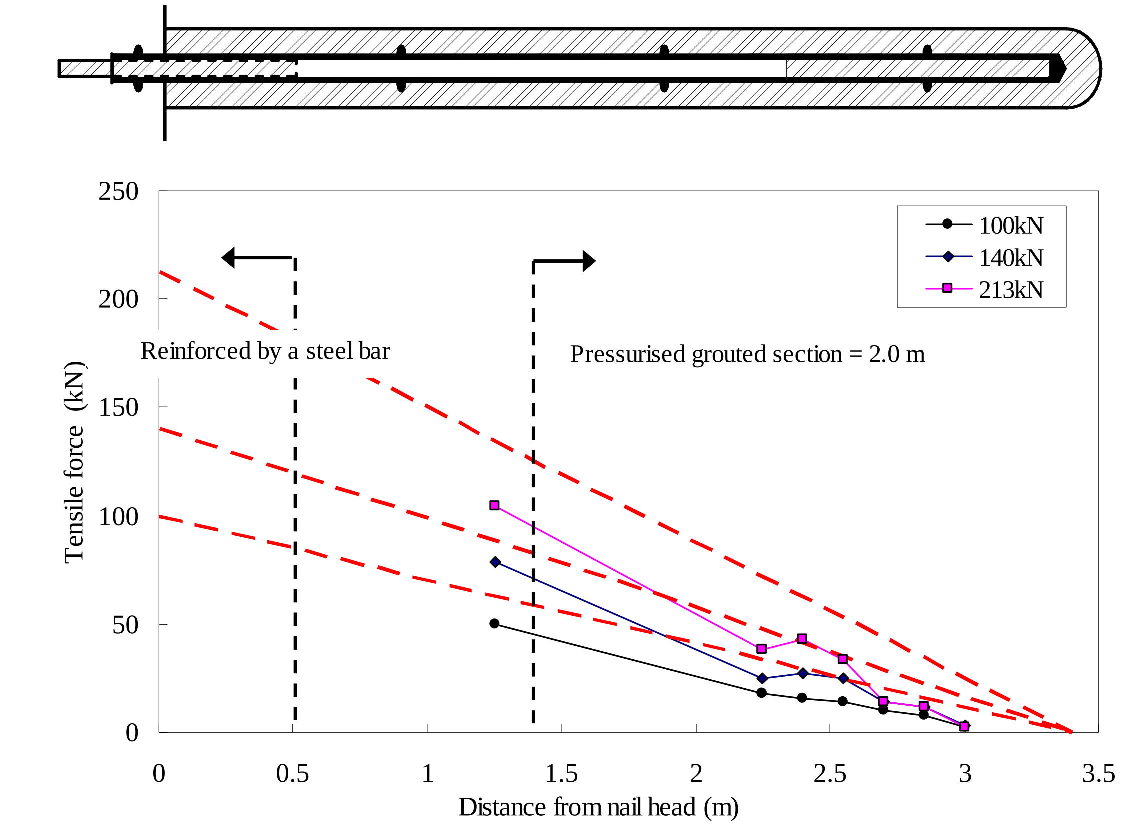

(a) GFRP soil nail No. 1

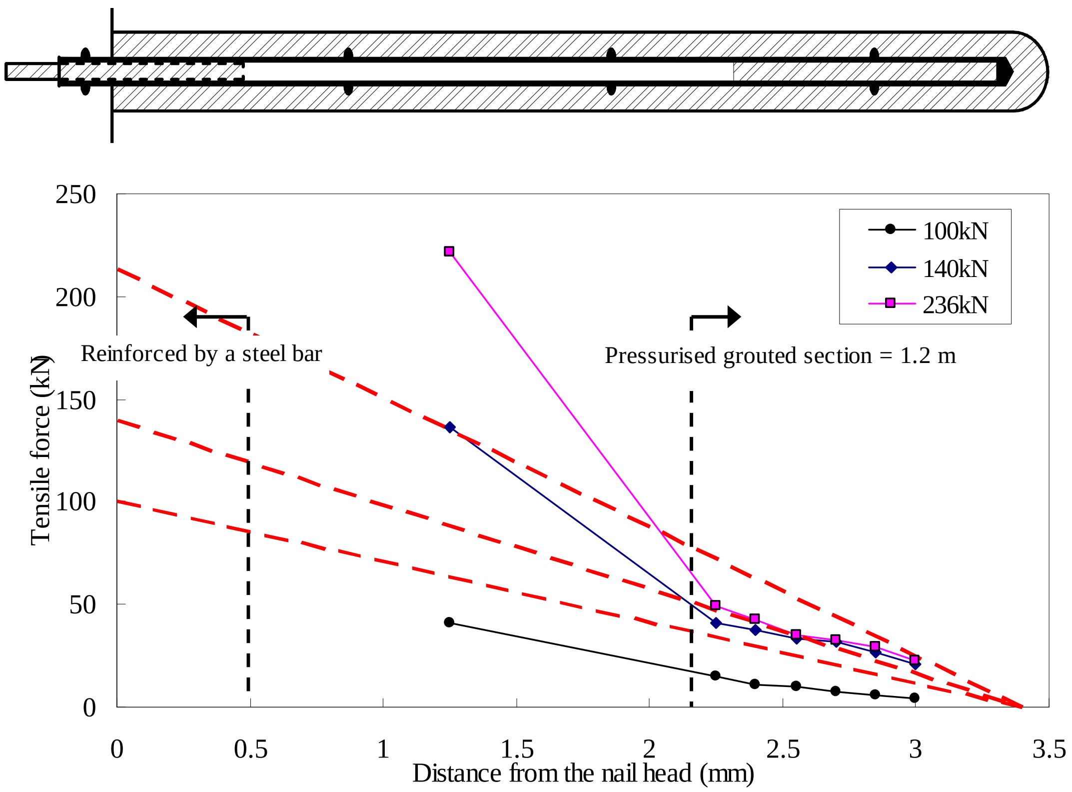

(b) GFRP soil nail No. 2

Figure 4.20 Distribution of calculated tensile forces along the GFRP soil nails in pullout tests

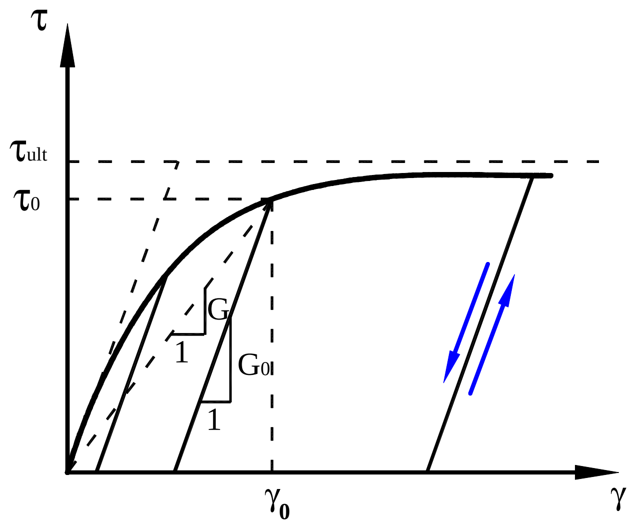

Figure 4.21 Simplified model of shear stress-strain relationship

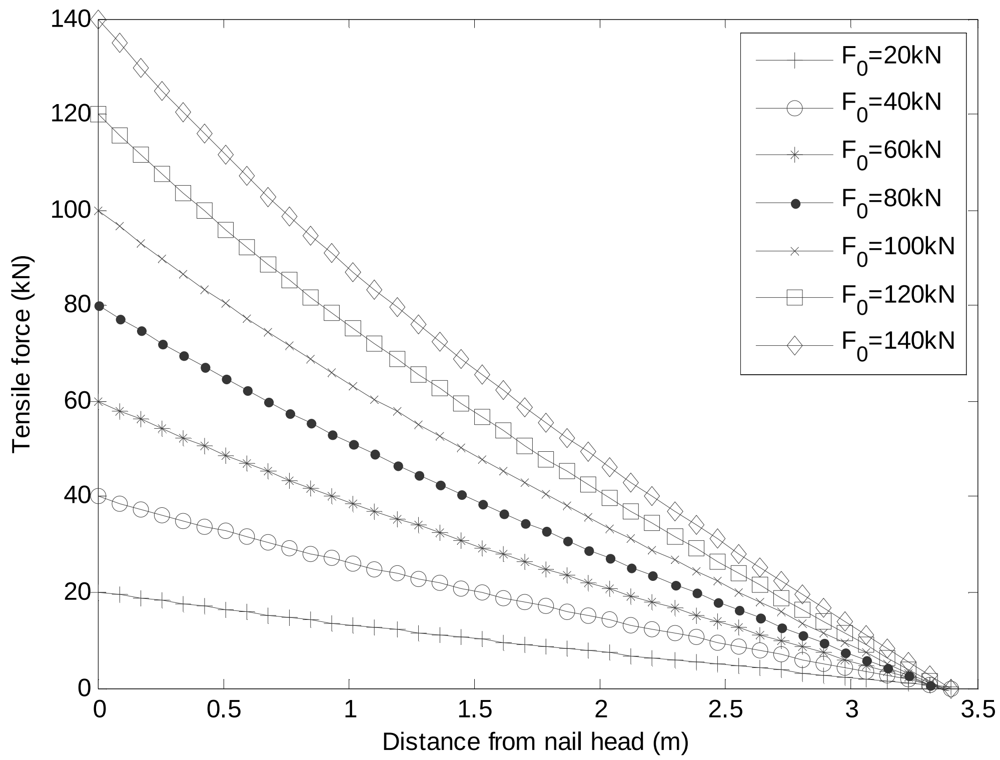

(a) Distribution of tensile forces along the GFRP soil nail during pullout test

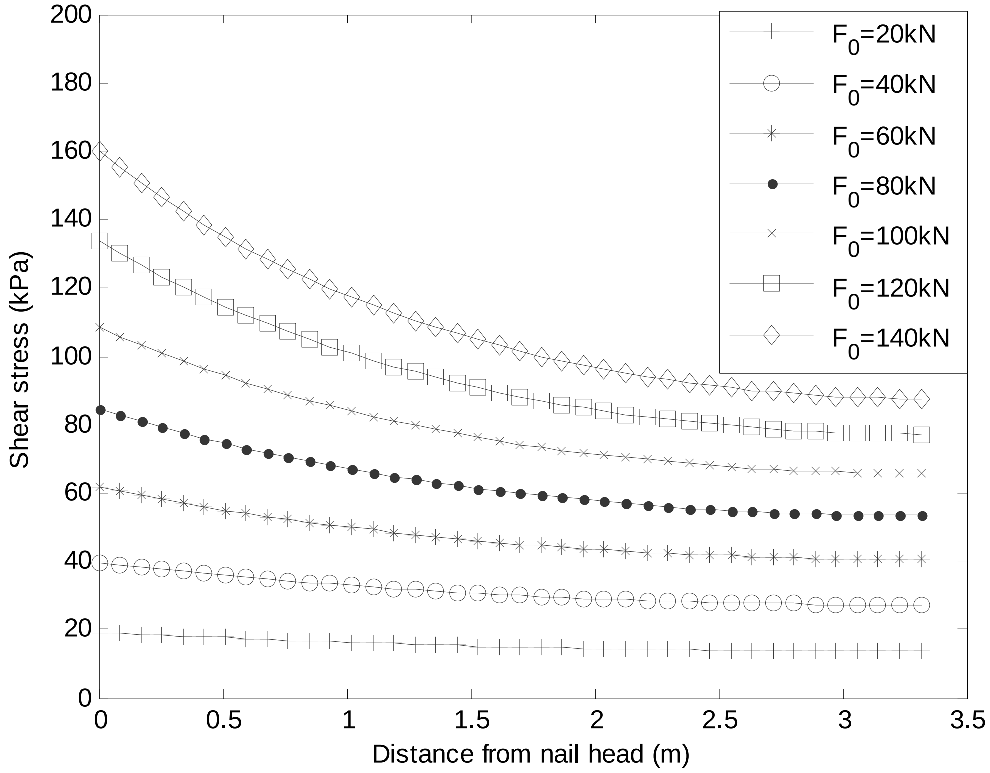

(b) Distribution of shear stress along the GFRP soil nail during pullout test

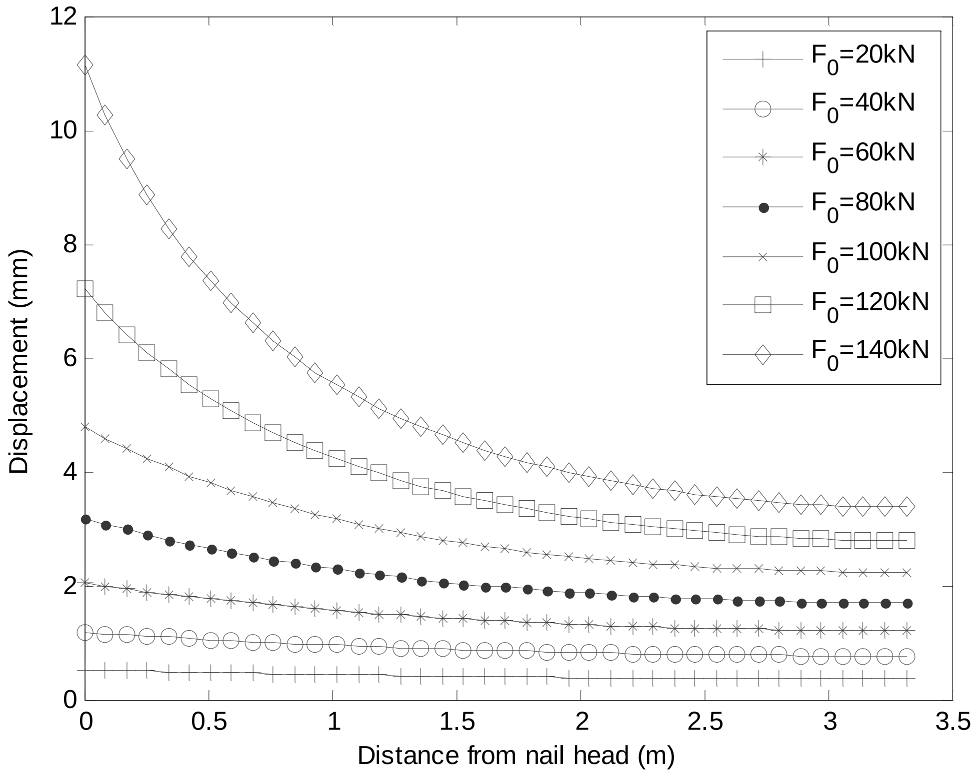

(c) Distribution of axial displacement along the GFRP soil nail during pullout test

Figure 4.22 Simulated pullout behavior of the GFRP soil nail

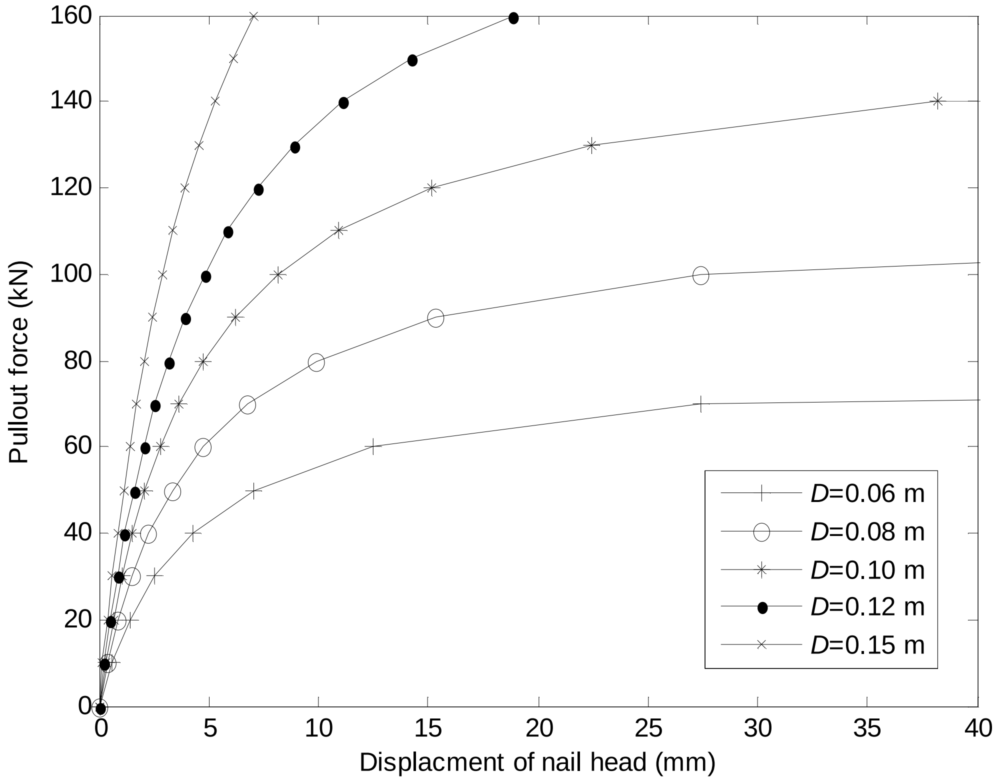

Figure 4.23 Effect of D on pullout behavior of GFRP soil nail

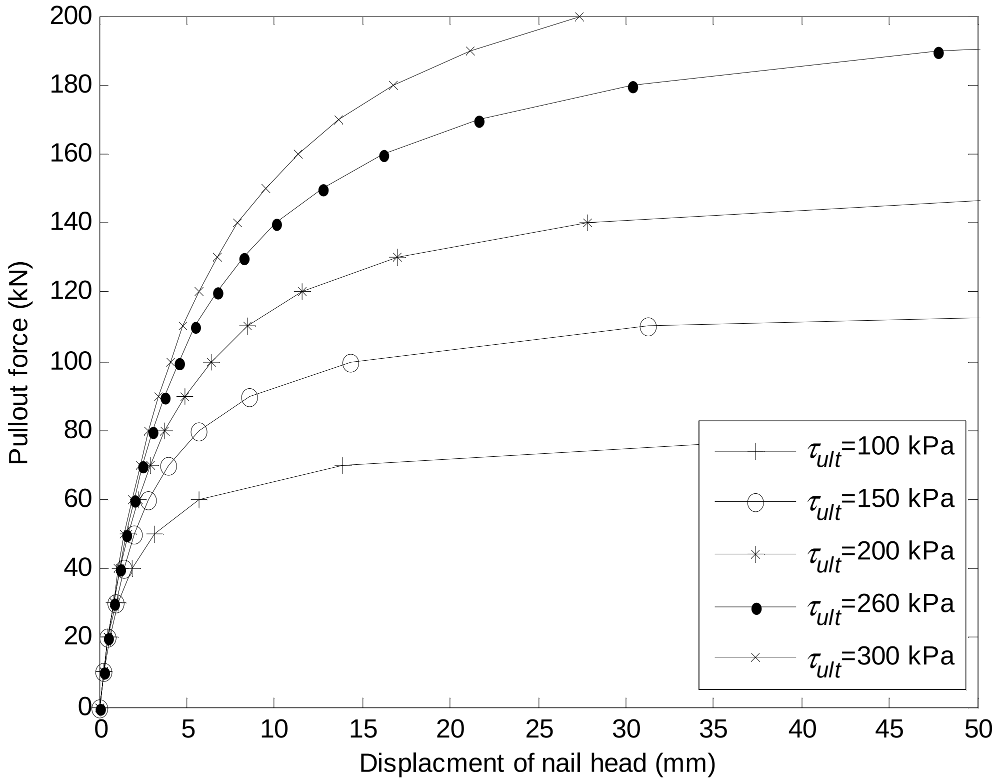

Figure 4.24 Effect of τ_{ult} on pullout behavior of GFRP soil nail

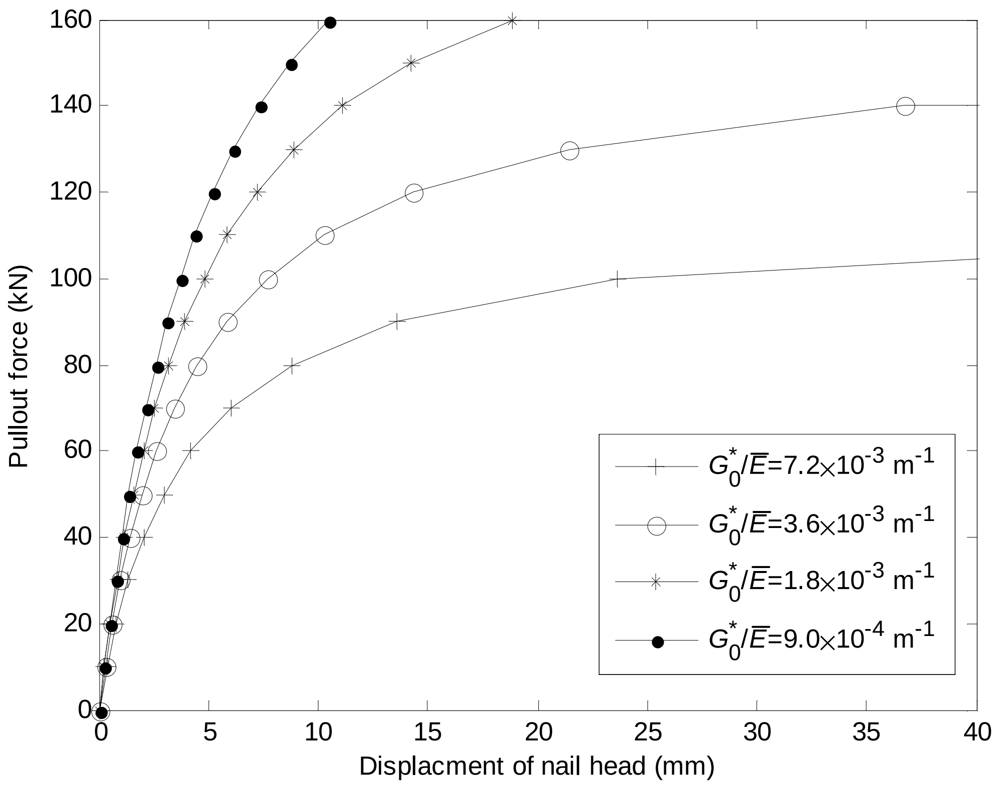

Figure 4.25 Effect of $G_0^* / \overline{E}$ on pullout behavior of GFRP soil nail

CHAPTER 5:

FIBER OPTIC MONITORING AND PERFORMANCE EVALUATION IN THE MODEL TESTS OF SHUANGJIANGKOU CAVERN GROUP

5.1 INTRODUCTION

Owing to the dramatic urbanization in developing countries, underground caverns have become one of the preferred construction options for powerhouses, transportations, energy storage facilities, and municipal utility systems. In the past two decades, a number of hydropower stations have been or are being constructed in China, such as the Three Gorges Dam project (Liu et al. 2003, a total electric generating capacity of 22,500 MW), Xiluodu Hydroelectric Power Station (Chen et al. 2004a, 12,600 MW), Baihetan Hydropower Station (12,000 MW), Pubugou Hydropower Station (Fu et al. 2008, 3,300MW), Ertan Hydropower Station (Zhu et al. 2008, 3,300MW), Xiaolangdi Hydroelectric Power Station (1,800 MW), and Zhanghewan Pumped Storage Power Station (1,000 MW). For each of them, a large-scale rock underground cavern will be excavated.

During the excavation of a cavern in rock masses, a change in the initial stress field will be induced, which may affect the overall stability of the cavern. The design and construction of caverns requires a careful consideration of geological condition and rock mass characteristics. For underground caverns, there are basically four types of instability, namely adverse structural geology, excessively high rock stress, weathering and / or swelling rock, and excessive groundwater pressure or flow (Hoek and Brown 1980). With the increase of excavation scale and geological complexity, it is of great importance to have a comprehensive understanding of different phenomena related to underground excavation, including the deformation patterns and failure mechanisms.

In this area, three approaches have been widely adopted, including engineering analogy method, numerical simulation, and physical modeling. The first method is not suitable for complex geological conditions. Numerical simulations of underground excavation have been gaining in popularity with the advancement of computation mechanics in recent years (e.g. Duddeck 1988; Dhawan et al. 2004; Li et al. 2005c; Hao and Azzam 2005). In comparison, physical model testing has a much longer history with certain advantages over numerical modeling. Meguid et al. (2008) presented a review of selected physical models that have been developed for studying soft ground tunneling and discussed some approaches used to record soil deformation and failure mechanisms induced by tunneling. For large-scale cavern projects, few precedent projects that have the similar geological and field-stress conditions can be found for contrast. Consequently, physical modeling and numerical simulation are the main methods for solving these problems (Zhu et al. 1993; Park and Adachi 2002; Sterpi et al. 2004; Zhu et al. 2004). Due to the constraint of experimental techniques, difficulties have been encountered in plane-strain model tests (Mair 1979; Mair et al. 1993; Nagai et al. 1996) and small-scale 3-D model tests (Heuer et al. 1969, Li et al. 2003), for instance, the generation of initial stress field, the simulation of excavation activities, and the measurements of physical quantities of the physical models. Li et al. (2005c) combined 3-D physical model tests and numerical simulation to study the performance of Xiluodu Cavern Group and discussed the advantages of this approach. Zhu et al. (2008a) conducted large-scale quasi 3-D geo-mechanical tests to analyze the stability of a cavern group with high *in-situ* stresses. Nevertheless, large-scale 3-D physical model tests, especially the overloading tests under true 3-D stress state, were seldom reported over the past few decades.

Recently, large-scale 3-D physical model tests on Shuangjiangkou Cavern Group at the acceleration of gravity (1 g) were conducted in Geotechnical and Structural Engineering Research Center, Shandong University. Major improvements in the model tests have been made in terms of experimental techniques and advanced measurement methods. This project is initiated by Prof. Wei-shen Zhu of Shandong University. The author took part in a) the instrumentation of the model, especially the utilization of FBG sensing bars, and b) the analysis of displacement monitoring results. Numerical simulation of the model tests were conducted by Prof. Zhu. In this chapter, the construction, test set-up and procedure of the model tests is briefly introduced. The observation and monitoring results are presented and analyzed in detail. The comparison of the experimental and numerical results indicates that the measured displacements fit well with those obtained from finite difference analysis.

5.2 PHYSICAL MODELING OF SHUANGJIANGKOU CAVERN GROUP

5.2.1 Project background

Shuangjiangkou Hydropower Station is located in Aba, Sichuan Province, China and on the upper reaches of Dadu River. It is one of the largest hydropower stations in the Dadu River basin, which has a maximum output of 2,000 MW (500 MW×4 units). The outcrop at the site mainly consists of Muzudu porphyritic biotite-potassium feldspar granite ($\gamma_{K_5}^2$) of the early Yansanian period and Keeryin biotite-muscovite monzonitic granite ($\eta_{\gamma 5}^{3}$) of the late Yanshanian period. From the *in-situ* stress measurement, the maximum principal stress near the underground cavern group is up to 38 MPa, which is seldom encountered for underground caverns in China. The *in-situ* stress field may be highly affected by the excavation procedure of the caverns.

The horizontal distance from the cavern group to the reservoir is about 420 m, and the overburden depth is about 421 m to 598 m. The cavern group mainly consists of the power house, the transformer house and the surge chamber, which are parallel to one another and separated by two rock walls with the thickness of 45 m. The dimensions of the three caverns are shown in Table 5.1. The proposed axial direction of the power house is N8°W. The angle between the axial direction and the major principal stress is 2.4°. Figure 5.1 shows the design layout of the hydropower station. No major faults are found in the project area and interlayer sliding is generally not visible. The rock is fresh and intact, mainly consisting of dense hard fine-medium grained porphyritic biotite-potassium feldspar granite and fine-medium grained biotite-muscovite monzonitic granite (CHIDI 2006).

Owing to the complexity of geometry, geological condition and *in-situ* stress fields, deformation and stability conditions of Shuangjiangkou cavern group need to be investigated in detail.

5.2.2 Model construction

According to the similitude laws, the prototype and the model should satisfy the equilibrium equations, geometric equations, physical equations, stress and displacement boundary conditions (Fumagalli 1973). The similarity ratio of the model was selected as 1:150. Table 5.2 lists the parameters of the prototype and the model. The similarity material in this study was made from barite powder, iron mineral powder, quartz powder, Grade I rosin and 99.9% purity industrial alcohol (Zhu et al. 2008a).

Precast blocks were used to construct the model and the monitoring holes for installing FBG sensing bars and multi-point extensometers were prepared beforehand. In this way, the consistency of the mechanical properties of the model material can be guaranteed and various sensors can be embedded in the designated positions during model construction. The model dimension was 2.5 m×2.0 m×0.5 m (width × height × thickness), as shown in Figure 5.2. The cavern group included the power house, the transformer house, the surge chamber, the busbar chamber, and partial tailrace tunnels. The model took full account of the spatial arrangement of two hydro-generating units.

In the physical model, the installation of rock bolts and pre-stressed cables for stabilizing the excavation were simulated (Zhu et al. 2009). A number of holes inside the sidewalls of the power house were prepared beforehand. During excavation, the model bolts made of polyethylene (PE) were inserted into the holes and grouted with the mixture of building adhesive and barite powder. A model cable consists of a cable head, a flexible steel wire, an extension spring and an anchor end. When the excavation reached the cable location, the model cables were installed in the sidewalls and the predetermined pre-stress was applied by tightening the screw on the cable head.

5.2.3 Test set-up and procedure

A steel structural frame developed by Geotechnical and Structural Engineering Research Center, Shandong University, was utilized in the model tests (Zhu et al. 2009). The frame shown in Figure 5.3 is used to accommodate the physical model and as a reaction device for loading. The frame mainly consists of a base, a door-shaped reaction frame, a layered reaction frame, structural walls, loading jacks, and combinational sliding walls. Compared with the test frames developed in the previous studies (Li et al. 2003), this frame has the advantages of high adaptability, high loading resistance, reduced friction on the model and ease of observation.

The hydraulic loading control system can simulate a wide range of *in-situ* stress level. Totally 5 hydraulic jacks are installed to generate gravity load from the top. In the left and right sides, 10 jacks are installed to apply stepwise lateral loads in the direction perpendicular to the axial direction of the caverns. These 15 jacks are controlled by the HLCS-1 hydraulic control system. Between the frame base and the model, 10 jacks are installed. A total of 16 jacks are installed for the four-step loading in the axial direction (4 jacks for each step), and controlled by the HLCS-2 hydraulic control system. The layout of the hydraulic jacks is depiected in Figure 5.4.

Two loading schemes were implemented in the model tests. One scheme was to simulate the stress filed, excavation and supporting in the actual project, where the vertical loads on the model were equal to the dead weight of rock masses at 600 m depth ($\sigma_3=\gamma h$). According to geotechnical investigation results, the lateral pressure coefficients are determined to be 2.375 (K_1) in the axial direction of the caverns (the direction of the maximum principal stress σ_1) and 1.5 (K_2) in the direction perpendicular to the axial direction (the direction of the intermediate principal stress σ_2). In the model tests, the caverns were excavated by manual drilling and boring. Due to the dimensional restriction of the model, the excavation sequence in the field is simplified to 21 steps in the model tests, which are presented in Figure 5.5 and Table 5.3.

The other scheme was to evaluate the behavior of the model under overloading condition. The *in-situ* stresses were increased to those equaling to overburden depths of 800 m, 1000 m, 1200 m, 1400 m, 1600 m and 1800 m, in stages. The vertical and horizontal loads were applied with the same lateral pressure coefficients K_1 and K_2.

5.2.4 Instrumentation

For Shuangjiangkou Cavern Group, the displacements in the surrounding rock masses are the main concerns for researchers and engineers, and are also the basis for reinforcement design. Moreover, displacement is the most important physical quantity to verify the numerical simulation and back analysis results (Sakurai 1997; Sitharam and Latha 2002; Sakurai et al. 2003; Li et al. 2005c; Zhu et al. 2008b). In practical engineering projects, field investigation is limited by: a) safety concerns that prohibit access to underground openings with potential collapse; b) expense of the instrumentation; c) most geotechnical instruments are installed after excavation and thus are not capable of capturing the whole deformation process during excavation. However, in physical modeling, it is feasible to acquire the whole process of rock deformation.

In the model tests, three measuring techniques, including the FBG sensing bars, the multi-point extensometers, and the digital photogrammetric system, were employed to monitor the displacements of the model during excavation and overloading in real time, as shown in Figure 5.4.

(1) FBG sensing bars

Three FBG sensing bars for 2-D measurement were utilized for measuring displacements in the surrounding rock masses in the vicinity of the side walls of the power house and the surge chamber, as shown in Figure 5.2 and Figure 5.5. On each bar, there were ten FBG strain sensors glued on the bar surface in pairs.

After several trial tests, a two component silicon adhesive was selected as the bonding material between the model and the FBG sensing bars. When the construction of the physical model was completed, a reasonable amount of silicon adhesive was injected in three predefined monitoring holes. Three 1 m long FBG sensing bars were inserted into the holes immediately and smoothly. All the FBG strain sensors survived the installation procedures. The direction of the FBG sensors glued on each bar was kept perpendicular to the excavation direction. After 24-hour curing of silica gel, the bonding between the FBG sensing bars and the physical model was considered to satisfy the deformation compatibility condition.

As the FBG sensing bars passed through the caverns into the rock masses with considerable distance to the excavation locations, the boundary conditions at both ends can be assumed to be $\begin{cases} u_0 = v_0 = w_0 = 0 \\ \left(\dfrac{du}{dz}\right)_{x=0} = \left(\dfrac{dv}{dz}\right)_{x=0} = 0 \end{cases}$ and $\begin{cases} u_L = v_L = w_L = 0 \\ \left(\dfrac{du}{dz}\right)_{x=L} = \left(\dfrac{dv}{dz}\right)_{x=L} = 0 \end{cases}$. The displacements of the surrounding rock masses in the direction of excavation were neglected for simplicity. Therefore, combining Eq. (3.6) with Eq. (3.7) and conducting linear interpolation of strain distributions, the distribution of horizontal displacements can be calculated.

(2) Multi-point extensometers

In order to measure the displacements in the surrounding rock masses, a miniature multi-point extensometer (MPE) measurement system developed by Zhu et al. (2008) was utilized. The system consists of high-precision grating rulers, fine steel wires with hammers, plastic casings, anchor heads at the measurement points, and a steel reference frame, as shown in Figure 5.6. The anchor heads were fixed on the measurement points in the model. When displacements occurred, they were transferred to the grating rulers through steel wires.

Two monitoring sections were defined along the axial direction of the cavern group. For each section, three and two sets of MPEs were installed near to the power house and the surge chamber, respectively. There were totally fifteen measurement points for each section.

(3) Digital photogrammetric system

The close range photogrammetric technique for determining displacements and strains used in this study has recently applied to a number of geotechnical engineering problems (Fischer and Keating 2005; Lee and Bassett 2006). In the model tests, the digital photogrammetric system developed by Prof. Yuan-hai Li of China University of Mining and Technology was utilized. This system consists of digital single lens reflective cameras, 200 W ordinary incandescent lamps, a number of color marks and the digital image processing software PhotoInfo. Li et al. (2007) successfully adopted this system for convergence measurements on the periphery of tunneling model tests.

Two monitoring sections I-I and II-II were defined along the axial direction of the cavern group. During excavation of the cavern group, color marks were adhered in steps. For each monitoring section, there are thirteen convergence measurement points, including one on the crown of the power house, six on the side walls of the power house and another six on the side walls of the surge chamber. Figure 5.7 shows a photograph of the power house taken after the reinforcements were placed. The layout of the convergence measurement points is also shown in this figure.

5.3 TEST RESULTS AND ANALYSIS

During the whole procedure of model testing, the temperature inside the model was measured by an embedded FBG temperature sensor. The temperature readings were used for temperature compensation of the FBG strain sensors glued on the FBG sensing bars, as shown in Figure 5.8.

5.3.1 Test results during excavation

For the measurement points in the surrounding rock masses at the monitoring section I-I, the variation of the horizontal displacement with excavation steps are shown in Figures 5.9 to 5.12.

During excavation of the model, the surrounding rock masses were overall stable. No obvious crack or catastrophic deformation was observed at the peripheries of the caverns. The actual displacements occurring in the field can be estimated as the monitoring results multiplied by the similarity ratio. From field monitoring results, the maximum displacement of the cavern side wall at the project site is approximately 42 mm. The displacements in the surrounding rock masses and at the monitoring points on the side walls are relatively regular. The deformation and failure mechanism shown in the model tests provide valuable information for the excavation design of this project.

5.3.2 Test results during overloading

The displacements in the surrounding rock masses measured during the overloading test, together with the corresponding numerical results, are shown in Figures 5.13 to 5.15.

It can be seen that, with the increase of overburden depth, the displacements developed dramatically when the overburden depth increased from 800 m to 1000 m. According to the similarity ratio and the displacements in the side walls during overloading, the maximum relative displacement in the surrounding rock masses in the field reached about 36 cm from 600 m to 800 m in depth.

Typical visible cracking phenomena during overloading are shown in Figures 5.16. It is observed that, when the loading was raised to an equivalent overburden depth of 800 m, a small amount of fractured rock masses began to drop down from the crown of the power house and cavity cracks appeared on the side walls of the surge chamber. With the increase of overburden pressure, several cracks developed on the crown of the power house until large blocks collapsed. When the overburden depth reached 1000 m, small flakes fell down from the side walls of the power house. Significant collapse also took place on the crown and side walls of the surge chamber. When the equivalent overburden depth was between 1600 m and 1800 m, flake spalling in the side walls of the power house became much more significant. On the crown and side walls of the surge chamber, several blocks collapsed. Considering the fact that no rock bolts and pre-stressed cables were installed for the surge chamber in the model tests, it can be concluded that these two types of reinforcements play an important role in stabilizing the caverns.

5.4 COMPARISON BETWEEN NUMERICAL SIMULATION RESULTS

The numerical simulation was conducted by Zhu et al. (2009). In their simulation, a 3-D numerical model, with the same dimensions of the physical model was developed using the FLAC^{3D} software (Itasca 2002). The shotcrete layer and the surrounding rock masses are represented by 8-node isoparametric solid elements. The rock bolts are simulated by rock bolt elements with only axial stiffness taken into account. The model is composed of 39,798 nodes and 35,440 elements, as shown in Figure 5.17. The Drucker-Prager criterion is adopted and the physical and mechanical parameters are equal to those of the model material. The comparison between experimental and numerical results is shown in Figures 5.9 to 5.15. In general, the variation trends of displacements obtained from physical modeling and numerical simulations are in good agreement.

From Figure 5.9, it is found that in some of the excavation steps, there are significant differences between the experimental and numerical results. However, when the excavation activity completed, the ultimate displacements is similar. It can be assumed that the discrepancies are because of the deformation adjustments between the sensing bars and the surrounding rock masses. In Figure 5.12, larger displacements of the side walls were measured by the digital photogrammetric system. This phenomenon may be induced by the adverse disturbing of manual excavation activities

In the overloading stage, the displacements calculated by numerical simulation increase basically linearly. To interpret the differences between measured and calculated displacements shown in Figures 5.13-5.15, it should be noted that the numerical simulation is based on continuum method. However, the physical model is made of a kind of brittle material, and the number of micro cracks increased gradually when the overburden loads were extremely high. The micro cracks opened and developed with the increase of overloading, and eventually large splitting cracks occurred. The opening displacements existed in the surrounding rock masses accounts for a large portion of the total deformation. The similar phenomena and results were reported in large-scale underground cavern groups in other countries (Yoshida et al. 2004).

5.5 SUMMARY

In this chapter, the monitoring results of 3-D physical model tests of Shuangjiangkou Cavern Group are presented in order to investigate different phenomena during excavation and overloading, such as deformation patterns and failure mechanisms. Based on the analysis of the experimental results and the comparisons with the numerical results, the following conclusions are obtained:

(a) FBG sensing bars have been successfully utilized for measuring the small deformation on the surface and inside of the surrounding rock masses. High-precision miniature multi-point extensometers and the digital photogrammetric technology have been applied for measurement of deformation in the surrounding rock masses. Reliable and accurate results have been obtained for engineering design applications.

(b) It is found that, according to the experimental and numerical results, the surrounding rock masses of the underground excavation are stable in overall. The cracking phenomenon and failure process in the surrounding rock masses at increased overburden depths have been observed in the overloading tests. The research results can provide valuable guidance for constructing large underground caverns in China.

Table 5.1 Dimensions of the prototype and the model of Shuangjiangkou Cavern Group

Item	*H* (m)		*B* (m)		*L* (m)	
	Prototype	Model	Prototype	Model	Prototype	Model
Power house	63	0.420	29.3	0.195	198	0.500
Tansformer chamber	25	0.167	20.5	0.137	108.5	0.500
Tailrace surge chamber	73.6	0.491	19.8	0.132	120	0.500

Notes: *H* - height; *B* - width; *L* – length

Table 5.2 Physical and mechanical properties of the prototype and the model materials of Shuangjiangkou Cavern Group (average values)

Type	γ (kN/m^3)	*E* (GPa)	ν	σ_c (MPa)	*c* (MPa)	φ (^{o})
Prototype	26.0	30	0.2	80	2	40
Model	26.0	0.2	0.2	0.533	0.013	40

Notes: γ- density; *E*- deformation modulus; ν-Poisson's ratio; σ_c-compressive strength; *c*- cohesion; φ- friction angle

Table 5.3 Excavation sequence of Shuangjiangkou Cavern Group in the model tests

Step No.	Excavation location			
	I	II	III	IV
1	I_1	II_1	III_1	-
2	I_2	II_2	III_2	-
3	I_3	-	III_3	-
4	I_4	-	III_4	-
5	I_1	II_1	III_1	-
6	I_2	II_2	III_2	-
7	I_3	-	III_3	-
8	I_4	-	III_4	-
9	I_1	II_1	III_1	-
10	I_2	II_2	III_2	-
11	I_3	-	III_3	-
12	I_4	-	III_4	-
13	I_1	II_1	III_1	-
14	I_2	II_2	III_2	-
15	I_3	-	III_3	-
16	I_4	-	III_4	-
17	I_1	II_1	III_1	-
18	I_2	II_2	III_2	-
19	I_3	-	III_3	-
20	I_4	-	III_4	-
21	-	-	-	IV

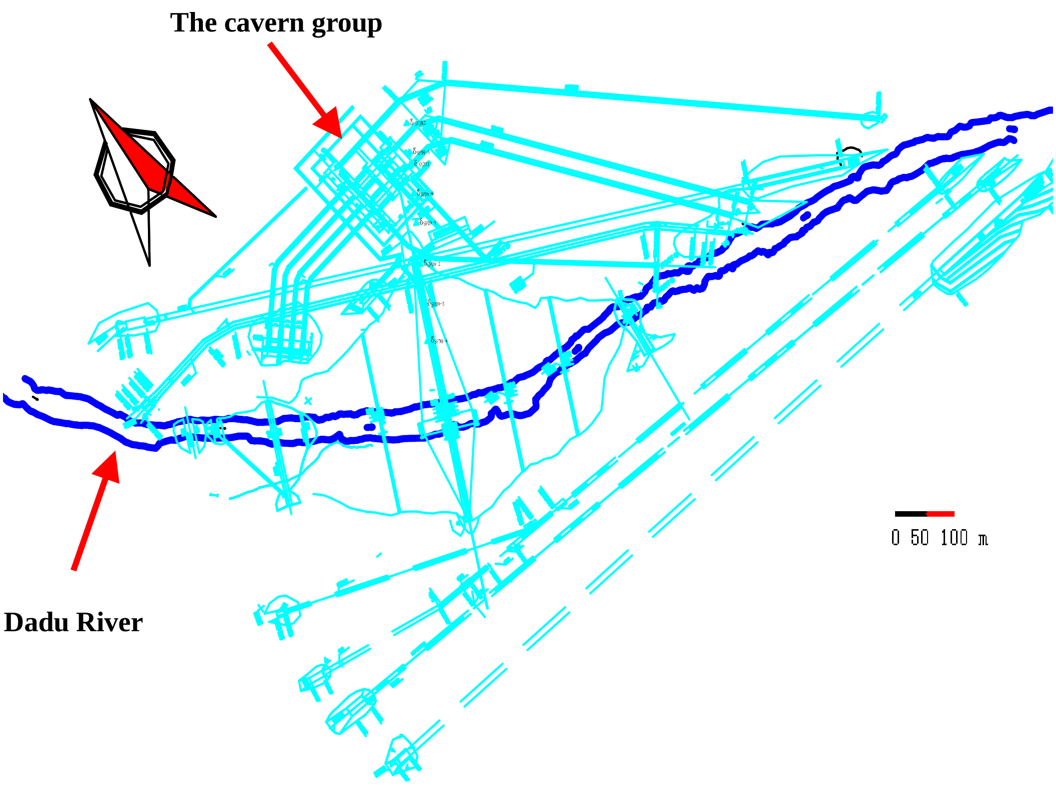

Figure 5.1 Design layout plan of Shuangjiangkou Hydropower Station

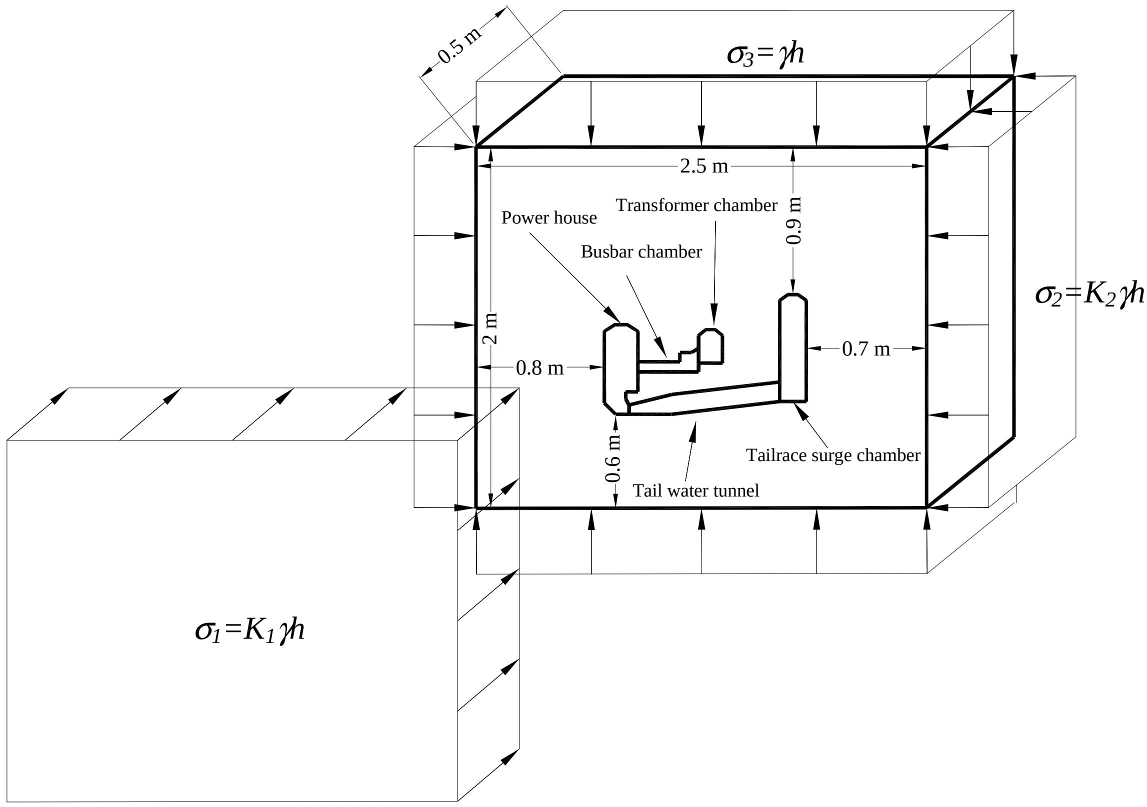

Figure 5.2 Dimensions of the physical model of Shuangjiangkou Cavern Group

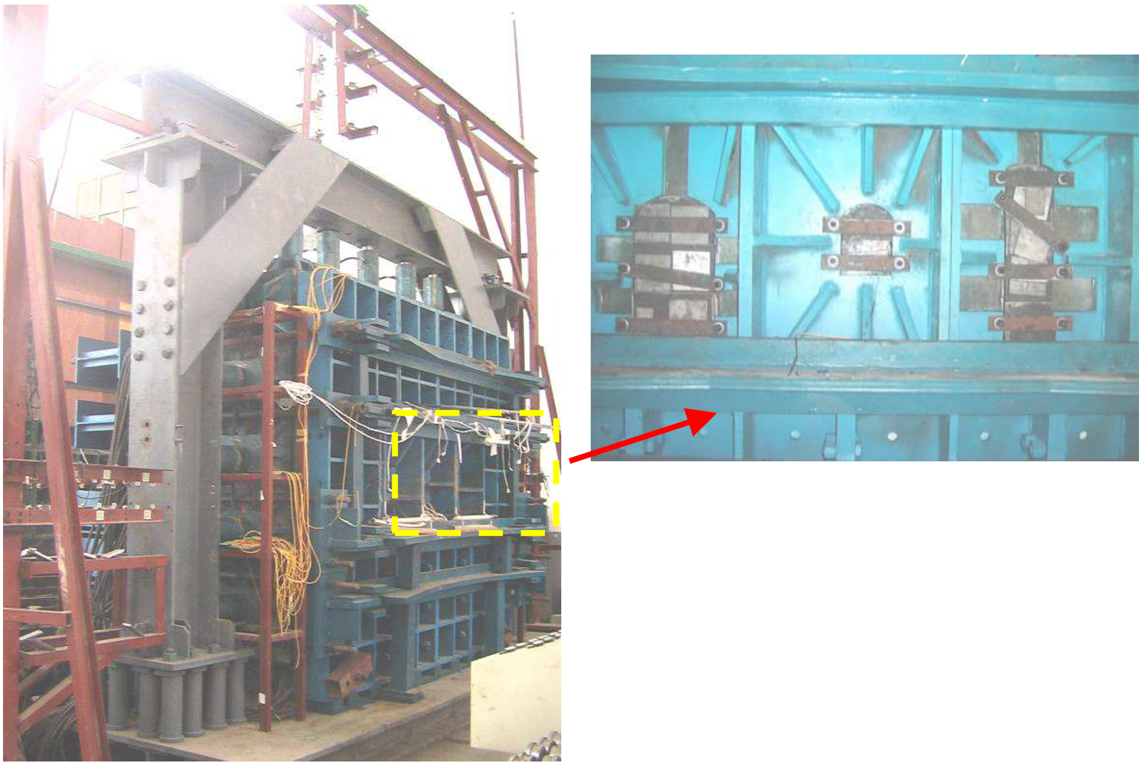

Figure 5.3 Photographs of the structural steel frame for conducting model tests

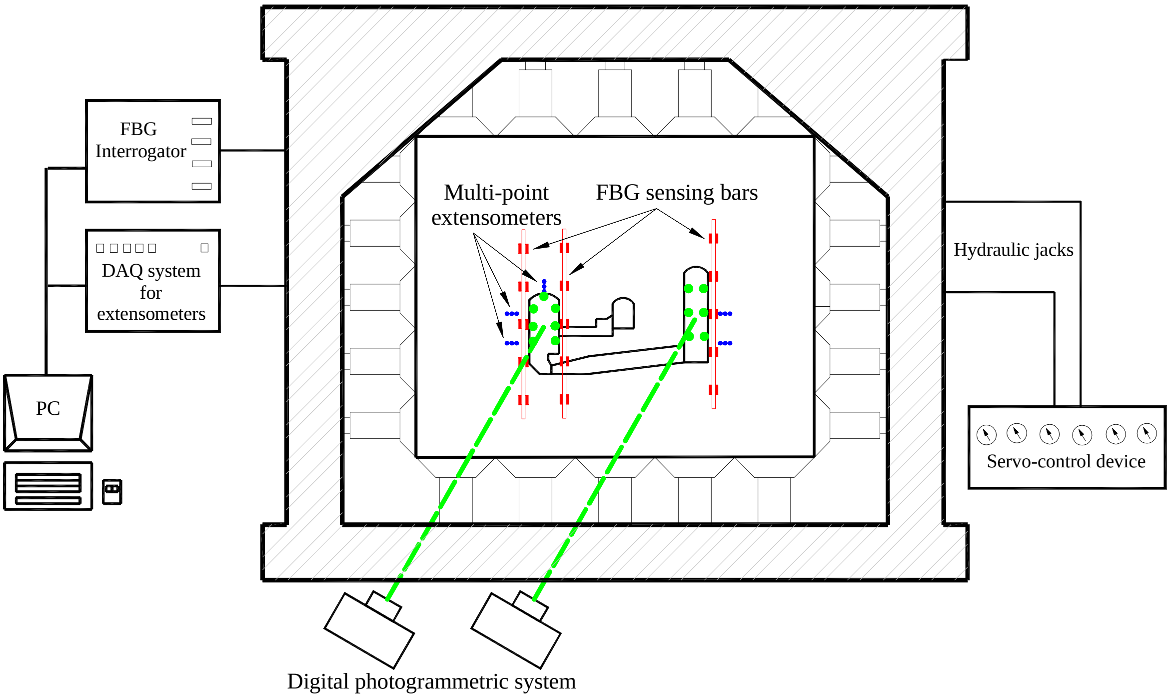

Figure 5.4 Set-up and instrumentation of the model tests

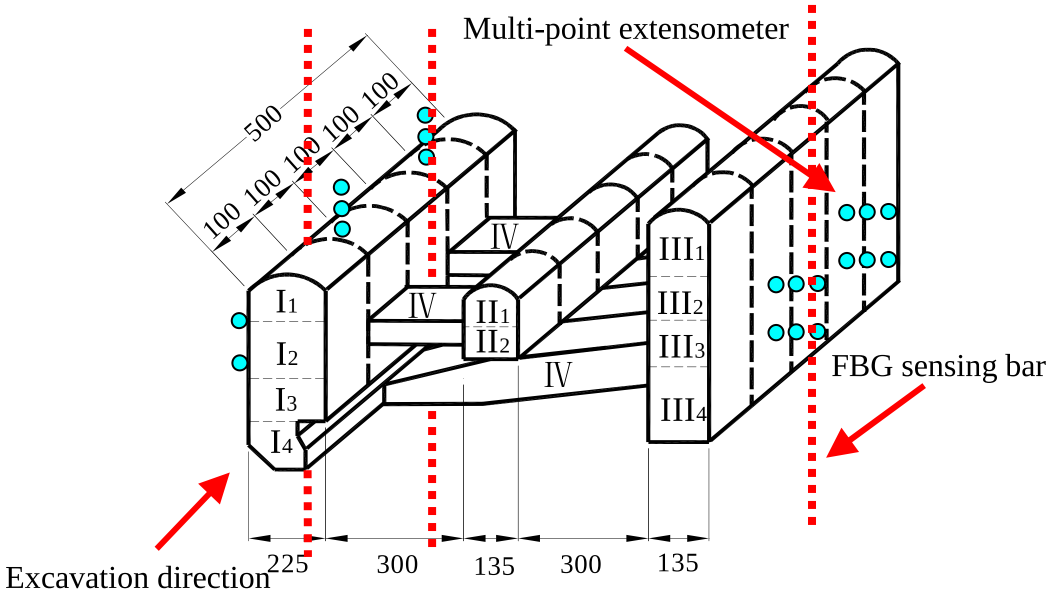

Figure 5.5 Excavation sequence of the cavern group model (unit: mm)

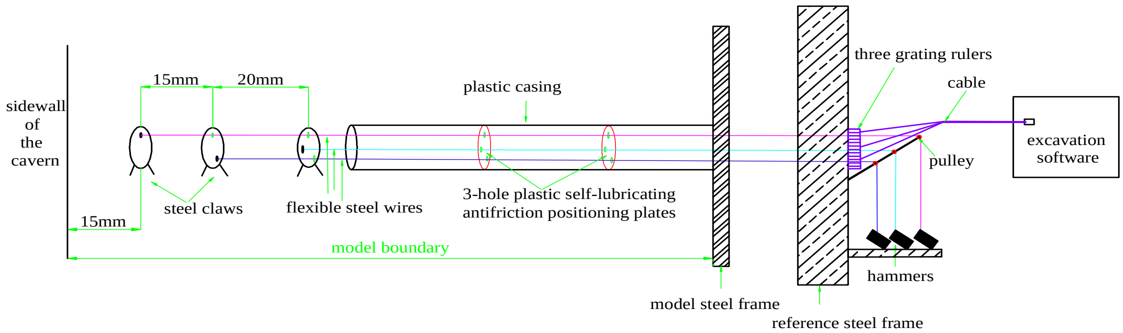

Figure 5.6 Working principle of the multi-point extensometer measurement system (after Zhu et al. 2009)

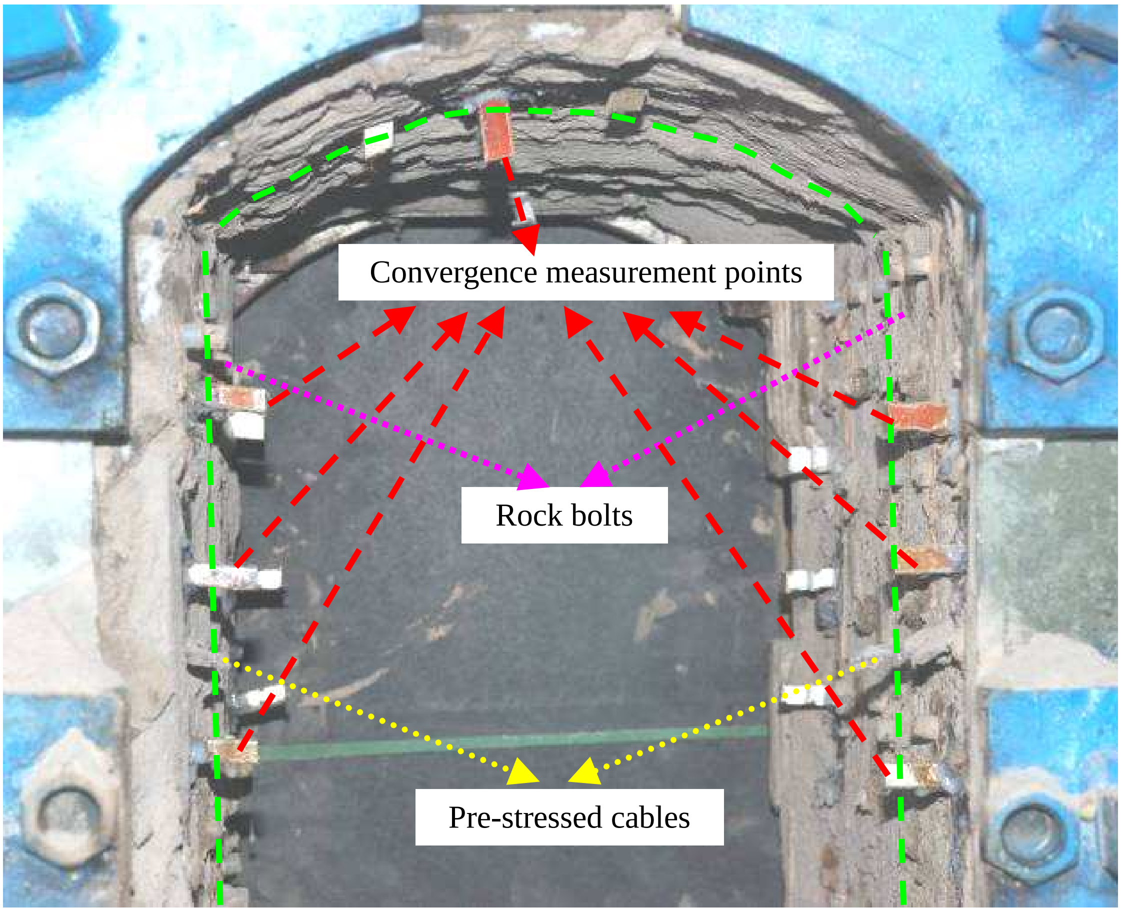

Figure 5.7 Layout of the convergence measurement points, the pre-stressed cables, and the rock bolts of the power house (monitoring section I-I)

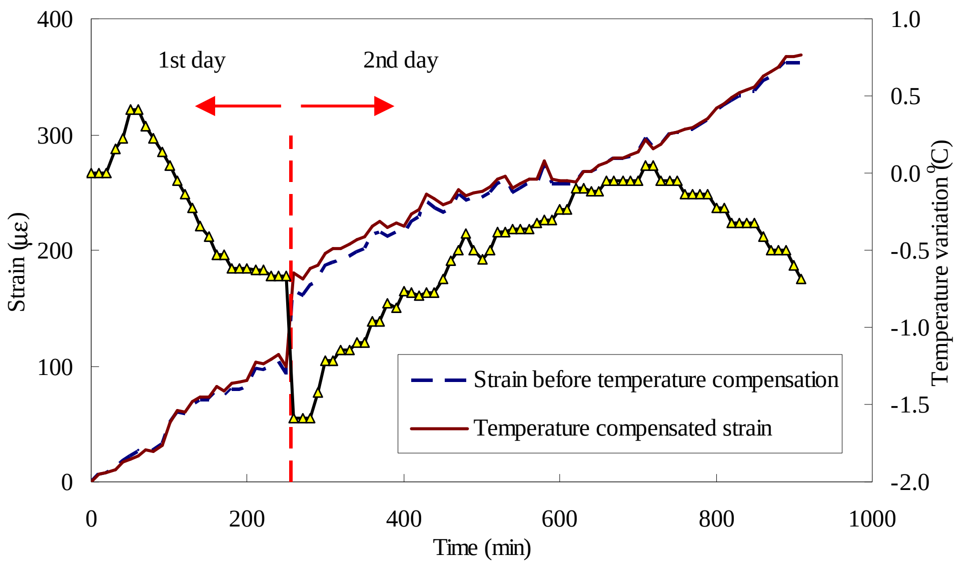

Figure 5.8 Temperature compensation of the measurements of FBG strain sensor No. 4

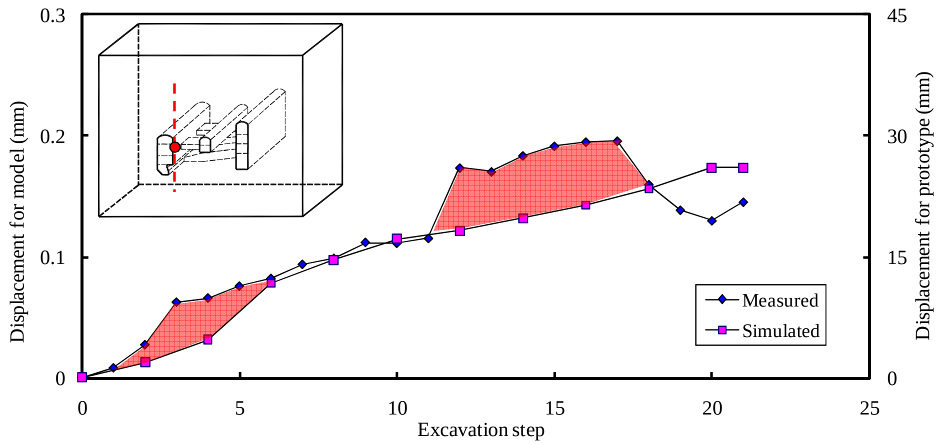

(a) The upstream side wall of the power house

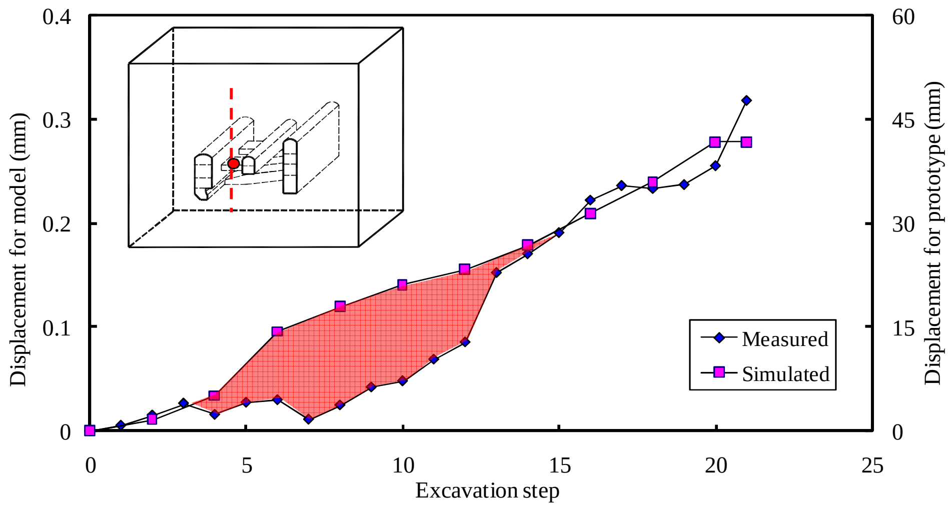

(b) The downstream side wall of the power house

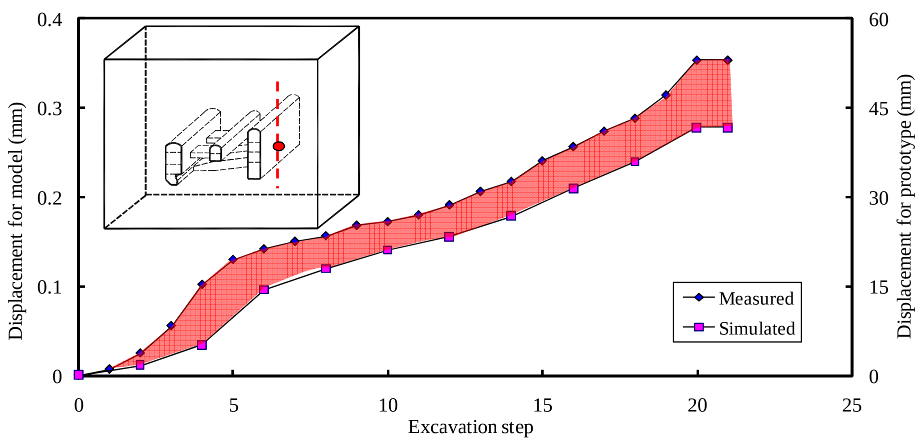

(c) The downstream side wall of the surge chamber

Figure 5.9 Comparison of simulated and measured displacements using the FBG sensing bars

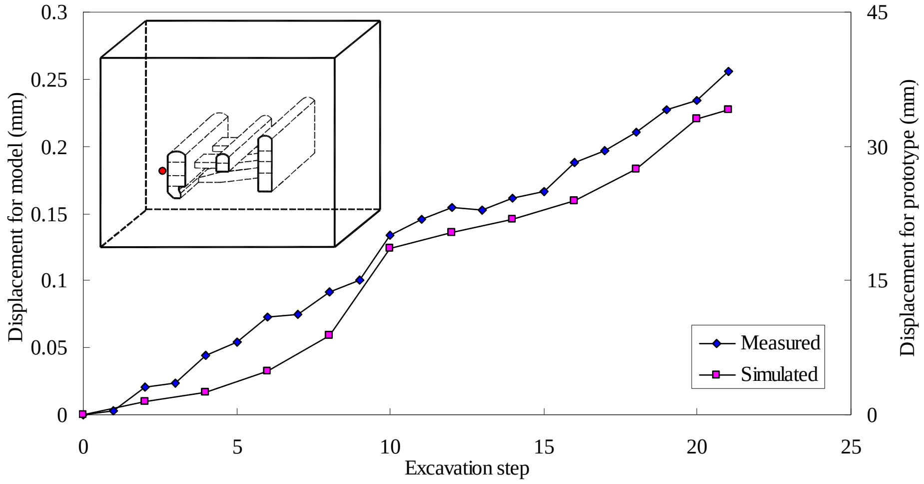

Figure 5.10 Comparison of simulated and measured displacements near the upstream side wall of the power house using multi-point extensometer No. 4

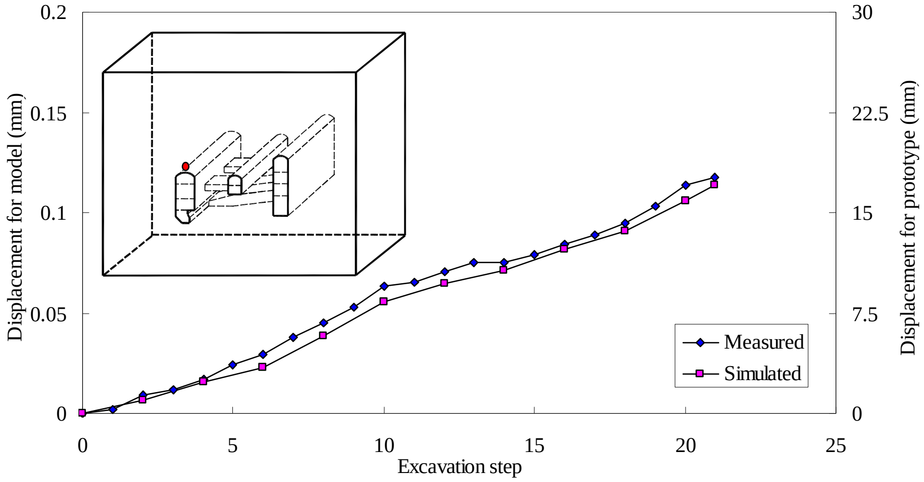

Figure 5.11 Comparison of simulated and measured displacements convergence of the arch crown of the power house using multi-point extensometer No. 8

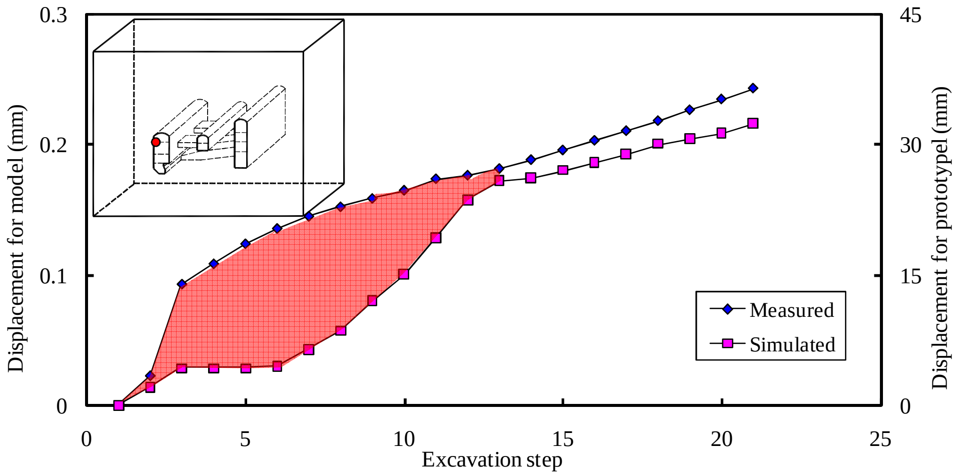

(a) Monitoring point No. 1 (near the upstream side wall of the power house)

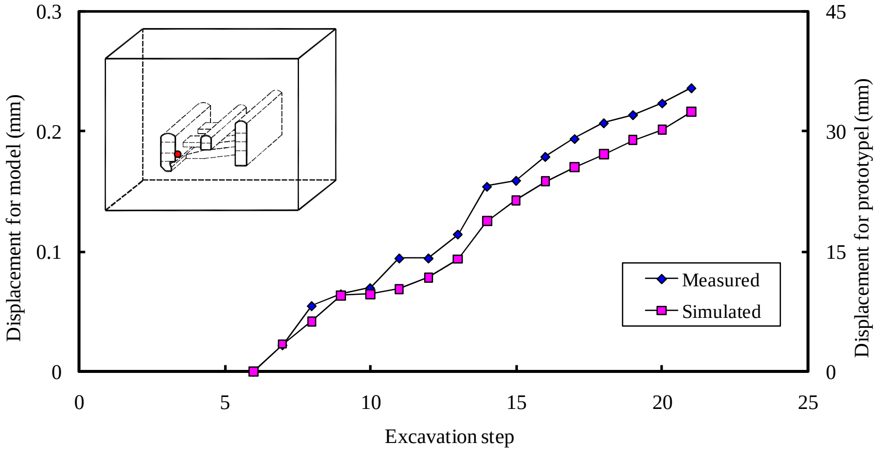

(b) Monitoring point No. 5 (near the downstream side wall of the power house)

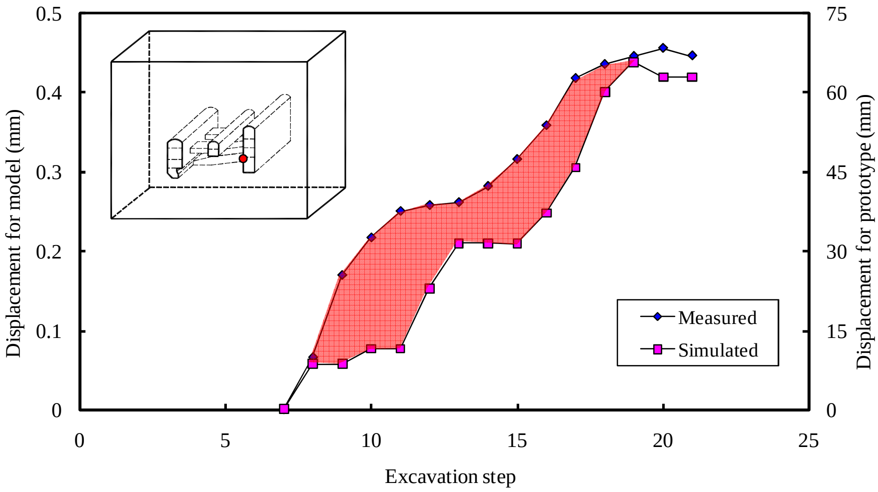

(c) Monitoring point No. 10 (near the upstream side wall of the surge chamber)

Figure 5.12 Comparison of simulated and measured displacements using the digital photogrammetric system

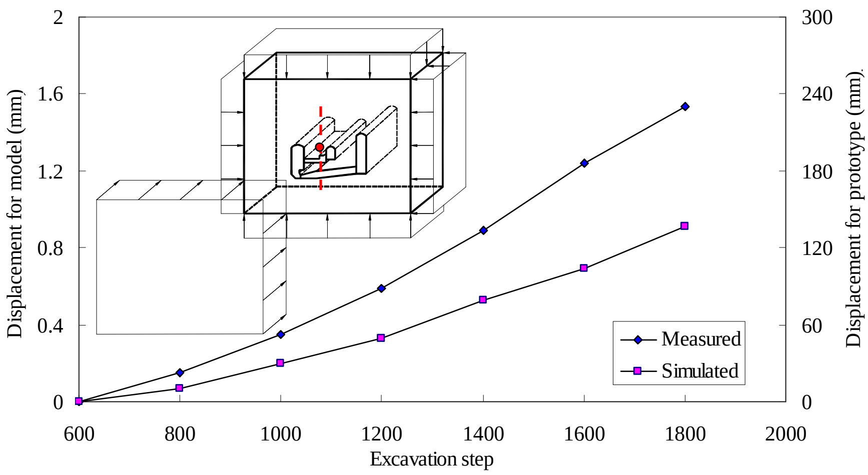

Figure 5.13 Comparison of simulated and measured displacements near the downstream side wall of the power house using the FBG sensing bar

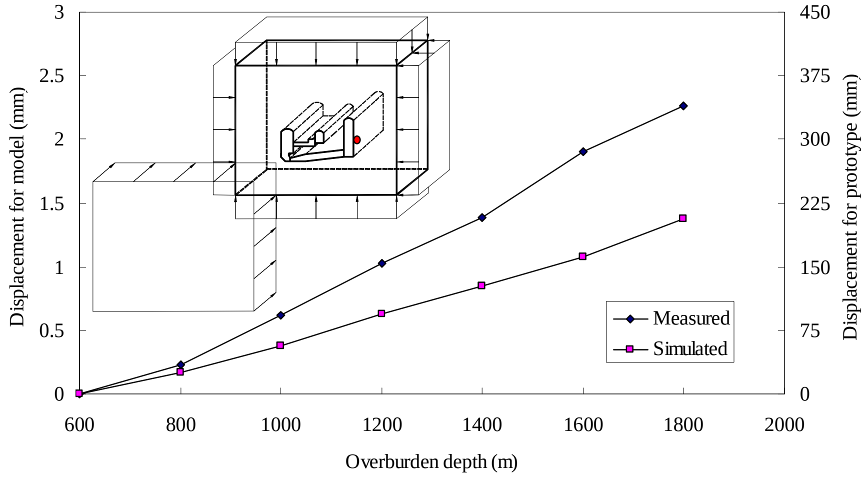

Figure 5.14 Comparison of simulated and measured displacements near the downstream side wall of the surge chamber using multi-point extensometer No. 14

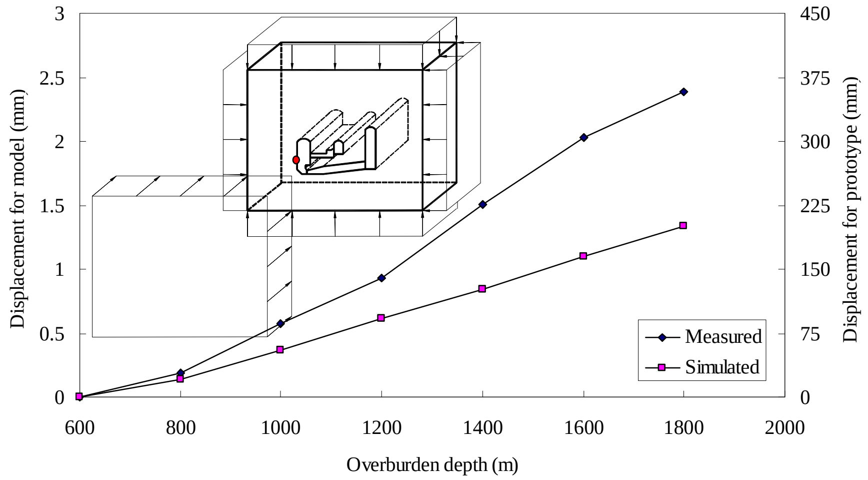

Figure 5.15 Comparison of simulated and measured displacements near the upstream side wall of the power house using the digital photogrammetric system (measurement point No. 6)

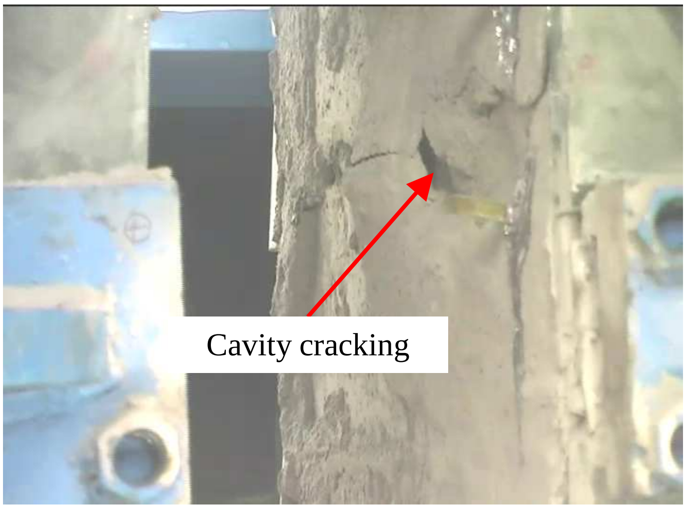

(a) Downstream side wall of the surge chamber under an overburden depth of 1000 m

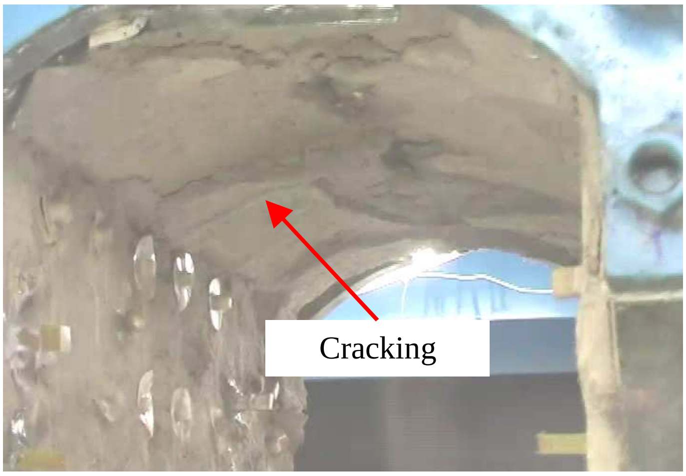

(b) Crown of the power house under an overburden depth of 1400 m

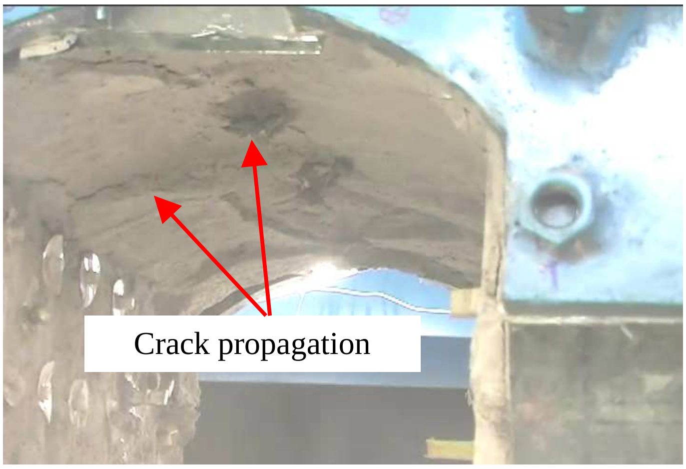

(c) Crown of the power house under an overburden depth of 1600 m

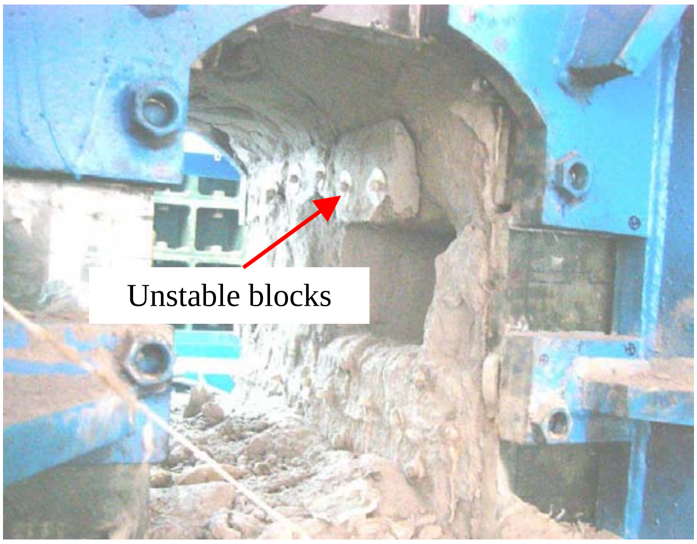

(d) Downstream side wall of the power house under an overburden depth of 1800 m

Figure 5.16 Photographs of the failure pattern of the cavern group model in overloading condition

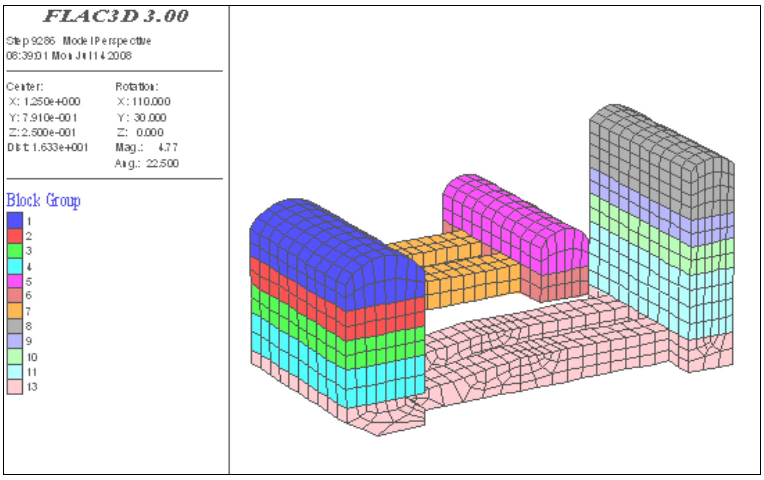

Figure 5.17 Finite difference model of Shuangjiangkou Cavern Group (after Zhu et al. 2009)

CHAPTER 6:

FIBER OPTIC MONITORING AND PERFORMANCE EVALUATION IN THE MODEL TEST OF WUDU DAM

6.1 INTRODUCTION

In the past two decades, a number of massive concrete gravity dams have been or are being constructed in China, such as Longtan Dam (the maximum height H=216.5m) (Zhang et al. 2002), Three-Gorges Dam (H=185m) (Liu et al. 2003a, 2003b; Li et al. 2005b), Xiangjiaba Dam (H=161m) (Zhou et al. 2008), Jiangya Dam (H=131m) (Yan et al. 2004), Baise Dam (H=130m) (Xu et al. 2007), and Baozhusi Dam (H=131m) (Chen et al. 2004b, 2008). In harsh conditions such as flooding and earthquake, dam safety becomes an issue of great concern.

The gravity dam is a high order statically indeterminate structure and the dam stability relies mainly on its self-weight. The field performance of the dam is affected by its surrounding environments, including hydrological and meteorological factors, reservoir rim, and potential seismic loading (ASCE Task Committee on Instrumentation and Monitoring Dam Performance 2000). Gravity dams are always required to be in the elastic state under working conditions and have adequate resistance to failure. The failure modes of concrete gravity dams can be grouped into three categories, namely overturning, cracking, and sliding (U.S. Army Corps of Engineers 1995). Given appropriate structural design, the overturning failure can be avoided. The cracking of concrete is a critical factor affecting the dam stability. This phenomenon has been extensively examined (Donlon and Hall 1991; Bhattacharjee and Léger 1993, 1994; Tinawi and Guizani 1994; Plizzari et al. 1995; Mao and Taylor 1997; Ghaemina and Ghobarah 1999; Barpi et al. 1999; Harris et al. 2000; Tinawi et al.2000; Javanmardi et al. 2005; Ftima and Léger 2006; Zhu and Pekau 2007) and various reinforcement techniques have been successfully utilized (Morin et al. 2002). The sliding can occur at the concrete-rock interface or within the rock foundation. Chopra and Zhang (1991) studied earthquake-induced sliding of a gravity dam monolith supported without bond on a horizontal, planar surface of rock and examined the estimation methods of sliding displacements. Mir and Taylor (1996) studied the base sliding response of rigid concrete gravity dams subjected to dynamic loading. Rochon-Cyr and Léger (2009) conducted shake table tests to study the sliding response of a gravity dam model including water uplift pressure. For dams on jointed and decomposed rock masses, or even soils with low shear strength and high compressibility, the failure of the dam-foundation system frequently occurred within the foundation instead of the concrete-rock interface (Barpi et al. 1999; Liu et al. 2003a, 2003b; Martt et al. 2005; Ren et al. 2008; Zhou et al. 2008). The deformation process and sliding mechanism of this type of failure have not been well defined in previous studies (Ruggeri 2001).

It has been caused wide attention in the field of dam engineering to evaluate the performance and safety of a high gravity dam under overloading condition (Ghaemina and Ghobarah 1998; Liu et al. 2003a, 2003b; Chen et al. 2004b, 2008). If the horizontal component of hydrostatic pressure on the upstream face is increased to a certain magnitude above the design value, a limiting state of the dam stability can be achieved, where the carrying capacity of the dam is fully exhausted. This makes it possible to investigate the dam failure behavior under excessive loading, considering the uncertainties of the upstream hydrostatic load. In this regard, the factor of safety of a gravity dam can be defined as the ratio between the maximum external load inducing the start of sliding instability and the upstream hydrostatic design load. There are mainly three approaches to study the overloaded dam performance, namely, limit equilibrium method, physical modeling, and numerical simulation. The limit-equilibrium method has difficult to analyze complex dam-foundation systems. Considerations regarding displacements are excluded in this method. In previous researches of numerical analysis of dams, the simulation results are highly dependent on the identification of geological conditions and constitutive models. Physical model testing can demonstrate the dam performance under any loading condition that experimental technologies can realize and be used to validate the numerical results. The current design specifications in China recommend using physical modeling for huge dams, especially those with complicated foundation condition (The State Economic and Trade Commission 1999; Ministry of Water Resources 2005). However, some difficulties have been encountered, such as simulating actual hydraulic and geological conditions, and obtaining accurate and reliable monitoring results (Plizzari et al. 1995; Ghobarah and Ghaemian 1998; Liu et al. 2003a).

This study, which is co-investigated with Prof. Lin Zhang of Sichuan University, concerns the performance of Wudu Dam under progressive overloading, with a particular focus on the sliding failure mechanism within the rock foundation. This issue was studied through a laboratory physical model test conducted in School of Water Resources and Hydropower Engineering, Sichuan University, with improved measuring technique for internal displacement using the FBG sensing bars. The author was in charge of a) the instrumentation work of the model test, b) analysis of the monitoring results, and c) numerical simulation of the model test.

6.2 PHYSICAL MODELING OF WUDU DAM

6.2.1 Project background

Recently Wudu Dam, a roller-compacted concrete (RCC) gravity dam located in Jiangyou, Sichuan Province of China, is being constructed as one of the main features of Wudu Reservoir (Figure 6.1). Wudu Reservoir is used for the storage of surplus winter flow in the Fu River to provide irrigation and power to citizens and has a total storage capacity of 5.72×10^8 m^3. Besides the concrete gravity dam and the industrial buildings behind it, a hydropower station with a total electric generating capacity of 150 MW is also located here.

Wudu Reservoir is located at the northern section of the tectonic belt of Longmen Shan bruchfalten zone. The rock masses, on which the dam is being built, are of the Devonian system and have very low deformation moduli. Moreover, the geological conditions in this area is very complex, with sub-layer faults and inter-layer fracture zones, forming a combination of a number of natural sliding planes, which further weakens the integrity of the rock foundation seriously. Wudu Dam has a crest length of 720m and a maximum height of 119 m. Potential dam failure during flood season or earthquake poses a severe threat to public safety.

6.2.2 Test set-up and procedure

In order to study the deformation mechanism of the dam structure under hydraulic pressure and determine the overloading factor of safety, a 1:150 scaled 2-D model dam was constructed in School of Water Resources and Hydropower Engineering, Sichuan University. The model was a simulation of Section No.19 of the prototype dam, with a height of 75 m and a downstream slope of 0.8. The geometry of the model dam is shown in Figure 6.2. The scales chosen for this model dam are shown in Table 6.1.

(1) Model construction

Table 6.2 summarizes the material properties of the prototype and the model dam. In China, roller compacted concrete (RCC) with a water/cement ratio of 0.45-0.60 and a compressive strength no less than 10-20 MPa for 90 d is widely used for constructing gravity dams (Ministry of Water Resources 2005). For physical models of dams, gypsum, plaster, barite, cement, bentonite, etc. are commonly used as similarity materials of concrete (Tinawi et al. 2000; Harris et al. 2000; Liu et al. 2003a). In this study, the material chosen for simulating the concrete dam body was a mixture of gypsum powder, barite powder, and water. After a series of laboratory tests, the optimal mixture ratio was obtained. The material properties shown in Table 6.2 satisfy all the similitude requirements of both deformation modulus and strength between the model and the prototype. In laboratory tests, this material was proved to have brittle failure characteristics like concrete (Chen et al. 2006).

Ten layers of prefabricated bricks were constructed to form a regular-jointed rock foundation. The bricks were made of barite powder (as the cementitious material), engine oil, and fusible polymer materials (as the admixture). The model material has scaled parameter values for density, modulus and shear strength and thus can simulate some basic characteristics of the prototype material. A Y32-50 hydraulic press machine was used to fabricate the artificial bricks with a size of 100 mm×100 mm×50 mm (length×width×height). Tight contacts were provided between the boundary of the dam foundation and the steel test frame during model construction. In engineering practice, special attentions are paid to the concrete-rock interface of a gravity dam and pressure grouting is frequently used to reinforce the bonding at this interface. Regarding this, the interface between the model dam and the rock foundation was glued by epoxy resin to ensure ideal bonding.

(2) Test conditions and procedures

During testing, a progressive overloading that simulated the increase of hydrostatic water pressure was loaded on upstream face of the model dam. The seepage pressure and the uplift pressure were neglected in this test for simplicity. The hydrostatic pressure was equalized by two servo-controlled hydraulic jacks arranged on the dam body. The lateral loading was applied as an overloading factor (OF) which is the ratio of the applied loading over the normal hydraulic loading on the model dam, i.e.

$$\mathrm{OF} = \frac{\frac{1}{2}\gamma H^2}{\frac{1}{2}\gamma_0 H^2} = \frac{\gamma}{\gamma_0} \tag{6.1}$$

where γ_0 is the actual density of water, γ is the assumed density of water in overloading condition, and H is the dam height. The safety degree of the dam structure can be evaluated in terms of overloading factors (Alonso et al. 1996). The entire process of dams developing from elastic state to failure state can be characterized by two overloading factors of safety, i.e. K_1 for initial cracking and K_2 for ultimate failure.

At the beginning of the test, half of the normal hydrostatic load, that is, an overloading factor of 0.5 was applied on the model dam. After the readings of all the instruments became stable, the lateral load was increased gradually with the overloading factors of 0.8, 1.0, 1.2, 1.4, 1.6, … until 7.4 when the dam-foundation system was completely destroyed.

6.2.3 Instrumentation

Three types of instruments were installed on the dam-foundation system, in order to investigate the deformation mechanism of the model dam under overloading and determine the factors of safety. The instrumentation details are shown in Figures 6.2 to 6.4.

(1) For the dam body, a tension zone indicates the formation of cracks in the concrete while a compression zone may result in crushing of concrete. To measure the magnitudes and directions of the principal stresses, a total of twelve electrical strain rosettes were installed on the dam body. They were connected to a data logger with full bridge configuration for data acquisition.

(2) For the measurement of surface displacements of the dam body, three horizontal and four vertical linear variable displacement transformers (LVDTs) were installed. The other nine LVDTs were installed below the dam toe for horizontal displacements measurement of the rock foundation. Two pairs of LVDTs were installed on the ground surface and kept a distance from the dam toe for the estimation of deformation influential range. A displacement digital display instrument was used to take their measurement.

(3) To monitor internal displacements induced by the overloading, two FBG sensing bars were installed inside the model dam. The FBG sensing bars used in this test had a diameter of 10 mm and a length of 500 mm. Each bar had ten FBG sensors and the sensor spacing was 100 mm.

Prior to testing, one of the FBG sensing bars was embedded in the dam body to monitor the internal deflection (horizontal displacement) and vertical relative displacement distribution from the dam top to the ground surface. The other FBG sensing bar was embedded in the downstream rock foundation near the dam toe, for monitoring ground settlements and horizontal displacement profiles in the dam foundation. To facilitate the installation, two predefined holes of 14 mm diameter and 500 mm depth were prepared during model construction. The gap between the bars and the holes was grouted with quick-set silicon glue. An optical sensing interrogator was used to record the Bragg wavelengths of the FBG sensing bars in real time.

6.3 TEST RESULTS AND ANALYSIS

6.3.1 Observations

During the overloading test, the readings of FBG sensors and displacement gauges increased simultaneously with the increase of loading. From zero to normal loading condition, no visible crack of the model dam was detected. The first crack appeared under the dam heel when the lateral loading was increased to an overloading factor of 3.0. This indicated that the shear resistance of the foundation at this location could not sustain the lateral loading any more. Because the dam foundation had regular mortar joints, the main horizontal crack trajectory was found between the first and second brick layers. When the overloading factor was raised to 4.0, crack propagation within the dam foundation became significant and the main vertical cracks at the dam heel developed quickly, showing that the dam foundation gradually lost its bearing capacity. Partial crush zone was seen at the dam toe, where the dam was subjected to compression-shear loading. When loading continued to increase, more and more horizontal cracks appeared in the foundation. When the overloading factor reached 7.4, the main horizontal crack completely formed at the shallow layer and the width of the main tension crack below the dam heel has a maximum value of about 6 mm (Figure 6.5). It was seen that at this moment, the deformation of the dam was mainly due to the horizontal shear sliding of the foundation. No visible damage of the dam body was detected during the whole process of overloading.

From the above observation, the failure of the dam-foundation system was caused by the sliding within the rock foundation. The overloading factors of safety K_1 and K_2 can be estimated to be around 3 and 4, respectively. The failure mode illustrated that the jointed rock foundation below the dam heel and toe were two weak locations and should be given adequate attention in the process of dam design and construction.

6.3.2 Performance of the dam body

(1) Surface displacements

The surface displacements of the dam body measured by seven LVDTs are shown in Figure 6.6. The results revealed a rotation tendency at the dam toe due to the increased upstream pressure. When the overloading factor was between 0 and 1, the overloading factor-displacement curves were approximately linear, indicating an elastic behavior of the dam-foundation system at this stage. Under the normal loading condition, the maximum horizontal and vertical displacements occurred at the dam crest and had the same value of 0.02 mm (3 mm for prototype). When the overloading factor reached 3.0, abrupt increases of displacement rates were found. The corresponding horizontal and vertical displacements at the dam crest were 0.49 mm and 0.09 mm (73.5 mm and 13.5 mm for prototype). When the lateral loading increased to an overloading factor of 4.0, another turning point of the displacement curves appeared. The measured horizontal displacements developed quickly and reached over 6 mm (900 mm for prototype) at an overloading factor of 5.8. At this stage, the displacements were mainly the horizontal rigid body motion (translation), which was due to the sliding within the rock foundation. This phenomenon is similar to the centrifuge modeling results of unnotched specimens done by Plizzari et al. (1995).

From the quantitative tendencies of the displacements shown in Figure 6.7, the cracking overloading factor of safety K_1 and failure factor of safety K_2 can be determined as 3.0 and 4.0 respectively, which is quite consistent with the estimation from observations.

(2) Internal displacements

The displacements of the dam body monitored by the FBG sensing bar are shown in Figure 6.8. The results reveal that the deformation was mainly the deflection of dam body in the horizontal direction and the maximum displacement occurred at the dam top. At the same time, the upstream dam body was subjected to slight tension at the vertical direction. During the whole process of overloading, the dam body was shown to behave elastically. Under the normal loading condition (OF=1), the maximum horizontal and vertical (relative) displacements inside the dam body near the upstream face were 0.010 mm and 0.001 mm (1.5 mm and 0.15 mm for prototype). At the failure point (OF=4), the horizontal and vertical displacements reached 0.337 mm and 0.004 mm (50.6 mm and 0.6 mm for prototype). The magnitudes of the displacements were considerably small and didn't reflect any stability problem of the dam-foundation system.

(3) Strains and stresses of the dam body

From the strain monitoring results shown in Figure 6.9, the strains gradually increased with the increase of lateral loading and a strain concentration was located at the dam heel. For most of the strain rosettes, the overloading factor-strain curves showed approximately linear relationships and the magnitudes of tensile strains were very small. High compressive strains dominated the dam toe but did not exceed the strain limit of the model material during the whole overloading process.

However, the measured strain in the 45^o direction at the dam toe demonstrated an abnormal overturning point at an overloading factor of 3.8. This can be considered as a signal that the dam toe turned from compression to tension, which was caused by stress redistribution within the rock foundation. The tensile strain at this point suddenly jumped to over 800 με at an overloading factor of 6.2.

The magnitudes and the directions of the principal stress can be determined by (Khan and Wang 2001)

$$\sigma_{1,2} = \frac{E}{1-\nu}\frac{\varepsilon_0+\varepsilon_{90}}{2} \pm \frac{1}{2}\frac{E}{1+\nu}\sqrt{\left(\varepsilon_0-\varepsilon_{90}\right)^2+\left(2\varepsilon_{45}-\varepsilon_0-\varepsilon_{90}\right)^2} \qquad (6.2)$$

$$\tan 2\alpha = \frac{2\varepsilon_{45}-\varepsilon_0-\varepsilon_{90}}{\varepsilon_0-\varepsilon_{90}} \qquad (6.3)$$

where E and ν are the Young's modulus and Poisson's ratio; ε_0, ε_{45}, and ε_{90} are the strains in the 0^o, 45^o and 90^o directions; $\sigma_{1,2}$ are the first and second principal stresses; α is the angle between the first principal stress and the 0^o direction.

The principle stress distributions on the dam body in Figure 6.11 show that the internal force of the dam system can automatically adjust under the external loading. Before the occurrence of sliding failure, the dam body behaved elastically without crushing or cracking. Because the dam-foundation interface was the essential component that transferred the external overloading to the dam foundation, accumulated strains at this interface were found as expected. The transferred high stresses led to crush failure below the ground surface.

6.3.3 Performance of the rock foundation

(1) Surface displacements

The surface displacements of the rock foundation measured by LVDTs are shown in Figure 6.12. The horizontal displacement curves measured by LVDT No. 12 and 17 agreed well with the dam body motion shown in Figure 6.5(a). Relatively small horizontal displacements were found at the lower part of the rock foundation. The displacements at the ground surface indicated that before the cracking of foundation, the deformation was only localized around the concrete-rock interface. Under the normal loading condition, the maximum horizontal and vertical displacements of the foundation are both 0.02 mm (3 mm for prototype). As soon as sliding of foundation occurred, the region of deformation spread dramatically, especially at the ground surface.

(2) Internal displacements

The horizontal and vertical displacements within the foundation under increased overloading forces are shown in Figure 6.12. The maximum horizontal and vertical (relative) displacements occurred 50 mm below the dam toe. Under the normal loading condition (OF=1), the maximum horizontal and vertical (relative) displacements were 0.046 mm and 0.003 mm (6.9 mm and 4.5 mm for prototype). The vertical displacements demonstrated highly nonlinear behavior. The results show that the rock foundation had subsidence below the dam toe, indicating that this location was subjected to strain concentration. However, there was an obvious turning point of the settlement-overloading curve at OF=4. This can be explained by the fact that the crack penetration resulted in dissipation of energy and therefore slowed down the settlement rates. At this stage, the horizontal and vertical displacements reached 1.313 mm and 0.074 mm (197.0 mm and 11.1 mm for prototype).

From the horizontal displacements shown in Figure 6.13(a), the cracking overloading factor of safety K_1 and failure factor of safety K_2 can be also identified to be 3.0 and

4.0 respectively. However, the settlement results in Figure 6.13(b) only indicate the ultimate failure of the dam structure.

Figure 6.14 demonstrates the horizontal displacement-depth relationship below the dam toe. At the beginning, the sliding of the rock foundation was seen to be limited to the shallow layer. With the increase of overloading, the ground below the dam was found to slide and shear cracks gradually formed and developed in the horizontal and vertical directions.

(3) Crack propagation and failure pattern

The crack propagation pattern was recorded by a digital camera during overloading. The photographs showed that the cracking was initiated at the base of the upstream side of the dam. During the formation of cracks in the foundation, the strains of the dam body did not undergo any sudden changes. As Ghaemina and Ghobarah (1998) stated, most of the energy input due to the increase of hydrostatic loading is dissipated by increased crack width at the heel where the crack was initiated. The ultimate failure pattern is shown in Figure 6.5. The visible cracks were located between the joints of the top four layers of bricks. The yield zone can be simplified as a triangle. The increase of overloading was accompanied by a corresponding increase of the height and the vertex angle once the first crack was induced.

6.3.4 Performance evaluation of the FBG sensing bar for internal displacement measurements

Because the surface-mounted LVDTs below the dam toe were located close to the embedded FBG sensing bar, their monitoring results can be used to check the reliability of the FBG sensing bar. Figure 6.15 is the comparison of horizontal displacements from the FBG sensing bar and from the corresponding LVDTs at 50 mm depth of the foundation. It is seen that their results fit well with each other in general. However, at the beginning, the FBG sensing bar measured a slight larger displacement than the LVDTs. Afterward, the discrepancies between the FBG sensing bar and the LVDTs decreased to zero and then gradually became negative. There may be three reasons for these phenomena:

Firstly, the Young’s modulus of the bar material (approximately 50 MPa) is not perfectly compatible with that of the model material. Compared with other locations of the dam foundation, larger deformation might develop in the vicinity of the FBG sensing bar.

Secondly, when the loading increased and cracks developed in the dam foundation, the horizontal displacements occurred mainly at the brick joints, which was 50 mm depth below the ground surface. The uneven deformation increased the on-plane shearing of the FBG sensing bar significantly and thus the basic assumptions of Euler-Bernoulli beam theory were not well satisfied. The crack propagation within the dam foundation further increased the measuring errors.

Finally, the displacements of the model dam were transferred to the FBG sensing bars by grouted silicon glue. There might be certain losses of displacements, especially when stresses accumulated to a considerable magnitude at these interfaces.

6.4 NUMERICAL STUDY OF THE MODEL TEST

To further investigate the deformation and failure characteristics of Wudu Dam under overloading condition, numerical simulation using a finite element analysis software

ANSYS is conducted (ANSYS 2007).

6.4.1 Properties of elements used in the numerical model

The 8-node SOLID45 element shown in Figure 6.16 is used to model the dam body and the foundation. The element has plasticity, creep, swelling, stress stiffening, large deflection, and large strain capabilities. Each node has three available degrees of freedom: translation in the x direction, translation in the y direction, and translation in the z direction.

Because no crack or crush of the dam body occurred during the overloading test, the material for dam body is assumed to be homogeneous, isotropic materials characterized by elastic parameters. The Drunker-Pracker model is used to model the rock foundation.

For the nine layers of horizontal mortar joints existing in the dam foundation, a series of contact elements are used to model the friction behavior at these interfaces. These elements are TARGE170 and CONTA173, each having 5 degrees of freedom at each node: translation in the *x*, *y* and *z* directions, and rotations about the x and z axes, shown in Figures 6.17 and 6.18. The contact elements overlay the solid elements describing the boundary of a deformable body that is potentially in contact with a target surface, element TARGE170. Element CONTA173 is used to represent contact and sliding between the target surface, TARGE170, and a deformable surface.

The frictional behavior is further characterized by the creation of the relationship between the normal stress and the shear stress for the contact pair, by introducing the Mohr-Coulomb model, i.e.

$$\tau = c + \sigma_n \tan\varphi = c + \sigma_n f \qquad (6.7)$$

where τ is the frictional stress, c is the contact cohesion, which provides sliding resistance when the normal pressure is zero, f is the coefficient of friction for the material modeling the contact pair, σ_n is the normal pressure at the contact pair.

6.4.2 Meshing and boundary conditions

The mesh details of the numerical model are shown in Figure 6.19. The bottom boundary of the model was fixed (no movements) and for lateral boundaries, the displacements in the *x* direction are fixed to be zero. The initial stress fields were generated within the dam and foundation by self-weights. The actual pressure distribution simulating hydrostatic hydraulic pressure was applied along the upstream vertical boundary on the dam body. To simulate the overloading condition, the pressure was raised in stages. Computed displacements of the dam-foundation system were compared to the model test results.

6.4.3 Results and discussions

(1) Initial stress condition

To study the performance of a gravity structure under external loading, the initial stress condition must be considered. Figure 6.20 shows the initial stress fields of the model dam. It is seen that the foundation under the dam body is in a compressive condition. Below the dam heel, slight tensile stresses can be found.

(2) Normal loading condition (OF=1)

The numerical simulation results for normal loading condition are shown in Figures 6.21 to 6.23. No plastic zone is seen within the dam foundation and the sliding of the contact elements is restrained in the shallow foundation.

(3) Overloading condition (OF=3)

When the hydraulic pressure is increased to OF=3, the numerical results in Figures 6.24 to 6.27 indicate that the deformation of the foundation are extended to the deeper locations. The upstream side of the dam body becomes to in tensile condition. A plastic zone is seen within the dam foundation and the contacting conditions of the contact elements vary correspondently.

6.5 SUMMARY

In this chapter, the results of a physical model test of Wudu Dam are presented. The structural response has been captured by various sensors, including strain rosettes, LVDTs and FBG sensing bars. Based on the experimental investigation, conclusions are obtained as follows:

(1) It has been found that physical model testing has certain advantages over other analyzing approaches for studying stability related issues of dam structures. In the physical model tests, the concrete dam body and the rock foundation with joints and weak layers can be simulated using similarity materials. The factor of safety can be reasonably defined as the ratio between the maximum external load inducing the start of sliding instability of the dam foundation and the upstream hydrostatic load applied to the dam. Therefore, it gives a convenient and straightforward indication of the foundation resistance against external loads. Moreover, by applying overloading, the captured monitoring results can reveal the potential sliding surfaces and the most critical failure pattern. Therefore, this method provides practical guidelines for the design and construction of the dam structure under investigation.

(2) Under overloading condition, the internal forces of gravity dam system including the

dam body and the rock foundation can adjust automatically. However, the self-adjusting capability of a gravity dam system is limited. If enough bonding resistance between the concrete dam body and the rough rock surface is provided, sliding failure may occur within the rock foundation. As soon as the external loading exceed the self-adjusting capability of the gravity dam, localized yield zones will be induced and develop in the foundation, leading to the ultimate failure of the dam structure.

(3) The results of the physical model test show that the stability of Wudu Dam is sufficient for the design load combination. Under the action of the normal working loads, the maximum horizontal displacement of the prototype dam structure will be less than 3 mm. The tension cracks of the overloaded dam initiate under the dam heel and the most critical potential sliding surface lies below the dam-foundation interface. The shear strengths of joints in the rock foundation play a dominant role in affecting the dam stability. In addition, the horizontal displacements at the dam toe and crest are the signs of potential failure, which should be paid special attention in dam safety monitoring.

(4) The comparison of the FBG sensing bar results with displacement gauge data indicated that the FBG sensing bars provides reliable measurements of internal displacements. From this study, it's worth pointing out that, to enhance the measurement accuracy, the compatibility of Young’s moduli of the bar material and the model material should be ensured and more FBG sensors are recommended to be installed on the sensing bar. Since the overloading test in this study is in a 2-D plain stress condition, the performance of FBG sensing bars in true three-dimensional (3-D) measurement should be investigated in future studies.

Table 6.1 Similarity coefficients between the prototype and the physical model of Wudu Dam

Physical parameters	Scale factors	Ratio (prototype/model)
Length	$C_L = \frac{L_p}{L_m}$	150
Density	$C_\gamma = \frac{\gamma_p}{\gamma_m}$	1
Displacement	$C_s = \frac{s_p}{s_m}$	150
Deformation modulus	$C_E = \frac{E_p}{E_m}$	150
Possion's ratio	$C_\nu = \frac{\nu_p}{\nu_m}$	1
Stress	$C_\sigma = \frac{\sigma_p}{\sigma_m}$	150
Strain	$C_\varepsilon = \frac{\varepsilon_p}{\varepsilon_m}$	1
Strength	$C_f = \frac{f_p}{f_m}$	150

Notes: The subscripts p and m denote that the corresponding parameters are of the prototype and the physical models, respectively.

Table 6.2 Physical and mechanical properties of the prototype and the physical model materials

Material	Property	Prototype	Model
Concrete	γ (kN/m^3)	24	24
	E (GPa)	20	0.133
	ν	0.2	0.2
Rock	γ (kN/m^3)	26	26
	E (GPa)	8.3	0.055
	ν	0.3	0.3
	c (kPa)	3000	20
	φ (^{o})	25	25
Rock joints	c (kPa)	0	0
	φ (^{o})	25	25

Notes: γ- density; E- deformation modulus; ν-Poisson's ratio; c- cohesion; φ- friction angle

Figure 6.1 Design sketch of Wudu Dam

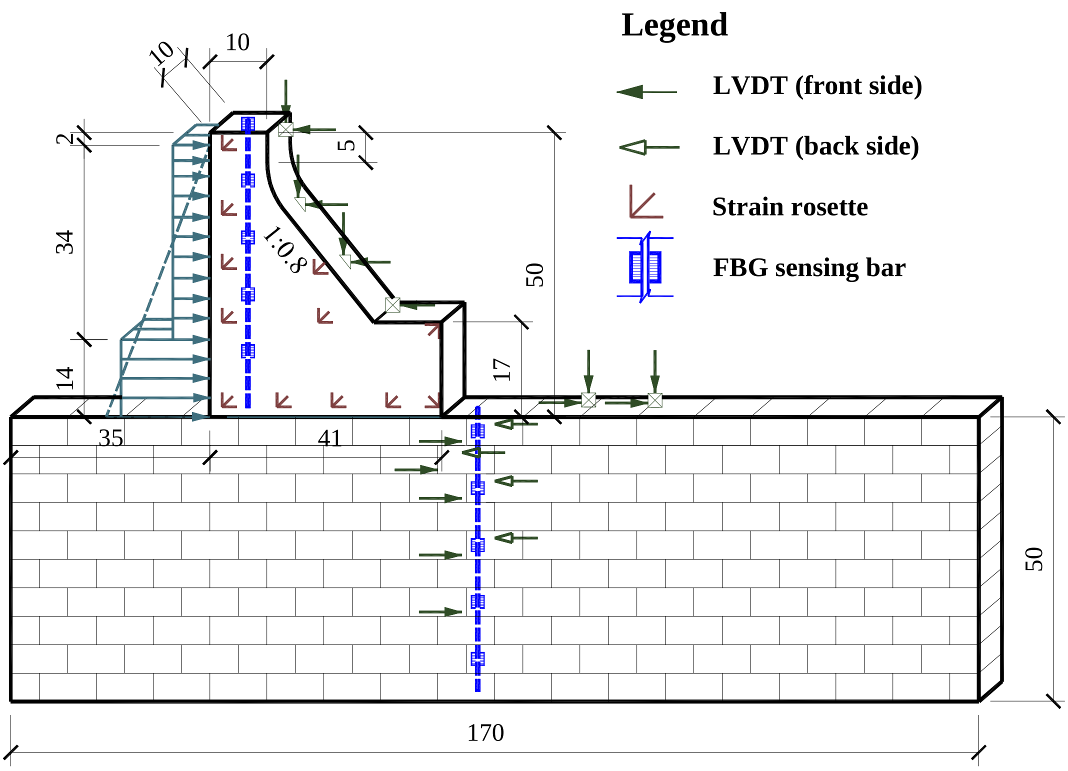

Figure 6.2 Dimensions of the model dam and instrumentation set-up (all dimensions in cm)

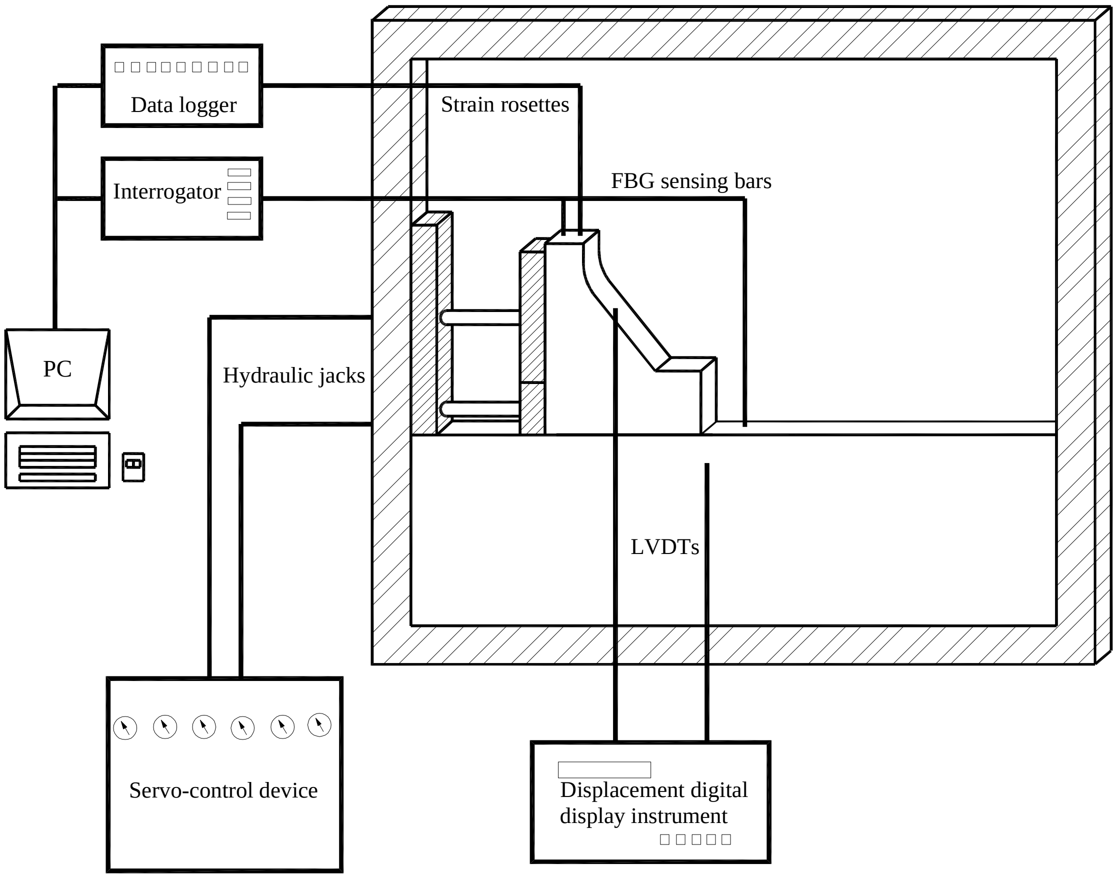

Figure 6.3 Loading and measurement system for the physical model test

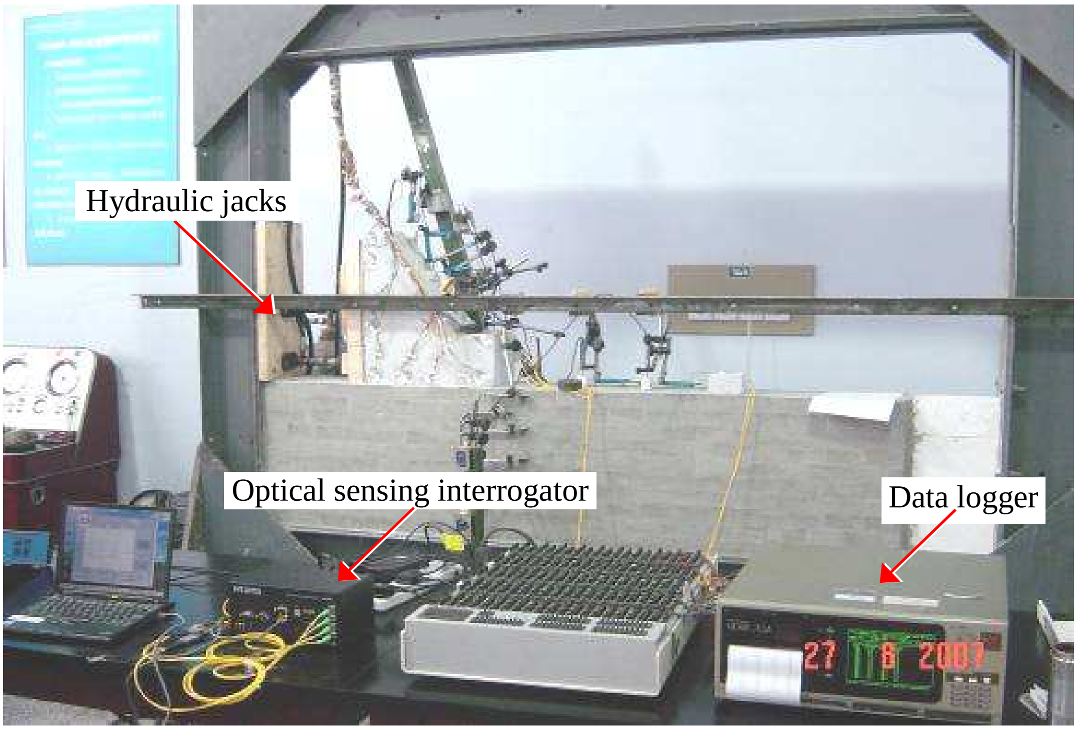

Figure 6.4 Photograph of the physical model test (monitoring in progress)

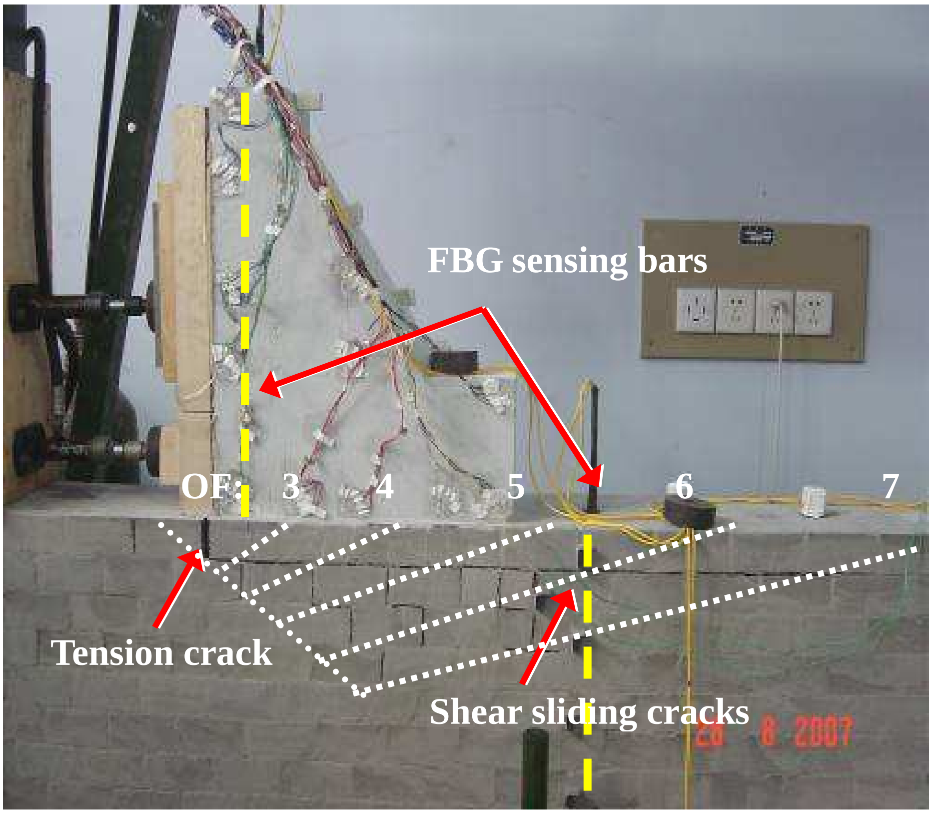

Figure 6.5 Photograph of sliding failure of the model dam (OF=7)

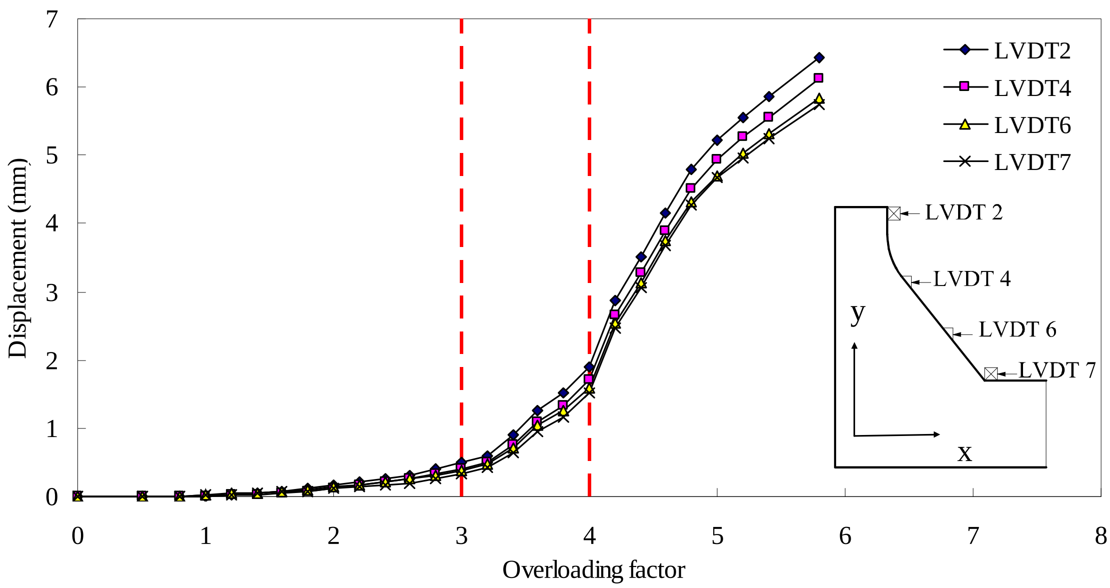

(a) Horizontal displacements of the monitoring points

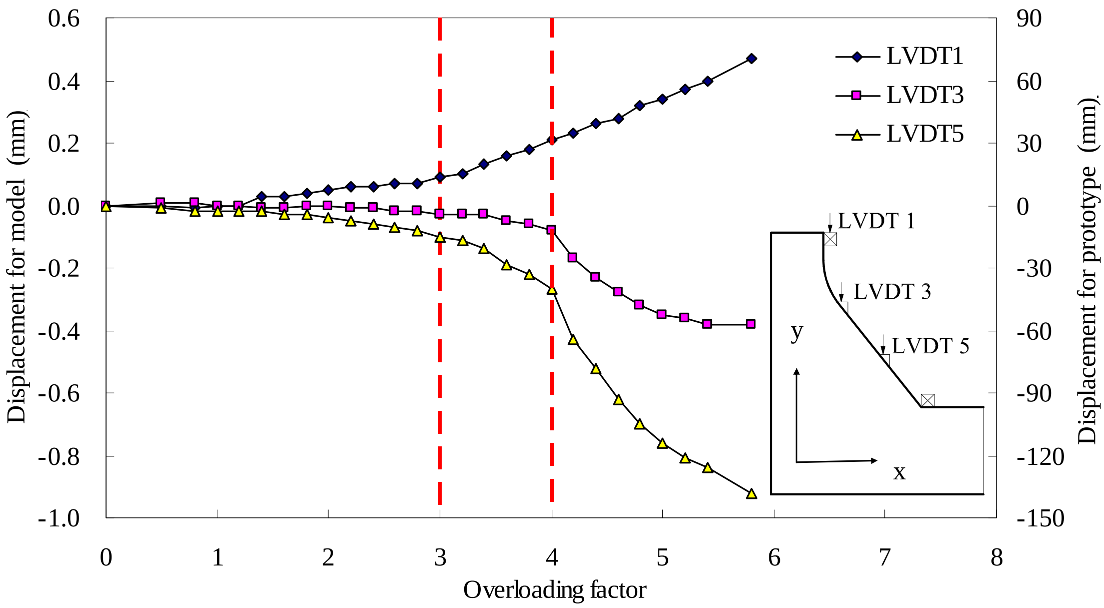

(b) Vertical displacements of the monitoring points

Figure 6.6 Surface displacements of the dam body measured by LVDTs during overloading (positive LVDT values for the *x*/*y* directions as shown)

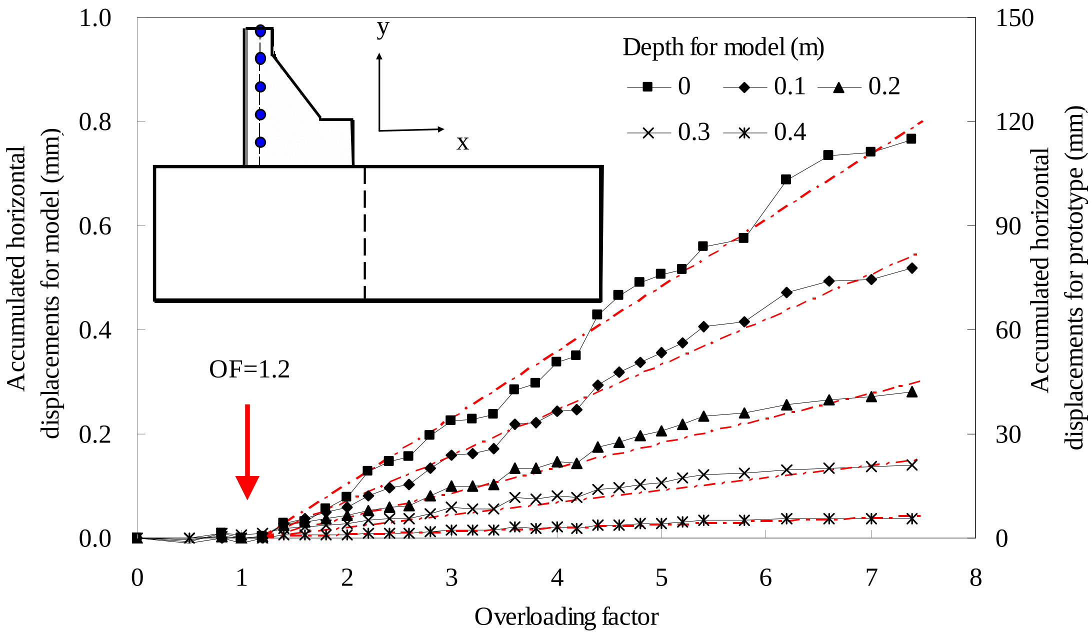

(a) Relationships of overloading factors and accumulated horizontal displacements with respect to ground level at different depths (positive displacements indicating movement of the dam body in the *x* direction)

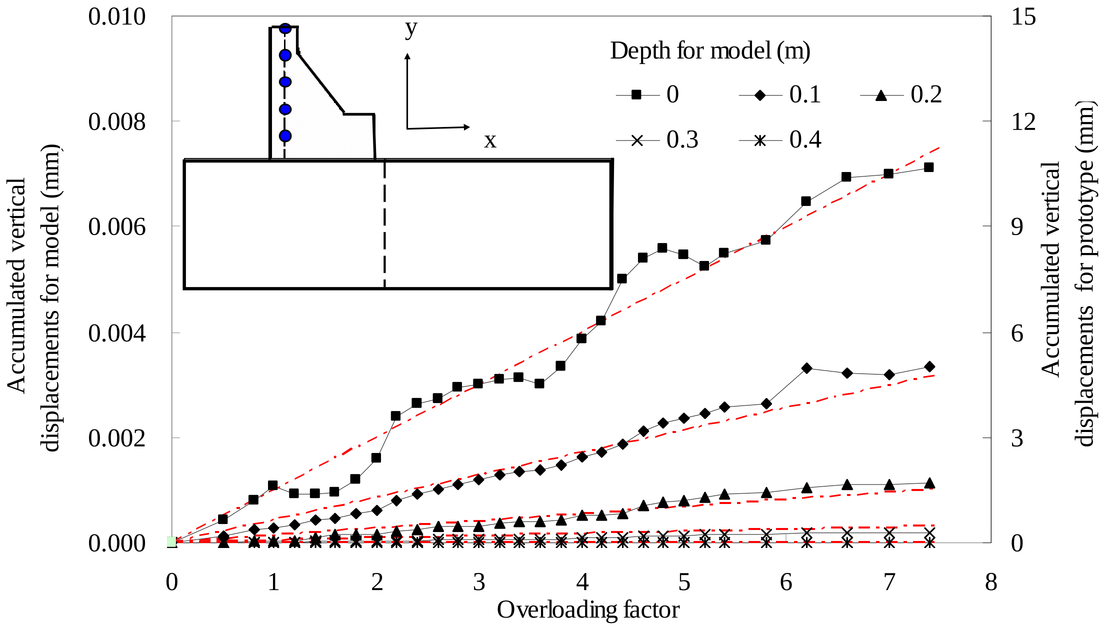

(b) Relationships of overloading factors and accumulated vertical displacements with respect to ground level at different depths (positive displacements indicating tension of the dam body)

Figure 6.7 Displacements of the mode dam body measured by the FBG sensing bar

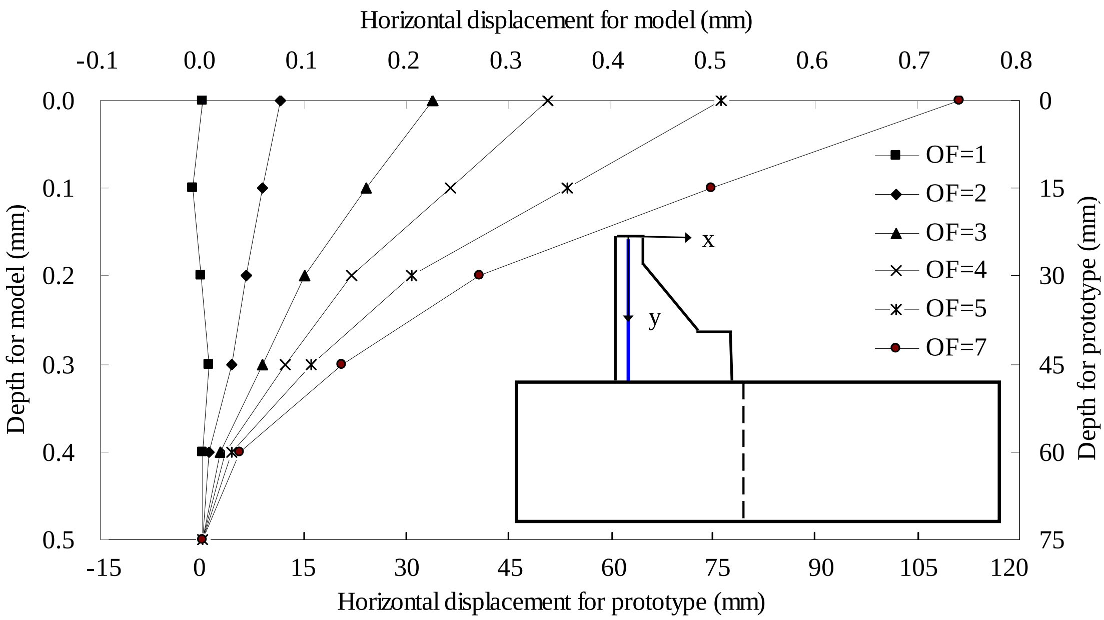

Figure 6.8 Profiles of horizontal displacements with respect to depths of the dam body under different overloading

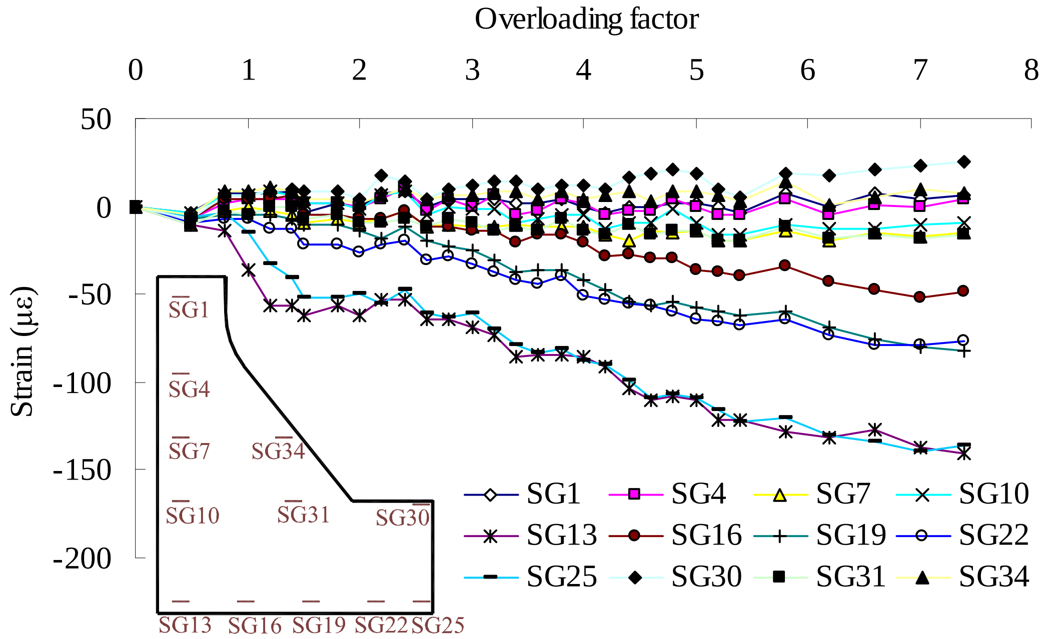

(a) Strains in the 0^{o} direction

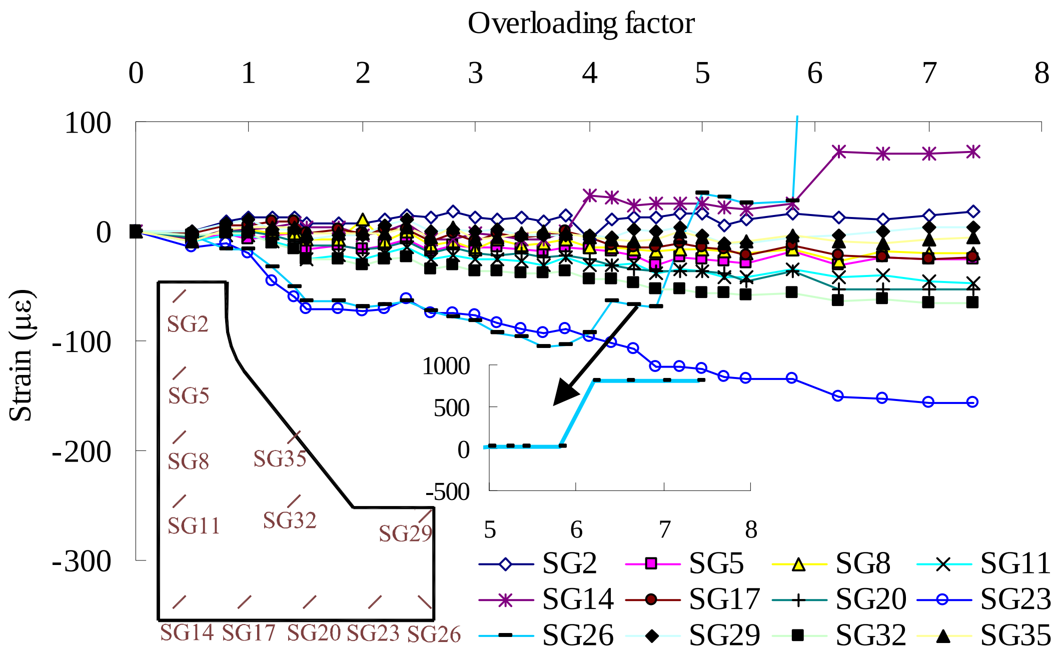

(b) Strains in the 45^{o} direction

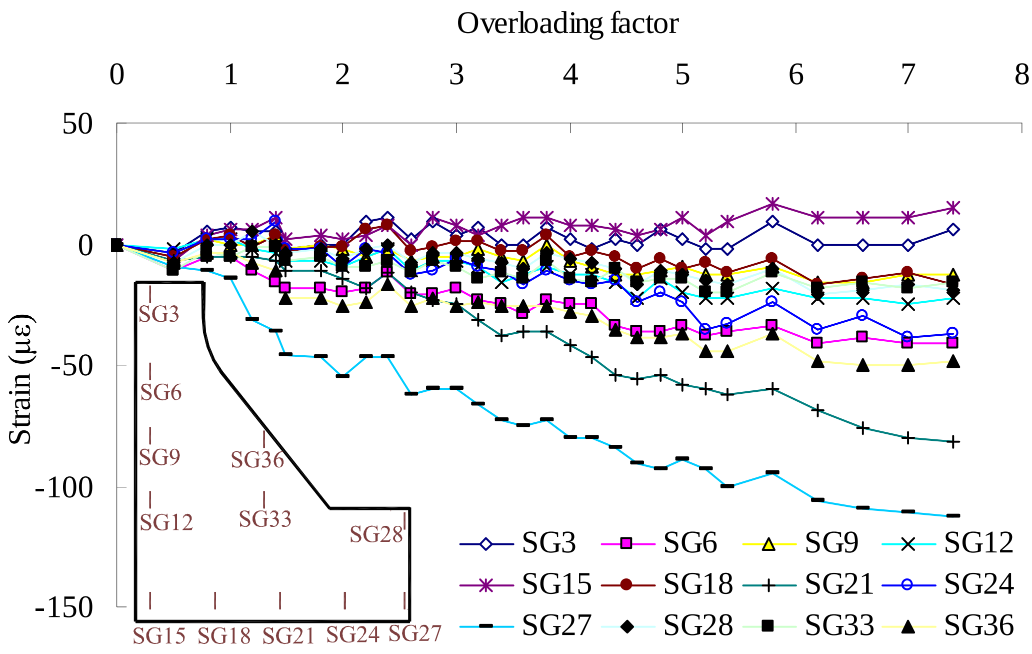

(c) Strains in the 90° direction

Figure 6.9 Strain development on the dam body measured by strain rosettes under overloading condition (strain: “+” for tension and “–“ for compression)

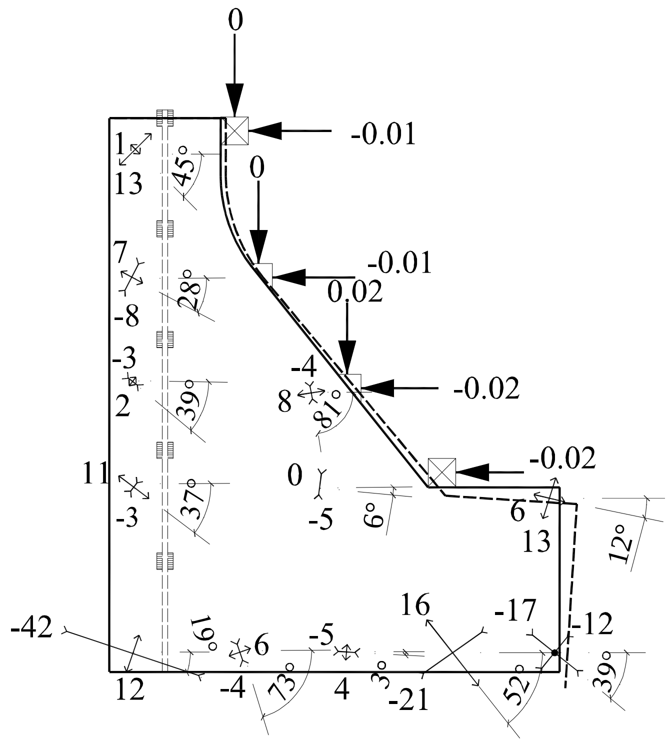

(a) OF=1.0

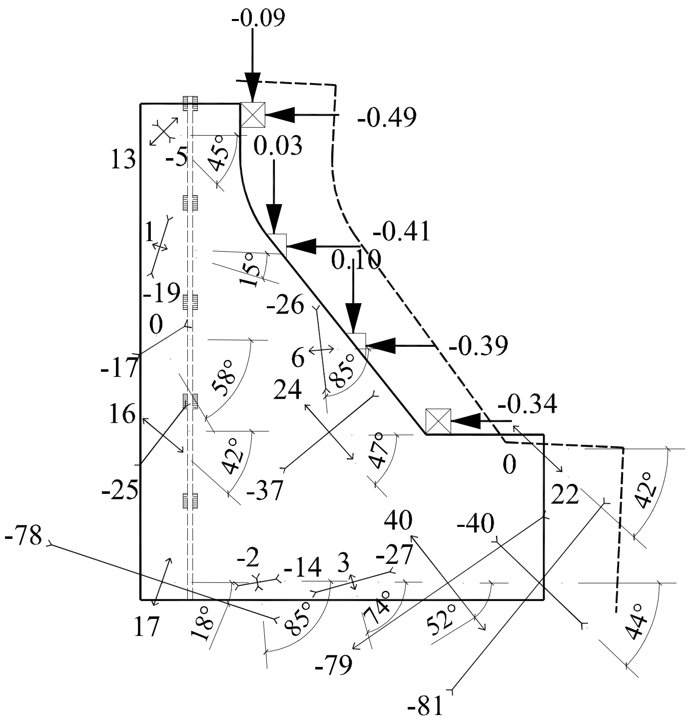

(b) OF=3.0

Figure 6.10 Principal strain distributions and surface displacements on the dam body measured by the strain rosettes and LVDTs (unit: με for strains, mm for displacements)

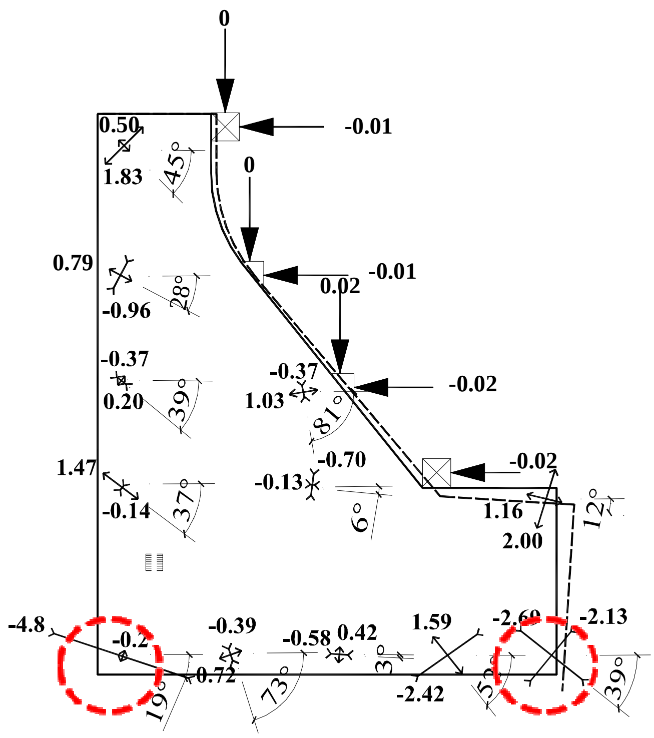

(a) OF=1

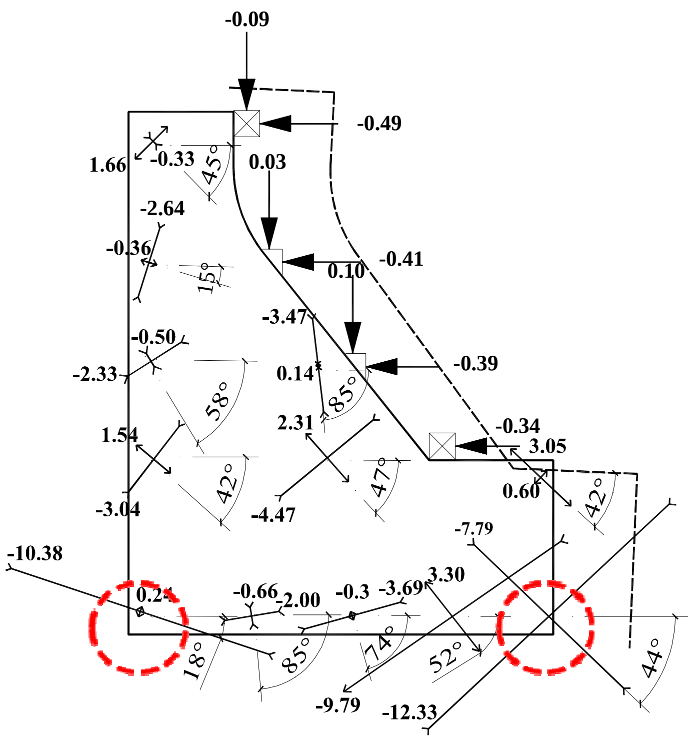

(b) OF=3

Figure 6.11 Principal stress distributions and surface displacements on the dam body measured by strain rosettes and LVDTs (unit: kPa for stresses, "+" for tension, "–" for compression, mm for displacements, positive LVDT value for the arrow direction as shown)

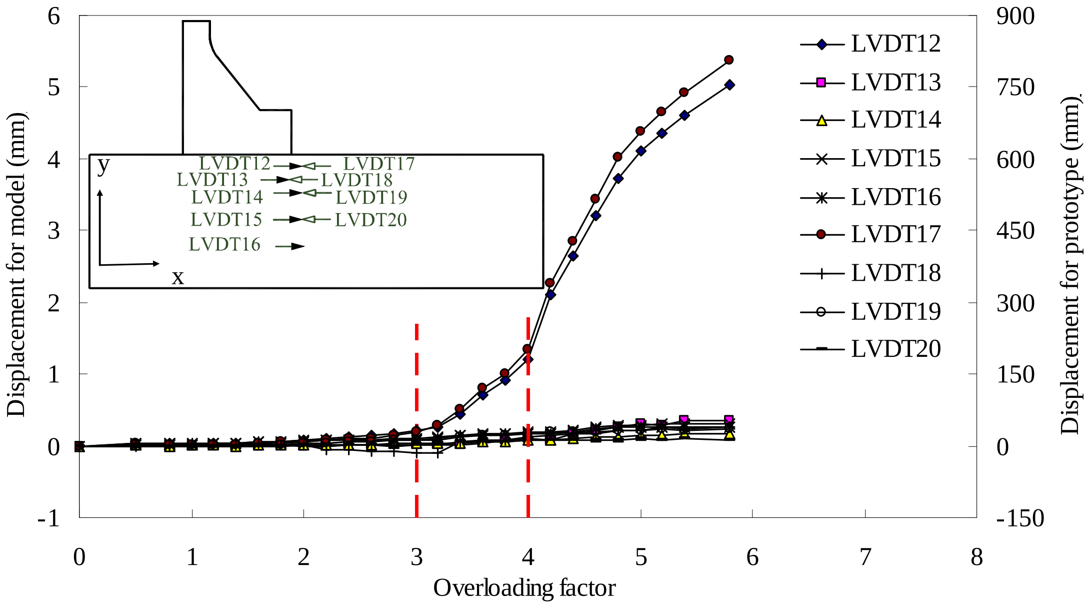

(a) Relationships of overloading factors and horizontal displacements below the ground surface

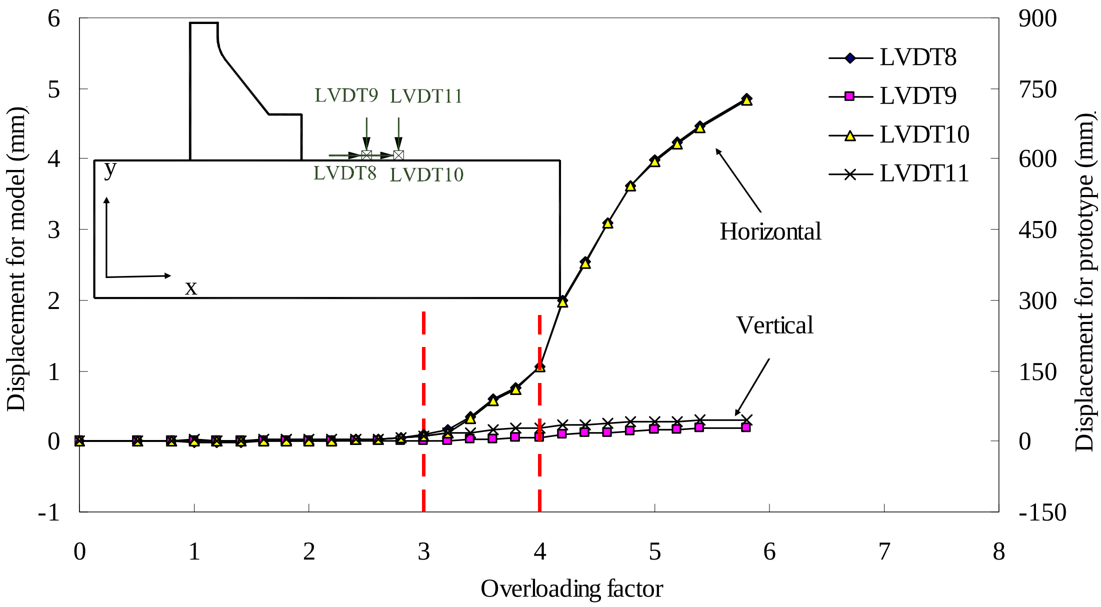

(b) Relationships of overloading factors and ground surface displacements

Figure 6.12 Displacements of the dam foundation measured by LVDTs

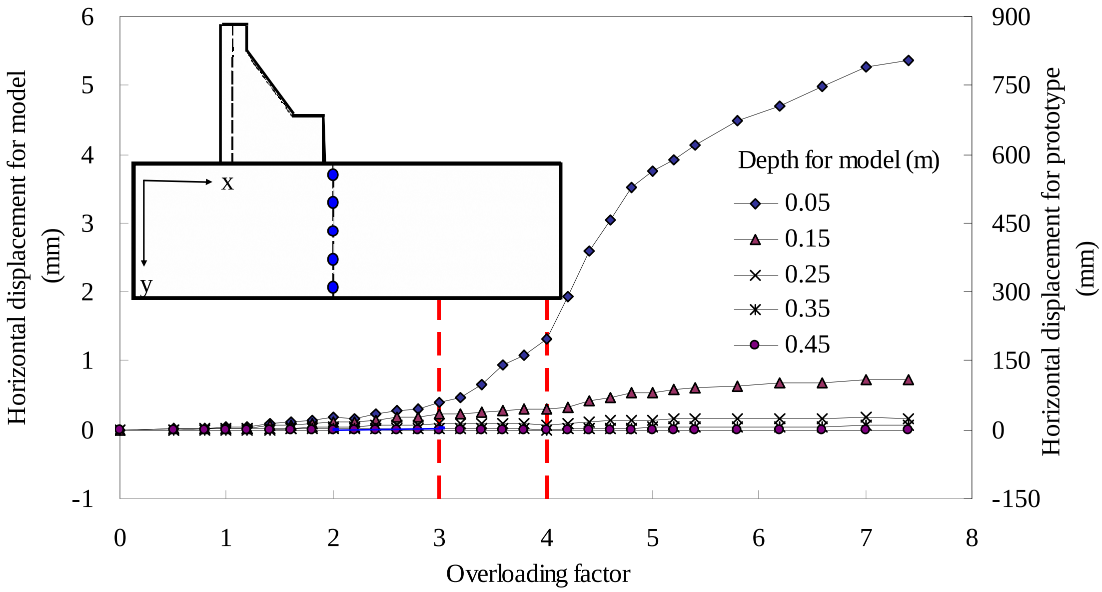

(a) Relationships of overloading factors and relative horizontal displacements

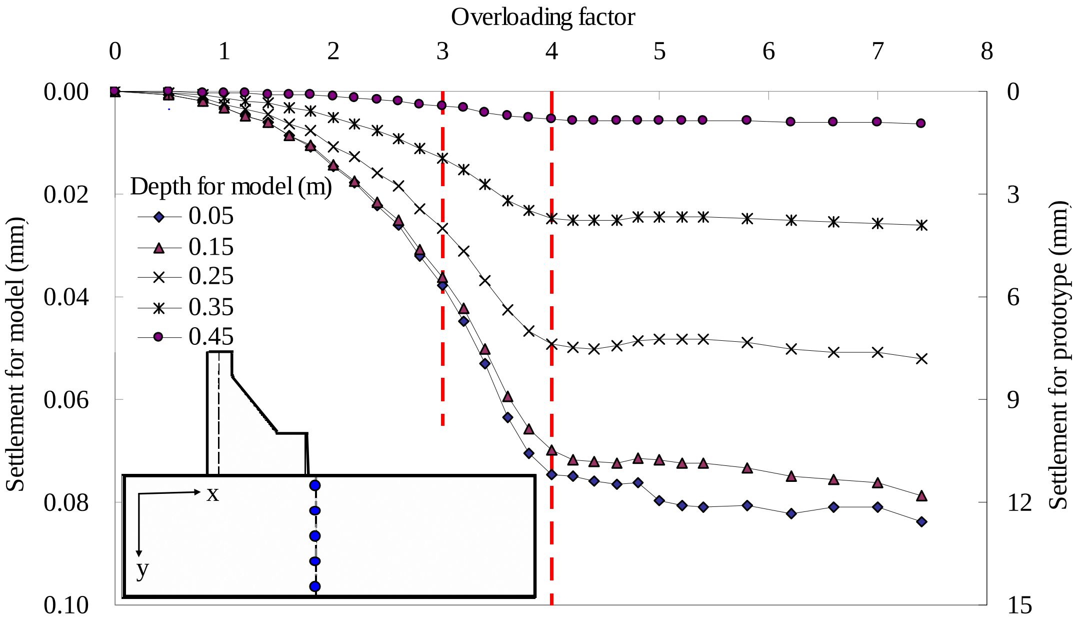

(b) Relationships of overloading factors and settlements (positive settlements indicate compression of the foundation)

Figure 6.13 Displacements of the dam foundation measured by the FBG sensing bar

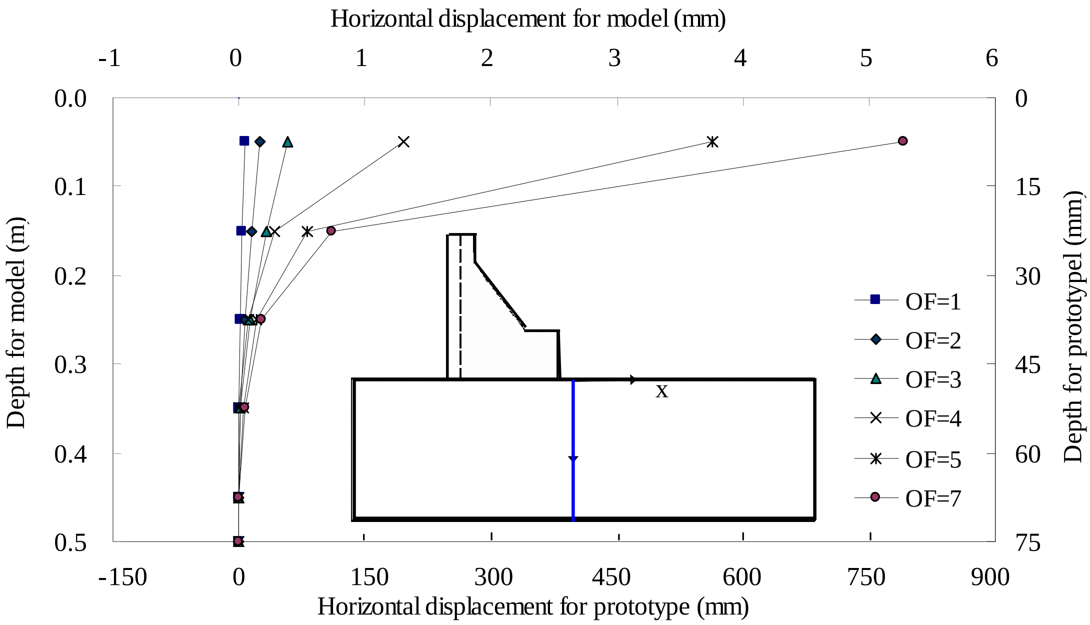

Figure 6.14 Profiles of horizontal displacements with respect to depths of the dam foundation under different overloading

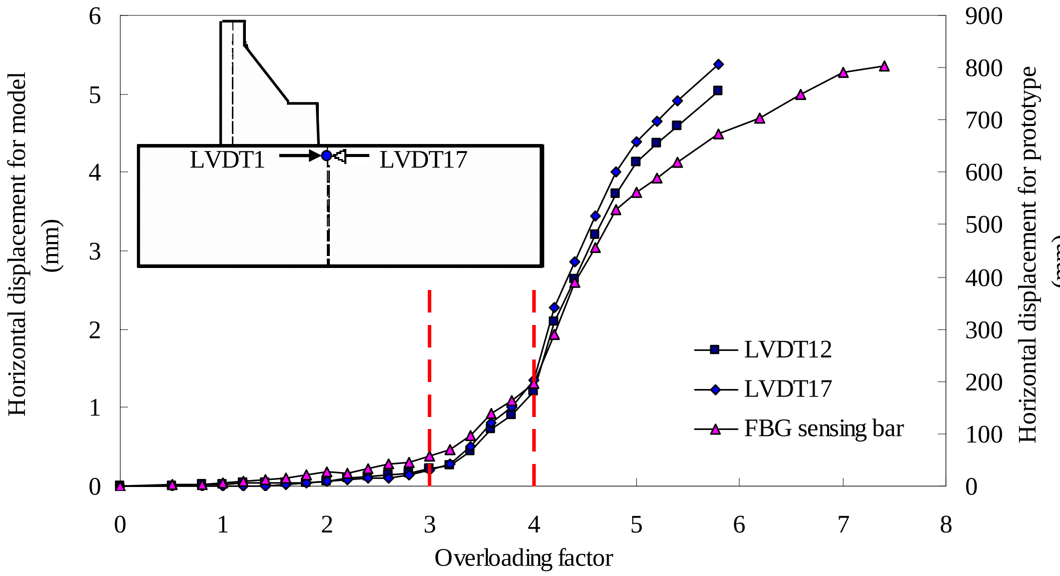

Figure 6.15 Comparison of the monitoring results of the horizontal displacement in the dam foundation (50 mm depth) measured by the FBG sensing bar and LVDTs

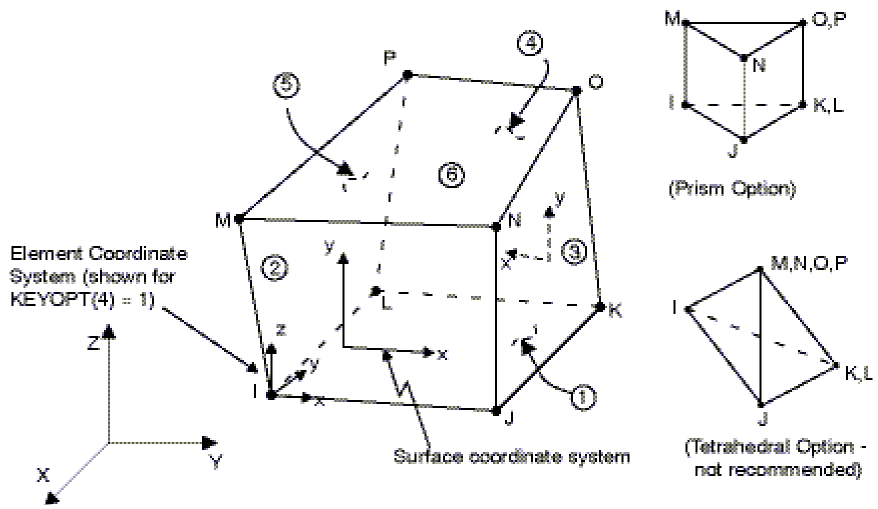

Figure 6.16 SOLID45 geometry (after ANSYS 2007)

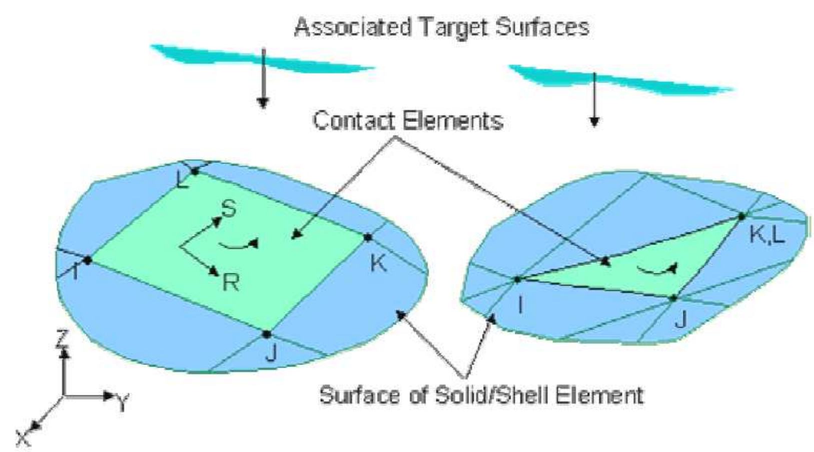

Figure 6.17 CONTA173 geometry (after ANSYS 2007)

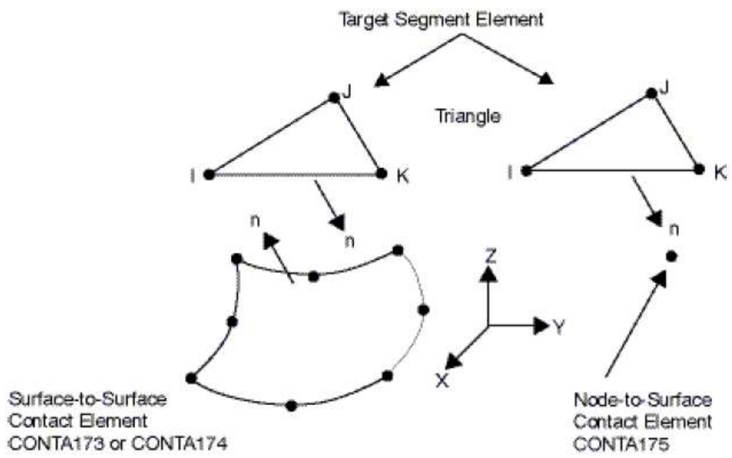

Figure 6.18 TARGE170 geometry (after ANSYS 2007)

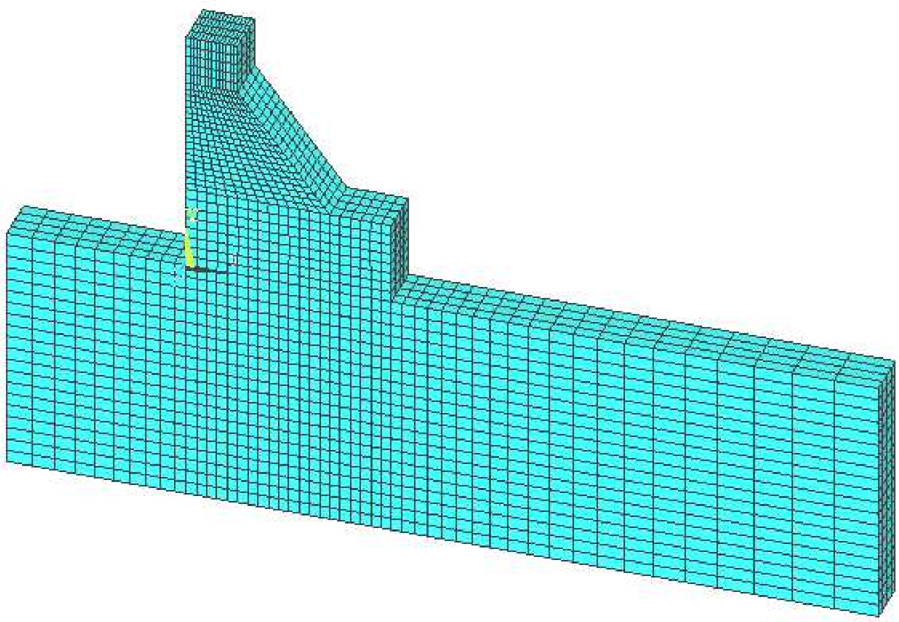

Figure 6.19 Meshing of the model dam

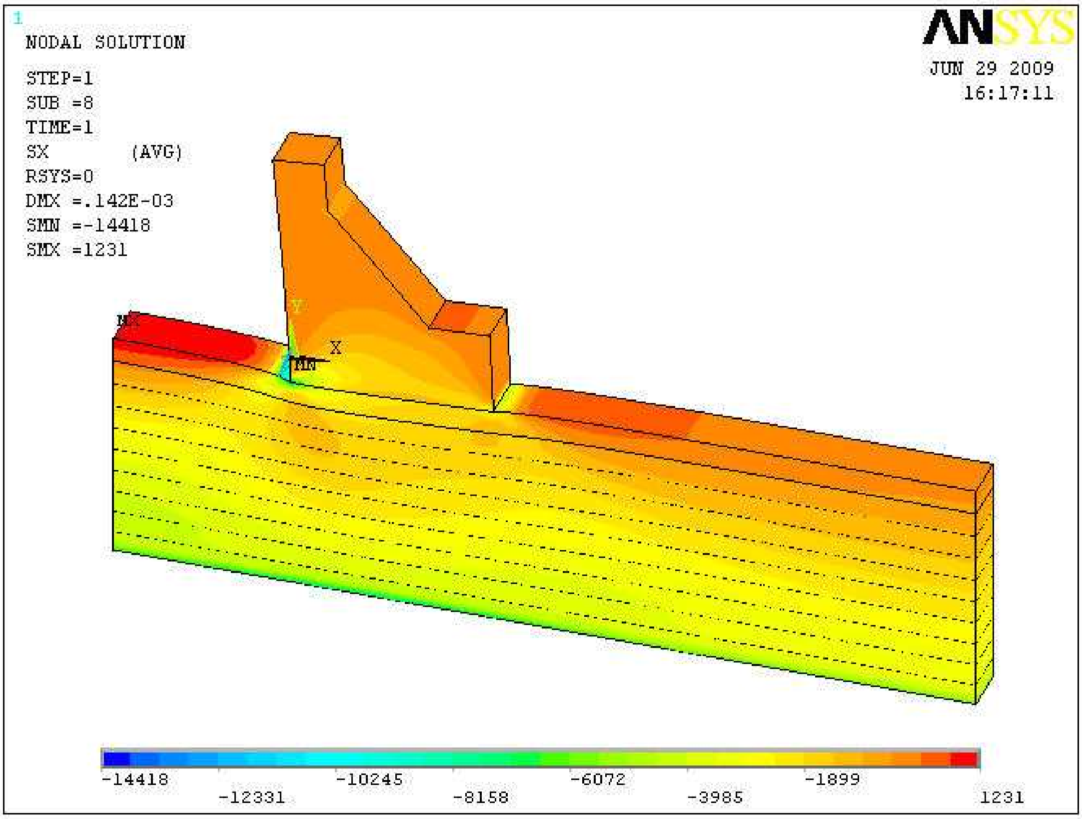

(a) Stresses in the x direction σ_x

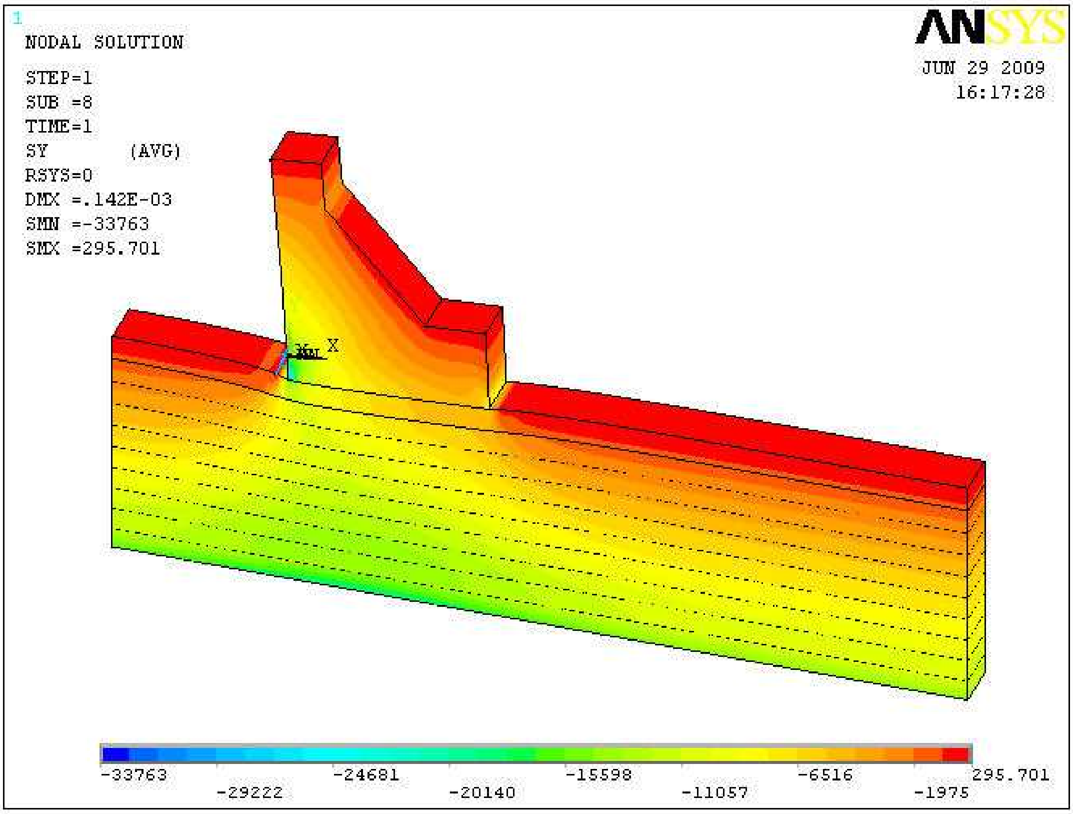

(b) Stresses in the y direction σ_y

Figure 6.20 Initial stress fields of the dam-foundation system

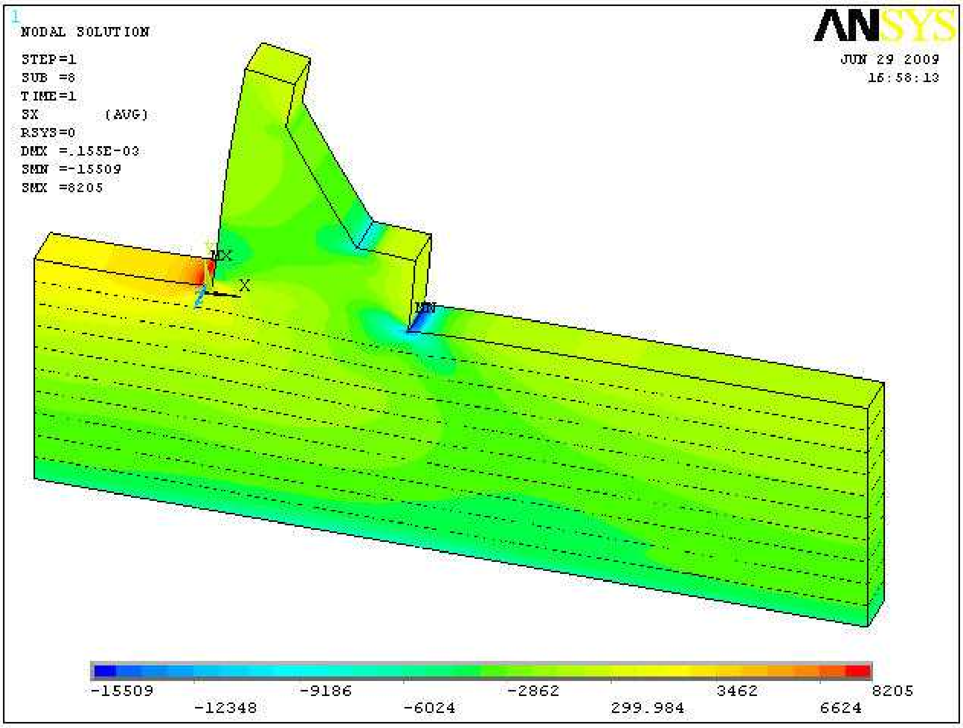

(a) Stresses in the x direction σ_x

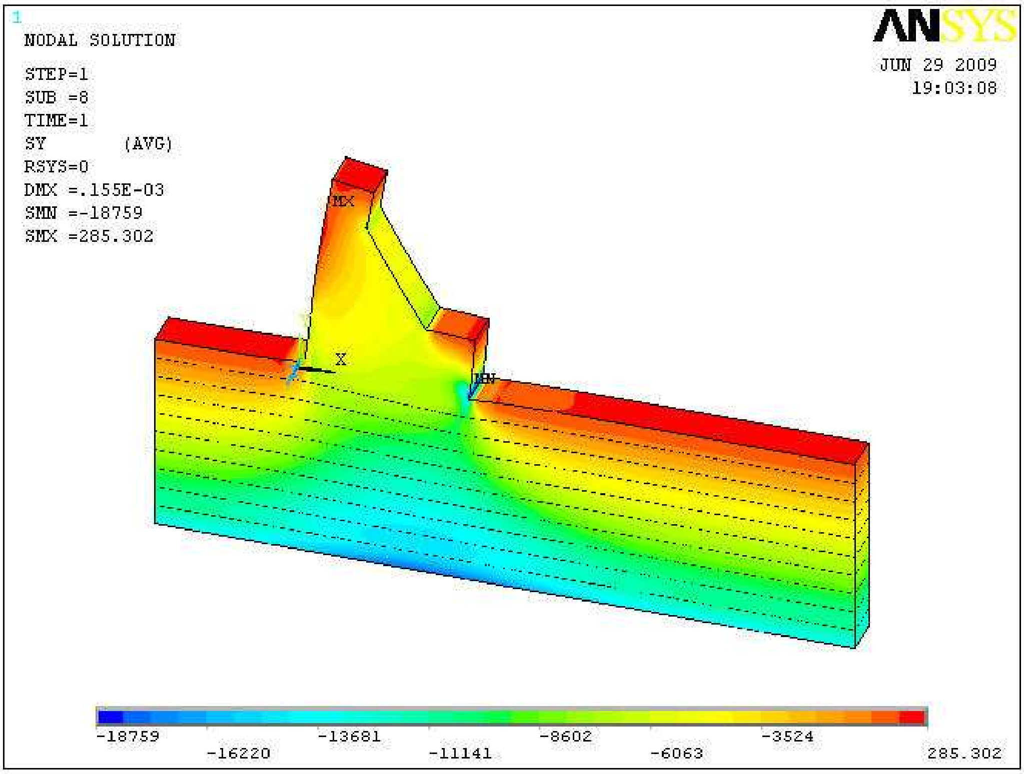

(b) Stresses in the y direction σ_y

Figure 6.21 Stress fields of the dam-foundation system (OF=1)

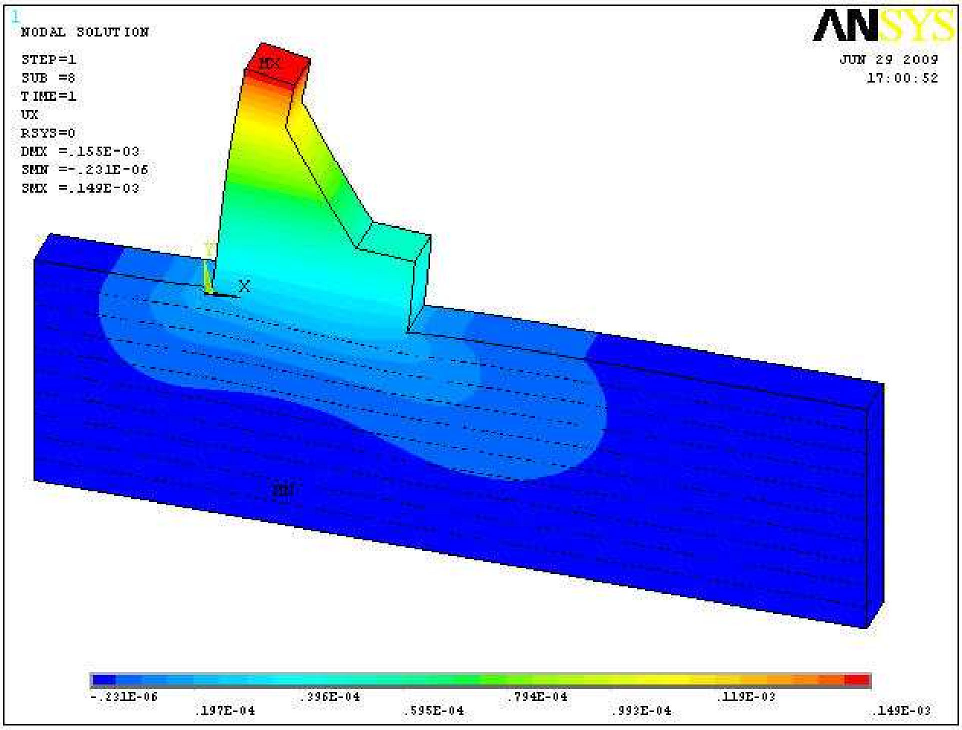

(a) Displacements in the x direction u_x

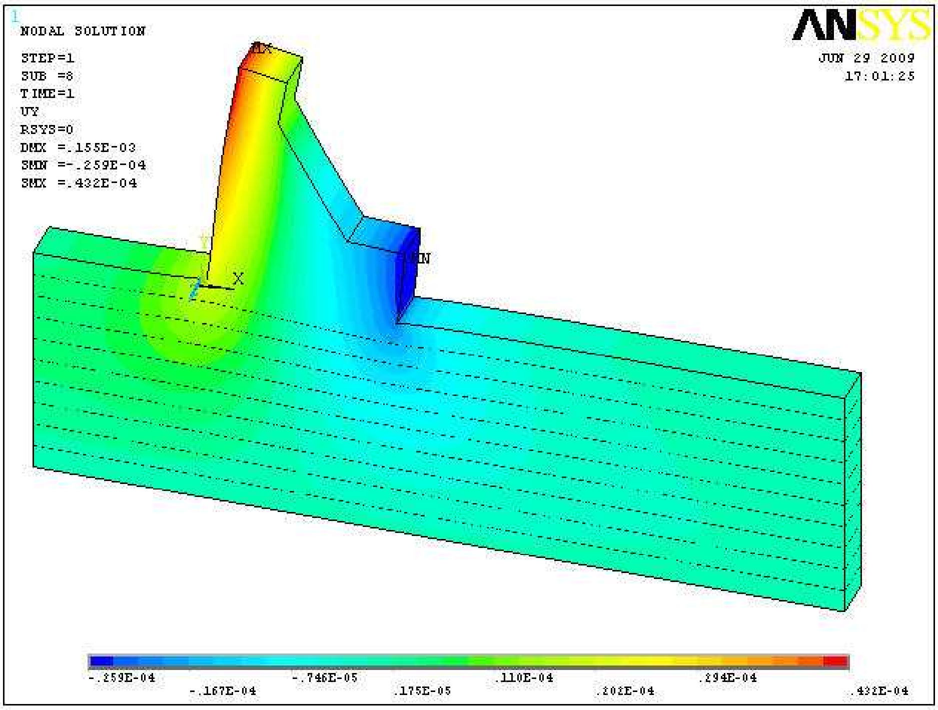

(b) Displacements in the y direction u_y

Figure 6.22 Contour of displacements of the dam-foundation system (OF=1)

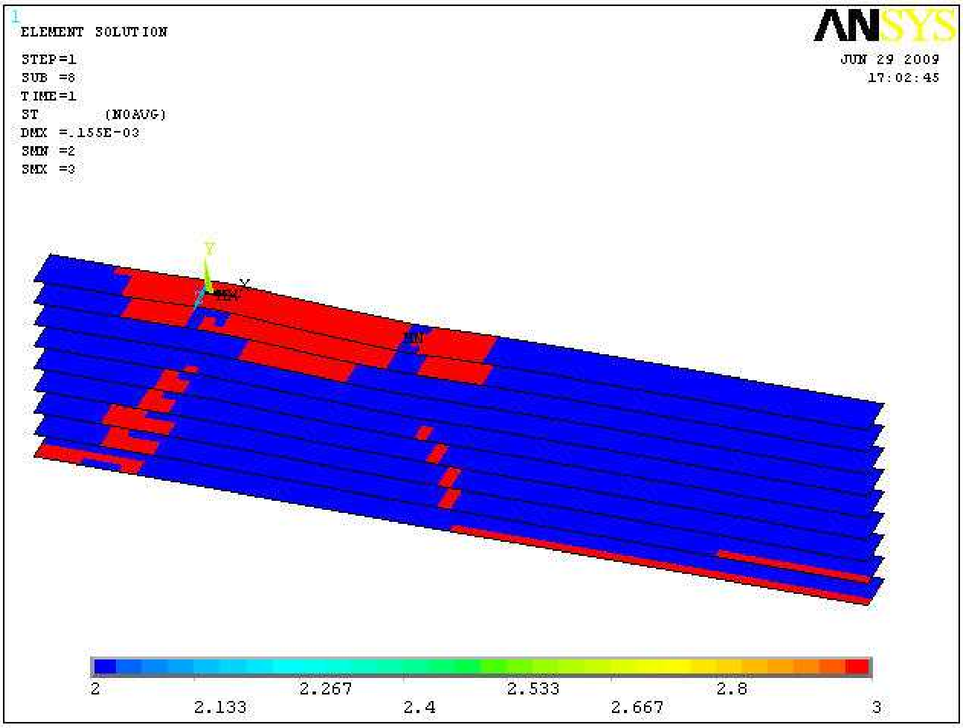

Figure 6.23 Contact conditions of the rock joints (OF=1)

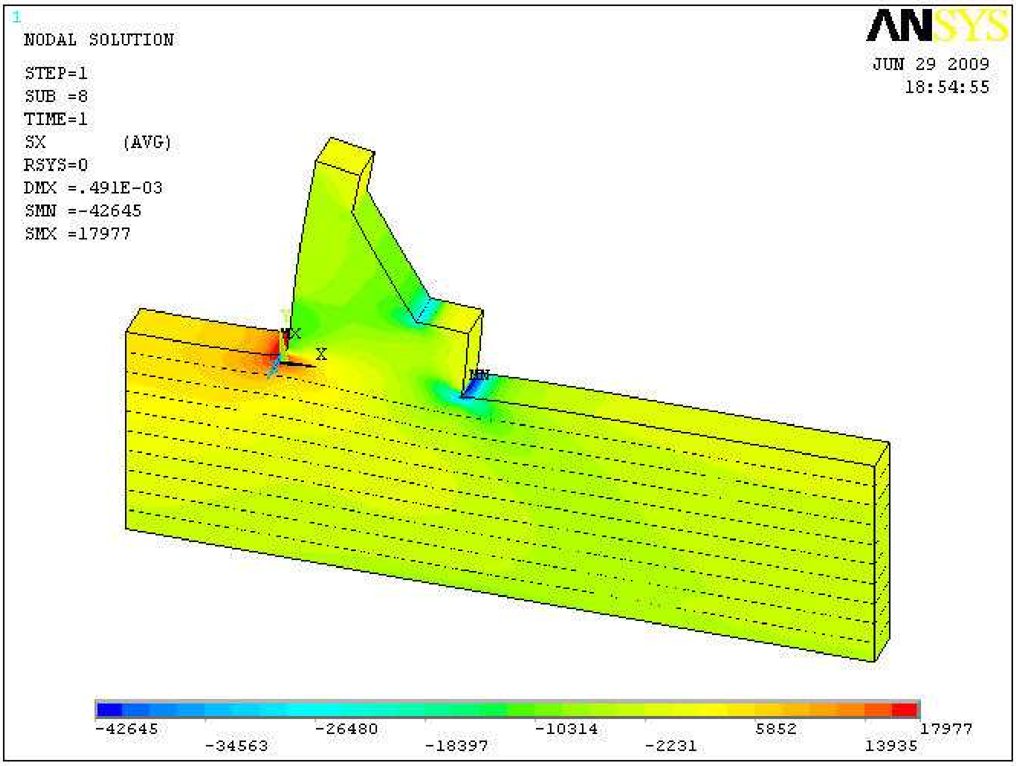

(a) Stresses in the *x* direction σ_x

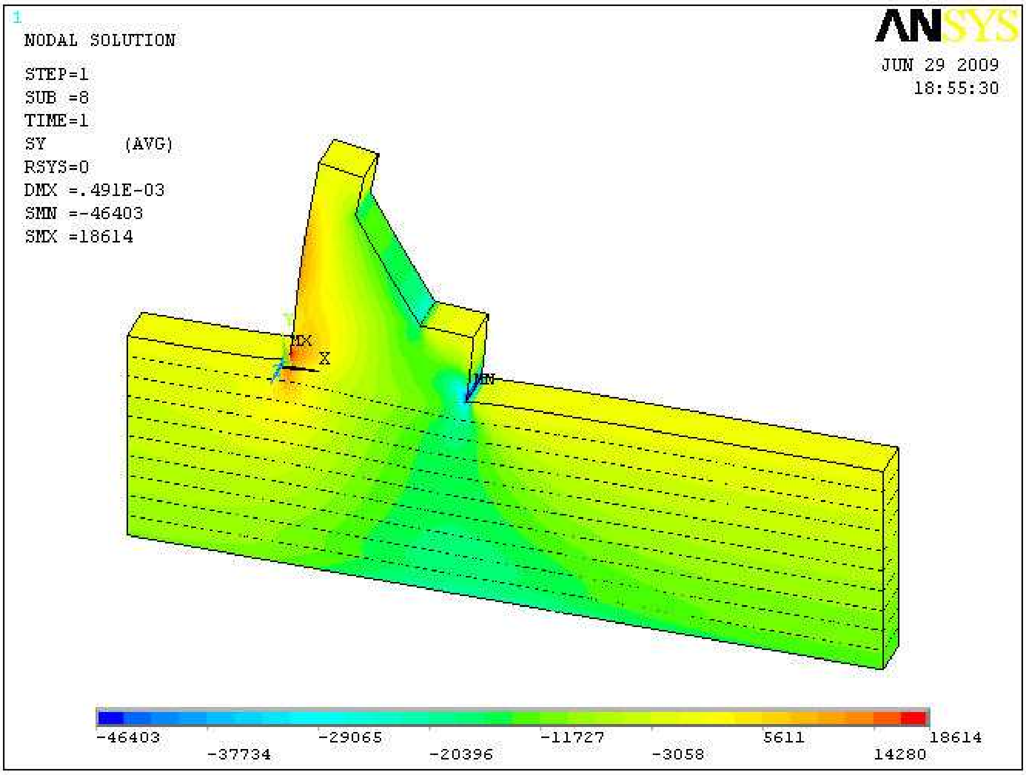

(b) Stresses in the y direction σ_y

Figure 6.24 Stress fields of the dam-foundation system (OF=3)

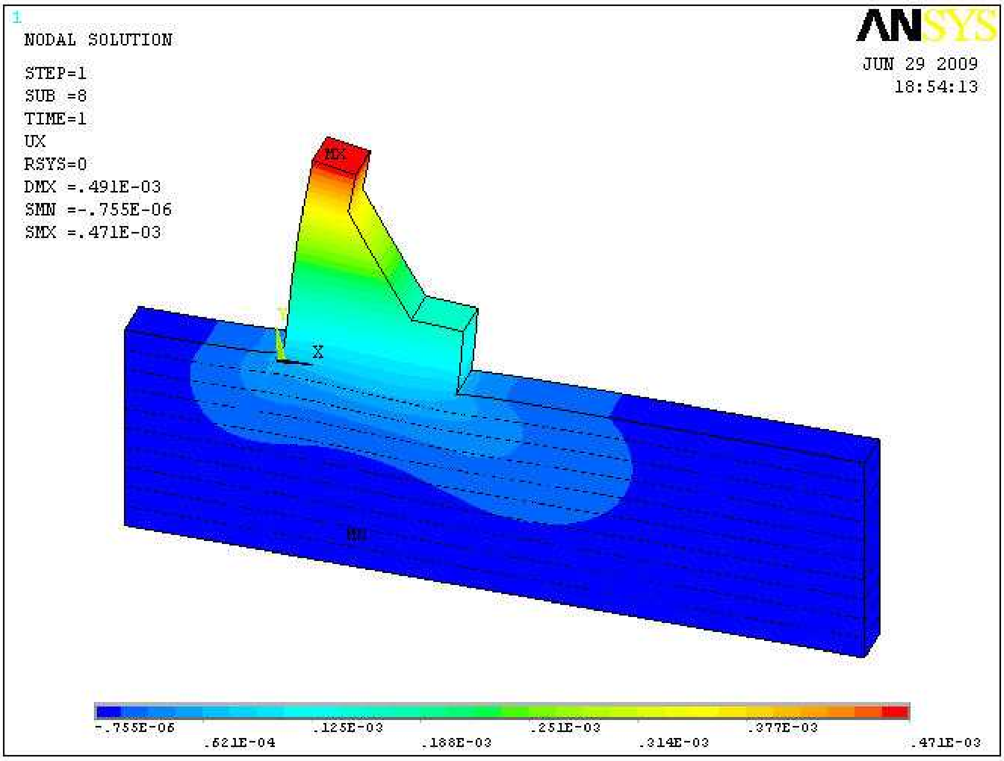

(a) Displacements in the x direction u_x

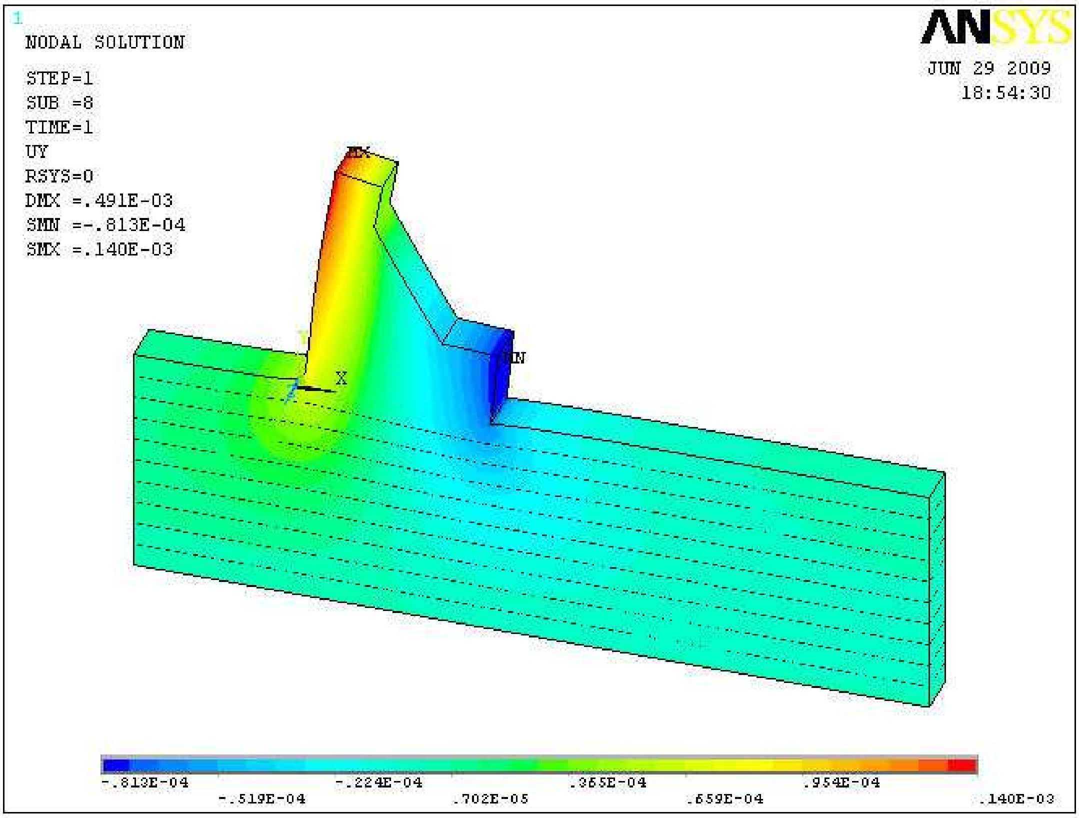

(b) Displacements in the y direction u_y

Figure 6.25 Displacement distributions of the dam-foundation system (OF=3)

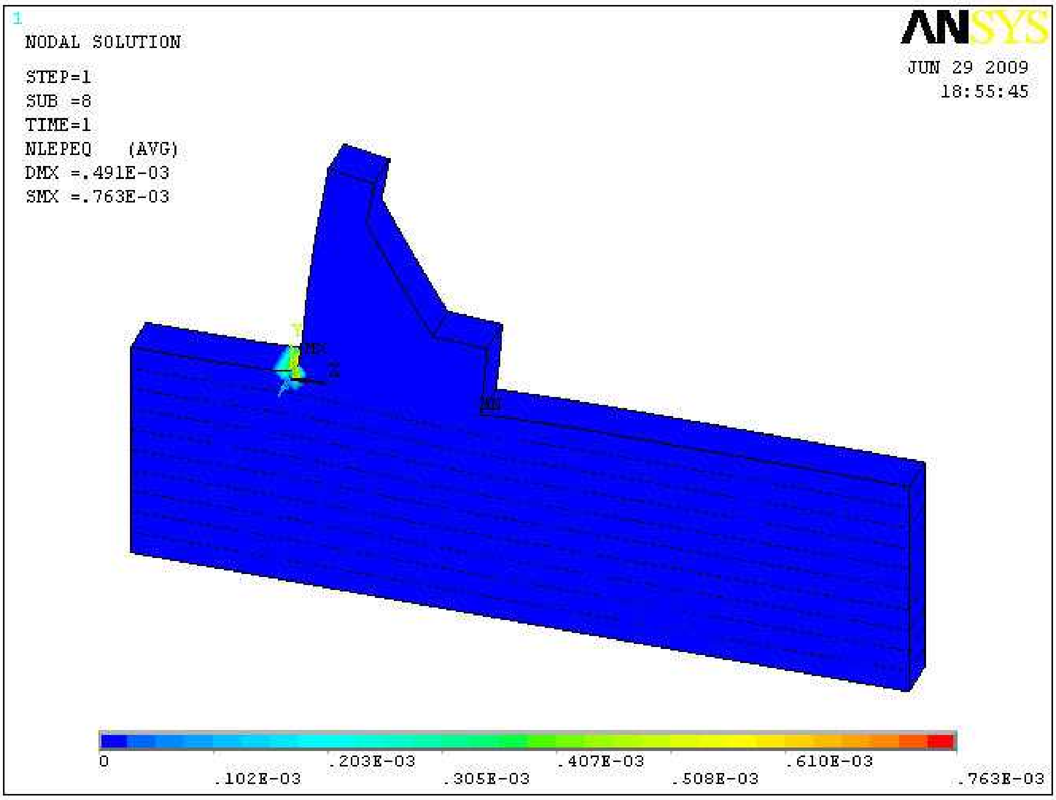

Figure 6.26 Contour of equivalent plastic strain in the dam-foundation system (OF=3)

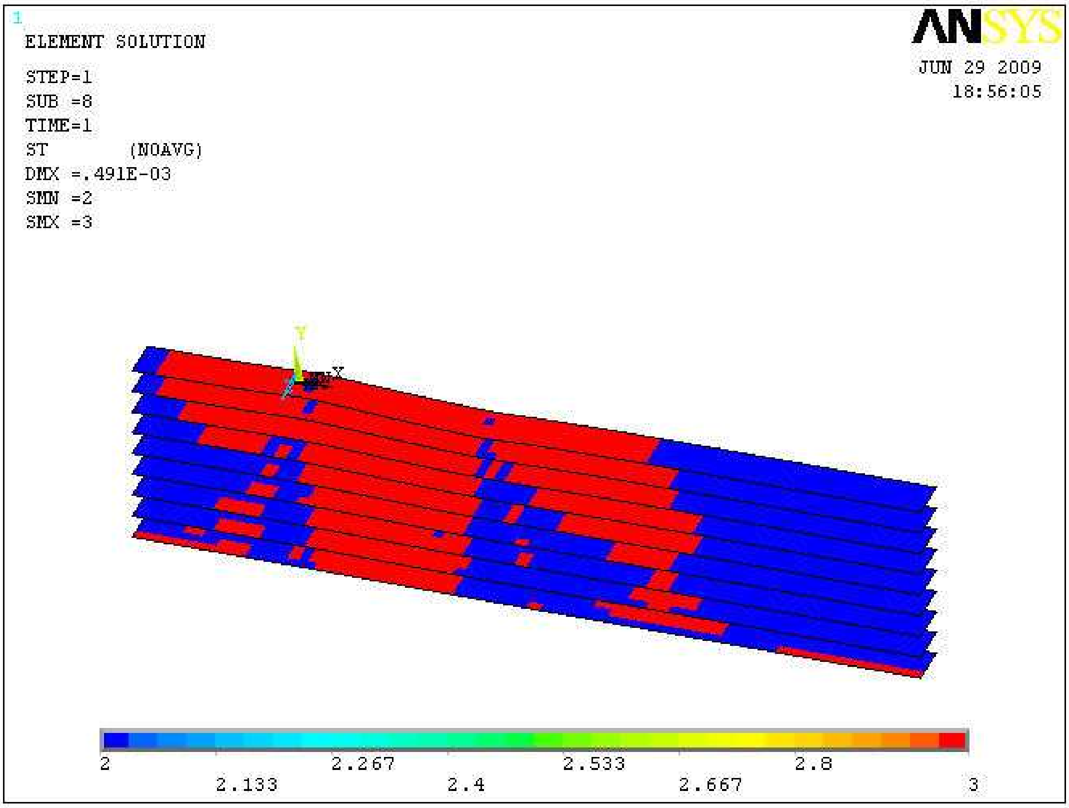

Figure 6.27 Contact conditions at the rock joints (OF=3)

CHAPTER 7:

FIBER OPTIC MONITORING AND PERFORMANCE EVALUATION OF A MAT FOUNDATION

7.1 INTRODUCTION

The current methods for foundation instrumentation using various instruments, such as extensometers, inclinometers and settlement gauges, have certain limitations including low accuracy and poor durability. The development of FBG sensors makes it possible to establish a fiber optic monitoring system for foundations, which has a number of advantages over conventional geotechnical instruments.

Recently, a multi-story building was planned to be constructed at the site of China Graduate School of Theology in Kowloon Tong, Hong Kong, as part of its redevelopment plan. A 10.3 m×11.3 m mat foundation was designed to support the superstructure. Since additional floors will be built as extension to the superstructure in the future, it is crucial to assess the field performance of the mat foundation during and after the construction stage.

To carry out field instrumentation and performance evaluation of the mat foundation, an FBG based monitoring system consisting of three types of FBG sensors has been installed at this site. Due to the harsh environments found in construction sites, the field installation of FBG sensors is a challenging task. This chapter introduces the instrumentation of this foundation and discusses the monitoring results.

7.2 FIELD INSTRUMENTATION

A mat foundation is a large slab, usually reinforced concrete, for transmitting the structural loads to the underlying soil. Different from isolated foundations such as strap footings, mat foundations can increase bearing capacity of the foundation and reduce total and differential settlements due to their continuous nature.

For mat foundations, the stress distributions and bending moments are associated with settlements. However, estimation of the settlements is complex. The settlement depends on the property and homogeneity of ground soils, the rigidity of the mat foundation and the superstructure with respect to the soil, the groundwater conditions, foundation geometry, and construction methods (Budhu 2008).

In-place inclinometers, settlement tubes and tube packaged strain sensing arrays using FBG technology have been installed in this foundation site to measure the settlement profiles underneath the mat foundation, settlements at different depths, and strain distributions inside the concrete slab, respectively. All these sensors were manufactured and calibrated in laboratory prior to field instrumentation. The arrangement of the instrumentation lines or points is shown in Figure 7.1 and Figure 7.2.

7.2.1 Tube packaged FBG strain sensing arrays

Two sets of tube packaged FBG strain sensing arrays were grouted inside the concrete slab, which is shown in Figure 7.3 to Figure 7.5. Each set consists of six tube packaged FBG strain sensing array of a length of 1950 mm. Two tube packaged FBG temperature sensors were installed near to the embedded strain sensors for temperature compensation. All the sensors showed satisfactory performance during and after concrete pouring. Unfortunately, two of the optical fiber cables for the strain sensing arrays No. 1A and the temperature sensor No. T1 were damaged by a labor, who was demolishing the foundation formwork. As a result, 9 FBG strain sensing arrays and 1 temperature sensor survived all the construction activities and successfully measured the strains and temperature in the mat foundation.

7.2.2 FBG settlement tubes

Two sets of FBG settlement tubes (total length L=4 m) as shown in Figure 7.6 were installed in two boreholes to measure the settlements at different depths below the ground surface. For each borehole, totally four settlement tubes were multiplexed in series (Figure 7.7). After field installation, only two FBG settlement tubes had signals, which were located at the first 2 m in the borehole A. This might be caused by the damage or excessive bending of the optical fiber cables.

7.2.3 FBG in-place inclinometers

Two FBG in-place inclinometers of 12 m shown in Figure 7.8 were placed horizontally in the soil 100 mm underneath the mat foundation. Totally 36 FBG sensors were adhered to each PVC casing and used to measure the tensile strains along the casing, as shown in Figure 7.9. Unfortunately, some FBG strain sensors were broken during installation and construction. The cables of casing No. E and No. F were damaged by the labors on site when they removed the concrete formworks.

7.3 MONITORING RESULTS AND ANALYSIS

7.3.1 Concrete strains inside the slab

During the construction stage, the field measurements were carried out every week and the monitoring intervals were reduced gradually according to the weather condition and construction rates.

The monitoring results of strain and temperature sensors inside the concrete slab are shown in Figure 7.10 to Figure 7.11. Figure 7.10 presents the monitoring results during concrete pouring of the mat foundation. It was observed that, the Bragg wavelengths of all the FBG sensors increased suddenly. Because the stiffness of concrete before initial setting was small and no strains occurred inside the concrete, the increase of wavelengths was mainly due to the rise of temperature. The discrepancy of the shift in wavelength for one of the FBG strain sensors and the temperature sensor nearby, shown in Figure 7.10(b), resulted from the thermal expansion of the aluminum tube.

Figures 7.11 and 7.12 are the monitoring results of strains inside the concrete after the foundation construction has been completed. The results indicate that the tensile strains inside the concrete slab were in a low range and the mat foundation structure remained safe. The temperature variation inside the foundation is shown in Figure 7.12. It is found that the increase of temperature due to hydration heat was less than 40 ^{o}C. The dissipation of concrete hydration heat took about two months.

7.3.2 Ground settlements

The monitoring results of settlement tubes are shown in Figure 7.13. The wavelengths of settlement tubes No.1 and No.2 increased and decreased sharply in the initial stage, as a result of the generation and dissipation of concrete hydration heat. The wavelengths of the FBG sensors were temperature-compensated by the readings of the tube packaged FBG temperature sensor. The measured settlements were shown in Figure 7.13(c). It should be noted that the settlements presented here were the compression of soil layer of 1 m thickness, i.e. the gauge length of the settlement tubes.

7.3.3 Settlement profiles of the ground surface

Several FBG sensors on the inclinometer casings were damaged after field installation. The strains monitored by all the survived FBG sensors are shown in Figure 7.14. The results show that all the strains measured by FBGs are smaller than 1000 με. It is indicated that the deflections in the ground soil were small. With the use of linear interpolation and numerical integration, the settlement profiles were calculated and shown in Figure 7.15. It is founded that prior to superstructure construction, the FBG inclinometers measured considerably large settlements. This can be explained by the compression of the cushion layer and stress concentration of the inclinometer casings at the initial condition. To eliminate the possible errors, the settlements were set to zero when the wavelength of most FBG sensors became stable (6 Mar 2007). Because temperature effect was significant, temperature compensation of FBG sensors were also conducted. The maximum settlement after 6 March 2007 is only 3.7 mm.

7.3.4 Discussions

From the above monitoring results, the mat foundation is proved to be safe and no large total or differential settlements are observed. The FBG based sensors are proved to be effective in the geotechnical instrumentation. Due to the characteristics of optical fiber sensors, special protection shall be provided. Otherwise the stability and accuracy of the reading signals cannot be fully ensured.

Winkler ground model is frequently used in the design of mat foundations, in which the surface settlement of any point is only proportional to the support reaction/pressure on this unit area. Because of the simplicity in design, Winkler model has been widely used in engineering applications. However, this model does not take into account the continuity of deformation in ground soil and the shear stresses in foundation. Moreover, one shortcoming of this model is that the subgrade reaction must be assumed or modeled mathematically beforehand.

Research results show that the interaction between foundation and superstructure is an important issue that should be taken into account in foundation design. The foundation structures and ground soil should be modeled in one analysis problem.

7.4 SUMMARY

Based on the monitoring results, the following findings are obtained:

(1) The settlements within ground soil are found to be small according to the monitoring results of the FBG in-place inclinometers;

(2) From the settlements measured by the FBG in-place inclinometers and the two surviving FBG settlement tubes, most of the settlements occurred in the 1 to 2 m soil layer below the ground surface. No excessive total or differential settlements were observed during the whole monitoring period.

(3) The measured tensile strains inside the foundation structure were small and indicated a “health condition” of the mat foundation.

(4) The temperature rise due to concrete hydration heat was less than 40 ^{o}C. The dissipation of heat inside the mat foundation took about two months. For massive concrete construction, the adverse effect of hydration including cracking and reduced strength should be controlled carefully.

From these findings, we can conclude that the mat foundation remain stable and safe during the monitoring period. Moreover, this study indicates that when properly packaged and installed, FBG sensors can survive harsh conditions associated with foundation construction. The developed FBG sensors are suitable for achieving health monitoring of the mat foundation in practice.

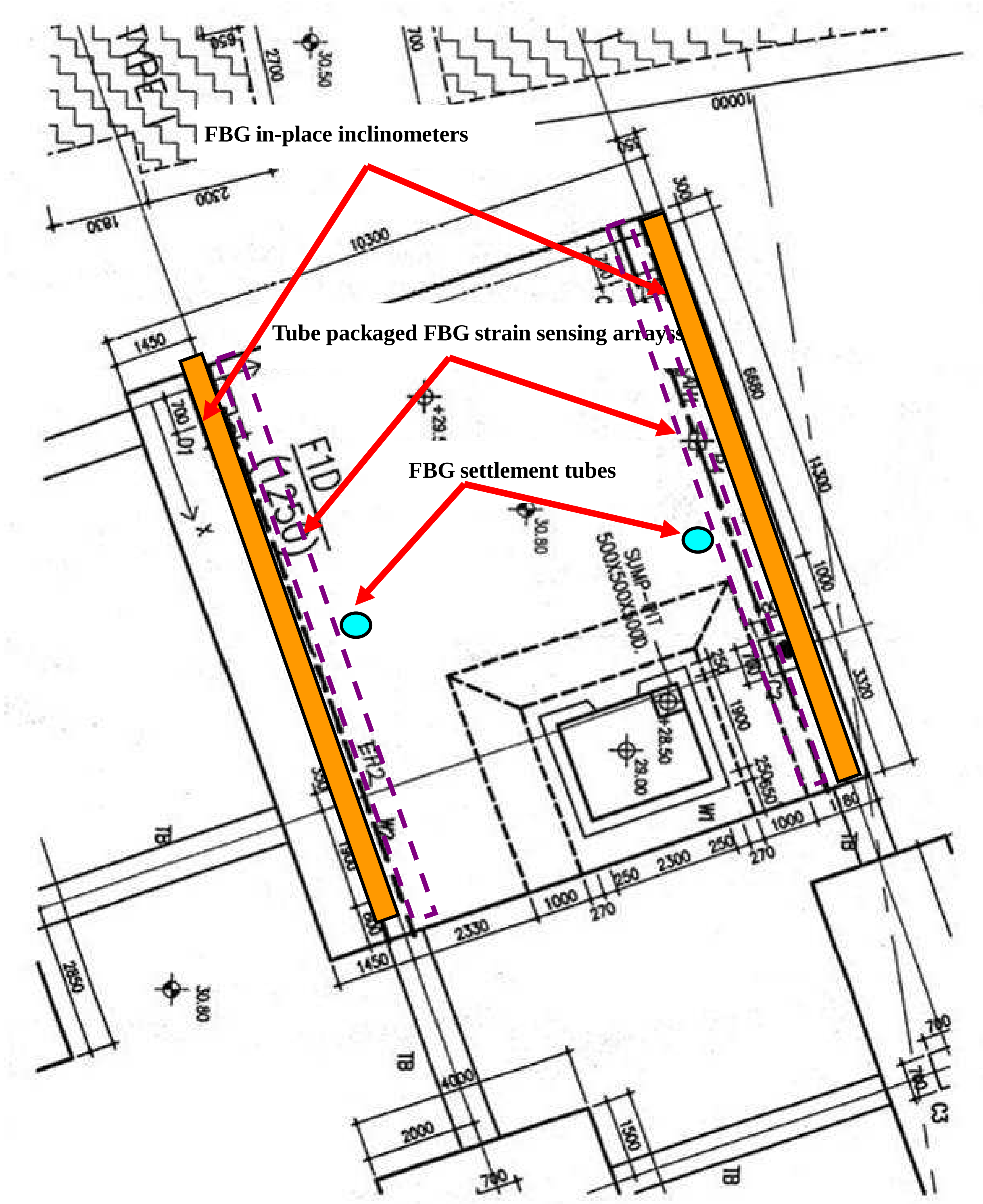

Figure 7.1 Arrangement of the instrumentation lines or points (plan view)

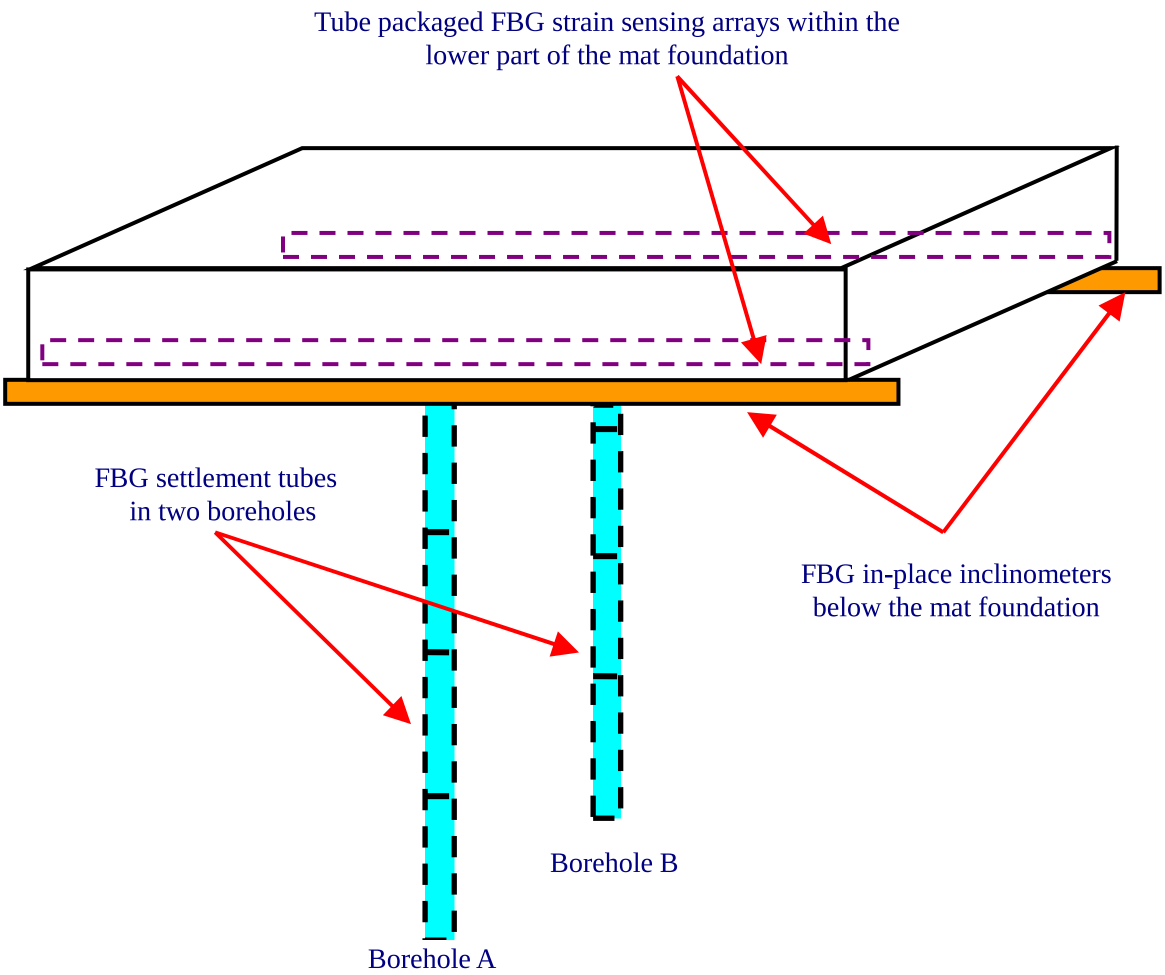

Figure 7.2 Arrangement of the foundation instrumentation lines (3-D view)

Figure 7.3 Photograph of the tube packaged FBG strain sensing arrays before field installation

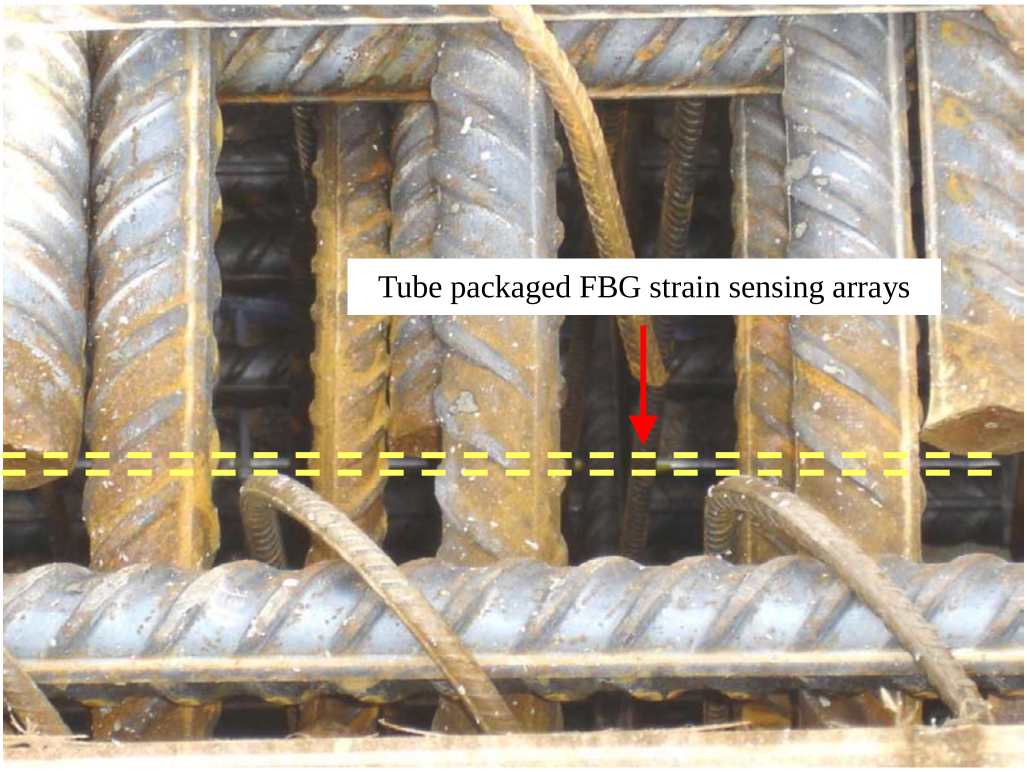

Figure 7.4 Field installation of the tube packaged FBG strain sensing arrays

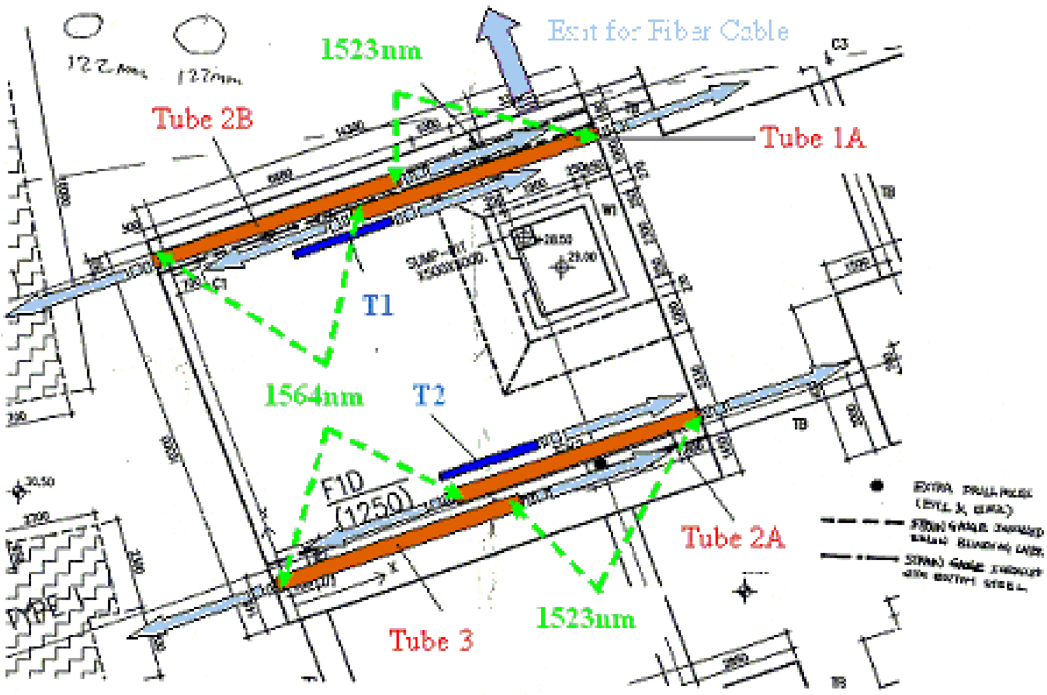

Figure 7.5 Location of all the tube packaged FBG strain sensing arrays inside the mat foundation

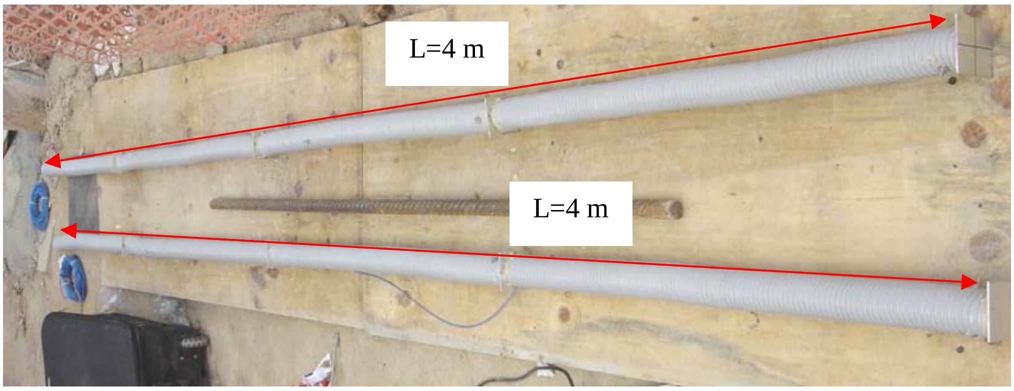

Figure 7.6 Photograph of the FBG settlement tubes on site before installation

(a) Preparation of a borehole for installing the FBG settlement tubes

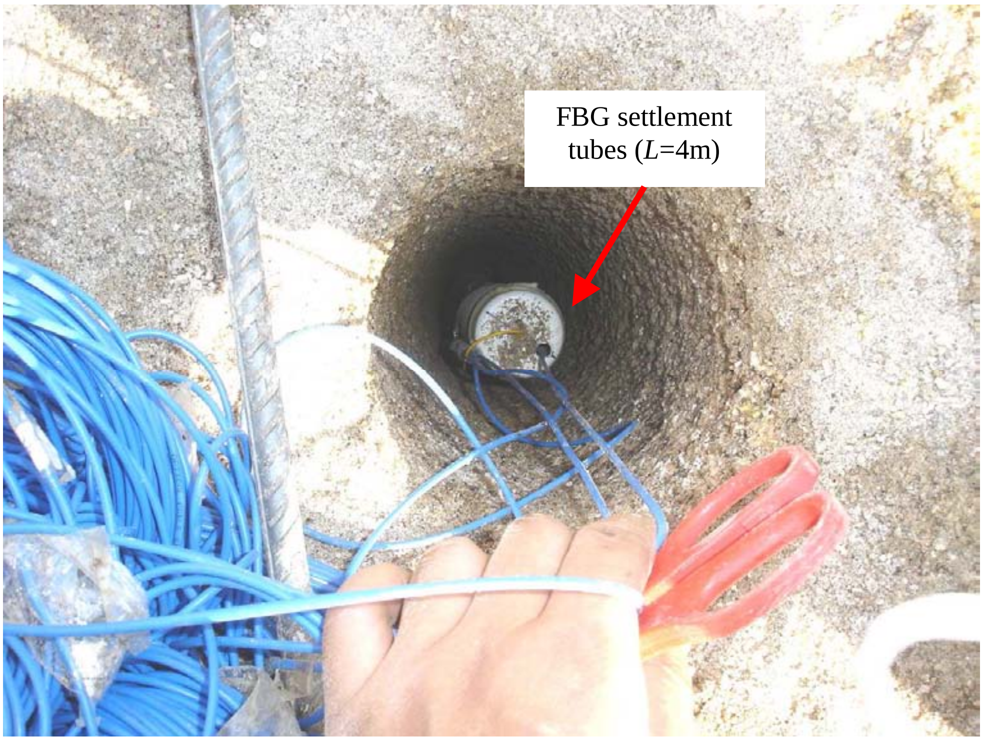

(b) Insertion of FBG settlement tubes into the borehole

Figure 7.7 Installation of the FBG settlement tubes on site

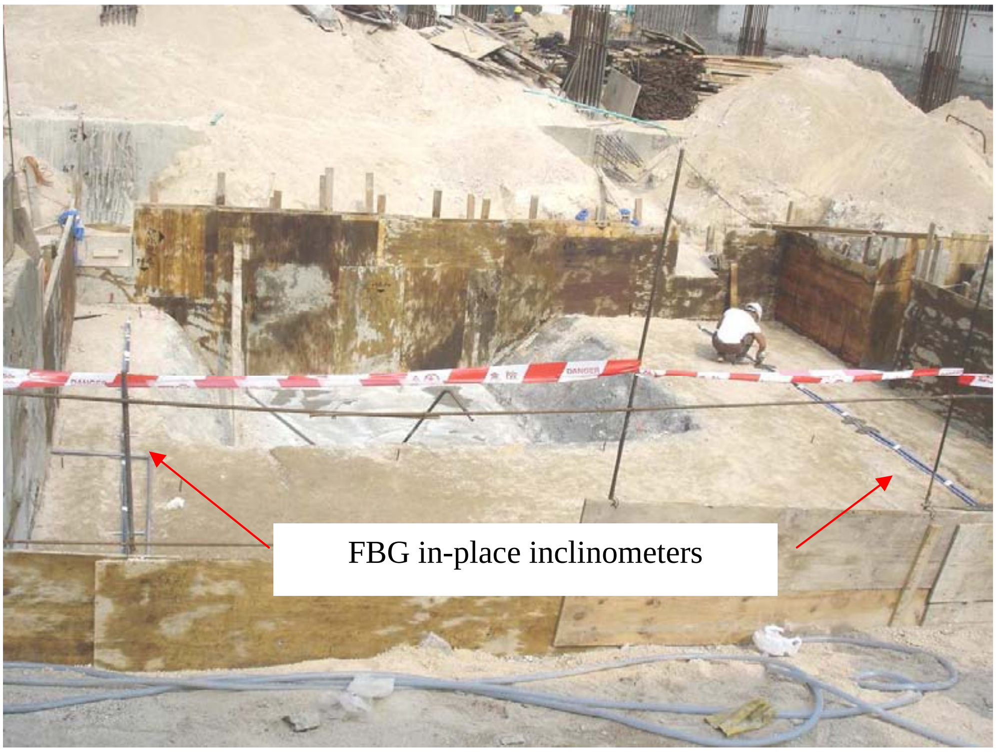

Figure 7.8 Installation of two sets of FBG in-place inclinometers on site

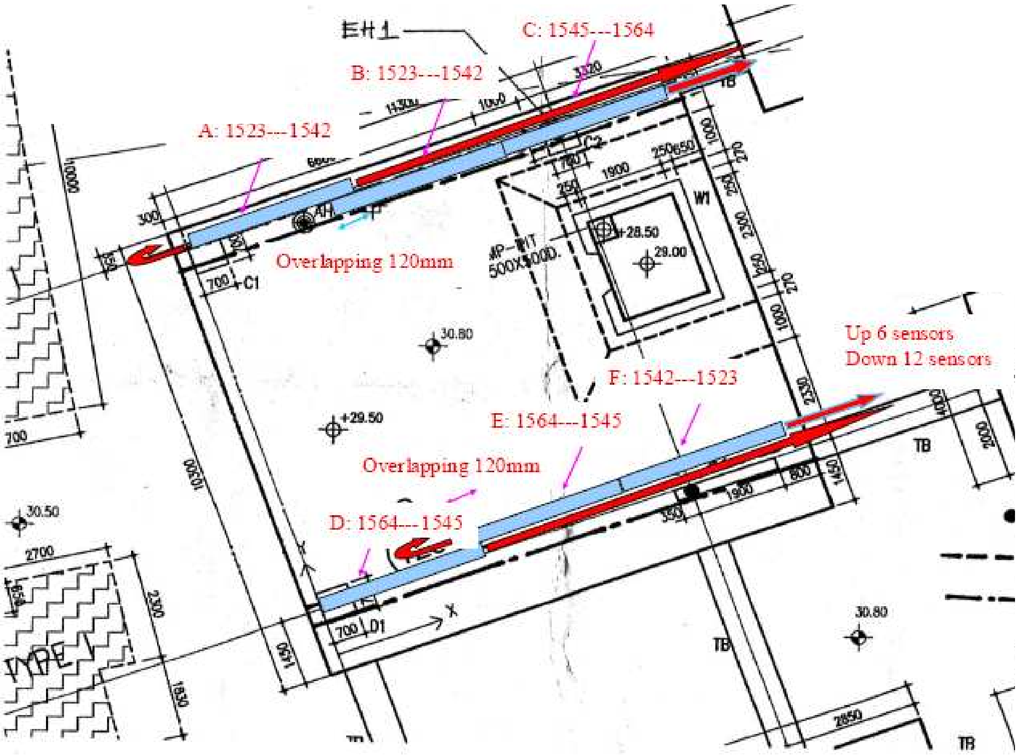

Figure 7.9 Location of the FBG in-place inclinometers underneath the mat foundation

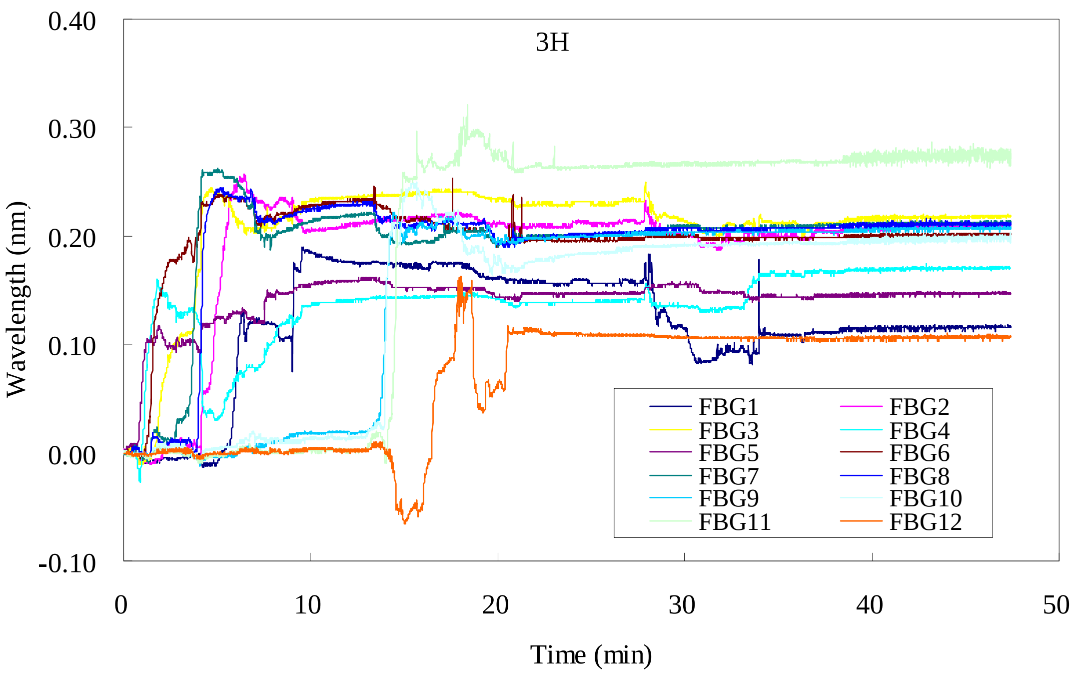

(a) Variation in the Bragg Wavelengths of the tube packaged FBG strain sensing arrays

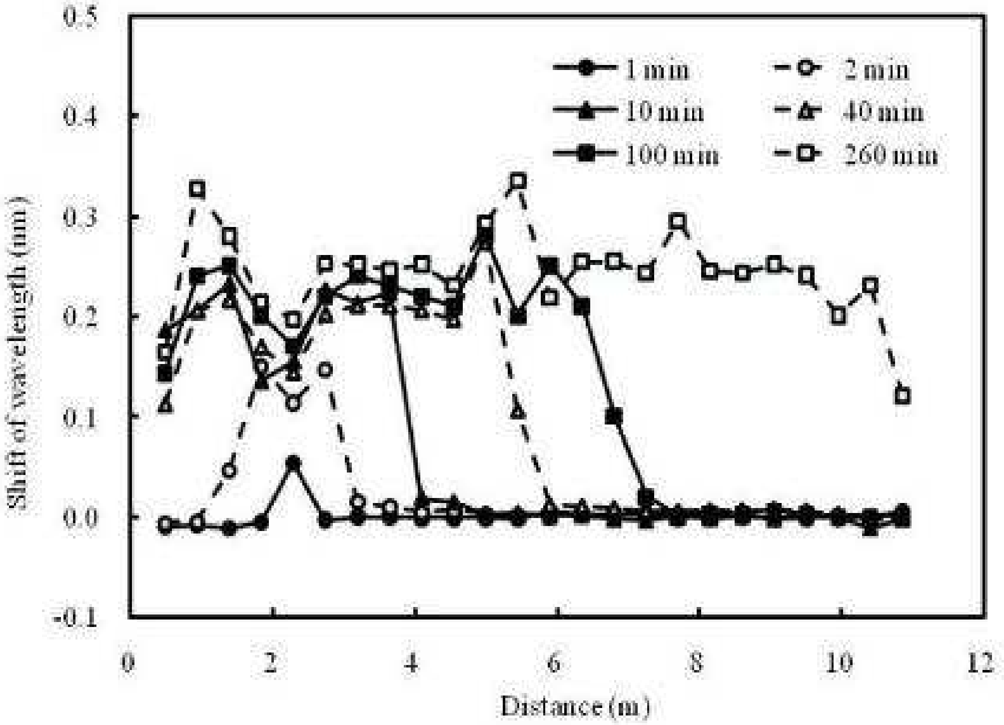

(b) Responses of the tube packaged FBG strain sensing arrays with respect to distance

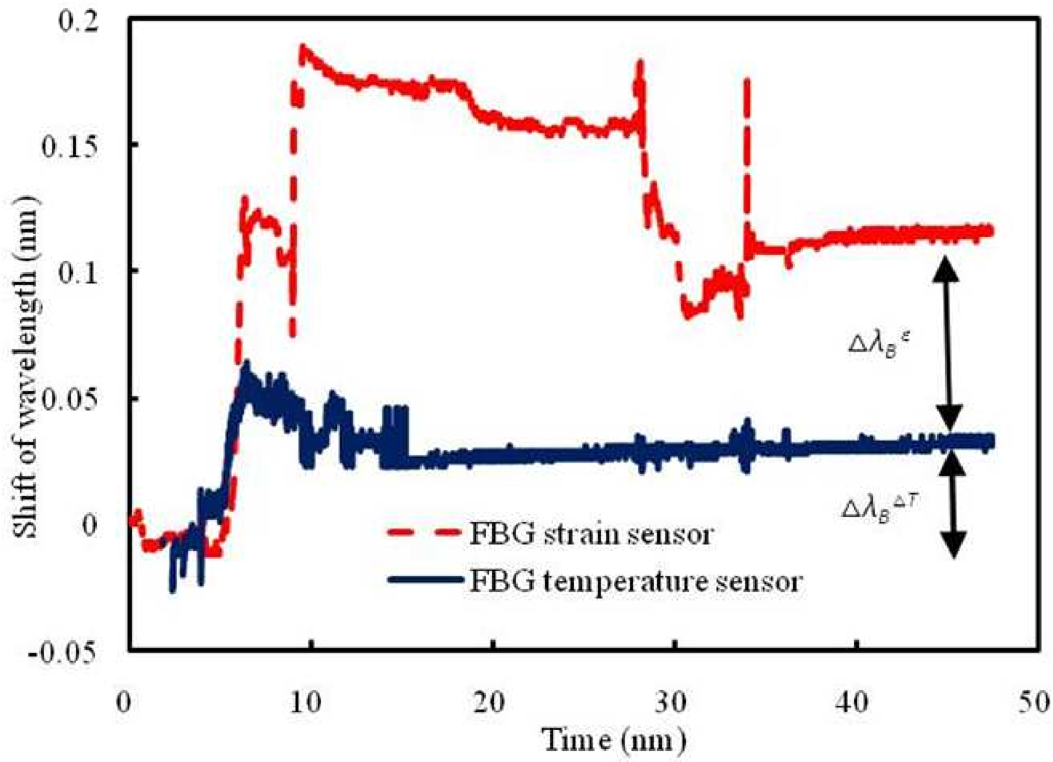

(c) Comparison of the wavelength variation between an FBG strain sensor and an FBG temperature sensor

Figure 7.10 Monitoring results of the tube packaged FBG strain sensing arrays and temperature sensor during concrete pouring

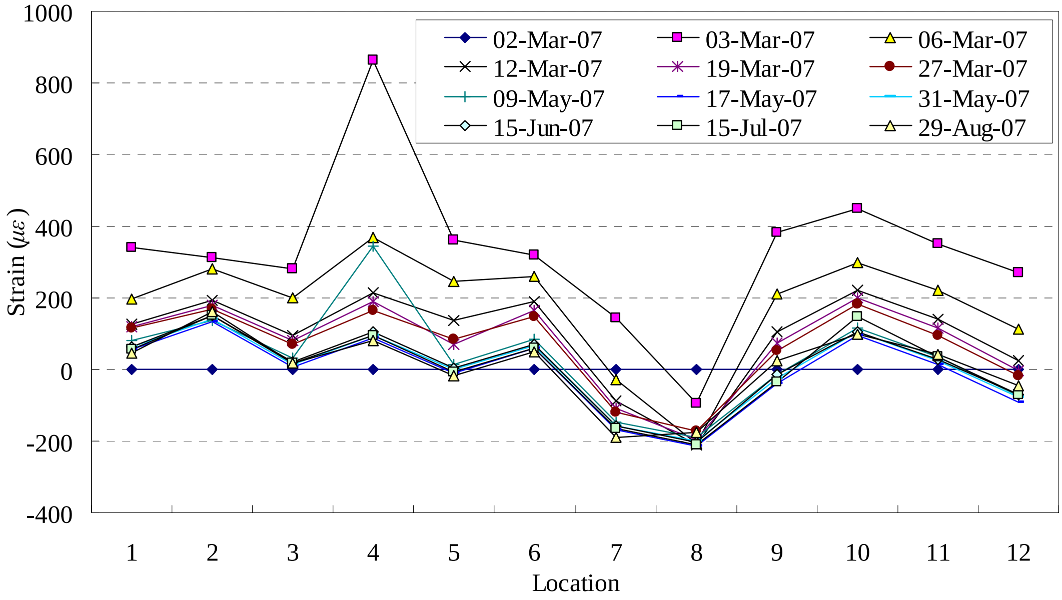

(a) Strains measured by the tube packaged FBG strain sensing arrays No. 2A

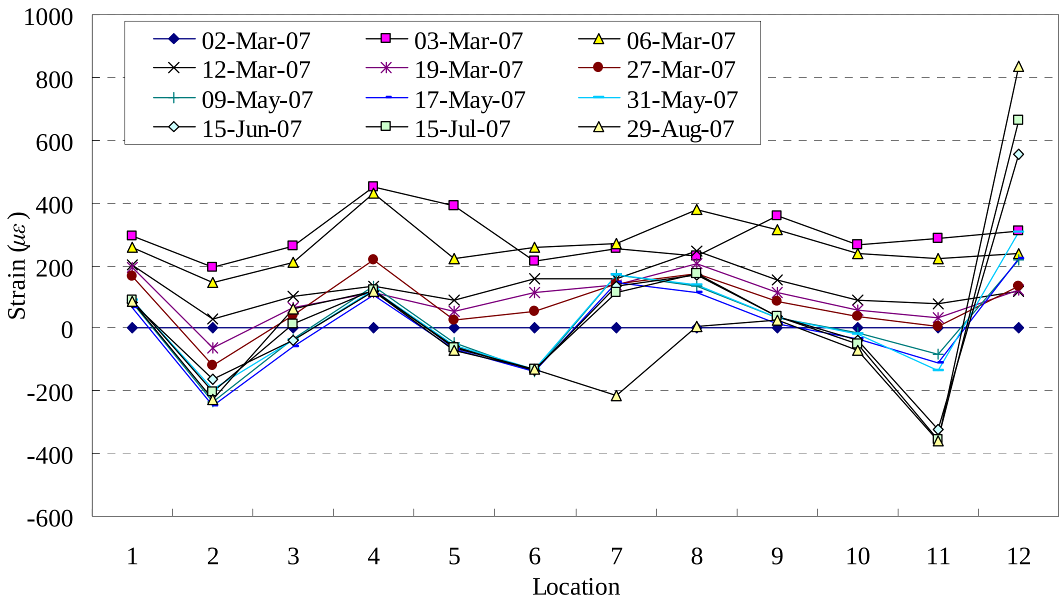

(b) Strains measured by the tube packaged FBG strain sensing arrays No. 2B

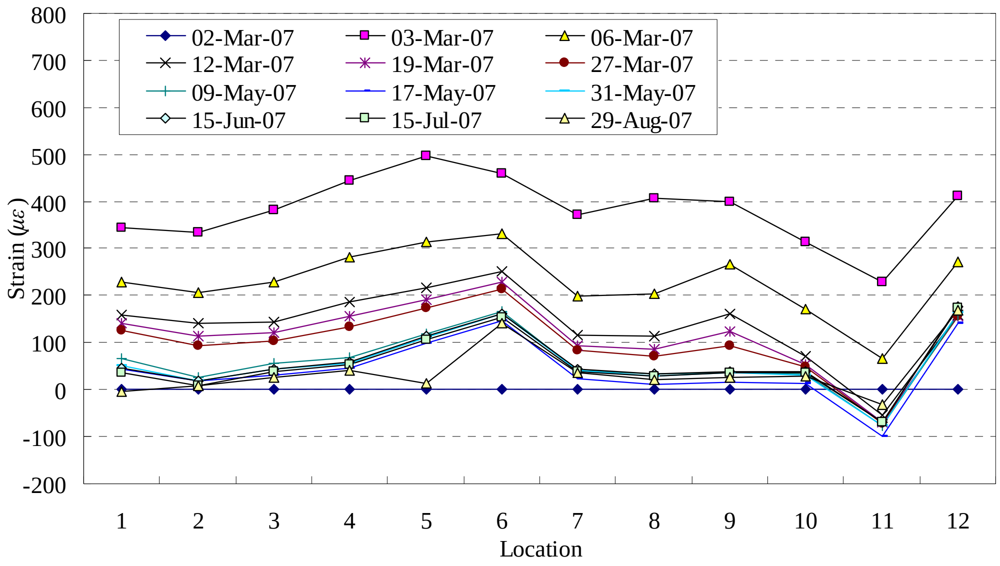

(c) Strains measured by the tube packaged FBG strain sensing arrays No. 3

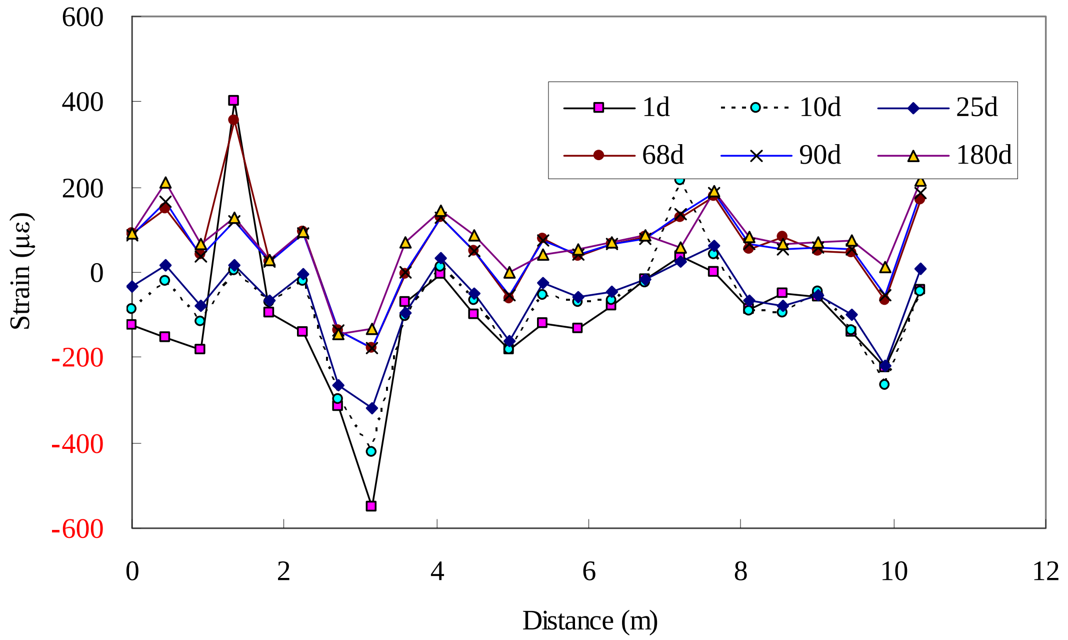

(d) Strain distributions along the tube packaged FBG strain sensing arrays No. 3 and No. 2A

Figure 7.11 Measured strains inside the concrete slab

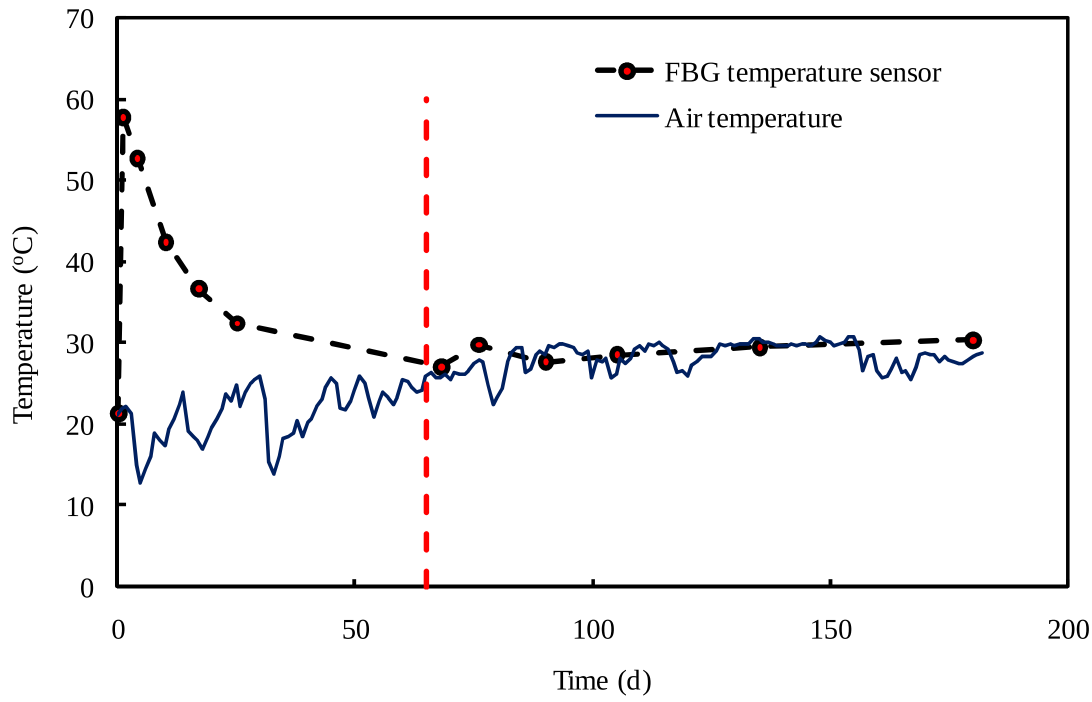

Figure 7.12 Monitoring results of temperature inside the concrete slab

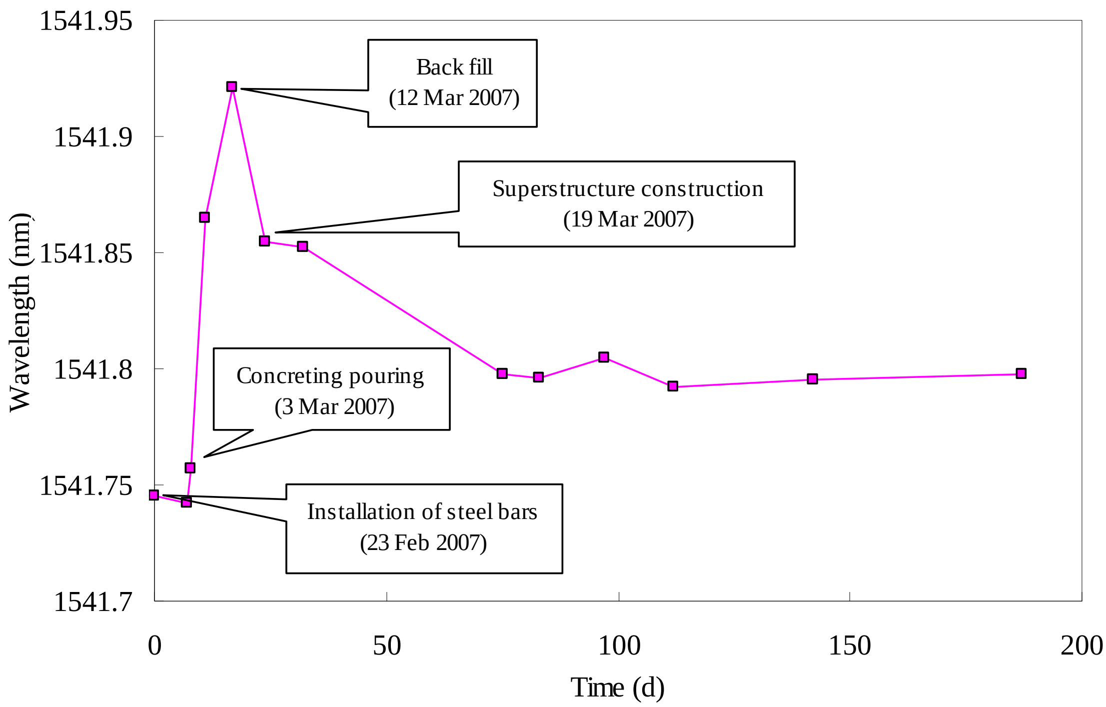

(a) Measured wavelength variation of settlement tube No. 1 (2 m depth)

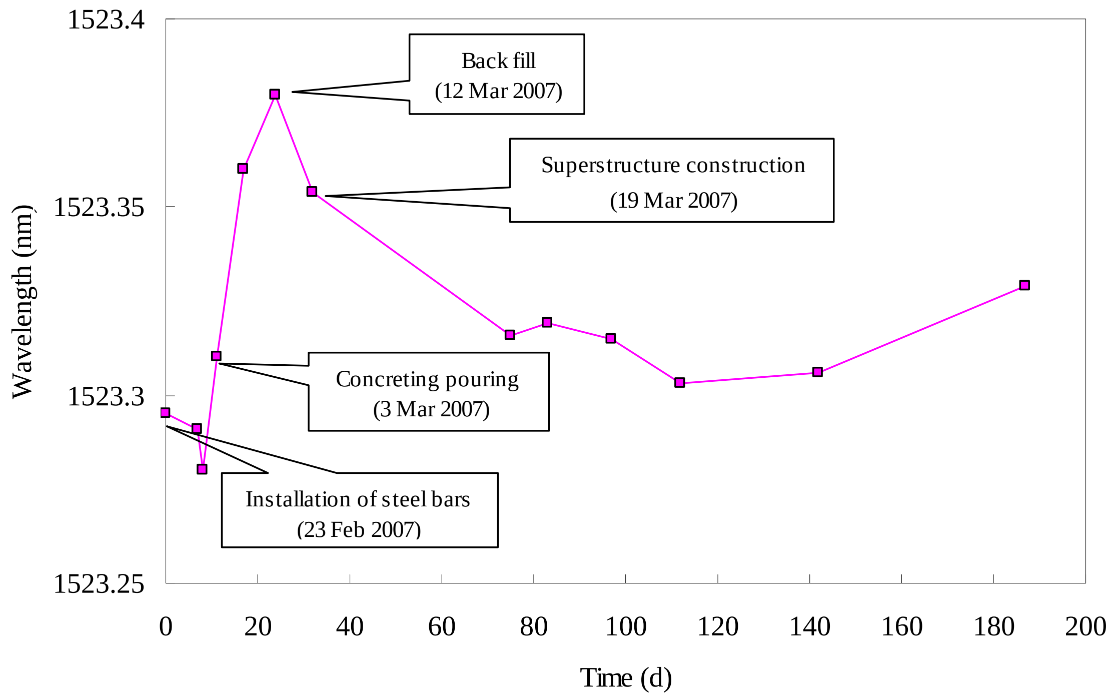

(b) Measured wavelength variation of settlement tube No. 2 (1 m depth)

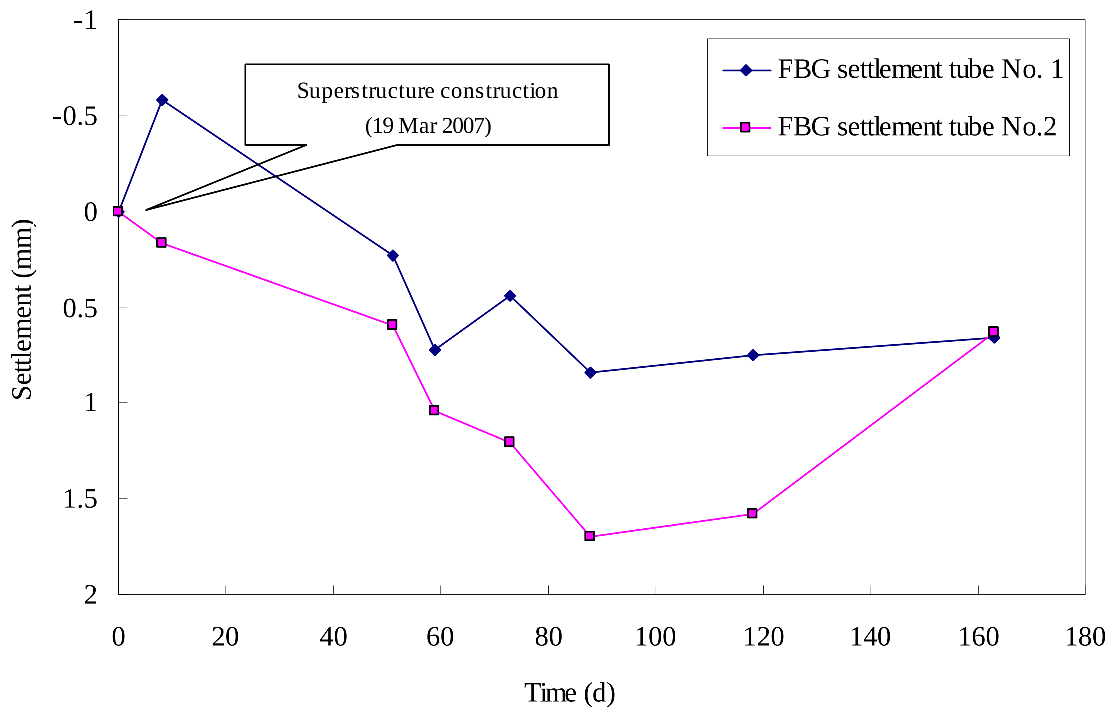

(c) Settlement-time relationship measured by settlement tubes No. 1 and No. 2

Figure 7.13 Monitoring results of the FBG settlement tubes

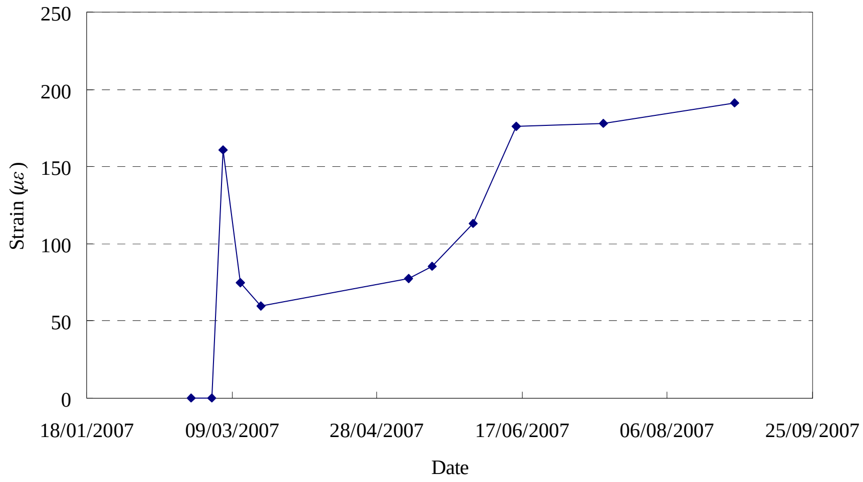

(a) FBG No. 7

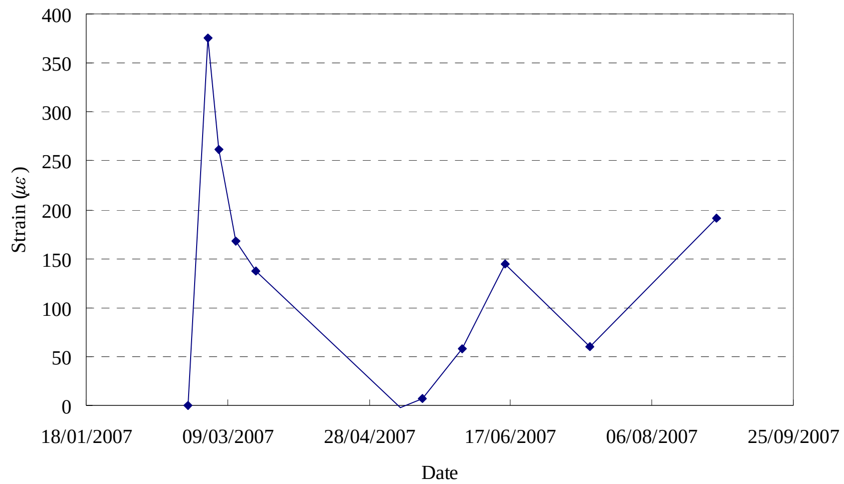

(b) FBG No. 13

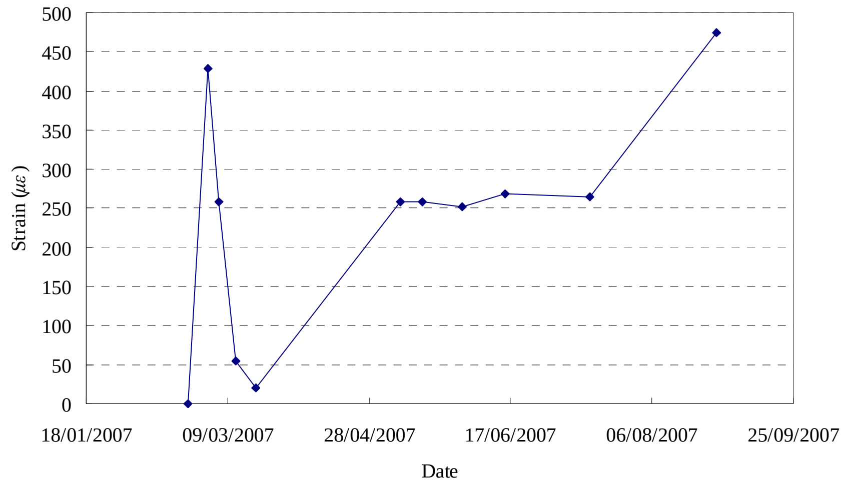

(c) FBG No. 14

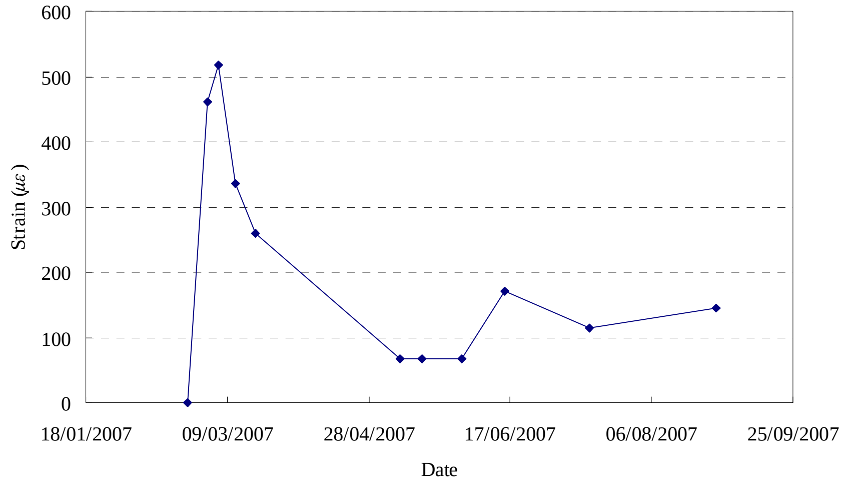

(d) FBG No. 15

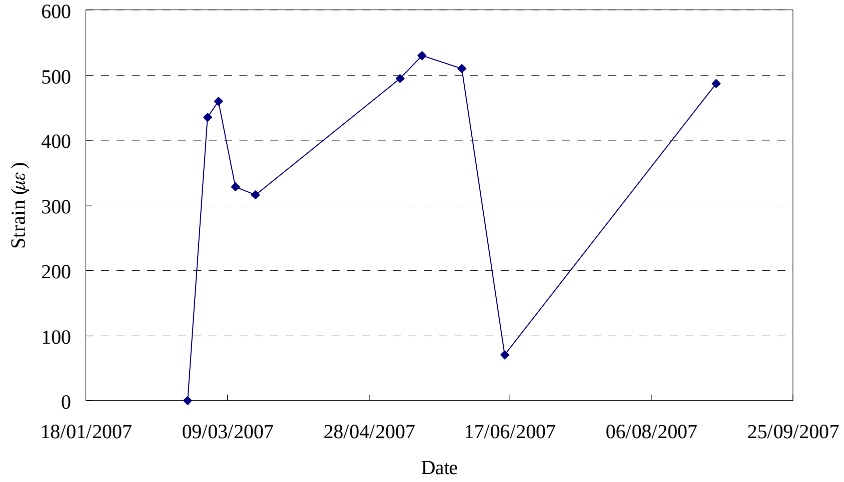

(e) FBG No. 21

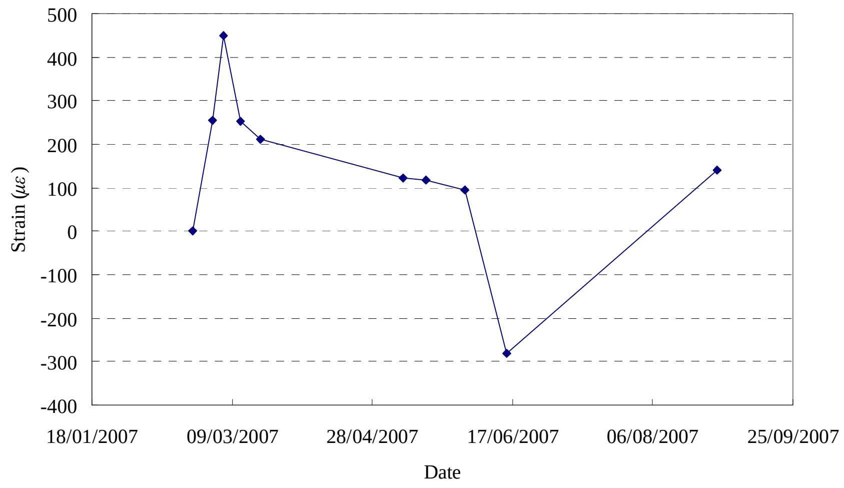

(f) FBG No. 22

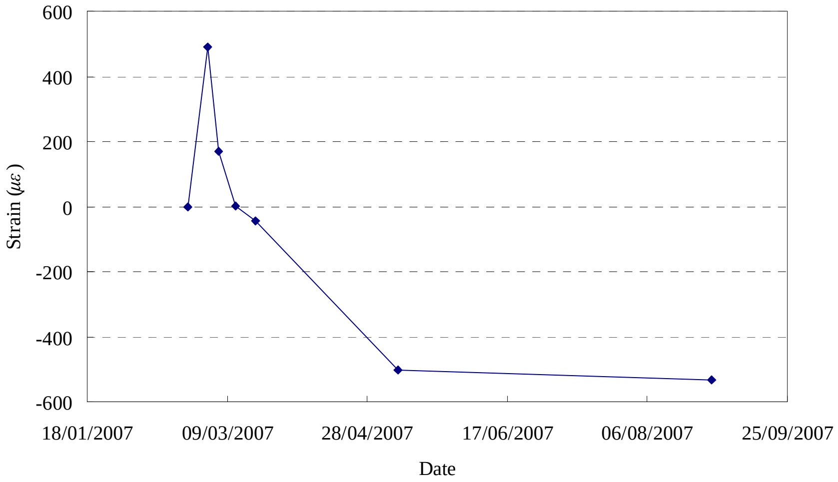

(g) FBG No. 23

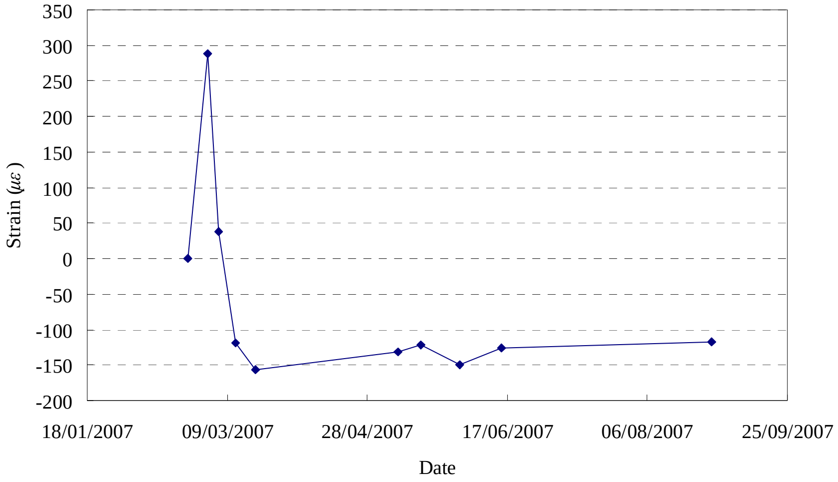

(h) FBG No. 24

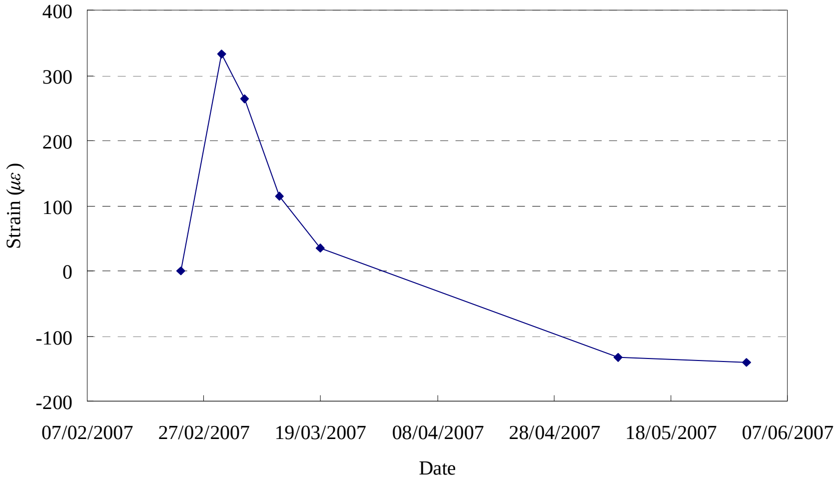

(i) FBG No. 29

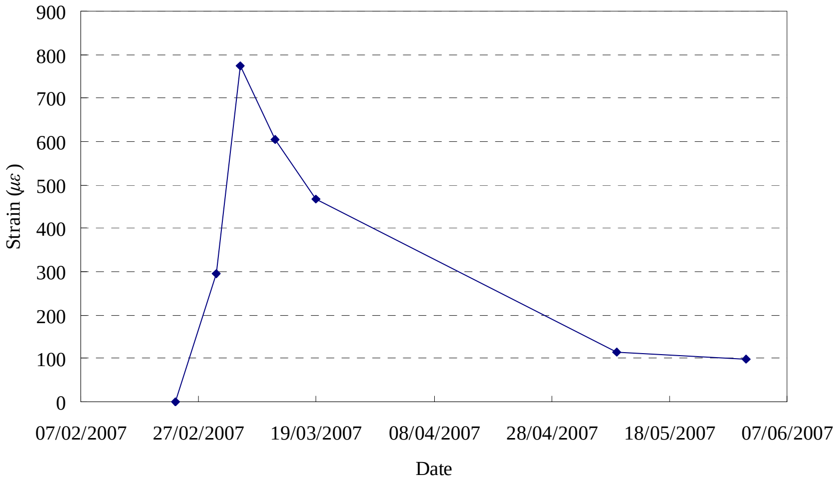

(j) FBG No. 30

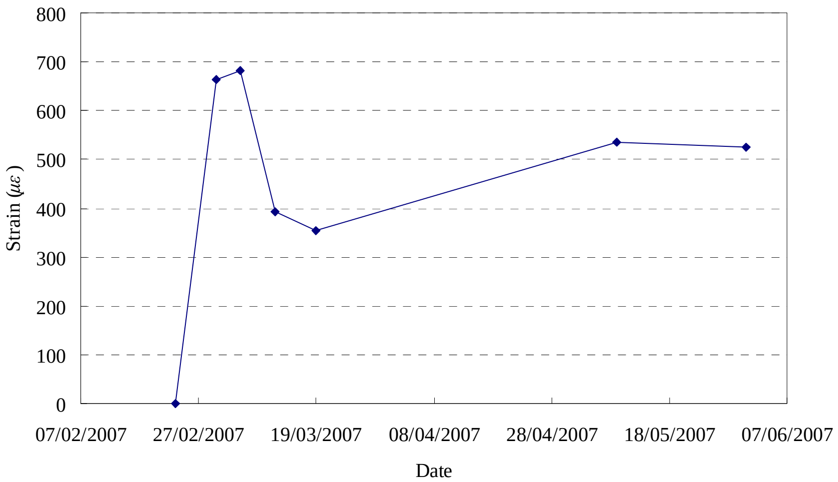

(k) FBG No. 31

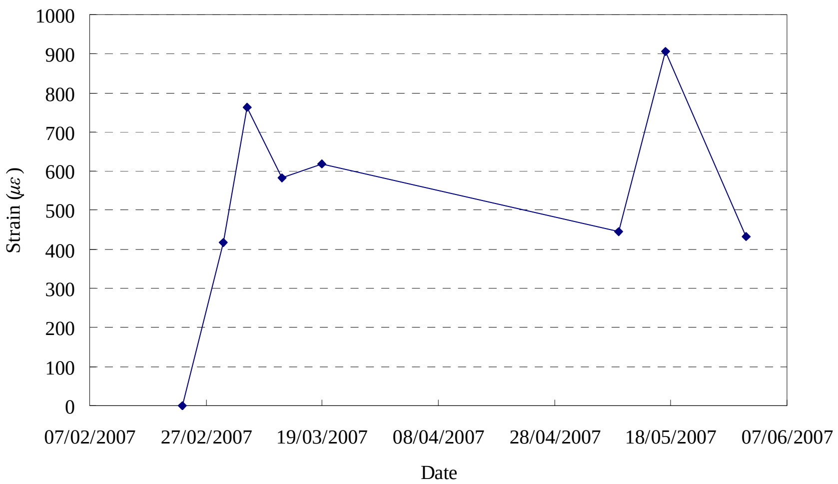

(l) FBG No. 32

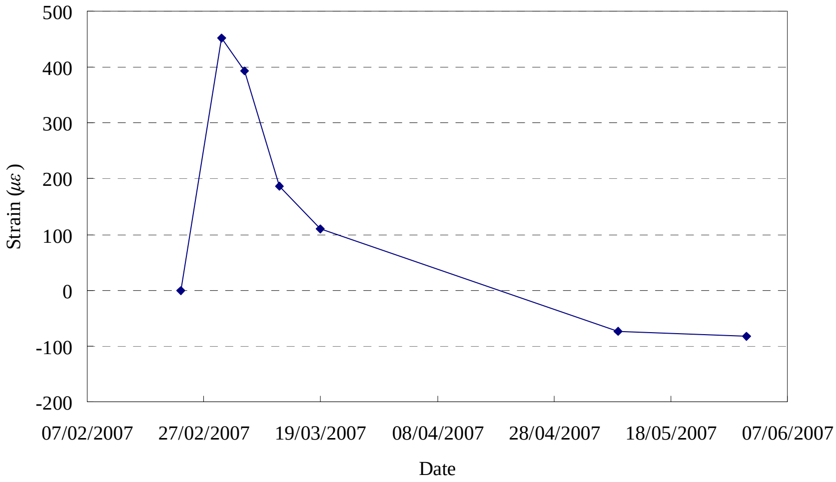

(m) FBG No. 33

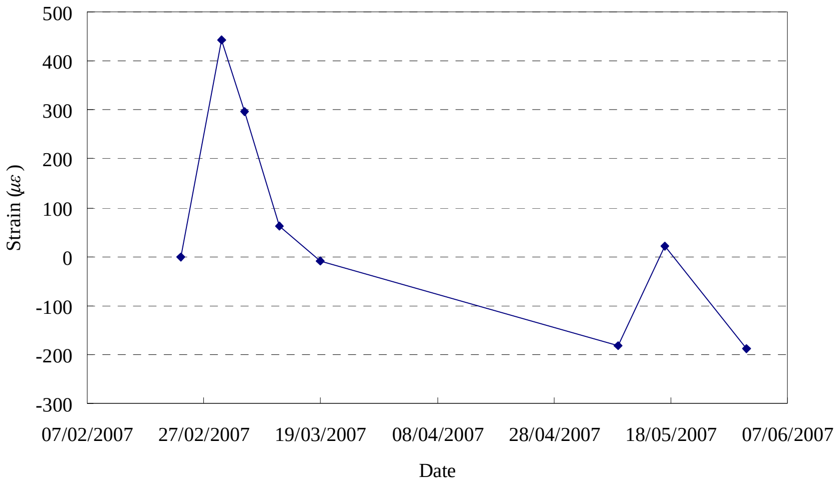

(n) FBG No. 34

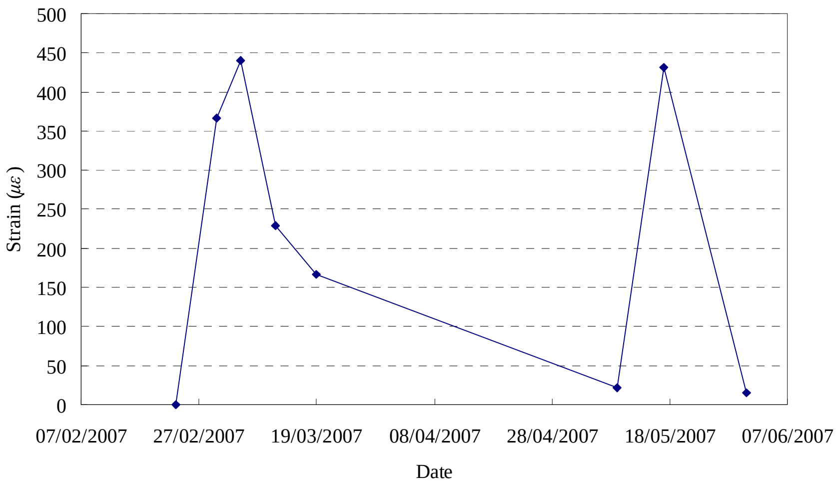

(o) FBG No. 35

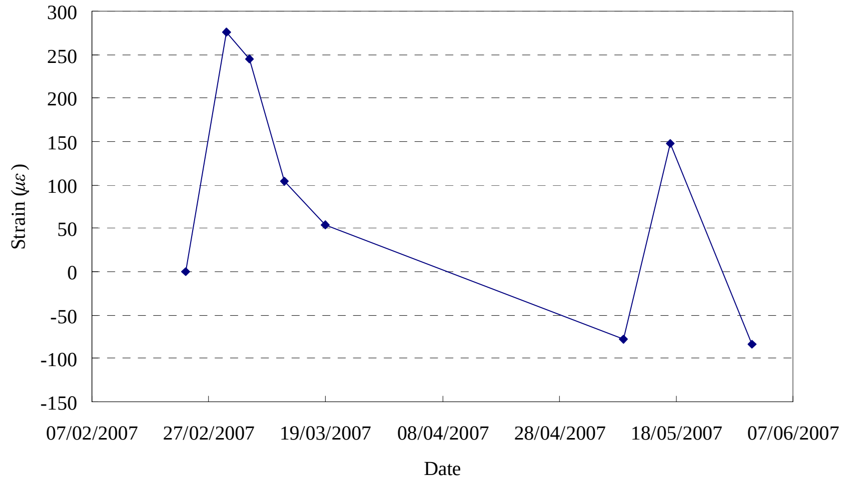

(p) FBG No. 36

Figure 7.14 Wavelength-time relationships of the FBG strain sensors on the in-place inclinometers

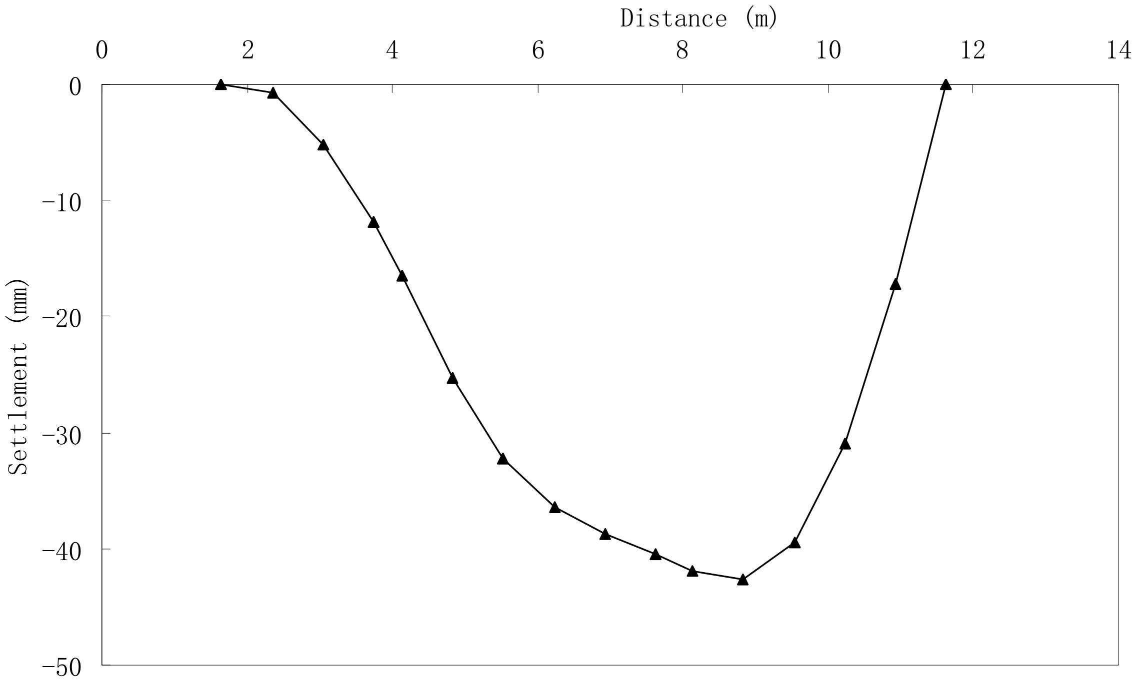

(a) Settlement profile measured prior to the superstructure construction stage (2 Mar 2007)

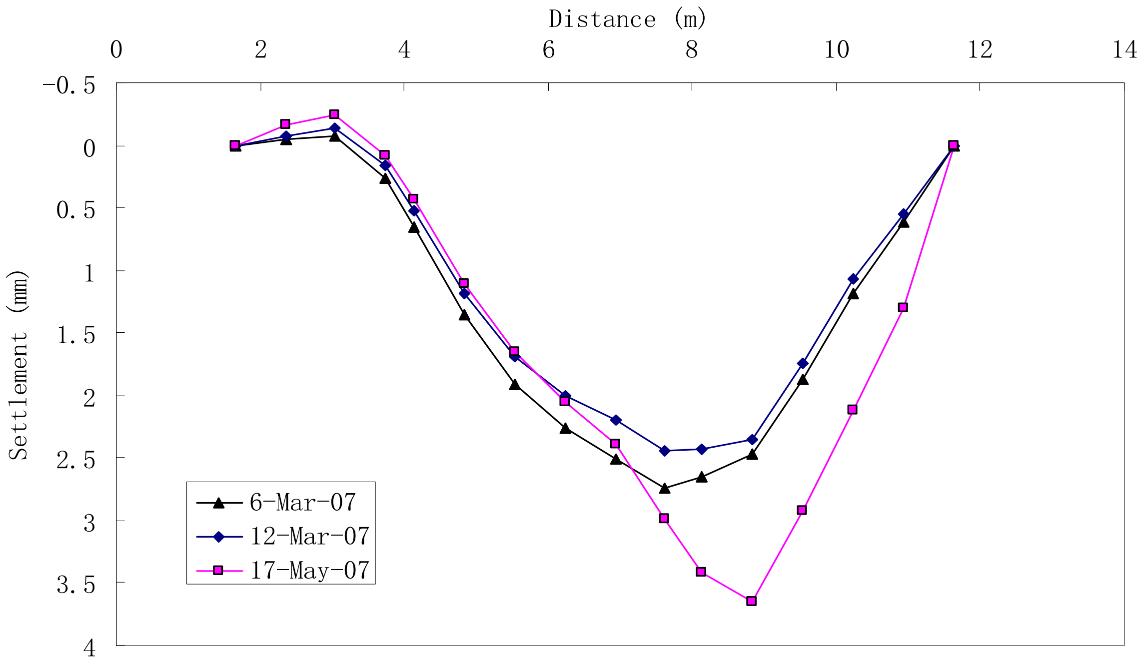

(b) Settlement profiles measured during the construction of superstructure

Figure 7.15 Monitoring results of settlement profiles under the mat foundation

CHAPTER 8:

FIBER OPTIC MONITORING AND PERFORMANCE EVALUATION OF A NEWLY STABILIZED SLOPE

8.1 INTRODUCTION

Long-term stability condition of slope is a complicated problem subject to the impact of rainfall, external loading variation, weathering of rock masses and so on. In Hong Kong, slope failure occurs frequently, especially in the rain season. Lots of engineering measures have been adopted to improve slope safety, but a number of issues in estimating slope stability condition are still not fully understood. For example, the rainfall infiltration has been recognized as an important factor to affect the stability of unsaturated soil slopes (Fredlund and Rahardjo 1993; Gasmo et al. 1999; Ng et al. 2003; Li et al. 2005a; Zhang et al. 2006). However, few researches have been conducted to study the effect of rainfall on structural components that are used to stabilize slopes.

As stated in Chapter 2, existing techniques for slope monitoring have limitations including low accuracy, poor durability and difficulty of integration. To meet the requirements of practical projects, FBG technology can be incorporated into a slope monitoring system to perform automatic monitoring of slope movements, strains and stresses of structural components in slopes, etc. In the light of the characteristics of slopes and requirements in geotechnical engineering, the application of FBG technology to field slope monitoring is presented and discussed in this chapter. A highway slope in Hong Kong has been instrumented with different types of FBG sensors developed by the author. Field installation techniques of these sensors are presented. Long-term monitoring data collected after the stabilization of the slope are presented and analyzed. The role of rainfall in affecting the loading condition of slope stabilizing components and the variation of slope movements are further discussed.

8.2 PROJECT BACKGROUND

The slope site under investigation is located at Luk Keng Road, Sheung Shui, New Territories, Hong Kong (Slope Registration No. 3NE-C/C135) (Figure 8.1). This government owned highway slope has a height of 10 m, a length of 51 m, and a slope angle of 35^{o}.

The geological conditions of the slope site are shown in Figure 8.2. In this area, the topography is diverse and the soil and rock masses are deeply weathered. In rain seasons, intensive rainfall will induce the surface infiltration process and the abrupt rise of ground water lever. The ground water lever is also affected by the tidal effects of Sha Tau Kok Hoi. Previous monitoring data reveal that the slope is subject to lateral movements back and forth, and localized deformation and failure has been observed in the vicinity of the slope toe. The potential instability of the slope poses a threat not only to the normal operation of the road transportation, but also to the safety of nearby residents. Therefore, the government has commissioned a local contractor to carry out slope stabilization measures, including soil nailing, anti-slide pile, and drainage facilities. To monitor the impact of construction work and provide early warning of impending failure, a fiber optic monitoring system based on FBG technology has been installed in this slope site, as well as the conventional monitoring systems installed by other companies.

8.3 FIELD INSTRUMENTATION

8.3.1 An FBG in-place inclinometer

The instrumentation details of the fiber optic monitoring system at this slope site are illustrated in Figure 8.3. The previous monitoring data indicate that, there may be a number of circular-shaped sliding surfaces within the slope. The locations and shapes of the sliding surfaces are varying dynamically with time. In order to determine the magnitude and direction of movements precisely and identify the critical sliding surface, a 150 mm-diameter and 15 m-long hole was drilled on the slope and an FBG in-place inclinometer was installed, as shown in Figure 8.4. The FBG inclinometer consists of a PVC casing with an outer diameter of 60 mm and an internal diameter of 50 mm and four surface glued optical fibers containing a series of FBG sensors. The FBG inclinometer was assembled in the field and grouted in the drillhole using a mixture of cement and bentonite. The monitoring results of the FBG inclinometer can be used to calculate the displacements in the *x* and *y* directions. The installation procedures are shown in Figure 8.5.

8.3.2 FBG strain sensors on a soil nail

In the slope stabilization work, a total of 4 rows of soil nails were installed. The nail length varies from 12 m to 14 m. The design axial force for each nail is in the range of 40 kN to 54 kN. The soil nails were installed in drillholes of 150 mm diameter. Plastic corrugated pipes were utilized in order to achieve double-layer anti-corrosion. In slope engineering, soil nails are used to resist the movement of slope masses above the sliding surface by tensile forces, and at the same time the soil nail will be subject to a certain extent of bending moments (Zhou et al. 2008). In order to capture the axial forces in the soil nails, a 14 m-long soil nail was instrumented with 20 surface glued FBG strain sensors on the upper and lower surfaces along the nail length. At the corresponding locations, 10 tube packaged FBG temperature sensors were also installed for temperature compensation, as shown in Figures 8.6 and 8.7.

8.3.3 FBG strain sensors on two soldier piles

In the slope stabilization work, the soldier piles installed at the slope toe were used to provide lateral loading to support the slope masses. They passed through the potential sliding surfaces and buried in a certain depth in the slope to provide anchorage. At the slope toe, 2 rows of 16 m-long soldier piles were installed at 1.8 m intervals, as shown in Figures 8.8 and 8.9. For the soldier piles, the main purpose of fiber optic monitoring is to verify their anti-sliding effect and provide long-term health monitoring. Therefore, two piles are selected to be instrumented with FBG sensors. The FBG strain and temperature sensors were glued on each of the two wings of the H-shaped steel pile. Based on the fiber-optic monitoring data, the bending moments and shear forces in the pile can be estimated.

8.4 MONITORING RESULTS AND ANALYSIS

In the slope site, the automatic data acquisition and wireless transmission were achieved using wireless Ethernet and Labview platform. Since March 2008, the monitoring work has been carried out. Figures 8.10 and 8.11 present the main monitoring data.

8.4.1 Strains on the soil nail

The monitoring results in Figure 8.10 indicate that the variation of tensile forces in the soil nail is shown to be consistent with monthly rainfall. This is mainly due to rainfall infiltration, which causes the increase of water content in soil masses and the rise of groundwater level, leading to the adjustments of stress fields and displacement fields. These phenomena are reflected in the soil nails, which provide bonding at the soil-nail interfaces. It can be seen that the stability condition of a soil nailed slope can be predicted through high-precision strain monitoring of the soil nails. If the maximum strains in the soil nails increase rapidly with respect to time, landslide may occur.

8.4.2 Strains on the soldier piles

For the soldier piles at the slope toe, since they are the main components to resist the downward forces, anti-sliding forces were found to increase gradually with time. The variation of strains of the soldier pile is not consistent with rainfall.

8.4.3 Slope movements

For the movements in the slope, the monitoring data show that the slope masses are not moving right in the *y* direction shown in Figure 8.3, but have a more complicated deformation pattern. However, the monitoring results indicate that the main sliding surface exists at a depth of about 9 m from the ground surface.

8.5 SUMMARY

The monitoring and early warning work in slope engineering is a long-term and difficulty task. Because the high-risk slopes are mainly distribtued far away from urban areas, the automation, integration, and remote data transmission in slope instrumentation is very important. Besides other technologies, FBG has high resolution, high resistance to EMI and multiplexible capacity and thus is suitable for establishing a slope monitoring system. The slope monitoring project introduced in this chapter provides a good example for verifying the feasibility of fiber optic sensing technology in field monitoring of slopes.

From the application point of view, fiber optic sensing technology in the area of slope instrumentation is still in trial period, and has not been widely recognized by civil engineers. Previous experiences indicate that, a team of experienced geotechnical engineers, optoelectronic engineers, and technical staff for field installation is a prerequisite for establishing a fiber optic monitoring system for geotechnical structures (Graver et al. 2004). In order to construct an effective, reliable and economical slope monitoring and early warning system, the advantages of fiber optic sensing technology should be fully utilized according to the slope conditions and monitoring requirements.

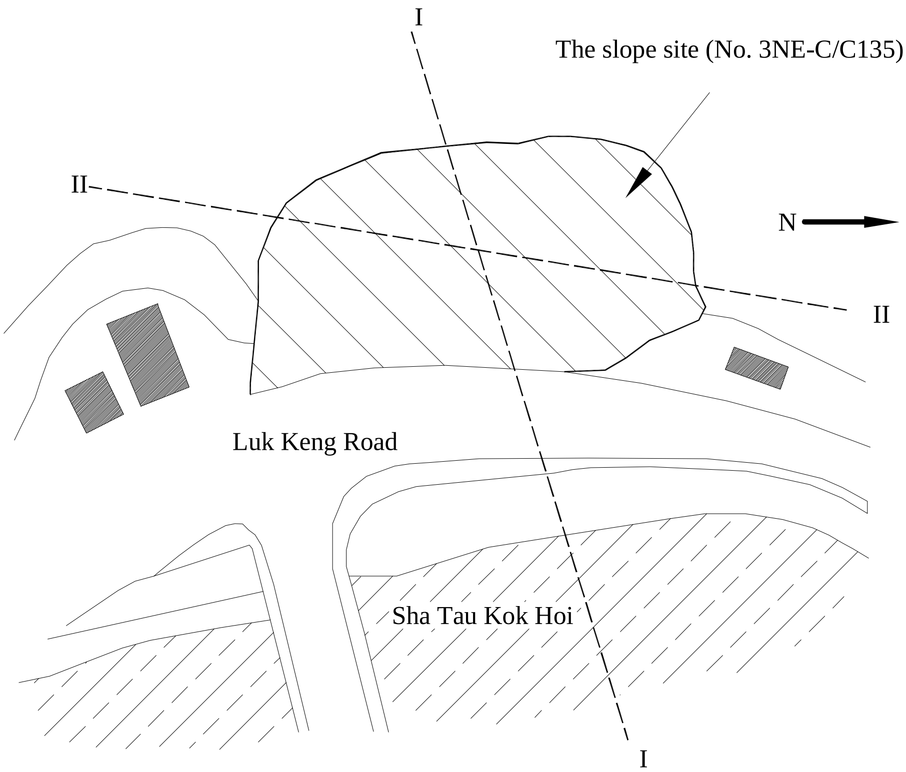

Figure 8.1 Location of the instrumented slope site

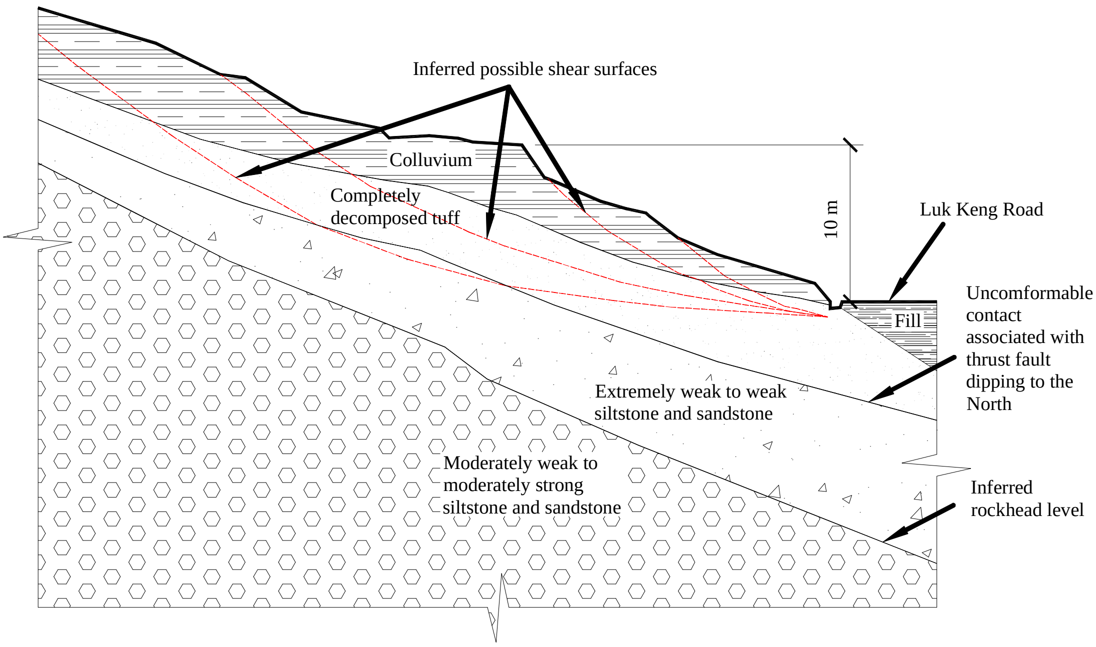

(a) Section I-I

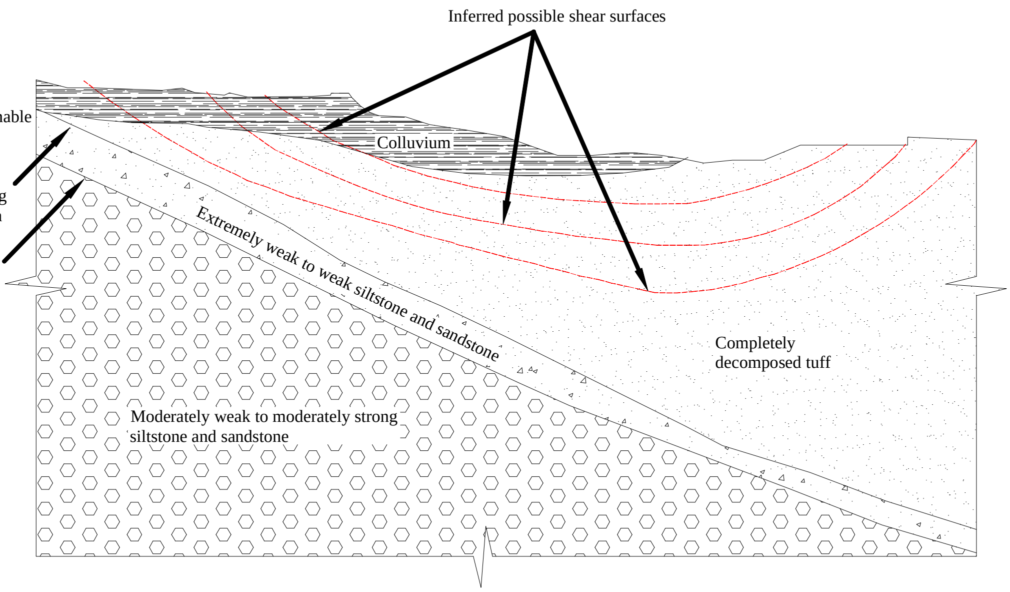

(b) Section II-II

Figure 8.2 Geological conditions of the slope site

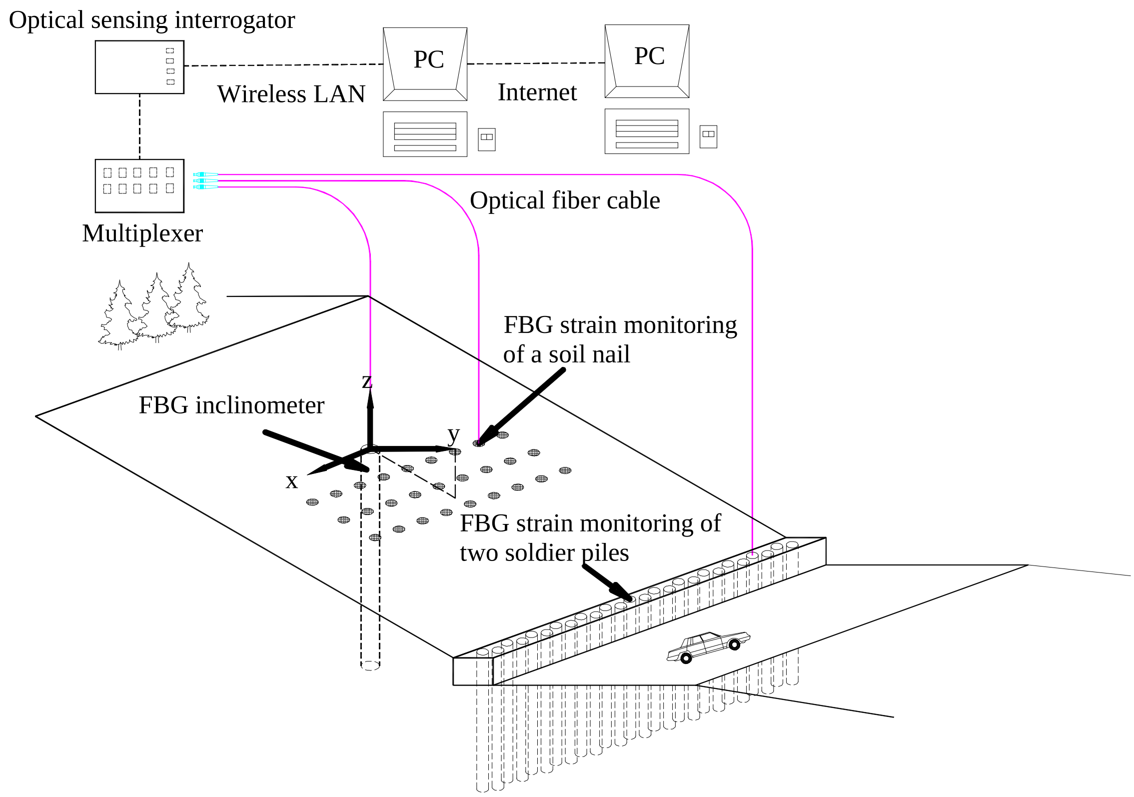

Figure 8.3 Illustration of the fiber optic instrumentation of the highway slope

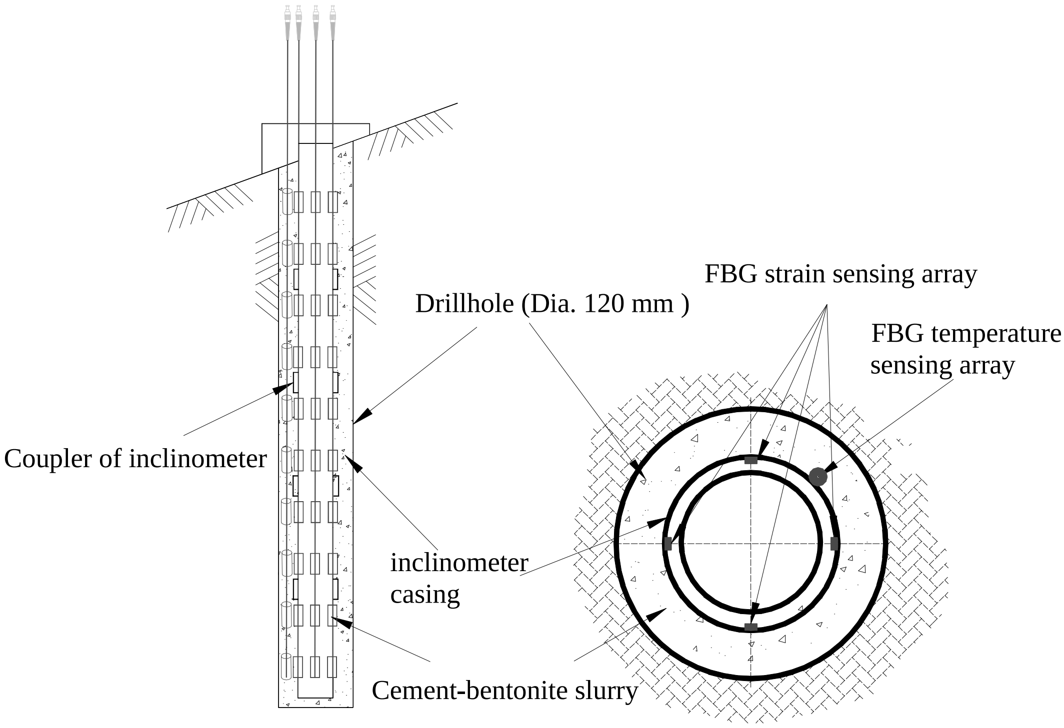

Figure 8.4 FBG in-place inclinometer installed in the slope

(a) Details of the FBG inclinometer prior to installation

(b) Inserting of the FBG inclinometer in the drillhole

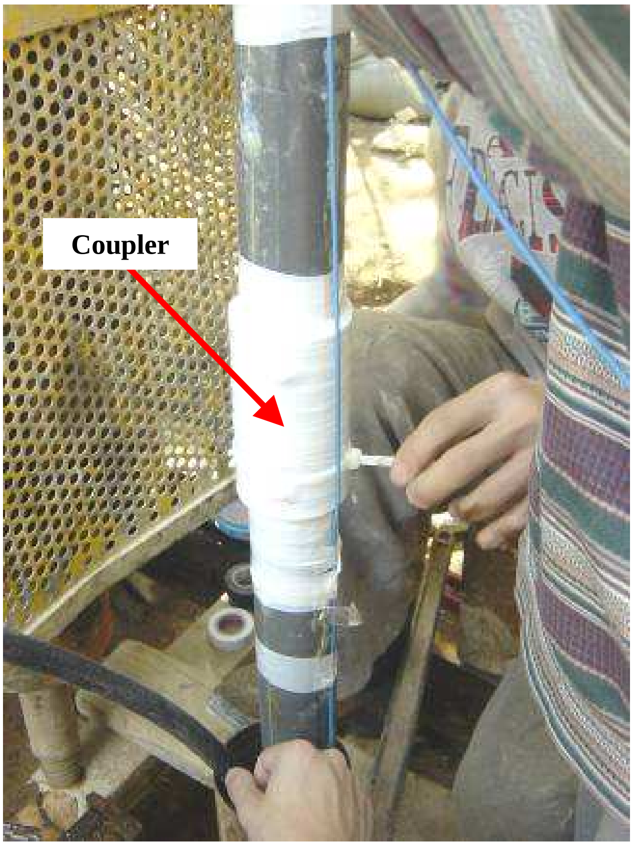

(c) Coupling of the FBG inclinometer

(d) Grouting of the drillhole

Figure 8.5 Photographs of the installation of the FBG in-place inclinometer

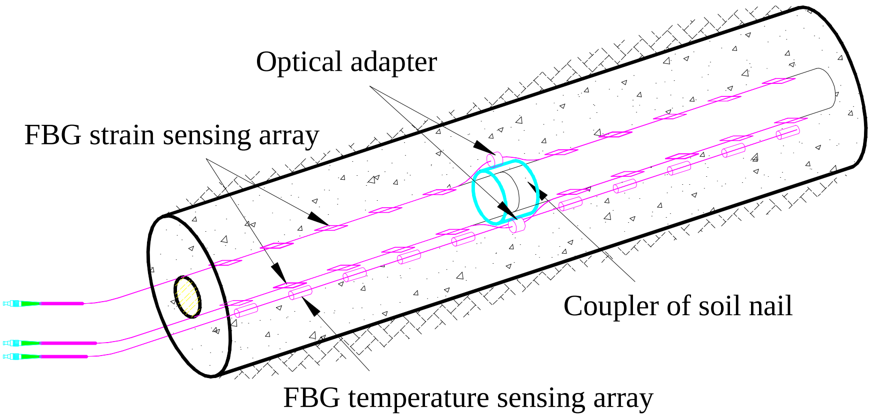

Figure 8.6 FBG strain sensors installed on a soil nail

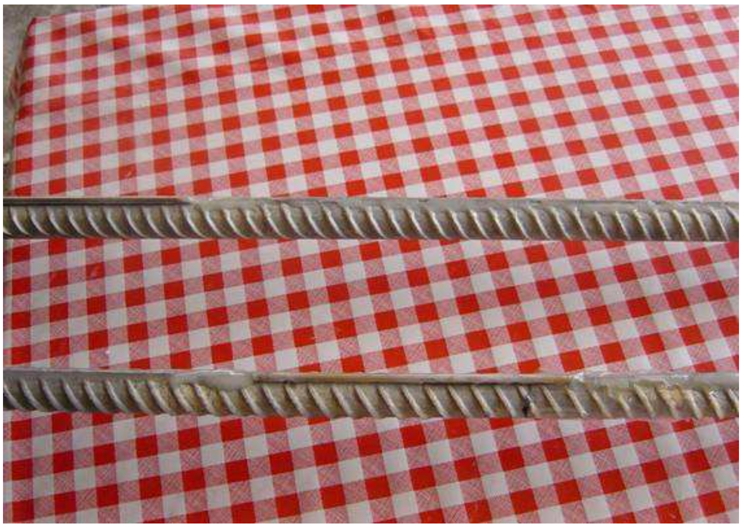

(a) Details of the soil nail instrumented with FBG strain and temperature sensors prior to installation

(b) Inserting the soil nail in the drillhole

(c) Connecting optical fiber cables at the coupling part

Figure 8.7 Installation of the instrument soil nail on site

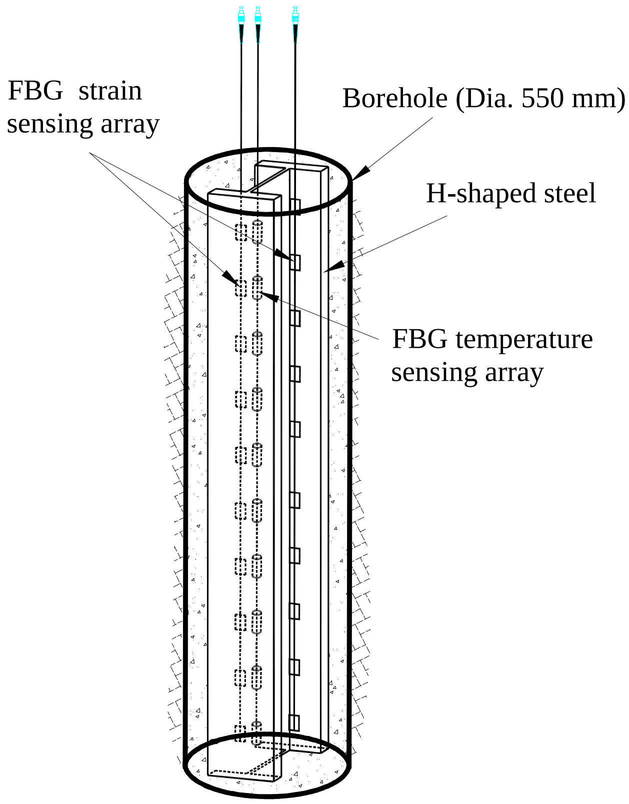

Figure 8.8 FBG strain sensors installed on a soldier pile

(a) Polishing of the H-shaped steel

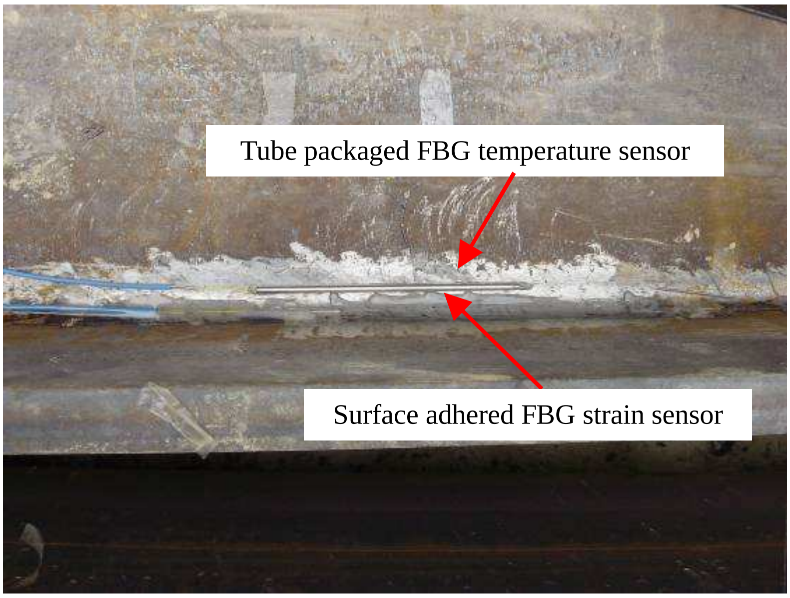

(b) Installation of FBG strain and temperature sensors

(c) Protection of optical fiber cables by PVC channels

(d) Embedding and grouting the H-shaped steel

(e) Constructed soldier-pile retaining wall

Figure 8.9 Photographs of the installation of the instrumented soldier piles

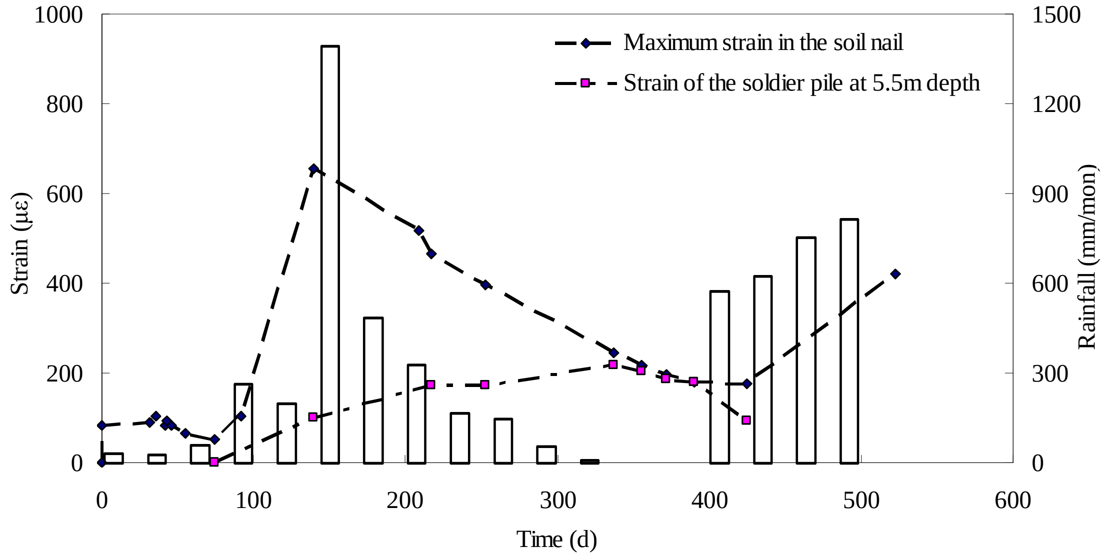

Figure 8.10 Monitoring results of the strains in the instrumented soil nail and one of the soldier piles by FBG sensors

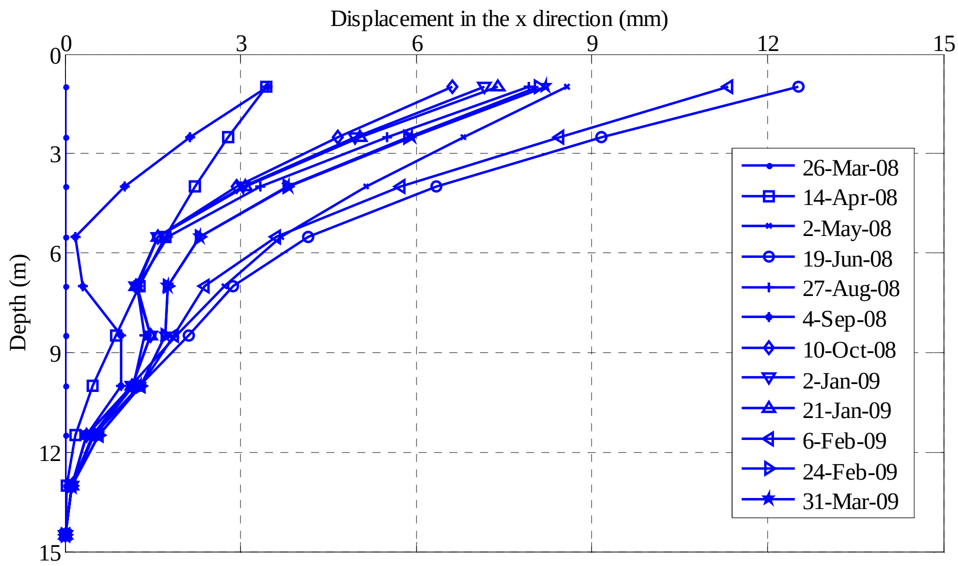

(a) Displacement in the *x* direction

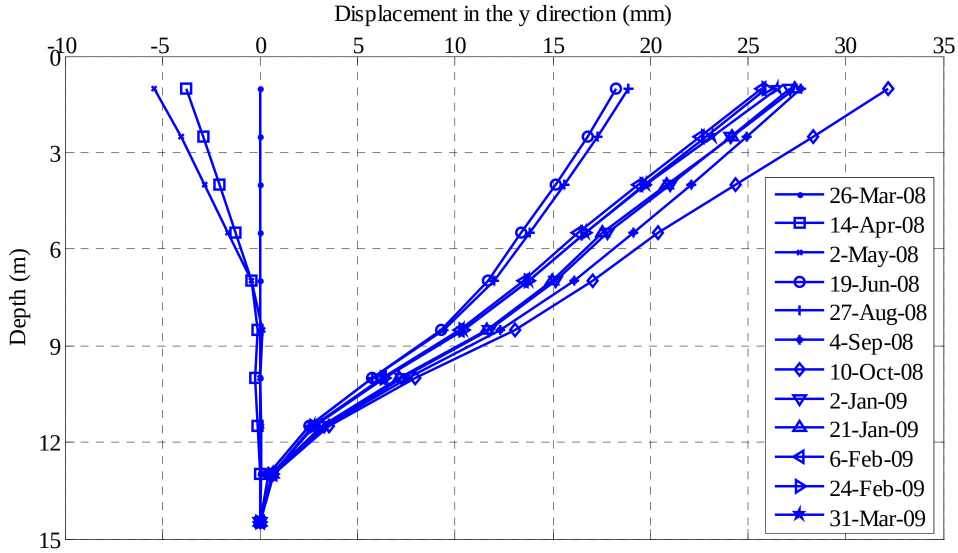

(b) Displacement in the *y* direction

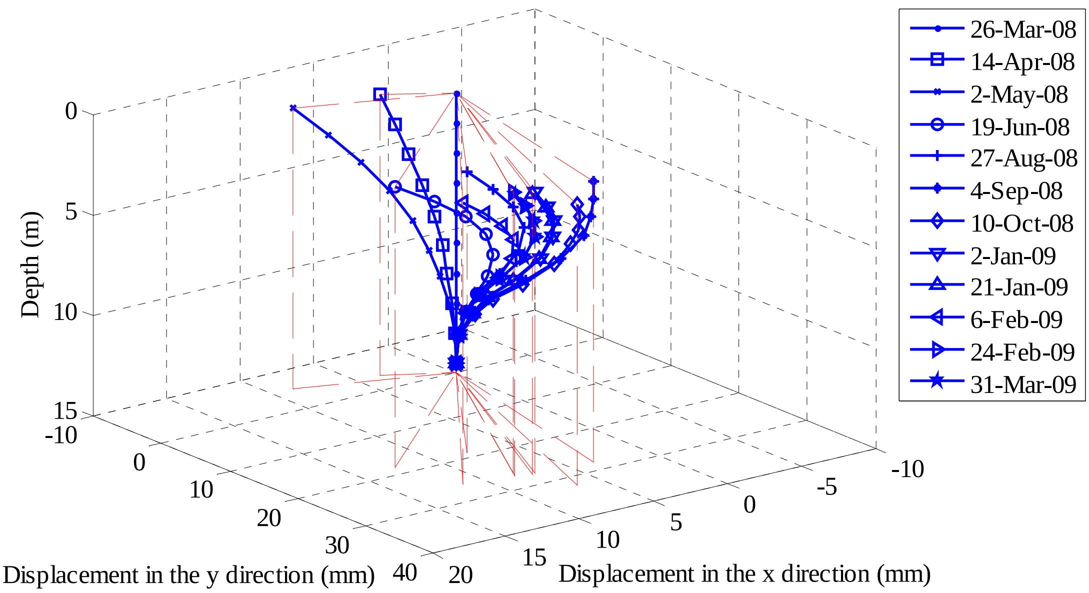

(c) 3-D view of the slope movements

Figure 8.11 Monitoring results of the slope movements by the FBG in-place inclinometer

CHAPTER 9:

SUMMARY, CONCLUSIONS AND SUGGESTIONS

9.1 SUMMARY

This study conducts a comprehensive investigation into fiber optic monitoring and performance evaluation of geotechnical structures.

Firstly, various geotechnical sensors based on fiber Bragg grating (FBG) technology are developed, including surface glued sensors, tube packaged sensors, embeddable sensing bars, in-place inclinometers, and settlement tubes. A series of calibration tests have been performed in laboratory to validate their reliability for geotechnical monitoring.

For small-scale physical models, the measurement of internal displacements is a difficult task. The FBG sensing bars developed in this study have been successfully embedded in two physical models and provided displacement monitoring during tests. Firstly, a three-dimensional (3-D) physical model of Shuangjiangkou Cavern Group was instrumented with three FBG sensing bars, together with multi-point extensometers (MPEs) and a digital photogrammetric system for displacement monitoring. After the excavation stage, the in-situ stress was increased in stages and the deformation and failure behavior of the cavern group under overloading condition was investigated. The second one is a two-dimensional (2-D) model of Wudu Dam rested on a highly jointed rock foundation. The FBG sensing bars, together with strain rosettes and linear variable displacement transformers (LVDTs), were installed on the model. It is found that the monitoring results are in good agreement with the results from the corresponding finite element analysis. Based on the experimental and numerical results, the failure mechanism and overloading factor of safety of the gravity dam are studied.

Finally, FBG based sensors have been successfully applied for typical geotechnical structures in the field. In four slope sites, the FBG sensors were installed on steel soil nails and GFRP soil nails for measuring strain distribution along the nail. The pullout forces and displacements were measured by load cell and LVDTs. Typical test data are presented and discussed in the thesis. In a mat foundation site in Hong Kong, an FBG based monitoring system consisting of various FBG sensors has been installed for monitoring the construction stage. Based on the monitoring results, implications on the current design assumptions are discussed. In a slope site in Hong Kong, the slope movements, strains in a soil nail and two stabilizing piles were monitored by an FBG based monitoring system during and after slope stabilization. Long-term monitoring results are presented in this thesis.

The original works of this thesis project can be summarized as follows:

(a) The feasibility of fiber optic sensors based on FBG technology in the application of geotechnical monitoring has been investigated. In Hong Kong, this is the first time that fiber optic sensing technology is utilized for monitoring geotechnical structures. Novel FBG sensors for measuring strains, displacements and temperatures have been developed in response to the requirements of geotechnical instrumentation.

(b) The pullout performance of steel and GFRP soil nail is studied and compared by full-scale field testing. FBG strain sensors have been successfully applied for strain monitoring of soil nails during pullout tests. Based on the test results of steel soil nails, the determination of pullout resistance using SPT *N* value is proposed. A simplified model is developed to simulate the pullout behavior of soil nails.

(c) Innovative FBG sensing bars have been successfully installed in physical models for measuring internal displacements with improved accuracy and reliability, together with conventional transducers. The monitoring results from the model tests of Shuangjiangkou Cavern Group and Wudu Dam were further analyzed and compared with numerical results, which indicates the deformation and failure mechanisms of these types of geotechnical structures.

(d) The FBG based fiber optic monitoring systems have been applied in a mat foundation and a slope site, which is the first time in Hong Kong. Special protection techniques were conducted to ensure the survival of the FBG sensors. The long-term monitoring results indicated the stability conditions of these two geotechnical structures.

9.2 CONCLUSIONS

(1) It is found that the FBG based sensors show apparent advantages in measuring strain, temperature, and displacement over conventional sensors. If properly packaged and protected, FBG sensors are reliable for field instrumentation of geotechnical structures.

(2) During pullout tests, the axial strain and stress distribution of soil nail along the grouted length cannot be assumed to be linear. The pullout-displacement relationships before failure can be modeled by hyperbolic functions. The simplified pullout model for soil nails can be used to predict the pullout behavior and help to determine the pullout resistance with high accuracy.

(3) The physical model testing of Shuangjiangkou Cavern Group indicates that during the whole process of underground excavation, the displacements in the surrounding rock masses were in considerably small range and no obvious crack or material damage were detected. In the model tests, a few cracks were observed when the in-situ stress equaled 2200 m overburden stresses. The comparison between experimental and numerical results leads to in-depth understanding of the influence of strain localization on the deformation behavior and overall stability of the cavern group.

(4) For concrete gravity dam, sliding within foundation is one of the key failure patterns. In this failure mode, crack propagation will initially develop at the dam heel and a triangular plastic zone will expand under the dam body. The crest displacement in the horizontal direction is the most critical parameter reflecting the dam stability condition.

(5) From the fiber optic monitoring results of the mat foundation of China Graduate School of Theology, the stability condition of the foundation is proved. The temperature rise due to concrete hydration heat should be controlled for massive concrete construction.

(6) It is found that the slope movements fluctuated with time and rainfall infiltration was a main factor affecting the slope stability condition. The strains and stresses in soil nails are proved to have the same tendency with rainfall. The soldier piles at the slope toe became to play a role in resisting the potential sliding after the slope movements towards downhill accumulated to certain values.

9.3 SUGGESTIONS

(1) FBG sensing technology has the advantages of high accuracy, immunity to

electromagnetic interference, and multiplexing. In this study, FBG is used to make strain, temperature and displacement sensors. Some of the previous researches in this area have studied the development of FBG sensor for measuring other physical parameters, e. g. pore pressure, acceleration, tilt and rainfall intensity. However, there are still no perfect solutions. The development of a cost-effective monitoring system consisting of a variety of FBG based sensors for measuring various geotechnical parameters remains to be investigated.

(2) In this study, the FBG sensors are only installed in two physical models for displacement measurements. The FBG sensors can also be applied to other types of geotechnical tests, including triaxial tests on soil/rock samples, centrifuge and shake table tests of scaled models. The effectiveness of the FBG sensing bar in 3-D displacement monitoring should be verified in future research.

(3) The simplified model of soil nail pullout behavior presented in Chapter 4 can be used to capture the soil nail performance. Further study is recommended to consider the dilation characteristics of soil, the occurrence of bending moments and shear stresses, and other effects in this model. The application of this model can be extended in the design of soil nailing, which also remains to be investigated.

(4) It has been found that the sliding within the foundation is one of the key failure modes of gravity dams. More experimental and numerical researches are recommended to further investigate the stability analysis method of a gravity dam and appropriate reinforcement measures for potential sliding failure. Moreover, as the physical modeling results is utterly dependent on the properties of the model materials, more studies should be conducted to develop new materials that can accurately simulate the prototype. Apart

from elastic modulus and shear strength, the similitude of critical strain and the ratio of uniaxial compressive and tensile strength should be ensured (Indraratna 1990).

(5) For cavern groups, more studies on the mechanism of rock bolts and pre-stressed cables for stabilizing the cavern roof and reducing the displacement are required to be carried out. The seismic performance of large-scale caverns is also a hot topic for engineering practice.

(6) From this study, it is found that the FBG technology has its own limitations. The strain limit of the FBG sensor is about 3000 $\mu\varepsilon$. For larger strain measurement, special design methods have to be adopted. In recent years, the technology of distributed fiber optic sensors has been developed rapidly. For large-scale infrastructures, the distributed sensor is more cost-effective and easier to be installed on site. The strain limit of this technology is beyond 10000 $\mu\varepsilon$. The application of fully-distributed sensors in geotechnical engineering is a new and promising research field.

APPENDICES

A1 OPTICAL FIBER

An optical fiber is a glass or plastic fiber designed to guide light along its length by total internal reflection. The basic structure of an optical fiber is shown in Figure A1.1. The fiber consists of three parts: the core, the cladding, and the coating. The core is a cylindrical rod of dielectric material and is generally made of Ge-doped glass. It is surrounded by a layer of material called the cladding. To confine the optical signal in the core, the refractive index of the core n_1 must be greater than that of the cladding n_2. The cladding reduces loss of light from the core into the surrounding air and reduces scattering loss at the surface of the core. It can also protect the fiber from absorbing surface contaminants. For extra protection from physical damage, the cladding is enclosed in an additional layer of coating. The coating, also known as buffering, is made of a type of plastic such as polymide or acrylate. For field applications, optical fibers are built into different kinds of cables. Normally a cable jacket of Teflon, polyvinyl-chloride (PVC), or a flexible stainless steel-armored sheath, is used to add mechanical strength to the bundle of fibers, as shown in Figure A1.2.

As an optical waveguide, optical fiber supports one or more confined transverse modes, by which lights can propagate along the fiber. There are two basic types of optical fiber, namely single-mode and multimode. Fiber which has a relatively narrow core and supports only one mode of transmission is called the single-mode or mono-mode fiber (SMF). SMF is normally a single stand of glass fiber with a core diameter of 9 μm and a cladding diameter of 125 μm. Compared with multimode fiber (MMF), the small core and single light-wave of SMF virtually eliminate any distortion that could result from overlapping light pulses, providing the least signal attenuation and the highest transmission speeds of any fiber cable type.

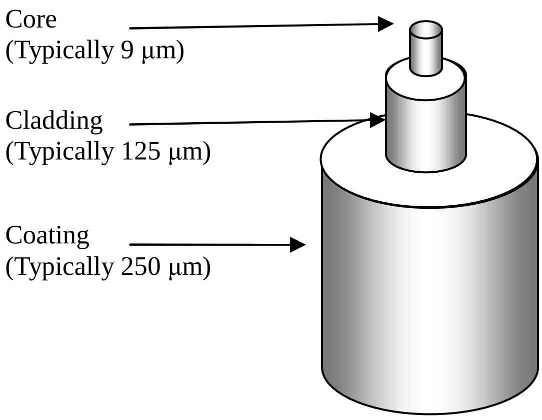

Figure A1.1 Illustration of the core, cladding and coating of an optical fiber

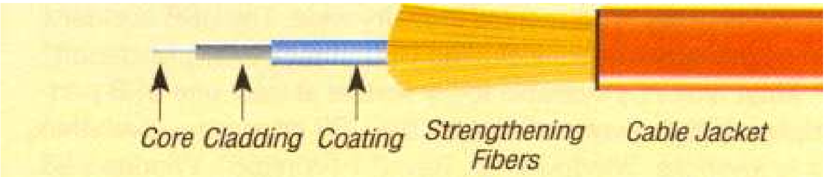

Figure A1.2 Structure of an optical fiber cable

A2 TYPES OF FIBER OPTIC SENSORS

According to the sensing principle, most fiber optic sensors used for civil infrastructure belong to one of the following categories.

(1) Intensiometric sensors

These sensors can form fully distributed sensing array. There are basically two kinds of intensiometer sensors: microbending and Brillouin optical time domain reflectometer (BOTDR) sensors.

Microbending sensors are intensity based sensors, which are based on the bend induced losses in optical fibers (normally for MMF). These sensors can be interrogated either in transmission or in reflection (observing the attenuation of the Rayleigh scattering). In the second case, the reading unit will be an optical time domain reflectometer (OTDR), which is a testing instrument used for analyzing the light loss in an optical fiber. OTDR will send a powerful light pulse in the waveguide and observe the changes in the reflected light due to local inhomogeneities along the fiber. The pulse losses correspond to specific interactions between the surrounding environment and the fiber. If the measurements are done in reflection, the system can be easily brought to in-line multiplexing. Other architectures are possible by using appropriate passive delay lines. Strain sensitivities of the order of $\mu\varepsilon$ have been demonstrated over short periods. Since the data is encoded in the intensity of the radiation, microbending sensors are subject to important performance degradation when applied to long-term measurements. Aging fibers, light sources, detectors and connections can decrease the amount of light independently from the deformations of the structure. Therefore, the long-term drift of this technology has to be considered carefully. However, these sensors are capable of monitoring sudden events like a partial structural failure or the appearance of a crack.

These events will produce a rapid change in the detected intensity that can be easily separated from the drift. The effect of temperature has to be compensated by using unstrained reference sensors. The reading units are usually rather inexpensive and simple, but specially manufactured fibers are required.

Brillouin optical time domain reflectometry (BOTDR) is another sensing technology that can form a distributed sensing network. The Brillouin effect is an interaction between the photons and the phonons in an optical fiber that results in a frequency shifted radiation traveling in the opposite direction of the monochromatic pump beam. The frequency shift depends on both the temperature and the strain of the optical fiber under measurement. By adding an appropriate modulation, it is possible to obtain a distributed sensor with a spatial resolution of 0.5 to 2 m. This is sufficient for most geotechnical structures such as dams, slopes and tunnels.

(2) Interferometric sensors

When high sensitivity is required, interferometric sensors are often the only option. Although fiber Bragg grating sensors are also based on optical interference, the term "interferometric sensor" is usually applied to two-path interferometers. The main types of interferometric sensors are Mach-Zehnder, Michelson and Fabry-Perot sensors. For all the sensors, the length change in one of the interferometer arms induces a change in the relative phase between the two interfering arms and therefore produces a sinusoidal intensity variation on the detector. Most interferometric sensors are incremental and require continuous monitoring. On the other side, sensitivities in the nanometer range can be achieved by appropriate demodulation of the interferometric signals. Depending on the length of the arms, both strain and deformation sensors can be realized.

(3) Spectrometric sensors

Fiber Bragg grating (FBG) sensors are the most used spectrometric sensors in civil engineering. They are wavelength-shift based and can be applied to both strain, displacement and, of course, temperature monitoring. These sensors are only sensitive to strain and temperature in the grating region that can be up to a few centimeters long. To obtain a displacement sensor, the fiber containing the Bragg grating has to be pre-stressed between two points at the extremities of the active region. Any deformation will change the distance between the two points and therefore the strain state of the grating. To obtain reliable measurements, the fiber has to be completely free and with a uniform tension. This usually requires the fiber to be installed in pipes with a sufficiently large diameter. Furthermore, the displacement precision will decrease with increasing sensor length. For these reasons, the Bragg grating sensors are better suited for strain monitoring. The gratings are glued directly to the host material. In this case, sensitivities down to 1 με can be achieved. The temperature apparent strain can be compensated with a reference grating or by using dual overlaid gratings at two well separated wavelengths.

FBG sensors can be multiplexed in most physical architectures. Many types of reading architectures have been demonstrated in order to analyze the spectral content of the light returned by the gratings. The cost and the size of the reading units vary according to their resolution, but portable reading units are now available for in-field applications.

Among all the fiber optic sensing technologies listed in Table A2.1, FBG can monitor strain, vibration and displacement as well as temperature. They also offer excellent resolution and measuring range, mulitplexable capacity, absolute measurement, and modest cost per channel.

Table A2.1 Main features of various fiber optic sensing technologies

Technical approach	Applications	Advantages	Disadvantages
Bragg gratings	Displacement Strain Vibration Temperature Pressure	Accurate Inherent WDM encoding Fiber integrated Facilitates distributive sensing Robust Distances over 25 km	Requires temperature and strain discrimination
Raman scattering	Temperature	Senses infinite points Fiber integrated Facilitates distributive sensing Robust Distances over 20 km	Limited to temperature OTDR detection limitations Cost
Brillouin scattering	Strain temperature	senses infinite points Fiber integrated Facilitates distributive sensing Robust Distances over 10 km	Requires temperature and strain discrimination OTDR detection limitations
Interferometric	Strain Rotation Temperature Pressure	Very accurate Can be Fiber integrated Distances up to 10 km	Best suited for single-point sensors Cost
Microbending	Strain Vibration Temperature	senses infinite points Fiber integrated Facilitates distributive sensing Robust Distances up to 20 km	OTDR detection limitations
Fluoreecence	Chemical sensing	Fast response Can be Fiber integrated	Requires flucreecensce dyes
Reflectivity	Displacement Accelerometer Vibration Surface roughnous (corrosion)	Noncontact Compact	Lossy Subject to contamination
Scattering	Chemical sensing	Noncontact Compact Broad function	Lossy Subject to contamination
Microrescnator	Strain Chemical sensing	Inherent wavelength encoding Very accurate Integration platform	Least mature of approaches
MEOMS (Microelecto-optic mechanical systems)	Accelerometer Vibration Chemical sensing	Compact Compatible with distributive sensing systems	Robust packaging

A3 FABRICATION OF FBG SENSORS

Currently, there are two major methods for manufacturing fiber Bragg grating: holographic method (Meltz et al. 1989) and phase mask method (Hill et al. 1993). The latter is the most popular for mass production and chosen in this study. The standard telecommunication fiber (Corning SMF-28e) is used to fabricate FBG sensor. The diameter of the coated fiber is 250 μm, while the core and cladding are 9 μm and 125 μm in diameter, respectively.

The complete manufacturing process of FBG-based components can be divided into four steps: 1) preparation of the photosensitive optical fiber, 2) recording of the grating, 3) thermal annealing and 4) packaging.

(1) Preparation of the photosensitive optical fiber

The optical fiber should be H_2-loaded for 48 h at 180 bar and 80 ^oC to make it photosensitive. Because UV radiation does not penetrate well through the acrylic (or polyimide) coatings that are on standard optical fiber, the next step of FBG manufacturing process consists of removing the coating from the region of the photosensitive fiber to be exposed to UV light. This is done by a mechanical stripping technique. The length of the uncoated section is recommended to be about 10-20 mm in general use. To insure long-term reliability and improved manufacturing yield, this step (as well as all manufacturing steps) should be performed very carefully and in a clean room environment. Extreme precautions should be taken during handling of the uncoated fiber and mechanical testing must be performed frequently during each manufacturing steps. To manufacture FBG sensor of high strength and large strain limit, the tensile strength of uncoated fiber should be no less than 100kpsi (689 MPa). The tensile test is conducted by a recoating machine.

a. Wavelength of gratings and optical fiber selection

Before making a grating, the wavelength range should be determined. The design Bragg wavelength depends mainly on the sensor demodulation and optical source used for the project. For most cases, a Bragg grating in the 1550 nm regime is needed. The standard optical fiber used for 1550 nm gratings should be single mode optical fiber. SMF-28 standard telecommunication optical fiber, which has a cutoff wavelength of about 1200 nm is suitable.

b. Wavelength separation

Sensor response determines the wavelength separation for Bragg grating arrays. Each Bragg grating should pose wavelength spacing sufficient enough such that no overlap will occur between two neighboring sensors. A good rule of thumb is to leave 1.5 nm of spacing for every 1000 micro strain the sensor will experience. When determining the wavelength separation, both tensile and compressive strains cases should be take into account. If all sensors will experience only tensile strains in application (such as monitoring a pressure vessel as it is loaded), this information can be used to aid in calculating the proper wavelength spacing.

c. Spatial separation

When manufacturing a Bragg grating array, it is always best to have knowledge of where on the structure (or system) each grating will be located. In this manner, the sensor array can be mapped out before the optical fiber is even loaded into the hydrogen chamber. The alternative method is to manufacture each Bragg grating individually and splice them together to form the array. For most applications this is sufficient, but when a high strength array is desired, the less fusion splicing that is required the better.

Standard optical fiber is sensitive to UV light, which is known as photosensitivity. The core region of optical fiber is doped with germanium in order to raise the index of fraction above that of pure silica in the cladding region. This provides the optical guiding properties for the fiber. The germanium also creates a quantity of GeO (germanium monoxide) which when exposed to UV radiation creates oxygen deficient centers. These defects cause a rise in the index of refraction. In general, this process is slow and is dependent on the intensity of the UV source.

After uncoating and tensile tests, the optical fibers are placed into the hydrogen load chamber and subject to Off Fred Laser. By loading the optical fiber with hydrogen, the process can be speeded up by inducing a second photosensitive effect. The introduction of hydrogen into the core allows the Ultraviolet (UV) radiation to create Si-OH which increases the refractive index of the core. These two effects combine to create the periodic variation of the refractive index in the core region.

(2) Making a Bragg grating using phase mask method

The fabrication devices should be connected to make FBG using phase mask method. A proper optical source, depending on the wavelength range of grating, and an optical spectrum analyzer (OSA) is required to monitor the FBG spectrum. Temporary connectors such as FC/APC can be used on the fiber ends to connect the Bragg grating with the light source and OSA.

The set-up of phase mask technique for manufacturing FBG is shown in Figure 2.8. The focus of the UV light from an excimer laser (Frequence=8 Hz) should be adjusted carefully using the cylindrical lens. The optical alignment for the formation method is very important for the set-up. An appropriate fiber holder using magnets helps to hold the optical fiber firmly without physical damage. A scrap piece of fiber is placed into the fiber holder to ensure the quality of the optical focus on the fiber. Precise translation stages are used to adjust the location of optical fiber appropriately. Throughout the whole fabrication process, the UV laser beam may drift. Adjustment has to be done on the set-up in order to compensate and maintain good alignment.

Phase masks are corrugated circular pieces of silica. Once a phase mask is received it should be placed into a phase mask holder. Each phase mask has a different pitch (periodicity) to the corrugated ridges on its surface. This pitch determines what wavelength of Bragg grating will be manufactured, which is marked down beforehand. The phase mask holder is designed for insertion into a rotational stage. The phase mask functions to split the incoming UV light into multiple diffracted beams. The two first order diffracted beams should be aligned properly by adjusting the rotational stage until the two diffracted beams lie along the same horizontal line. The configuration is quite sensitive to mechanical instabilities and may be difficult to implement for efficient mass-production.

A good FBG sensor should have a reflectivity of 90% or above and a transmission spectrum less than 0.25 nm at 3 dB, which can be calculated by the reflected or transmitted spectrum.

(3) Post processing of Bragg gratings

FBG are quite durable, but their properties may change during some time after fabrication. After a Bragg grating is fabricated, steps must be taken to ensure its survivability.

a. Re-coating and marking

To protect the optical fiber, the region of buffer (coating) that is removed may be replaced using re-coating device. The location of each Bragg grating should be marked with a pre-determined color by permanent markers.

b. Annealing

Due to the influx of hydrogen, the average refractive index of the Bragg grating is slightly elevated. Over time, as the hydrogen leaks out, the refractive index will decrease causing a shift in the Bragg wavelength. To prevent this phenomenon during measurement, an annealing procedure should be applied to the Bragg gratings. Typical standard annealing is to bake them in an oven for 4 hours at 80 ^{o}C. If the application will be at higher temperatures, then the Bragg gratings should be annealed at 25 ^{o}C over the operating temperature. This process will speed the release of hydrogen and stabilize the Bragg wavelength.

c. Storage

Bragg gratings should be stored in a humidity free area. Each Bragg grating array should be individually tagged and a record of the array specifics should be maintained. This will allow the end user of the gratings and/or arrays to trouble shot any anomalies during the testing phase.

REFERENCES

Adimi, R., and Benmokrane, B. (1997). Fatigue behaviour of GFRP bars embedded in concrete. Proceedings of Annual Conference of Canadian Society of Civil Engineering, Montréal, 121-130.

Alonso, E., Carol, I., Delahaye, C., Gens, A., and Prat, P. (1996). Evaluation of factor of safety in discontinuous rock. International Journal of Rock Mechanics and Mining Sciences & Geomechanics Abstracts, 33(5), 513-537.

Al-Salloum, Y. A., and Almusallam, T. H. (2007). Creep effect on the behavior of concrete beams reinforced with GFRP bars subjected to different environments. Construction and Building Materials, 21(7), 1510-1519.

American Concrete Institute (ACI) Committee 440. (1996). State-of-the art report on fiber-reinforced plastic (FRP) reinforcement for concrete structures. ACI Report No. 440R-96, ACI, Detroit, MI.

American Concrete Institute (ACI) Committee 440. (2001). Guide for the design and construction of concrete reinforced with FRP bars. ACI Report No. 440.1 R-01, ACI, Farmington Hills, MI.

American Concrete Institute (ACI) Committee 440. (2004). Prestressing concrete structures with FRP tendons. ACI Report No. 440.4 R-04, ACI, Farmington Hills, MI.

ANSYS, Inc. (2007). ANSYS Documentation for Release 11.0. Canonsburg, PA.

ASCE Task Committee on Instrumentation and Monitoring Dam Performance. (2000). Guidelines for Instrumentation and Measurements for Monitoring Dam

Performance. ASCE, Reston, VA.

Ashford, S. A., and Jakrapiyanun, W. (2001). Drivability of glass FRP composite piling. Journal of Composites for Construction, 5(1), 58-60.

Au, H. Y., Khijwania, S. K., and Tam, H. Y. (2008). Fiber Bragg grating based accelerometer. Proceedings of SPIE, 7004, Paper No. 70042S.

Baek, W., Moriwaki, T., and Sasaki, Y. (2007). Study of a displacement measurement method inside a small-sized model ground in laboratory test. Geotechnical Testing Journal, 30(5), 409-417.

Baldwin, C., Poloso, T., Chen, P., Niemczuk, J., Kiddy, J., and Ealy, C. (2001). Structural monitoring of composite marine piles using fiber optic sensors. Proceedings of SPIE, 4330, 487-497.

Bakis, C. E., Nanni, A., Terosky, J. A., and Koehler, S. W. (2001). Self-monitoring, pseudo-ductile, hybrid FRP reinforcement rods for concrete application. Composites Science and Technology, 61(6), 815-823.

Bank, L. C. (1989). Shear properties of pultruded glass FRP materials. Journal of Materials in Civil Engineering, ASCE, 2(2), 118-122.

Barpi, F., Ferrara, G., Imperato, L., and Valente, S. (1999). Lifetime of concrete dam models under constant loads. Material and Structures, 32(2), 103-111.

Beekman, A., Mallner, A. J., and Sutterer, K. (2007). Fiberglass nail pullout capacity for rapid soil landslide remediation. Transportation Research Board 86th Annual Meeting, Washington, D.C., Paper No. 01042056.

Benmokrane, B., Xu, H., and Bellavance, E. (1996). Bond strength of cement grouted glass fibre reinforced plastic (GFRP) anchor bolts. International Journal of Rock Mechanics and Mining Sciences & Geomechanics Abstracts, 33(5), 455-465.

Bhattacharjee, S. S., and Léger, P. (1993). Seismic cracking and energy dissipation in concrete gravity dams. Earthquake Engineering and Structural Dynamics, 22(11), 991-1007.

Bhattacharjee, S. S., and Léger, P. (1994). Application of NLFM models to predict cracking in concrete gravity dams. Journal of Structural Engineering, ASCE, 120(4), 1255-1271.

Bray, J. D., Seed, R. B., and Seed, H. B. (1993). 1 g small-scale modelling of saturated cohesive soils. Geotechnical Testing Journal, 16(1), 46-53.

Budelmann, H., and Rostàsy, F. S. (1993). Creep rupture behavior of FRP elements for prestressed concrete: phenomenon, results, and forecast models. Fiber-reinforced plastic reinforcement for concrete structures. ACI, Farmington Hills, MI, 87-100.

Budhu, M. (2008). Foundations and Earth Retaining Structures. John Wiley & Sons, Inc.

Burland, J. B., and Burbridge, M. C. (1985). Settlement of foundations on sand and gravel. Structures and Buildings, Proceedings of ICE, 78(6), 1325-1381.

Byrne, R. J., Cotton, D., Porterfield, J., Wolschlag, C., and Ueblacker, G. (1998). Manual for design and construction monitoring of soil nail walls. Report No. FHWA-SA-96-069R, Federal Highway Administration, Washington, D.C.

Carter J. P., Desai C. S. , Potts, D. M., Schweiger H. F. and Sloan S. W. (2000). Computing and computer modelling in geotechnical engineering. Proceedings of GeoEng 2000 Conference on Geotechnical and Geological Engineering, Melbourne, 1157-1252.

Chang, C. -C., Johnson, G., Vohra, S., and Althouse, B. (2000). Development of fiber Bragg grating based soil pressure transducer for measuring pavement response. Proceedings of SPIE, 3986, 480-488.

Chang, M. -H., Mitchell, J. K., and Seed, R. B. (1999). Model Studies of the 1988 Kettleman Hills Landfill Slope Failure. Geotechnical Testing Journal, 22(1), 61–66.

Chang, T. Y., Li, D. S., Sui, Q. M., Jia, L., Wei, Z. X., and Cui, H. G. (2007).

Applications of fiber optic Bragg grating sensing technology in a forked tunnel model. Proceedings of IEEE International Conference on Automation and Logistics, Jinan, 1652-1657.

Chen, J. Y., Li, J., and Zhou, J. (2004a). Seismic analysis of large 3-D underground caverns based on high performance recursive method. International Journal of Solids and Structures, 41(11-12), 3081-3094.

Chen, S. H., Li, Y. M., Wang, W. M., and Shahrour, I. (2004b). Analysis of gravity dam on a complicated rock foundation using an adaptive block element method. Journal of Geotechnical and Geoenvironmental Engineering, ASCE, 130(7), 759-763.

Chen, S. H., Qiang, S., Shahrour, I., and Egger, P. (2008). Composite element analysis of gravity dam on a complicated rock foundation. International Journal of Geomechanics, ASCE, 8(5), 275-284.

Chen, Y., Zhang, L., He, X. S., Chen, J. Y., and Hu, C. Q. (2006). Evaluation of model similarity of induced joints in a high RCC arch dam. Proceedings of the 6th Conference of Physical Modeling in Geotechnics, Hong Kong, 413-417.

Cheng, Y. M., Choi, Y. -K., Yeung, A. T., Tham, L. G., Au, A. S. K., Wei, W. B., and Chen, J. (2009). New soil nail material-pilot study of grouted GFRP pipe nails in Korea and Hong Kong. Journal of Materials in Civil Engineering, ASCE, 21(3), 93-102.

Chengdu Hydroelectric Investigation and Design Institute (CHIDI). (2006). The Reasonable Layout and Surrounding Rock Stability Research of Huge Scale Underground Cavern Groups. Chengdu. (in Chinese)

Cheung, P. Y., Wong, M. C., and Yeung, H. Y. (2006). Application of rainstorm nowcast to real-time warning of landslide hazards in Hong Kong. WMO PWS Workshop on Warnings of Real-Time Hazards by Using Nowcasting Technology, Sydney, Australia, 1-21.

Choi, Y. K., Woo, S. B., Kwon, O. Y., Park, J. H., and Han, H. H. (2003). Shear strength characteristics and behaviour of ground grouted using FRP reinforcing members. Proceedings of 12th Asian Regional Conference on Soil Mechanics and Geotechnical Engineering, Singapore, World Scientific Publishing, 461-464.

Chopra, A. K., and Zhang, L. (1991). Earthquake-induced base sliding of concrete gravity dams. Journal of Structural Engineering, ASCE, 117(12), 3698-3719.

Chu, L. -M., and Yin, J. -H. (2005). Comparison of interface shear strength of soil nails measured by both direct shear box tests and pullout tests. Journal of Geotechnical and Geoenvironmental Engineering, ASCE, 131(9), 1097-1107.

Dewynter, V., Rougeault, S., Boussoir, J., Roussel, N., Ferdinand, P., and Wileveau, Y. (2005). Instrumentation of borehole with fiber Bragg grating thermal probes: study of the geothermic behaviour of rocks. Proceedings of SPIE, 5855, 1016-1019.

Dhawan, K. R., Singh, D. N., and Gupta, I. D. (2004). Three-dimensional finite element analysis of underground caverns. International Journal of Geomechanics, ASCE, 4(3), 224-228.

Ding, X. -L., Huang, D. -F., Yin, J. -H., Chen, Y. -Q,, Lau, C. K., Yang, Y. –W., Sun, Y. R., Chen, W., and He, X. -F. (2003). Development and field testing of a multi-antenna GPS system for deformation monitoring. Wuhan University Journal of Natural Sciences, 8(2), 671-676.

Donlon, W. P., and Hall, J. F. (1991). Shaking table study of concrete gravity dam monoliths. Earthquake Engineering and Structural Dynamics, 20(8), 769-86.

Du, W. -C., Tao, X. -M., and Tam, H. -Y. (1999). Fiber Bragg grating cavity sensor for simultaneous measurement of strain and temperature. IEEE Photonics Technology Letters, 11(1), 105-107.

Duddeck, H. (1991). Application of numerical analyses for tunnelling. International Journal for Numerical and Analytical methods in Geomechanics, 15(4), 223-239.

Dunnicliff, J. (1993). Geotechnical Instrumentation for Monitoring Field Performance, John Wiley & Sons Inc, New York.

Dutta, P. K., and Hui, D. (2000). Creep rupture of a GFRP composite at elevated temperatures. Computers and Structures, 76(1-3), 153-161.

Ellyin, F., and Kujawski, D. (1992). Fatigue testing and life predictions of fibre glass reinforced composites. Advanced composite materials in bridges and structures. K.W. Neale, and P. Labossiere, eds., Canadian Society of Civil Engineering, Montreal, 111-118.

Falciai, R., and Trono, C. (2005). Displacement fiber Bragg grating sensor with temperature compensation. Proceedings of SPIE, 5855, 787-790.

Feng, M. Q., Suzuki, H., and Yokoi, I. (1995). Development of optical sensing systems for smart civil infrastructures. Smart Materials and Structures, 4, A114-A120.

Fischer, M. P., and Keating, D. P. (2005). Photogrammetric techniques for analyzing displacement, strain, and structural geometry in physical models: Application to the growth of monoclinal basement uplifts. GSA Bulletin, 117(3-4), 369-382

Frank, A., Nellen, P. M., Brönnimann, R., and Sennhauser, U. (1999). Fiber optical Bragg grating sensors embedded in GFRP rockbolts. Proceedings of SPIE, 3670, 497-504.

Fredlund, D. G., and Rahardjo, H. (1993). Soil Mechanics for Unsaturated Soils. John Wiley & Sons, Inc., New York.

Frost, J. D., and Han, J. (1999). Behavior of interfaces between fiber-reinforced polymers and sands. Journal of Geotechnical of Geoenvironmental Engineering, ASCE, 125(8), 633-640.

Ftima, M. B., and Léger, P. (2006). Seismic stability of cracked concrete dams using rigid block models. Computers and Structures, 84(28), 1802-1814.

Fumagalli, E. (1973). Statical and Geomechanical Models. Springer-Verlag, New York.

Gasmo, J., Hritzuk, K. J., Rahardjo, H., and Leong, E. C. (1999). Instrumentation of an unsaturated residual soil slope. Geotechnical Testing Journal, 22(2), 128-137.

Geotechnical Engineering Office (GEO). (2005). Good practice in design of steel soil nails for soil cut slopes. GEO technical guidance note no. 23, Civil Engineering and Development Dept., Government of Hong Kong Special Administrative Region, Hong Kong.

Geotechnical Engineering Office (GEO). (2008). Guide to Soil Nail Design and Construction. Geoguide 7, Civil Engineering and Development Dept., Government of Hong Kong Special Administrative Region, Hong Kong.

Ghaemina, M., and Ghobarah, A. (1999). Nonlinear seismic response of concrete gravity dams with dam-reservoir interaction. Engineering Structures, 21(4), 306-315.

Ghobarah, A., and Ghaemian, M. (1998). Experimental study of small scale dam models. Journal of Engineering Mechanics, ASCE, 124(11), 1241-1248.

Gomez, J. E., Filz, G. M., and Ebeling, R. M. (2003). Extended hyperbolic model for sand-to-concrete interfaces. Journal of Geotechnical of Geoenvironmental Engineering, ASCE, 129(11), 993-1000.

Graver, T., Inaudi, D., and Doornink, J. (2004). Growing market acceptance for fiber-optic solutions in civil structures. Proceedings of SPIE, 5589, 44-55.

Hanna, T. H. (1973). Foundation Instrumentation. Trans Tech Publications, Cleveland.

Hao, Y. H., and Azzam, R. (2005). The plastic zones and displacements around underground openings in rock masses containing a fault. Tunnelling and Underground Space Technology, 20 (1), 49-61.

Harper, J. S., Smart, B. G. D., and Sommerville, J. M. (1995). Recent applications of soil nails and cables in the UK. Anchors in Theory and Practice, Balkema, Rotterdam, 163-172.

Harris, D. W., Snorteland, N., Dolen, T., and Travers, F. (2000). Shaking table 2-D models of a concrete gravity dams. Earthquake Engineering and Structural Dynamics, 29(6), 769-787.

Hettiarachchi, H., and Brown, T. (2009). Use of SPT blow counts to estimate shear strength properties of soils: energy balance approach. Journal of Geotechnical and Geoenvironmental Engineering, ASCE, 134(6), 830-834.

Heuer, R. E., and Hendron, A. J. (1969). Geomechanical model study of the behavior of underground openings in rock subjected to static loads. Report 1 of Development of modeling Techniques Sponsored by U.S. Defense Atomic Support Agency.

Hill, K. O., Fujii, Y., Johnson, D. C., and Kawasaki, B. S. (1978). Photosensitivity in optical fiber waveguides: application to reflection filter fabrication. Applied Physics Letters, 32(10), 647-649.

Hill, K. O., Malo, B., Bilodeau, F., Johnson, D. C. and Albert, J. (1993). Bragg gratings fabricated in monomode photosensitive optical fiber by UV exposure through a phase mask. Applied Physics Letters, 62(10), 1035-1037.

Hill, K. O., Malo, B., Vineberg, K. A., Bilodeau, F., Johnson, D. C. and Skinner, I. (1990). Efficient mode conversion in telecommunication fibre using externally written gratings. Electronics Letters, 26(16), 1270-1272.

Hirayama, H. (1990). Load-settlement analysis for bored piles using hyperbolic transfer functions. Soils and Foundations, 30(1), 55-64.

Ho, Y. T., Huang, A. B., and Lee, J. T. (2006). Development of a fibre Bragg grating sensored ground movement monitoring system. Measurement Science and Technology, 17, 1733-1740.

Ho, Y. -T., Huang, A. -B., and Lee, J. -T. (2008). Development of a chirped/differential optical fiber Bragg grating pressure sensor. Measurement Science and Technology, 19, 1-6.

Hoek, E., and Brown, E. T. (1980). Underground Excavation in Rocks. The Institution of Mining and Metallurgy, London.

Hong, Y. -S., Wu, C. -S., and Yang, S. -H. (2003). Pullout resistance of single and double nails in a model sandbox. Canadian Geotechnical Journal, 40(5), 1039-1047.

Inaudi, D. (1997). Fiber Optic Sensor Network for the Monitoring of Civil Engineering Structures. PhD Thesis, EPFL, Lausanne, Switzerland.

Indraratna, B. (1990). Development and applications of a synthetic material to simulate soft sedimentary rocks. Geotechnique, 40(2), 189–200.

Independent Commission against Corruption (ICAC) of the government of Hong Kong. http://www.icac.org.hk/new_icac/eng/cases/piling/front.html.

Iskander, M., and Hassan, M. (1998). State of the practice review in FRP composite piling. Journal of Composites for Construction, ASCE, 2(3), 116-120.

Itasca Consulting Group, Inc. (2002). FLAC ^{3D} version 3.0 User Manual. Minneapolis, MN.

Javanmardi, F., Leger, P., and Tinawi, R. (2005). Seismic water pressure in cracked concrete gravity dams: experimental study and theoretical modeling. Journal of Structural Engineering, ASCE, 131(1), 139-150.

Jiang, G., Dawood, M., Peters, K., and Rizkalla, S. (2008). Self-monitoring fiber reinforced polymer strengthening system for civil engineering infrastructures. Proceedings of SPIE, 6934, Paper No. 693406.

Junaideen, S. M., Tham, L. G., Law, K. T., Lee, C. F., and Yue, Z. Q. (2004). Laboratory study of soil-nail interaction in loose, completely decomposed granite. Canadian Geotechnical Journal, 41(2), 274-286.

Kalamkarov, A., Saha, G., Rokkam S., Newhook J., and Georgiades, A. (2005). Strain and deformation monitoring in infrastructure using embedded smart FRP reinforcements. Composites Part B: Engineering, 36(5), 455-467.

Kalamkarov, A. L., Fitzgerald, S. B., MacDonald, D. O., and Georgiades, A. V. (1999). On the processing and evaluation of pultruded smart composites. Composites Part B: Engineering, 30(7), 753-763.

Kalamkarov, A. L., Georgiades, A. V., MacDonald, D. O., and Fitzgerald, S. B. (2000a). Pultruded fiber reinforced polymer reinforcements with embedded fiber optic sensors. Canadian Journal of Civil Engineering, 27(5), 972-984.

Kalamkarov, A. L., MacDonald, D. O., Fitzgerald, S. B., and Georgiades, A. V. (2000b). Reliability assessment of pultruded FRP reinforcements with embedded fiber optic sensors. Composite Structures, 50(1), 69-78.

Kang, H. -K., Ryu, C. -Y., Hong, C. -S., and Kim, C. -G. (2001). Simultaneous measurement of strain and temperature of structures using fiber optic sensor. Journal of Intelligent Material Systems and Structures, 12, 277-281.

Kashiwai, Y., Daimaru S., Sanadab, H., and Matsuic H. (2008). Development of borehole multiple deformation sensor system. Proceedings of SPIE, 7004, Paper No. 70041P-1.

Khan, A. S., and Wang, X. (2001). Strain Measurements and Stress Analysis. Prentice Hall, London.

Kim, N. -S., and Cho, N. -S. (2004). Estimating deflection of a simple beam model using fiber optic Bragg-grating sensors. Experimental Mechanics, 44(4), 433-439.

Kim, S. H., Hwang, Y. C., Kim, N. Y., and Choi, Y. K. (2001). Reinforcing method of rock slope using FRP pipe. Proceedings of International Conference on Landslides-Causes, Impacts and Countermeasures, Davos, Switzerland, 535-543.

Kister, G., Winter, D., Leighton, J., Badcock, R. A., Tester, P. D., Krishnamurthy, S., Boyle, W. J. O., Grattan, K. T. V., and Fernando, G. F. (2007). Methodology and integrity monitoring of foundation concrete piles using Bragg grating optical fibre sensors. Engineering Structures, 29(9), 2048-2055.

Kondner, R. L. (1963). Hyperbolic stress-strain response: cohesive soil. Journal of the Soil Mechanics and Foundation Engineering Division, ASCE, 89(1), 115-143.

Lai, S. -Y., Lin, P. -S., Hsieh, M. -J., and Jim, H. -F. (2005). Regression model for evaluating liquefaction potential by discriminant analysis of the SPT *N* value. Canadian Geotechnical Journal, 42(3), 856-875.

Lau, K. T., Yuan, L., Zhou, L. M., Wu, J., and Woo, C. H. (2001). Strain monitoring in FRP laminates and concrete beams using FBG sensors. Composite Structures, 51(1), 9-20.

Lee, Y.J., and Bassett, R. H. (2006). Application of a photogrammetric technique to a model tunnel. Tunnelling and Underground Space Technology, 21(1): 79-95.

Lee, W., Lee, W. -J., Lee, S.-B., and Salgado, R. (2004). Measurement of pile load transfer using the Fiber Bragg Grating sensor system. Canadian Geotechnical Journal, 41(6), 1222-1232.

Legge, T. F. H., Swart, P. L., Zyl, G van, and Chtcherbakov, A. A. (2006). A fibre Bragg grating stress cell for geotechnical engineering applications. Measurement Science and Technology, 17, 1173-1179.

Leng, J. S., Winter, D., Barnes, R. A., Mays, G. C., and Fernando, G. F. (2006). Structural health monitoring of concrete cylinders using protected fibre optic sensors. Smart Materials and Structures, 15(2), 302-308.

Li, A. G., Yue, Z. Q., Tham, L. G., Lee, C. F., and Law, K. T. (2005a). Field-monitored variations of soil moisture and matric suction in a saprolite slope. Canadian Geotechnical Journal, 42(1), 13-26.

Li, H. -N., Li, D. -S., and Song, G. -B. (2004). Recent applications of fiber optic sensors to health monitoring in civil engineering. Engineering Structures, 26(11), 1647-1657.

Li, Q. S., Li, Z. N., Li, G. Q., Meng, J. F., and Tang, J. (2005b). Experimental and numerical seismic investigations of the Three Gorges dam. Engineering Structures, 27, 501-13.

Li, Y. H., Jing, H. W., Liu, G., and Zhou, Z. G. (2007). Study on application of digital close range photogrammetry to model test of tunnel in jointed rock masses. Chinese Journal of Rock Mechanics and Engineering, 26(8), 1684-1690. (in Chinese)

Li, Z. K., Liu, H., Dai, R., and Su, X. (2005c). Application of numerical analysis principles and key technology for high fidelity simulation to 3-D physical model tests for underground caverns. Tunnelling and Underground Space Technology, 20(4), 390-399.

Li, Z. K., Lu, D. R., Wang, A. M., Nakayama, H., and Sun, J. S. (2003). Development and application of new technology for 3D geomechanical model test of large underground group caverns. Proceedings of ISRM 2003, Technology roadmap for rock mechanics, South African Institute of Mining and Metallurgy, 769-772.

Lin, C. P., and Tang, S. H. (2005). Development and calibration of a TDR extensometer for geotechnical monitoring. Geotechnical Testing Journal, 28(5), 1-8.

Lin, M. W., and Thaduri, J. (2006). Structural deflection monitoring using an embedded ETDR distributed strain sensor. Journal of Intelligent Material Systems and Structures, 17(5), 423-430.

Lin, Y. B., Chang, K. C., Chern, J. C., and Wang, L. A. (2005). Packaging methods of fiber-Bragg grating sensors in civil structure applications. IEEE Sensors Journal, 5(3), 419-424.

Liu, J., Feng, X. T., and Ding, X. L. (2003b). Stability assessment of the Three-gorges Dam foundation, China using physical and numerical modelling-Part II. numerical modelling. International Journal of Rock Mechanics and Mining Sciences, 40(5), 633-652.

Liu, J., Feng, X. T., Ding, X. L., Zhang, J., and Yue, D. M. (2003a). Stability assessment of the Three-gorges Dam foundation, China using physical and numerical modelling-Part I. physical model tests. International Journal of Rock Mechanics and Mining Sciences, 40(5), 609-631.

Liu, J. -G., Schmidt-Hattenberger, C., and Borm, G. (2002). Dynamic strain measurement with a fibre Bragg grating sensor system. Measurement, 32(2), 151-161.

Lo, Y. L., and Sirkis, J. S. (1997). Simple method to measure temperature and axial strain simultaneously using one in-fiber Bragg grating sensor. Proceedings SPIE, 3042, 237-243.

Luo, S. Q., Tan, S. A., and Yong, K. Y. (2000). Pull-out resistance mechanism of a soil nail reinforcement in dilative soils. Soils and Foundations, 4(1), 47-56.

Mair, R. J. (1979). Centrifugal modelling of tunnel construction in soft clay. Ph.D. Thesis. Cambridge University Engineering Department, UK.

Mair, R. J., Taylor, R. N., and Bracegirdle, A. (1993). Subsurface settlement profiIes above tunnels in clays. Geotechnique, 43(2), 315-320.

Majumder, M., Gangopadhyay, T. K., Chakraborty, A. K., Dasgupta, K., and Bhattcharya, D. K. (2008). Fibre Bragg gratings in structural health monitoring - present status and applications. Sensors and Actuators A: Physical, 147(1), 150-164.

Mao, M., and Taylor, C. A. (1997). Non-linear seismic cracking analysis of medium-height concrete gravity dams. Computers and Structures, 64(5-6), 1197-1204.

Martinez, A., Khrushchev, I., and Bennion, I. (2006). Direct inscription of Bragg gratings in coated fibers by an infrared femtosecond laser. Optics Letters, 31(11), 1603-1607.

Martt, D. F., Shakoor, A., and Greene, B. H. (2005). Austin Dam, Pennsylvania: the sliding failure of a concrete gravity dam. Environmental and Engineering

Geoscience, 11(1), 61-72.

Meguid, M. A., Saada, O., Nunes, M. A., and Mattar, J. (2008). Physical modeling of tunnels in soft ground: a review. Tunnelling and Underground Space Technology, 23(2), 185-198.

Meltz, G., Morey, W. W., and Glenn, W. H. (1989). Formation of Bragg gratings in optical fibers by a transverse holographic method. Optics Letters, 14(15), 823-825.

Metje, N., Chapman, D. N., Rogers, C. D. F., Henderson, P., and Beth, M. (2008). An optical fiber sensor system for remote displacement monitoring of structures - prototype tests in the laboratory. Structural Health Monitoring, 7(1), 51-63.

Meyerhof, G. G. (1976). Bearing capacity and settlement of pile foundations. Jounral of Geotechnical Engineering Division, ASCE, 102(GT3), 195-228.

Micron Optics, Inc. (2004). Si425 Optical Sensing Interrogator Instruction Manual. Atlanta, USA.

Micron Optics, Inc. (2007). Sm125 Optical Sensing Interrogator Instruction Manual. Atlanta, USA.

Mihailov, S. J., Smelser, C. W., Lu, P., Walker, R. B., Grobnic, D., Ding, H., Henderson, G., and Unruh, J. (2003). Fiber Bragg gratings made with a phase mask and 800-nm femtosecond radiation. Optics letters, 28(12), 995-997.

Milligan, G. W. E., and Tei, K. (1998). The pull-out resistance of model soil nails. Soils and Foundations, 38(2), 179-190.

Millis, S. W., Ho, A. N. L., Chan, E. K. K., Lau, K. W. K., and Sun, H. W. (2008). Instrumentation and real time monitoring of slope movement in Hong Kong. Proceedings of 12th International Conference of International Association for Computer Methods and Advances in Geomechanics, Goa, India, 4563-4576.

Ministry of Water Resources, P.R. China. (2005). Design Specification for Concrete Gravity Dams (SL319-2005). Chinese Water Conservancy and Hydro-electric

Power Publishers, Beijing. (in Chinese)

Mir, R. A., and Taylor, C. A. (1996). An investigation into the base sliding response of rigid concrete gravity dams to dynamic loading. Earthquake Engineering and Structural Dynamics, 25(19), 79-98.

Miyata, K. (1996). Walls reinforced with fiber reinforced plastic geogrids in Japan. Geosynthetics International, 3(1), 1-11.

Morey, W. W., Meltz, G., and Glenn W. H. G. (1989). Fiber optic Bragg grating sensors. Proceedings of SPIE, 1169, 98-107.

Morin, P. B., Leger, P., and Tinawi, R. (2002). Seismic behavior of post-tensioned gravity dams: shake table experiments and numerical simulations. Journal of Structural Engineering, ASCE, 128(2), 140-152.

Moyo, P., Brownjohn, J. M. W., Suresh, R., and Tjin, S. C. (2005). Development of fiber Bragg gating sensors for monitoring civil infrastructure. Engineering Structures, 27(12), 1828-1834.

Nellen, P. M., Frank, A., Broennimann, R., and Sennhauser, U. J. (2000). Optical fiber Bragg gratings for tunnel surveillance. Proceedings of SPIE, 3986, 263-270.

Nagai, T., Shogo, K., and Sun, J. (1996). Behavior of jointed rock masses around an underground opening under excavation using large-scale physical model tests. Proceedings of the Symposium on Rock mechanics, 116-120.

Ng, C. W. W., Zhan, L. T., Bao, C. G., Fredlund, D. G., and Gong, B. W. (2003). Performance of an unsaturated expansive soil slope subjected to artificial rainfall infiltration. Geotechnique, 53(2), 143-157.

Nkurunziza, G., Benmokrane, B., Debaiky, A.S., and Masmoudi, R. (2005). Effect of sustained load and environment on long-term tensile properties of glass fiber-reinforced polymer reinforcing bars. ACI Structural Journal, 102(4), 615-621.

Othonos, A., and Kalli, K. (1999). Fiber Bragg Gratings: Fundamentals and

Applications in Telecommunications and Sensing. Artech House, London.

Park, S. H., and Adachi, T. (2002). Laboratory model tests and FE analyses on tunneling in the unconsolidated ground with inclined layers. Tunnelling and Underground Space Technology, 17(2), 181-193.

Plizzari, G., Waggoner, F., and Saouma, V. E. (1995). Centrifuge modelling and analysis of concrete gravity dams. Journal of Structural Engineering, ASCE, 121(10), 1471-1479.

Posey, R., and Vohra, S. T. (1999). An eight-channel fiber-optic Bragg grating and stimulated Brillouin sensor system for simultaneous temperature and strain measurements, IEEE Photonics Technology Letters, 11(12), 1641-1643.

Pradhan, B., Tham, L. G., Yue, Z. Q., Junaideen, S. M., and Lee, C. F. (2006). Soil-nail pullout interaction in loose fill materials. International Journal of Geomechanics, ASCE, 6(4), 238-247.

Quiros, G. W., and Reese, L. G. (1977). Design procedures for axially loaded drilled shafts. Research Report No. 3-5-72-176, Center for Highway Research, University of Texas at Austin.

Ren, L., Li, H., Sun, L., and Li, D. (2004). FBG sensors for on-line temperature measurements, Proceedings of SPIE, 5319, 94-99.

Ren, L., Li, H. N., Li, X., Zhou, J., and Xiang, L. (2006). Application of FBG sensors in rolled concrete dam model. Proceedings of SPIE, 6174, Paper No. 617436.

Ren, X. H., Shu, J. Q., Ben, N. H., and Ren, H. Y. (2008). Stability analysis of concrete gravity dam on complicated foundation with multiple slide planes. Water Science and Engineering, 1(3), 65-72.

Rochon-Cyr, M., and Légerb, P. (2009). Shake table sliding response of a gravity dam model including water uplift pressure. Engineering Structures, 31(8), 1625-1633.

Roger, H., Chen, L., and Choi, J.-H. (2002). Effects of GFRP reinforcing rebars on shrinkage and thermal stresses in concrete. Proceedings of 15th ASCE Engineering Mechanics Conference, New York, 1-8.

Rossi, G. L., and Rondini, C. (2003). Development of a load cell based on Fiber Bragg Gratings Sensors. Proceedings of SPIE, 5144, 585-592.

Ruggeri, G. (2001). Sliding safety of existing gravity dams. http://cnpgb.inag.pt/IcoldClub/documents/Sliding_safety_FinalReport.pdf

Sakurai, S. (1997). Lessons learned from field measurements in tunneling. Tunnelling and Underground Space Technology, 12(4), 453-460.

Sakurai, S., Akutagawa, S., Takeuchi, K., Shinji, M., and Shimizu, N. (2003). Back analysis for tunnel engineering as a modern observational method. Tunnelling and Underground Space Technology, 18(2-3). 185-196.

Sato, T., Honda, R., Shibata, S., and Takegawa, N. (2000) Ground strain measuring system using optical fiber sensors. Proceedings of SPIE, 3986, 180-190.

Sawicki, A. (2000). Mechanics of Reinforced Soil. Balkema, Rotterdam.

Schlosser, F. (1982). Behaviour and design of soil nailing. Proceedings of International Symposium on Recent Development in Ground Improvement Techniques, Bangkok, Thailand, 399-413.

Schmidt-Hattenberger, C., and Borm, G. (1998). Bragg grating extensometer rods (BGX) for geotechnical strain measurements. Proceedings of SPIE, 3483, 214-217.

Schmidt-Hattenberger, C., Borm, G. and Amberg, F. (1999). Bragg grating seismic monitoring system. Proceedings of SPIE, 3860, 417-424.

Schmidt-Hattenberger, C., Naumann, M., and Borm, G. (2002). Dynamic strain detection using a fiber Bragg grating sensor array for geotechnical applications. Proceedings of European Workshop on Smart Structures in Engineering and Technology, Presquile de Giens, France, 227-232.

Schmidt-Hattenberger, C., Naumann, M. and Borm, G. (2003a). Fiber Bragg grating strain measurements in comparison with additional techniques for rock mechanical testing. IEEE Sensors Journal, 3 (1), 50-55.

Schmidt-Hattenberger, C., Straub, T., Naumann, M., Borm, G., Lauerer, R., Beck, C., and Schwarz, W. (2003b). Strain measurements by fiber Bragg grating sensors for in-situ pile loading tests, Proceedings of SPIE, 5050, 289-294.

Schroeck, M., Ecke, W., and Graupner, A. (2000). Strain monitoring in steel rock bolts using FBG sensor arrays. Proceedings of SPIE, 4074, 298-304.

Sen, R., Lyer, S., Issa, M., and Shahawy, M. (1991). Fiberglass pretensioned piles for marine environment. Advanced Composites Materials in Civil Engineering Structures, ASCE, New York, 348-359.

Shiu, Y. K., and Cheung, W. M. (2003). Long-term durability of steel soil nails. GEO Report No. 135, Civil Engineering and Development Dept., Government of Hong Kong Special Administrative Region, Hong Kong.

Singhvi, A., and Mirmiran, A. (2002). Creep and durability of environmentally conditioned FRP-RC beams using fiber optic sensors. Journal of Reinforced Plastics and Composites, 21(4), 351-373.

Sitharam, T. G., and Latha, G. M. (2002). Simulation of excavations in jointed rock mass using a practical equivalent continuum approach. International Journal of Rock Mechanics and Mining Sciences, 39(5), 517-525.

Skłodowski, M. (2003). Theory of application of fiber optics sensors to settlement monitoring of historical structures. Proceedings of AMAS Workshop on Smart Materials and Structures, Jadwisin, 291-299.

Spalton, C. D., Frame, J. A., and Fern, M. W. (1997). Instrumentation for slopes in Hong Kong. Proceedings of the Annual Seminar on Slope Engineering in Hong Kong. Balkema, Rotterdam, 267-275.

Sterpi, D., and Cividini, A. (2004). A Physical and numerical investigation on the stability of shallow tunnels in strain softening media. Rock mechanics and Rock Engineering, 37(4). 277-298.

Su, L. -J., Chan, T. C. F., Yin, J. -H., Shiu, Y. K., and Chiu, S. L. (2008). Influence of overburden pressure on soil-nail pullout resistance in a compacted fill. Journal of Geotechnical Geoenvironmental Engineering, ASCE, 134(9), 1339-1347.

Swann, L. H., Lorimer, M. J., Li, R. P. M, Chan, T. C. F., and Leung, F. W. K. (2007). Instrumented soil nail pull-out tests in decomposed tuff and working bond study. Proceedings of 27th HKIE Geotechnical Division Annual Seminar, Hong Kong, 287-292.

Talebinejad, I., Fischer, C., and Ansari, F. (2009). Low frequency fiber optic accelerometer for civil structural health monitoring. Proceedings of SPIE, 7294, Paper No. 729412.

Teng, L., Feng, L., Lin, H., Zhang, B., and Liu, C. (2006). A new fiber Bragg grating accelerometer. Proceedings of SPIE, 6357, Paper No. 63574C.

The State Economic and Trade Commission, P.R. China. (2000). Design Specification for Concrete Gravity Dams (DL5108-1999). China Electric Power Press, Beijing. (in Chinese)

Tinawi, R., and Guizani, L. (1994). Formulation of hydrodynamic pressure in cracks due to earthquake in concrete dams. Earthquake Engineering and Structural Dynamics, 23(7), 699-715.

Tinawi, R., Leger, P., Leclerc, M., and Cipolla, G. (2000). Seismic safety of gravity dams: from shake table experiments to numerical analysis. Journal of Structural Engineering, ASCE, 126(4), 518-529.

Tjin, S. C., Hao, J. Z., and Malik, R. (1998). Fiber optic pressure sensor using fiber Bragg grating. Proceedings of SPIE, 3429, 123-130.

U.S. Army Corps of Engineers. (1995). Engineering and Design-Gravity Dam Design.

Department of the Army, Washington, D.C.

Walton, J. M., and Yeung, Y. T. C. (1986). Fatigue performance of structural strands of pultruded composite rods. Journal of Institution of Mechanical Engineering, London, C/286/86, 315-320.

Wong, H. N., Ho, K. K. S., and Sun, H. W. (2006). The role of slope instrumentation in landslide risk management-Hong Kong Experience. Proceedings of the Conference on Landslide, Sinkhole, Ipoh, Malaysia, 1-33.

Wood, D. M. (2004). Geotechnical Modeling. Spon Press, London.

Xu, Q. J., Li, X., and Chen, Z. Y. (2007). Three-dimensional stability analysis of the dam foundation at Baise. Frontiers in Architecture and Civil Engineering in China, 1(2), 217-221.

Yan, F. Z., Tu, X. B., and Li, G. C. (2004). The uplift mechanism of the rock masses around the Jiangya dam after reservoir inundation, China Engineering Geology, 76, 141-154.

Yang, Y. W., Bhalla, S., Wang, C., Soh, C. K., and Zhao, J. (2007). Monitoring of rocks using smart sensors. Tunnelling and Underground Space Technology, 22(2), 206-221.

Yeung, A. T., Cheng, Y. M., Tham, L. G., Au, A. S. K., So, S. T. C., and Choi, Y. K. (2007). Field evaluation of a glass-fiber soil reinforcement system. Journal of Performance of Constructed Facilities, ASCE, 21(1), 26-34.

Yoshida, H., Horii, H., and Uno, H. (1995). Micromechanics-based continuum theory for jointed rock mass and analysis of large-scale cavern excavation. Proceedings of the 8th International Conference on Rock Mechanics, Tokyo, 689-692.

Yoshida, Y., Kashiwai, Y., Murakami, E., Ishida, S., and Hashiguchi, N. (2002). Development of the monitoring system for slope deformations with fiber Bragg grating arrays. Proceedings of SPIE, 4694, 296-303.

Zhang, C. H., Wang, G. L., Wang, S. M., and Dong, Y. X. (2002). Experimental tests of rolled compacted concrete and nonlinear fracture analysis of rolled compacted concrete dams. Journal of Materials in Civil Engineering, 14(2), 108-115.

Zhang, T. L. T., Ng, C. W. W., and Fredlund, D. G. (2006). Instrumentation of an unsaturated expansive soil slope. Geotechnical Testing Journal, 30(2), 1-11.

Zhang, W., Dai, J., Sun, B., Du, Y. (2007). FBG sensor network in Qinghai-Tibet Railway monitoring system. Proceedings of SPIE, 6830, Paper No. 68301.

Zhao, Y., and Ansari, F. (2002). Embedded fiber optic sensor for characterization of interface strains in FRP composite. Sensors and Actuators A: Physical, 100(2-3), 247-251.

Zhao, Y., Yang, J., Peng, B. -J., and Yang, S. Y. (2005). Experimental research on a novel fiber-optic cantilever-type inclinometer. Optics and Laser Technology, 37, 555-559.

Zhou, W., Chang, X. L., Zhou, C. B., and Liu, X. H. (2008) Failure analysis of high-concrete gravity dam based on strength reserve factor method. Computers and Geotechnics, 35(4), 627-636.

Zhou, W. -H., and Yin, J. -H. (2008). A simple mathematical model for soil nail and soil interaction analysis. Computers and Geotechnics, 35, 479-488.

Zhou, Z., Graver, T. W., Hsu, L., and Ou, J. -P. (2003). Techniques of advanced FBG sensors: fabrication, demodulation, encapsulation and their application in the structural health monitoring of bridges. Pacific Science Review, 5, 116-121.

Zhu, X. Y., and Pekau, O. A. (2007). Seismic behavior of concrete gravity dams with penetrated cracks and equivalent impact damping. Engineering Structures, 29, 336-345.

Zhu, W. S., Li, Y., Zhang, L., Xin, X. L., Sun, L. F., and Ma, Q. S. (2008a). Model test and numerical analyses on the stability of a cavern group. Proceedings of 42nd US

Rock mechanics Symposium and 2nd US-Canada Rock mechanics Symposium, San Francisco, Paper No. ARMA 08-194.

Zhu, W. S., Sui, B., Li, X. J., Li, S. C., and Wang, W. T. (2008b). A methodology for studying the high wall displacement of large scale underground cavern complexes and it's applications. Tunnelling and Underground Space Technology, 23(6), 651-664.

Zhu, W. S., and Wang, P. (1993). Finite element analysis of jointed rock masses and engineering application. International Journal of Rock Mechanics and Mining Sciences & Geomechanics Abstracts, 30(5), 537-544.

Zhu, W. S., Zhang, Q. B., Sun, L. F., Zhang, L., Li, S. -C., Zhang, Q. -Y., Yin, J. -H., and Zhu, H. -H. (2009). Study on application of displacement measurement method in 3-D physical model tests of cavern complex. Proceedings of 43rd US Rock Mechanics Symposium, Asheville, Paper No. ARMA 08-194.

Zhu, W. S., and Zhao, J. (2004). Stability and Modeling of Underground Excavations in Fractured Rocks. Elsevier, Amsterdam.

Zornberg, J. G., Mitchell, J. K., and Sitar, N. (1997). Testing of reinforced slopes in a geotechnical centrifuge. Geotechnical Testing Journal, 20(4), 470-480.